

**Development of new 1D metal based nanomaterials:  
Synthesis, characterisation and applications**



**Daniel Kehoe**

A thesis submitted to the University of Dublin, Trinity College for  
the degree of Doctor of Philosophy

School of Chemistry

Trinity College

Dublin 2

2019





# Summary

The main aim of this project was to develop new 1D metal based nanomaterials and explore their use for potential applications in catalysis. This work involves the synthesis, characterisation, and application of new AuAg ultrathin nanowires and studies the use of vortexing as method of inducing chirality in large aspect ratio Ag nanowires.

Chapter 1 provides a literature review and background information on the synthesis and application of 1D nanomaterials, particularly ultrathin materials. Topics such as chirality, plamonics and fuel cells are also discussed in detail. In addition the aims of the project are also outlined.

Chapter 2 provides information on the synthetic and experimental protocols used in this work. The characterisation techniques and equipment used are also detailed.

Chapter 3 describes a tunable synthesis of water soluble ultrathin AuAg nanowires using a novel protocol. The influence of various parameters in this synthesis and further optimization our protocol using temperature control are investigated. A new ultrathin AuAg nano-necklace structure was also synthesised and characterised. The ultrathin 1D AuAg nanomaterials were further used as catalysts for the electro-oxidation of ethylene glycol.

---

The chiral modification of 1D ultrathin AuAg nanomaterials using a facile ligand exchange method is detailed in Chapter 4.

In chapter 5 we investigate the use of our ultrathin AuAg nanowires as templates for the synthesis of novel 1D Pt, Rh, and RhPt nanomaterials. The resulting Pt and RhPt nanomaterials were further used as anodic catalysts for the electro-oxidation of methanol and formic acid.

Chapter 6 is dedicated to studying the influence of stirring on the observed chiroptical activity of large aspect ratio Ag nanowires. This chapter also includes the development of new chiral plasmonic-excitonic Ag nanowire@ quantum dot hybrid nanostructures.

Finally, chapter 7 outlines the overall conclusions and details future plans and some preliminary work.

# Declaration

This thesis is submitted for the degree of Doctor of Philosophy to the University of Dublin, Trinity College and has not been submitted before for any degree or examination to this or any other university. Other than where acknowledged, all work described herein is original and carried out by the author alone. Permission is granted so that the Library may lend or copy this thesis upon request. This permission covers only single copies made for study purposes, subject to normal conditions of acknowledgement.

---

Daniel kehoe

# Acknowledgements

First and foremost I would like to express my sincere thanks to my supervisor, Prof. Yurri Gun'ko for giving me the opportunity to work in his research group and for his excellent guidance and understanding throughout my Ph.D.

I would like to thank all the technical staff in the school of Chemistry (Manuel, Patsy, Tom and Mark) and in the Cocker Lab (Peggy, Peter and Gary). I would especially like to thank Neal Leddy, Clive Downing and Eoin Mc Carty for training me on TEM and SEM, without your help this work would not have been possible. I would also like to thank my collaborators Dr. John Gough and Prof. Louise Bradley (School of Physics, Trinity College Dublin) and to Luis (School of Chemistry, Trinity College Dublin) for his help with electrochemistry and trying to teach me spanish.

Thanks to all the members of the Gun'ko past and present. Finn and Sarah thanks so much for your help and putting the long hours in for

---

the EDX work. Thanks to the rest of the group for all the random office banter and deep scientific discussions: Shelley, Fearghal, Gary, Xue, Vera, Marina, Natalia, Olan, Alex and Raquel. Also I would like to thank my students particularly Thomas Sanchez, for all their help.

Finally, I would also like to thank all my family for their constant support. Mam, Dad, Elisha and Hayley: thanks for always being there for me and always encouraging me in everything. Last but not least, I would like to thank my fiancée Hilary, for encouraging me from day one and for all the much needed coffee breaks, I could not have done this without you.

# Abbreviations

0D = 0 dimension

1D = 1 dimension

2D = 2 dimension

3D = 3 dimension

a.u = arbitrary units

ACW = Anti-clockwise

ATR-IR = Attenuated total reflectance- Infrared

BINAP = (1,1-Binaphthalene-2,2-diyl)bis(diphenylphosphine)

CA = Chronoamperometry

CD = Circular dichroism

CTAB = Cetrimehylammonium bromide

CW = Clockwise

CV = Cyclic voltammetry

Cys= Cysteine

D- = Dextrorotary

DFT = Density functional theory

DMF = N,N-dimethylformamide

---

DNA = Deoxyribonucleic acid  
DnR = Dot'n'rod  
DTAB = Dodecyltrimethylammonium bromide  
EDX = Elemental dispersive x-ray  
EG = Ethylene glycol  
EGOR = Ethylene glycol oxidation reaction  
GCE = Glassy carbon electrode  
Glu = Gluthathione  
HAADF = High angle annular dark field  
HR-TEM = High resolution transmission electron microscopy  
 $J_b$  = Current density (backward scan)  
 $J_f$  = Current density (forward scan)  
L- = Levorotary  
LH = Langmuir-Hinshelwood  
M = Molar  
MW = molecular weight  
NNL = Nano-necklace  
NT = Nanotube  
np = Nanoparticle  
NW = Nanowire  
Oam = Oleylamine  
PVP = Polyvinyl pyrrolidone  
QD = Quantum dots

---

STEM = Scanning transmission electron microscopy

SEM = Scanning electron microscopy

TC= texture coefficient

TEM = Transmission electron microscopy

TGA = Thioglycolic acid

TP = Tetrapod

UV-Vis = Ultraviolet- visible

WORM = Write-once-read many times

XRD = X-ray diffraction



# Contents

<b>1</b>	<b>Introduction</b>	<b>1</b>
1.1	What are 1D nanomaterials and why do we need them ?	1
1.2	Synthesis of 1D nanomaterials . . . . .	3
1.2.1	Template synthesis of 1D nanomaterials . . . . .	5
1.2.2	Ligand controlled synthesis of 1D nanomaterials	6
1.3	Synthesis and application of ultrathin 1D nanomaterials . . . . .	8
1.4	1D Plasmonic metal nanomaterials . . . . .	14
1.5	Chirality and chiral nanomaterials . . . . .	17
1.5.1	Intrinsic chirality . . . . .	19
1.5.2	Ligand induced chirality . . . . .	21
1.5.3	Structural chirality . . . . .	24
1.6	Fuel cells . . . . .	27
1.6.1	Anode compartment . . . . .	29
1.6.2	Cathode compartment . . . . .	32
1.6.3	1D nanomaterials as Anodic catalyst . . . . .	33

---

1.7	Aims of the project . . . . .	35
<b>2</b>	<b>Experimental methods</b>	<b>58</b>
2.1	Chemicals and general materials . . . . .	58
2.2	Instrumentation and Preparation . . . . .	59
2.2.1	UV-Vis absorbance spectroscopy . . . . .	59
2.2.2	Circular Dichroism (CD) . . . . .	60
2.2.3	Attenuated total reflectance Infra-red spectroscopy (ATR-IR) . . . . .	61
2.2.4	X-Ray powder diffraction (XRD) . . . . .	62
2.2.5	Scanning Electron Microscopy (SEM) . . . . .	63
2.2.6	Transmission Electron Microscopy (TEM) . . . . .	65
2.2.7	Scanning Transmission Electron Microscopy (STEM)	67
2.2.8	Energy dispersive X-ray Spectroscopy (EDX) . . . . .	69
2.2.9	Electrochemistry . . . . .	70
2.3	Experimental protocols . . . . .	75
2.4	Experimental protocols of chapter 3 . . . . .	75
2.4.1	Synthesis of ultrathin AuAg nanowires . . . . .	75
2.4.2	Synthesis of ultrathin AuAg nano-necklaces . . . . .	75
2.4.3	Catalytic reduction of 4-nitrophenol using Ul- trathin AuAg nanowires . . . . .	76
2.4.4	Ultrathin AuAg nanowires as anodic catalyst for ethylene glycol oxidation . . . . .	76

---

2.4.5	AuAg nano-necklaces as anodic catalysts for ethylene glycol oxidation . . . . .	77
2.4.6	Experimental protocols of chapter 4 . . . . .	78
2.4.7	Chiral modification of 1D ultrathin AuAg nanomaterials . . . . .	78
2.4.8	Experimental protocols of chapter 5 . . . . .	78
2.4.9	Templated synthesis of RhPt dendritic nanowires	78
2.4.10	Templated synthesis of Pt dendritic nanowires .	79
2.4.11	1D Pt and RhPt assemblies for electrocatalytic oxidation of methanol, ethanol and formic acid .	79
2.4.12	Synthesis of AuAg nanowires@ Rh nanoparticle hybrid structures . . . . .	80
2.5	Experimental protocols of chapter 6 . . . . .	80
2.5.1	Synthesis of ultra-long Ag nanowires . . . . .	80
2.5.2	Synthesis of Ag nanowire@ quantum dot hybrid structures . . . . .	81
<b>3</b>	<b>Ultrathin AuAg nanowires</b>	<b>84</b>
3.1	Introduction . . . . .	84
3.2	Synthesis and characterisation of Ultrathin AuAg nanowires	87
3.3	Analysis of the pre-diluted solution . . . . .	96
3.4	Monitoring the formation of ultrathin AuAg nanowires following dilution . . . . .	99

---

3.5	Control study - investigating the role of Ag and Au in the formation of the nanowires . . . . .	103
3.6	Study on the effect of various solvents on nanowire formation . . . . .	106
3.7	Effect of dilution factor on nanowire formation . . . . .	113
3.8	Influence of different molecular weight PVP on nanowire synthesis . . . . .	115
3.9	Effect of temperature on nanowire synthesis . . . . .	121
3.10	Characterisation of AuAg nanowires synthesised by ageing at 25°C . . . . .	126
3.11	AuAg nano-necklaces . . . . .	129
3.12	Ultrathin AuAg nanowires for the catalytic reduction of 4-Nitro-phenol . . . . .	141
3.13	Electro-oxidation of ethylene glycol using Ultrathin AuAg nanowires as anodic catalysts . . . . .	146
3.14	Electro-oxidation of ethylene glycol using AuAg nano-necklaces as anodic catalysts . . . . .	153
3.15	Conclusion and future work . . . . .	157
<b>4</b>	<b>Chiral modification of 1D ultrathin AuAg nanostructures</b>	<b>172</b>
4.1	Introduction . . . . .	172

---

4.2	Chiral modification and characterisation of 1D AuAg nanostructures . . . . .	174
4.3	Time Monitored CD analysis of L-Glutathione modification . . . . .	185
4.4	Investigating the influence of thiol accessibility on lig- and exchange . . . . .	189
4.5	Conclusion and future work . . . . .	191
<b>5</b>	<b>Ultrathin AuAg nanowires as templates</b>	<b>197</b>
5.1	Introduction . . . . .	197
5.2	Synthesis and characterisation of Pt and RhPt dendritic nanowires . . . . .	200
5.3	Monitoring dendritic nanowire formation . . . . .	209
5.4	Investigating the role of the template . . . . .	212
5.5	Synthesis and characterisation of AuAg@Rh hybrid nanos- tructures . . . . .	214
5.6	Monitoring of AuAg@Rh hybrid formation . . . . .	221
5.7	Effect of Rh concentration on the template coverage . . . . .	225
5.8	Tuning of Rh coverage by varying reaction time . . . . .	229
5.9	Pt and RhPt dendritic nanowires as anodic catalysts for fuel cell applications . . . . .	232
5.9.1	Electro-oxidation of methanol . . . . .	234
5.9.2	Electro oxidation of formic acid . . . . .	238

---

5.10	Conclusion and future work . . . . .	242
<b>6</b>	<b>Chiral anisotropic nanostructures</b>	<b>253</b>
6.1	Introduction . . . . .	253
6.2	Synthesis and characterisation of ultra-long Ag Nanowires	256
6.2.1	Effect of stirring orientation on induced chirality	258
6.2.2	CD analysis of aligned Ag nanowires . . . . .	263
6.3	Vortex assisted synthesis of Ag NW @ quantum dot hybrid structures . . . . .	266
6.3.1	Synthesis and characterisation of Ag NW @ nano- nail hybrid structure . . . . .	266
6.3.2	Investigating the growth mechanism of Ag NW @ nano-nail hybrid structure . . . . .	273
6.3.3	Investigating the effect of stirring on helice chi- rality . . . . .	275
6.3.4	Investigating the effect of the capping agent on the helice chiralty . . . . .	278
6.3.5	Ag nanowire@ Dot'n'rod hybrid structures . . . . .	281
6.3.6	Investigation of the growth mechanism of Ag NW @ Dot n rod hybrid structure . . . . .	286
6.4	Photoluminescent analysis of Ag NWs @DnR hybrid structure . . . . .	290
6.5	Conclusion and future work . . . . .	294

---

<b>7</b>	<b>Conclusions and future work</b>	<b>305</b>
7.1	Conclusions . . . . .	305
7.2	Future work and preliminary studies . . . . .	307
7.2.1	Investigating the effect of the capping agent on the morphology of RhPt dendritic nanowires . .	308
7.2.2	Ag nanowire@ quantum tetrapod hybrid structure	310
7.2.3	Ag nanowire@ AuAg nanowire hybrid structure	314
<b>8</b>	<b>Appendix</b>	<b>i</b>

# List of Figures

1.1	Classification of nanomaterials by dimensionality. . . .	2
1.2	A proposed mechanism for 1D nanomaterial formation using a surfactant micelle: A) formation of cylindrical micelle, B) growth of 1D material inside a micelle and C) removal of the template. D-F) same process only the exterior of an inverted micelle is used as the template. Image reproduced from ref 29. . . . .	6
1.3	Proposed mechanism for PVP directed growth of Ag NWs, where the arrows represent the migration of Ag atoms to the 111 facets and the grey region represents the PVP capped 100 facets. Image reproduced from ref 39. . . . .	8
1.4	MOF as templates for ultrathin Au and Pd nanomaterials. Image reproduced from ref 65. . . . .	9
1.5	Schematic presentation of the synthesis of Pt NT and Pd Nws using Te NWs as sacrificial templates. Image reproduced from ref 74 . . . . .	11



---

1.6	Olelyamine micelle proposed for ultrathin anisotropic growth of Au nanowires. Image reproduced from ref 43.	12
1.7	Light scattering images of HaLa cells following A) no treatment, B) treatment from non-transferrin conjugated polyelectrolyte capped Au NRs and c) treatment with transferrin conjugated polyelectrolyte capped Au NRs. Image reproduced from ref 101 . . . . .	15
1.8	Local electric field distribution showing the maxima (top) and minima (bottom) emission at the branched NW as a function of polarisation angle. Image reproduced from ref 104. . . . .	17
1.9	S-Thalidomide (left) and R-Thalidomide (right) enantiomers. . . . .	18
1.10	TEM images (A and B) and atomistic models of right (C) and Left (D) screw dislocations. Image reproduced from ref 134. . . . .	21
1.11	Chiral memory effect for CdTs nanocrystals. Image reproduced from ref 146. . . . .	23
1.12	proposed confirmation of cinchonadine on a Pt surface. Image reproduced from ref 149. . . . .	24
1.13	Helical self assemblies of Au nanorods. Image reproduced from ref 159. . . . .	26

---

1.14	TEM (A,C) and corresponding TEM tomography images (B,D) of Au NWs prepared from left and right handed templates respectively. Image reproduced from ref 162. . . . .	27
1.15	Basic principle of a direct methanol fuel cell. Image reproduced from ref 167 . . . . .	28
1.16	Proposed mechanisms for the electro-oxidation of methanol. Image reproduced from ref 172. . . . .	30
1.17	Proposed mechanismss for the electro-oxidation of EG. Image reproduced from ref 180. . . . .	31
1.18	Proposed mechanisms for the oxygen reduction reaction. Asterix denotes an adsorbed species. Image reproduced from ref 182. . . . .	33
2.1	Principle of ATR-IR. Image reproduced from reference 1. . . . .	61
2.2	Basic set-up of a scanning electron microscope. image reproduced from ref 2. . . . .	64
2.3	Basic set-up of a Transmission electron microscope. Image reproduced from ref 3. . . . .	66
2.4	Basic set-up for scanning transmission electron microscope. Image reproduced from ref 4. . . . .	68
2.5	Basic principle of EDX. Image reproduced from ref 5. . . . .	70

---

2.6	Electrochemical cell set up with working electrode (green), reference electrode (white) and counter electrode (red).	72
3.1	Schematic presentation of the preparation of AuAg NWs (top) and TEM images (bottom) of NWs produced fol- lowing dilution with water after various days of aging. .	88
3.2	UV-vis spectra of NWs produced following dilution af- ter each day of aging. . . . .	90
3.3	HR-TEM images of NWs produced following dilution after 1 day of aging . . . . .	91
3.4	XRD pattern for AuAg ultrathin nanowires. . . . .	92
3.5	STEM analysis of AuAg nanowires produced following dilution after 1 day of aging. . . . .	94
3.6	STEM-EDX map (top) of AuAg nanowires where A and B denotes the L-and K- line of Au and C denotes the L- line of Ag and the associated EDX spectrum (bottom).	95
3.7	TEM image (A), STEM image (B), size distribution (C) and UV-Vis spectrum (D) (with photograph inset of solution ) of pre-diluted solution. . . . .	97
3.8	HAADF STEM (A) and EDX map of pre-diluted AuAg NWs were and B and C denotes the L- line of Ag and M- line of Au respectively. The associated EDX spectrum (bottom) is also detailed. . . . .	98

---

3.9	TEM analysis monitoring the growth of AuAg nanowires following dilution with water . . . . .	100
3.10	UV-Vis analysis monitoring the growth of AuAg nanowires following dilution with water. . . . .	101
3.11	TEM images of Ag control after 1 (A) and 3 (B) days aging following dilution and UV-Vis spectra of products produced following dilution after each day. . . . .	104
3.12	TEM image of Au control after 1 (A) and 3 (B) days aging following dilution and UV-Vis spectra of products produced following dilution after each day. . . . .	105
3.13	TEM (left) and UV-Vis(right) analysis of nanowires produced following dilution with water (A), methanol (B), ethanol (C) and isopropanol (D) after 1 day of aging. Photograph inset of final solution. . . . .	108
3.14	TEM (left) and UV-vis(right) analysis of nanowires produced following dilution with water (A), methanol (B), ethanol (C) and isopropanol (D) after 2 day of aging. Photograph inset of final solution. . . . .	109
3.15	TEM (left) and UV-vis(right) analysis of nanowires produced following dilution th water (A), methanol (B), ethanol (C) and isopropanol (D) after 3 days of aging. Photograph inset of final solution. . . . .	110

---

3.16	TEM images and UV-Vis spectra studying the effect of 5 ml (left) and 10 ml (right) dilution factors on nanowire growth. . . . .	113
3.17	Kinetic curves for rate of formation of AuAg nanowires following dilution with 5 and 10 mL at 324 nm. . . . .	114
3.18	TEM (left) and UV-Vis spectra (right) studying the effect of 29K (A), 40K (B), 55K (C) and 360K (D) PVP on nanowire growth following dilution after 1 day of aging. . . . .	117
3.19	TEM images (left) and UV-Vis spectra (right) studying the effect of 29K (A), 40K (B), 55K (C) and 360K (D) PVP on nanowire growth following dilution after 3 days of aging. . . . .	120
3.20	TEM and UV-Vis analysis of products following dilution after aging at various temperatures for 18 hrs. . . . .	122
3.21	Reaction presentation summarizing the products produced following dilution after aging at various temperatures for 18 hrs. . . . .	124
3.22	TEM images of Ag and Au control produced following dilution after aging at 20°C (A and B) and 25°C (C and D). . . . .	125
3.23	HR-TEM image of AuAg NWs produced following dilution after aging at 25°C for 18 hrs. . . . .	126

---

3.24	HAADF STEM image (A), EDX line profile (B) and EDX spectrum (C) of AuAg NWs produced following dilution after aging at 25 °C . . . . .	127
3.25	XRD pattern of AuAg NWs produced following dilution after aging at 25 °C . . . . .	128
3.26	TEM images and size distributions of the various regions of the AuAg NNLs. . . . .	131
3.27	UV-Vis spectrum of AuAg NNLs . . . . .	133
3.28	HR-TEM analysis of the various regions of the AuAg NNLs . . . . .	134
3.29	STEM analysis of AuAg NNLs. . . . .	136
3.30	XRD pattern of ultrathin AuAg NNLs. . . . .	137
3.31	EDX line map analysis of AuAg NNLs. . . . .	139
3.32	TEM image of 35°C aged solution prior to dilution. . .	141
3.33	UV-Vis analysis monitoring the catalytic reduction of 4-nitrophenol using ultrathin AuAg nanowires produced after 1 day( top) and 3 days (middle) and kinetic curves for the rate of reduction (bottom) at 400 nm . . . . .	143
3.34	CV curves (top) at 50 mV s <sup>-1</sup> and i-t curves over 4000 s at 0.2 V (bottom) for 3.6 and 9.2 nm AuAg NWs versus saturated Calomel electrode in a 1 M KOH solution containing 0.5 M EG. . . . .	149

---

3.35	CV analysis at scan rates of 35, 50, 75 and 90 mV s <sup>-1</sup> for 9.2 (A) and 3.6 nm (B) AuAg NW versus saturated Calomel reference electrode and corresponding plot of current density vs square root of scan rate (C) in a 1 M KOH solution containing 0.5 M EG. . . . .	152
3.36	CV analysis (top) at 50 mV s <sup>-1</sup> and i-t curve over 4000 s at 0.2 V (bottom) for AuAg NNLs versus saturated Calomel electrode in a 1 M KOH solution containing 0.5 M EG. . . . .	154
3.37	CV analysis (top) at scan rates of 25, 35, 50, 75 and 90 mV s <sup>-1</sup> versus saturated Calomel electrode and plot of current density vs square root of scan rate (bottom) for AuAg NNLs in a 1 M KOH solution containing 0.5 M EG. . . . .	156
4.1	CD and UV-Vis spectra (left) for D and L- Cys capped AuAg NWs and TEM image (right) of L-Cys capped AuAg nanowires. . . . .	178
4.2	IR spectra of PVP and PVP capped AuAg NWs (top) and L-Cys and L-Cys capped AuAg NWs (bottom). . .	179
4.3	CD and UV-Vis spectra (left) and TEM image (right) of AuAg nanowires modified with L-Glutathione. . . .	182
4.4	IR spectra of PVP and PVP capped AuAg NWs (top) and L-Glu and L-Glu capped AuAg NWs (bottom). . .	183

---

4.5	CD spectra of NNL and AuAg NWs (3.6 nm av.diameter) modified with L-Cys (left) and L-Glu capped NNL (right).	184
4.6	TEM images of 3.6 nm AuAg nanowires (A) and NNLs (B) modified with L-Cys. . . . .	185
4.7	Time monitored CD analysis (top) and plot of CD signal with respect to time at 350 nm (bottom) for L-Glu ligand exchange with AuAg NWs. . . . .	186
4.8	Time monitored CD analysis (top) and plot of CD signal with respect to time at 350 nm (bottom) for L-Glu ligand exchange with AuAg NNLs. . . . .	188
4.9	IR spectra of PVP and TGA capped AuAg NWs with structure of TGA inset. . . . .	190
4.10	TEM image of AuAg NWs capped with TGA. . . . .	191
5.1	TEM images of Pt (A) and RhPt (B) dendritic nanowires and associated size distributions. . . . .	201
5.2	UV-Vis spectra of Pt (left) and RhPt (right) dendritic nanowires. . . . .	202
5.3	HR-TEM images of Pt dendritic nanowires (left) and RhPt dendritic nanowires (right). . . . .	203
5.4	HAADF STEM image of Pt (left) and RhPt (right) dendritic nanowires. . . . .	204
5.5	XRD analysis of Pt (bottom)and RhPt (top) of dendritic nanowires. . . . .	205



---

5.6	HAADF STEM image (A), EDX maps of Pt and Rh L lines (B) and EDX spectrum (C) of RhPt dendritic NWs. The red lines in the spectrum highlight the absence of Ag and Au peaks. . . . .	207
5.7	HAADF STEM image (A), EDX line profile (B) and EDX spectrum (C) of Pt dendritic NWs. . . . .	208
5.8	TEM images monitoring the formation of RhPt dendritic nanowires over time. . . . .	210
5.9	UV-Vis spectra monitoring the formation of RhPt dendritic nanowires over time. . . . .	211
5.10	TEM images of Rh, Pt and RhPt controls in the absence of templates and associate UV-Vis spectra. . . . .	213
5.11	HR-TEM images of AuAg@Rh hybrid structure . . . .	215
5.12	UV-Vis spectra of AuAg NWs and AuAg@Rh hybrid structure. . . . .	217
5.13	STEM images of AuAg@Rh hybrid nanostructure (top) and size distribution of Rh nanoparticles (bottom). . .	218
5.14	XRD analysis of AuAg NWs (bottom) and AuAg@Rh hybrid structure (top). . . . .	219
5.15	HAADF STEM image (A), EDX line profile (B) and EDX spectrum (C) of AuAg NWs@Rh hybrid structure.	221
5.16	TEM images monitoring the growth of AuAg@Rh hybrid structure over time. . . . .	222

---

5.17	UV-Vis analysis monitoring the formation of AuAg@Rh hybrid structure over time (A) and UV-Vis spectra of the final supernatant (B) and purified precipitate (C). . .	223
5.18	TEM image of supernatant from the time monitored study of AuAg@Rh formation. . . . .	225
5.19	TEM analysis detailing the variation in Rh coverage on AuAg NWs with a change in Rh concentration . . . . .	227
5.20	Reaction scheme detailing the change in coverage associated with a change in Rh concentration. . . . .	228
5.21	HR-TEM images of AuAg@Rh hybrids produced after 3 min (left) and 12 min (right). . . . .	230
5.22	HAADF-STEM analysis of AuAg@Rh hybrids produced after 3 min (top) and 12 min (bottom). . . . .	231
5.23	CV analysis of methanol oxidation at 50 mV s <sup>-1</sup> for Pt and RhPt dendritic NWs versus Ag/AgCl reference electrode in a 0.5 M perchloric acid solution containing 1M methanol. . . . .	234
5.24	CV analysis at scan rates of 25, 50, 75 and 90 mV s <sup>-1</sup> for Pt(A) and RhPt dendritic (B) NWs versus Ag/AgCl reference electrode and corresponding plot of current density vs square root of scan rate (C) in a 0.5 M perchloric acid solution containing 1 M Methanol. . . . .	237

---

5.25	CV analysis of formic acid oxidation at 50 mV s <sup>-1</sup> for Pt and RhPt dendritic NWs versus Ag/AgCl reference electrode in a 1 M H <sub>2</sub> SO <sub>4</sub> solution containing 0.5 M Formic acid. . . . .	238
5.26	CV analysis at scan rates of 35, 50, 75 and 90 mV s <sup>-1</sup> for Pt(A) and RhPt dendritic (B) NWs versus Ag/AgCl reference electrode and corresponding plot of current density vs square root of scan rate (C) in a 1 M H <sub>2</sub> SO <sub>4</sub> solution containing 0.5 M formic acid. . . . .	241
6.1	SEM image (A), UV-vis spectrum (B) with photograph of solution in-set and size distribution (C) of Ag NWs.	257
6.2	CD spectra of CW and ACW stirred Ag NWs (top). Time monitored CD spectra of Ag NWs (bottom) showing the change in chiroptical activity following 10 mins of ACW stirring. . . . .	259
6.3	SEM image of ACW stirred Ag NWs. . . . .	261
6.4	Experimental set up (A), photograph of the dried sample (B) and SEM image (C) of Ag NWs dried on a glass slide while continuously stirring ACW. . . . .	262
6.5	Unaligned (A) and aligned (B) Ag NWs on a quartz substrate viewed through a X50 microscope. . . . .	264
6.6	CD response of the aligned Ag NWs on a quartz substrate to left and right circularly polarised light. . . . .	265

---

6.7	TEM images (A and B), size distributions (C-E)) and emission spectrum (F) of CdSe/CdS nano-nails. . . . .	267
6.8	CD spectra of L- and D- capped CdSe/CdS nano-nails.	268
6.9	SEM image of hybrid structure after 8 days of aging using a racemic solution of cys capped nano-nails. . . . .	269
6.10	SEM images showing left (top) and right (bottom) handed helices after 8 days of aging using a racemic solution of Cys capped nano-nails. . . . .	270
6.11	STEM image (top) and EDX spectrum (bottom) of self assembled nano-nails after 8 days of aging using a racemic solution of Cys capped nano-nails. . . . .	272
6.12	SEM image of a racemic mixture of L- and D-Cys capped nano-nails aged in the absence of Ag nanowires after 8 days. . . . .	273
6.13	SEM images (left), CD and UV-Vis (right) spectra monitoring the formation of hybrid structure over several days. A racemic mixture of L- and D-Cys capped nano-nails were used in this case. . . . .	274
6.14	SEM images (left) and CD (right) analysis monitoring the formation of Ag nanowire- nano-nail hybrid structure over various days for CW and ACW stirring using a racemic mixture of Cys capped nano-nails. . . . .	276

---

6.15	SEM image (top) and CD analysis (bottom) of Ag NW @nano-nail hybrid structure after 8 days of aging using D- and L-cysteine capped nano-nails. The SEM image is of L-Cys capped nano-nails respectively. . . . .	279
6.16	SEM image (top), CD and UV-Vis spectra (bottom) of Ag NW @nano-nail hybrid capped with TGA after 8 days of aging . . . . .	281
6.17	TEM images (top), size distributions (middle) and emission spectrum (bottom) of CdSe/CdS DnRs. . . . .	283
6.18	CD spectra of L- and D- capped CdSe/CdS DnRs. . . . .	284
6.19	SEM image of Ag NWs@ DnR hybrid structure after 8 days of aging using a racemic solution of D- and L-Cys capped DnRs. . . . .	285
6.20	SEM images (left), CD and UV-Vis analysis (right) monitoring the formation of the Ag@ DnR hybrid structure over 8 days of aging with continuous stirring using TGA capped DnRs. . . . .	287
6.21	SEM images (left), CD and UV-Vis spectra (right) of hybrid structure after 4 and 8 days of aging using a racemic solution of Cys capped DnRs. . . . .	289
6.22	FLIM image (left) and corresponding photoluminescence spectrum (right) of Ag NW@ DnR hybrid structure. . . . .	291

---

6.23	SEM image of Ag NW@ DnR hybrid structure overlaid on its corresponding FLIM image. . . . .	292
7.1	Structure of DTAB (A), TEM images (B and C) and UV-Vis spectra of DTAB (D) and DTAB capped RhPt assemblies (E). . . . .	309
7.2	TEM images (top), size distributions (middle) and emission and UV-Vis spectrum (bottom) of CdSe/CdS TPs.	311
7.3	SEM images (left), CD and UV-Vis analysis (right) monitoring the formation of the Ag@ TP hybrid structure over 8 days of aging using TGA capped TPs. . . .	313
7.4	SEM images (left), CD and UV-Vis analysis (right) monitoring the formation of the Ag@ AuAg hybrid structure over 4 days of aging using L-Cys capped AuAg NWs.	316
7.5	TEM images (left), CD and UV-Vis analysis (right) for L-cys capped AuAg NWs dispersed in water (A) and in ethanol (B). . . . .	318
7.6	SEM images of L-cys capped AuAg NWs dispersed in ethanol, pre (A) and post (B) vortex stirring and associated CD spectra (C). . . . .	319
A1	TEM images showing the reproducibility of the day aged synthesis of AuAg NWs following the dilution step.	i

---

A2	Size distribution of ultrathin AuAg NWs produced after 3 days of aging with average diameter of 3.6 nm. . . . .	ii
A3	Size distribution of ultrathin AuAg NWs produced using a dilution factor of 5 after 1 day of aging with average diameter of 8 nm. . . . .	ii
A4	Size distribution of ultrathin AuAg NWs produced using a dilution factor of 10 after 1 day of aging with average diameter of 8.8 nm. . . . .	iii
A5	Size distribution of ultrathin AuAg NWs produced using 29K PVP after 1 day of aging with average diameter of 4.3 nm. . . . .	iii
A6	Size distribution of ultrathin AuAg NWs produced using 55K PVP after 1 day of aging with average diameter of 7.5 nm. . . . .	iv
A7	Size distribution of ultrathin AuAg NWs produced using 360K PVP after 1 day of aging with average diameter of 9.2 nm. . . . .	v
A8	TEM images showing the reproducibility for the temperature controlled synthesis at 20(A), 25 (B) and 35 °C (C) following the dilution step. . . . .	vi
A9	Size distribution of ultrathin AuAg NWs produced after aging for 18 hours at 25°C with average diameter of 3.6 nm. . . . .	vii

---

A10	Comparison of IR spectra from PVP and Cys capped AuAg NWs with ascorbic acid. . . . .	viii
A11	TEM images showing the reproducibility for the synthesis of Pt (Left) and RhPt (right) dendritic NWs . . .	ix
A12	Size distribution of RhPt dendritic NWs produced after 2.5 mins with average diameter of 15.1 nm. . . . .	x
A13	Size distribution of RhPt dendritic NWs produced after 10 mins with average diameter of 15.5 nm. . . . .	x
A14	Size distribution of RhPt dendritic NWs produced after 15 mins with average diameter of 22.4 nm. . . . .	xi
A15	Size distribution of RhPt dendritic NWs produced after 25 mins with average diameter of 24.7 nm . . . . .	xi
A16	TEM images showing the reproducibility for the synthesis of AuAg@Rh hybrid nanostructures. . . . .	xii
A17	CV analysis of H <sub>2</sub> SO <sub>4</sub> at 50 mV s <sup>-1</sup> for Pt (top) and RhPt dendritic (bottom) NWs versus Ag/agCl reference electrode in a 1 M H <sub>2</sub> SO <sub>4</sub> solution. . . . .	xiii
A18	ESCA noramlised CV analysis of formic acid oxidation at 50 mV s <sup>-1</sup> for Pt (top) and RhPt (bottom) dendritic NWs versus Ag/AgCl reference electrode in a 1 M H <sub>2</sub> SO <sub>4</sub> solution containing 0.5 M Formic acid. . . . .	xv
A19	SEM images of Ag NW@DnR hybrid structure showing complete coverage of the NW after 16 days of aging. . .	xvi



# List of Tables

3.1	Texture coefficient analysis of AuAg ultrathin NWs produced after 1 day of aging . . . . .	93
3.2	Change in peak position following dilution with various alcohols . . . . .	112
3.3	Texture coefficient analysis of AuAg ultrathin NWs produced after 25°C . . . . .	129
3.4	d spacing values in each region of the AuAg NNLs . . .	135
3.5	Texture coefficient analysis of AuAg NNL . . . . .	138
3.6	Catalytic reduction of 4-Nitrophenol by various noble metal nanomaterials . . . . .	146
3.7	Electro-oxidation of EG by various Au based catalysts in alkaline medium . . . . .	151
4.1	Chiral modification of ultrathin AuAg nanowires . . .	176
5.1	Texture coefficient analysis of Pt dendritic NWs . . . .	206
5.2	Electro-oxidation of methanol by various Pt based catalyst in acidic media. . . . .	236

5.3	Electro-oxidation of formic acid by various Pt based catalyst in acidic media. . . . .	240
8.1	Texture coefficient analysis of AuAg ultrathin NWs produced after 1 day of aging . . . . .	xvii

# Chapter 1

## Introduction

### 1.1 What are 1D nanomaterials and why do we need them ?

The field of nano research has progressed significantly in recent years and continues to grow unabated. The development of new and exciting nanostructures with unique properties has undoubtedly broadened many areas in science from sensing and electronics to biomedical applications.

What are nanomaterials? Nanomaterials are classed as any material having at least one dimension confined between 1-100 nm. The word nano derives from the greek work "nanos" meaning dwarf and deals with materials that are 1 billionth of any unit. It is due this small size domain that nanomaterials exhibit chemical and physical proper-

ties unseen in the bulk material. The main feature that discriminates the various types of nanomaterials is their dimensionality. Using the scheme by Pokropivny and Skorokhod a nanomaterial is defined as 0D, 1D, 2D or 3D depending on the number of dimensions that are not confined to the nanoscale (Figure 1.1).<sup>1</sup> For instance 0D nanomaterials have all dimension confined to the nanoscale and are typically spherical particles or clusters. 1D nanomaterials on the other hand have at least 2 dimensions confined to the nanoscale and show preferential growth along one given direction. These include structures such as nanowires, nanofibers and nanorods. In the case of 2D nanomaterials, these have 2 dimensions outside the nanoscale and include nanosheets while 3D nanomaterials have all dimension out of the nanoscale and include nanoscaffolds. For the purpose of this work only one 1D nanomaterials will be considered

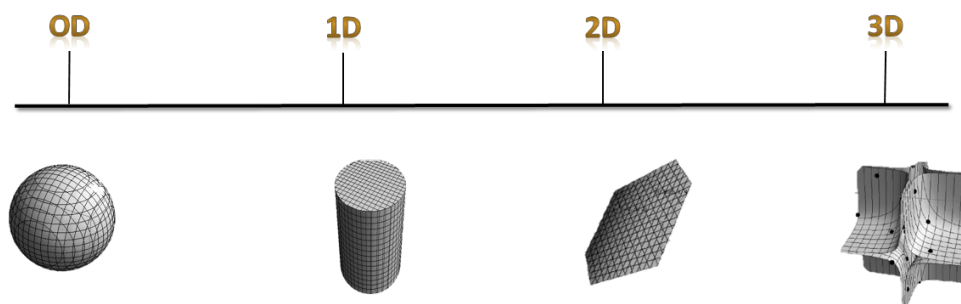


Figure 1.1: Classification of nanomaterials by dimensionality.

The demand for new 1D nanomaterials continues to grow each year as

these materials offer inherently interesting mechanical, electronic and optical properties.<sup>2-5</sup> These features make 1D nanomaterials crucial for our future technology and are currently being extensively developed for the next generation of flexible and wearable soft devices.<sup>6</sup> In addition, 1D nanomaterials have large surface-to-volume ratios making them also ideal for catalysis and sensing. Over the next few sections the underlying theory behind the synthesis, properties and applications of 1D nanostructures will be discussed.

## 1.2 Synthesis of 1D nanomaterials

The synthesis of 1D nanomaterials, and indeed all nanomaterials involves 2 fundamental steps, namely nucleation and growth. The nucleation process involves the formation of seeds which act as building blocks. As the concentration of seeds increases they aggregate and grow to form a larger structure. Control over this growth process is key to producing anisotropic 1D nanostructures. Typically a seed mediated growth approach is used to produce 1D nanomaterials.<sup>7,8</sup> This involves the reduction of metal precursor(s) in the presence of pre-made seeds. These pre-made seeds act as a template to guide the growth of the resulting nanomaterial. This heterogeneous nucleation method has the benefit of reducing spontaneous nucleation from oc-

curing and offers greater shape control. The growth mechanism of 1D nanomaterials is commonly described by an oriented attachment type mechanism.<sup>9,10</sup> This is a "match and dock" process whereby, the resulting nanostructure is formed by the alignment and fusion of seeds or nanoparticles. Factors such as coulombic interactions, Van der Waals interactions and dipole interactions have been attributed as the main driving forces in this mechanism.

Over the years various synthetic methods have been developed to achieve 1D growth and are categorised as either "top-down" or "bottom-up" methods. "Top-down" methods include chemical vapour deposition (CVD)<sup>11-13</sup> and vapour-liquid-solid methods.<sup>12,14</sup> While these methods produce high purity nanomaterials they require high operating temperatures, strict experimental conditions and require technically challenging and expensive equipment. In relation to "bottom-up" approaches, these have been recognised as more viable means to producing 1D nanomaterials on a large scale. These methods by comparison to "top down" are in general faster, cheaper and more facile. The most common "bottom up" approaches for producing 1D nanomaterials are templating and ligand control methods.

### 1.2.1 Template synthesis of 1D nanomaterials

Templating is one of the most effective methods of achieving controlled synthesis of 1D nanomaterials. In this approach, the template serves as scaffold to guide the 1D anisotropic growth of the material. Templating is categorised as either "hard" or "soft" depending on the choice of template used. Hard templates include the use of porous materials like aluminium oxide,<sup>14,15</sup> carbon nanotubes<sup>16,17</sup> and mesoporous silicas.<sup>18,19</sup> These methods use the pore channels as a matrix for growing the 1D nanomaterials. The benefit of this technique is that the resulting nanomaterial can be tailored by changing the dimensions of the pores in which they are grown. Aluminium oxide is notably one of the most widely used hard templates.<sup>20</sup> Typically sol-gel<sup>21,22</sup> or electrodeposition methods<sup>20,23</sup> are used to fill the pores in these processes.

In the case of soft templating, this involves the use of soft matter like polymers,<sup>24,25</sup> biomolecules<sup>26-28</sup> and mesophase surfactants<sup>29-32</sup> to control 1D anisotropic growth. Surfactants in particular represent an interesting class of soft template as these rely on the formation of ordered vesicles, micelles or liquid films which act as reactors where nanomaterials can be grown (Figure 1.2).<sup>33</sup> For example cetyltrimethylammonium bromide (CTAB) forms cylindrical micelles and many research groups have utilized this as an effective method for producing

Au nanorods.<sup>34-38</sup> One of the major benefits of soft templating, especially with surfactants, is that the template material can be easily removed after the synthesis. Compared to hard templating, post synthesis removal of the template is a significant issue requiring additional and often harsh synthetic steps.

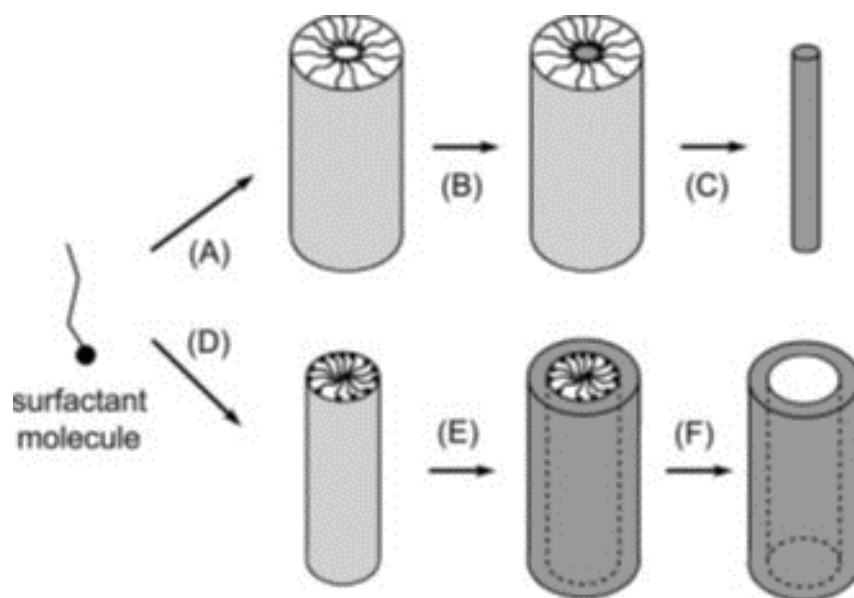


Figure 1.2: A proposed mechanism for 1D nanomaterial formation using a surfactant micelle: A) formation of cylindrical micelle, B) growth of 1D material inside a micelle and C) removal of the template. D-F) same process only the exterior of an inverted micelle is used as the template. Image reproduced from ref 29.

### 1.2.2 Ligand controlled synthesis of 1D nanomaterials

Ligand control synthesis involves the use of capping agents which pref-



erentially bind onto different facets of the seeds. Since the facets are capped to different extents anisotropic growth can thus occur on the least protected (capped) facet(s). For instance polyvinylpyrrolidone (PVP) is widely used in the synthesis of Ag NWs.<sup>39–42</sup> Xia *et al.*<sup>43</sup> demonstrated using a typical polyol method the reduction of  $\text{AgNO}_3$  into Ag NWs using ethylene glycol as the solvent and reducing agent and PVP as the capping agent. In this reaction the reduction of  $\text{AgNO}_3$  results in the formation of multiply twinned Ag nanoparticles with a decahedron shape. These nanoparticles present 111 facets on the ends and 100 facets on the sides. Since PVP binds more strongly to the 100 facets elongation and growth occurs at the 111 facets resulting in NWs (Figure 1.3). These ligand controlled methods are highly versatile and are widely used to produce nanomaterials of various morphologies.<sup>44,45</sup> In addition purification and recovery of products from this method can be simply achieved by processes like centrifugation.

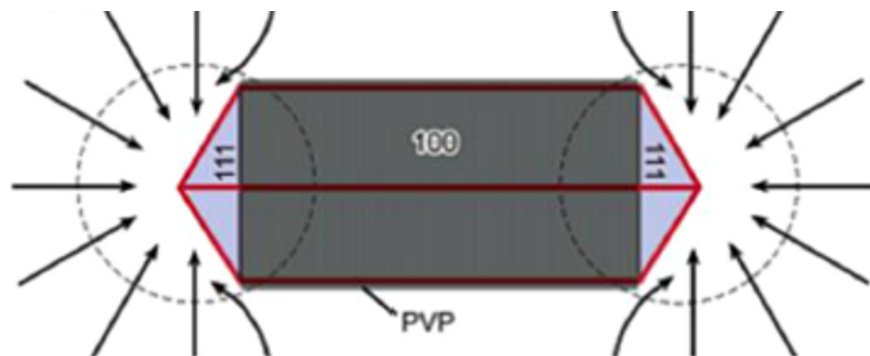


Figure 1.3: Proposed mechanism for PVP directed growth of Ag NWs, where the arrows represent the migration of Ag atoms to the 111 facets and the grey region represents the PVP capped 100 facets. Image reproduced from ref 39.

### 1.3 Synthesis and application of ultrathin 1D nanomaterials

The development of nanomaterials in the ultrathin domain (below 10 nm), has attracted much attention in recent years. As mentioned previously size effects have a profound influence on the behaviour of nanomaterials. Interest in these materials not only stems from their increased surface area, but they have also been shown to exhibit unique properties unseen in corresponding nanomaterials outside this domain (above 10 nm) such as magnetism,<sup>46,47</sup> localisation<sup>48</sup> and quantum size effects.<sup>49</sup>

Over the last decade significant breakthroughs in synthetic methods have seen a major development of a wide variety of metal,<sup>46,47,50–55</sup> metal oxide,<sup>56–59</sup> inorganic<sup>60,61</sup> and organic ultrathin nanomaterials.<sup>62,63</sup> For the purpose of this work however only metallic ultrathin nanomaterials will be discussed. Synthetically, template based techniques have long been realised as effective means to achieving ultrathin metallic nanomaterials. Templates such as zeolites,<sup>64,65</sup> mesoporous silica<sup>66–68</sup> and metal organic frameworks<sup>69</sup> (Figure 1.4) have been used, in the controlled synthesis of ultrathin nanomaterials. As mentioned, the draw back to this method however is the removal of the template post synthesis which often involves harsh treatments that are potentially damaging to the synthesised material.

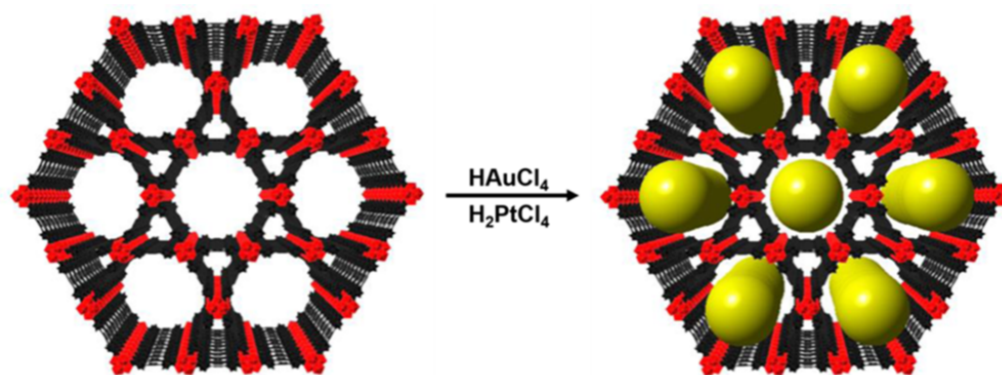


Figure 1.4: MOF as templates for ultrathin Au and Pd nanomaterials. Image reproduced from ref 65.

Currently sacrificial templating has been realized as an effective route

to overcoming this problem.<sup>70,71</sup> This method involves the galvanic replacement of the template, in this case an ultrathin nanomaterial, resulting in dissociation of the template and the ultrathin dimension being preserved in the product.<sup>72,73</sup> Ultrathin Te NWs in particular have undoubtedly become one of the most employed sacrificial templates, as Te is a relatively cheap template material and facile large scale synthesis have been developed.<sup>74-77</sup> In addition, the redox potential of Te makes it suitable for the synthesis of Pt and Pd based nanomaterials which is being exploited to produce a range of novel catalytic materials. For example Work by Liang *et al.*<sup>78</sup> demonstrated the use of ultrathin Te NWs as sacrificial templates for the synthesis of ultrathin Pt nanotubes (NTs) and Pd NWs (Figure 1.5). The authors propose that the difference in product between Pt and Pd is due to the difference in molar volume, with twice the amount of Pd produced compared to Pt per mole of Te. The versatility of the Te ultrathin NWs as sacrificial templates was further highlighted by Wang and co workers.<sup>70</sup> The authors in this case interestingly showed that by adjusting the PH of a solution containing the  $\text{TeO}_3^{-2}$  by product following templating that it is possible to recycle Te NWs with high efficiency. This green protocol undoubtedly paves the way for sustainable templating in the future.

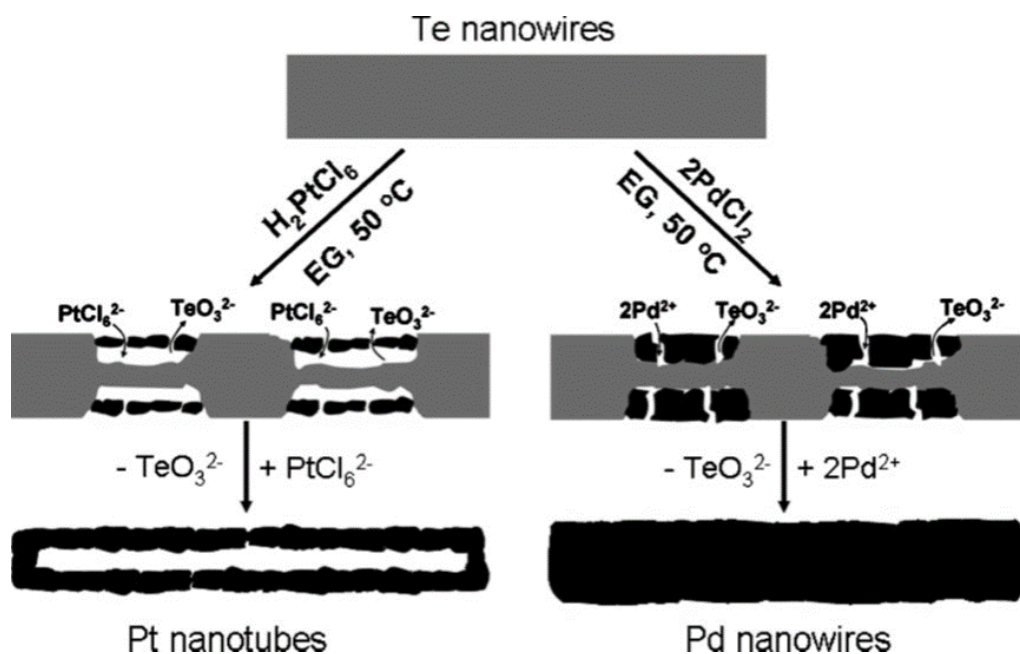


Figure 1.5: Schematic presentation of the synthesis of Pt NT and Pd Nws using Te NWs as sacrificial templates. Image reproduced from ref 74

Additional templates such as ultrathin Au<sup>79</sup> and Cu<sup>80,81</sup> NWs, and even amyloid fibers<sup>82</sup> are emerging as effective sacrificial templates for producing ultrathin 1D nanomaterials.

More recently wet chemical methods using ligand control are becoming more widely used. As mentioned previously (section 1.2) this method relies on the use of suitable ligands to guide the formation and in this case restrict the growth of the material to the ultrathin domain. Organic reagents such as octadecene, oleylamine (Oam) and oleic acid are the most commonly used ligands.<sup>52,83–88</sup> The benefit of this method is that it does not require any additional synthetic steps such as the preparation of templates. This ligand directed synthesis involves the

preferential binding of the ligand on specific facet(s) of the seed material with subsequent growth occurring on the more exposed facets. In the case of Oam, ultrathin 1D anisotropic growth was proposed to occur by the formation of micelles (Figure 1.6). Since the binding of Oam at the tip of the micelle is weak this facilitates controlled anisotropic growth at these sites.<sup>47,89</sup> Interestingly Lu *et al.*<sup>90</sup> has alternatively proposed that oleylamine produces ultrathin Au NWs via the degradation of a polymeric like [oleylamine-AuCl] inorganic complexes. A general mechanism for the role of Oam however still remains in question.

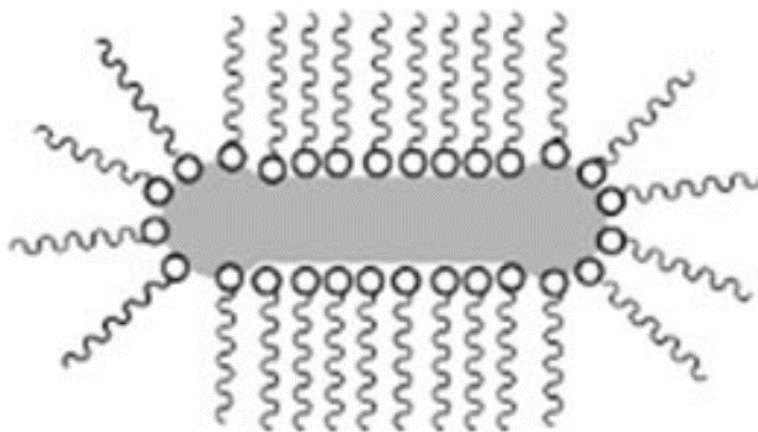


Figure 1.6: Oleylamine micelle proposed for ultrathin anisotropic growth of Au nanowires. Image reproduced from ref 43.

Tunability in the ligand controlled approach has also been demonstrated by simply varying the ligand concentration. Since Oam and oleic acid can also serve as reducing agents and solvents their concen-

tration can significantly effect the resulting nanomaterial. An example of this was reported by Wang *et al.*<sup>90</sup> in which using an Oam to oleic acid ratio of 1:1 or just Oam affords ultrathin Au NWs with diameters of 9 nm and 3 nm, respectively.

Furthermore, ethylene glycol (EG) is also suitable ligand for the controlled synthesis of 1D ultrathin nanomaterials.<sup>54,91,92</sup> Xia *et al.*<sup>55</sup> in particular recently showed that ultrathin Pt NWs with a diameter of 3 nm can be produced in high yield using a mixture EG and N,N-dimethylformamide (DMF) under solvothermal conditions. Products from these modified polyol type synthesis involving EG, have the advantage of being miscible in water or alcohols making further processing such as for device applications more facile. This is a necessary step in order to progress the field of ultrathin nanomaterials for more cost efficient, large scale applications in the future.

Ultrathin 1D nanomaterials have become promising candidates for a broad range of applications. Due to their large surface to volume ratios and tunability of both morphology and composition, these materials have shown remarkable catalytic performances particularly in electro-catalysis for direct fuel cells. This will be discussed in more detail in section 1.6. In addition to catalysis, 1D ultrathin nanomaterials have also been employed in electronic devices.<sup>86,93-95</sup> Ultrathin

AuAg NWs capped with Pluronic 123 in particular have been used as the active component in memory devices, exhibiting write-once-read-many times (WORM) switching type behaviour.<sup>96</sup> Further examples of electronic applications include the use of ultrathin Ag<sup>54</sup> and Cu<sup>50</sup> NWs for low haze transparent conductors. The field of ultrathin nanomaterials is rapidly evolving and with it brings new and interesting materials with unique properties. These materials will undoubtedly broaden our capabilities and potentially expand many areas of science.

## 1.4 1D Plasmonic metal nanomaterials

Over the last decade the development of plasmonic metal nanomaterials has resulted in significant progress in many areas such as optoelectronics,<sup>97</sup> sensing<sup>98,99</sup> and photocatalysis.<sup>100,101</sup> Au and Ag based nanomaterials are the most commonly used plasmonic metals as they can exhibit a strong surface plasmon resonance (SPR) in the visible and near-infrared (NIR) region of the spectrum. SPR is an optical phenomenon which arises when an incident beam of light interacts with surface electrons in the conduction band of the metal. This causes the surface electrons to collectively oscillate and resonate with the incident beam. SPR strongly depends on several factors such as the size and shape of the material and the dielectric constant of the



surrounding medium.<sup>102</sup> To this end, 1D nanomaterials in particular have demonstrated remarkable optical properties suitable for a wide range of applications. For example Au nanorods (NR) which exhibit a strong longitudinal SPR mode along their length and a transverse SPR mode along their width are extensively used for bioimaging applications.<sup>103,104</sup> Ding *et al.*<sup>105</sup> in particular showed that polyelectrolyte capped Au NRs conjugated with transferrin are highly effective contrast agents in HaLa cells due to their strong longitudinal SPR (Figure 1.7). Au NR offer multiple advantages for bioimaging such as tunability of plasmonic peaks by varying their aspect ratio, good biocompatibility and they do not undergo photobleaching like their fluorophore based counterparts.

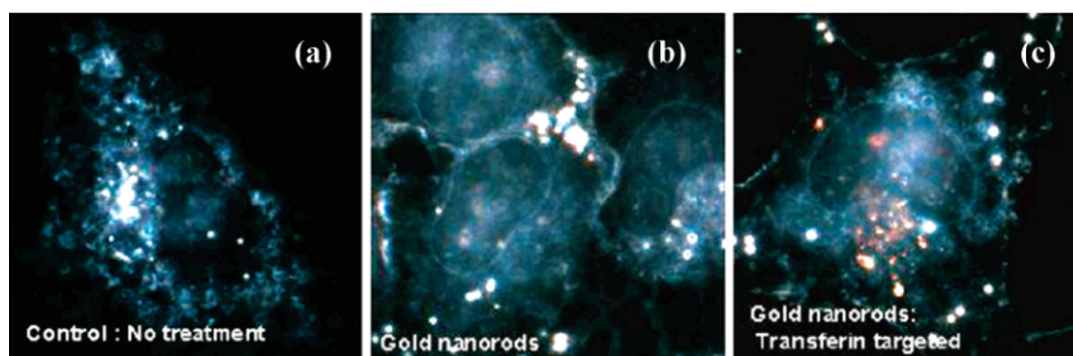


Figure 1.7: Light scattering images of HaLa cells following A) no treatment, B) treatment from non-transferrin conjugated polyelectrolyte capped Au NRs and c) treatment with transferrin conjugated polyelectrolyte capped Au NRs. Image reproduced from ref 101

Ag NWs are another prominent example of 1D plasmonic metal nano-

materials and have been envisaged to play an important role in future optoelectronic devices.<sup>106,107</sup> For instance Fang *et al.*<sup>108</sup> demonstrated that branched Ag NWs can be used as plasmonic beam routers. The authors show that by varying the polarisation angle of the incident beam on these NWs it is possible to direct relative intensity of surface plasmon polaritons to either the main NW or branched NW (Figure 1.8). Interestingly when emission from the main NW was at a minimum, emission from branched NW was at a maximum and vice versa. Ag NWs have also been used in organic solar cells as transparent conductors.<sup>109,110</sup> Due to their plasmonic properties Ag NW networks can offer greater transmittance compared to indium tin oxides.

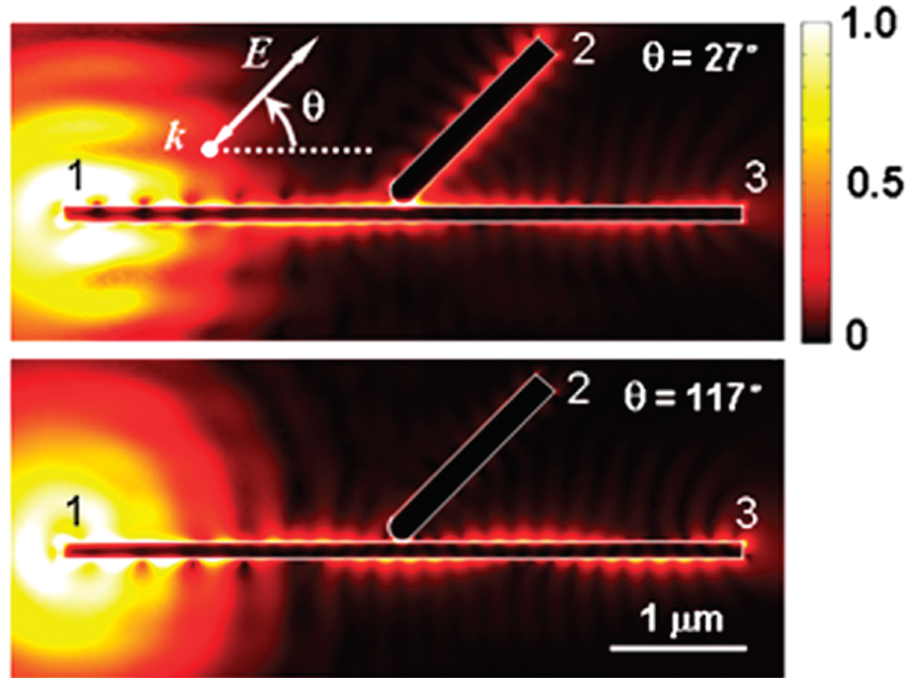


Figure 1.8: Local electric field distribution showing the maxima (top) and minima (bottom) emission at the branched NW as a function of polarisation angle. Image reproduced from ref 104.

## 1.5 Chirality and chiral nanomaterials

Chirality is a fascinating occurrence in the natural world, which plays a very important role in chemistry, biology and medicine. In chemistry, chiral molecules exist in two mirror-image forms, which are non-superimposable in three dimensions and termed enantiomers. Well-known examples of chiral molecules include proteins, DNA, sugars, amino-acids, enzymes, and a huge range of drugs, including ibupro-

fen (common anti-inflammatory and analgesic) and L-Dopa (effective on Parkinson disease). One of the most prevalent examples of the importance of chirality was seen in the case of Thalidomide (Figure 1.9). Originally developed in the 1950s this drug was aimed at targeting morning sickness. It was soon found however, that while the S-enantiomer was bioactive, and alleviated the symptoms of morning sickness the other enantiomer, produced due to racemization in vivo, had devastating effects on the unborn child resulting in fetal abnormalities.

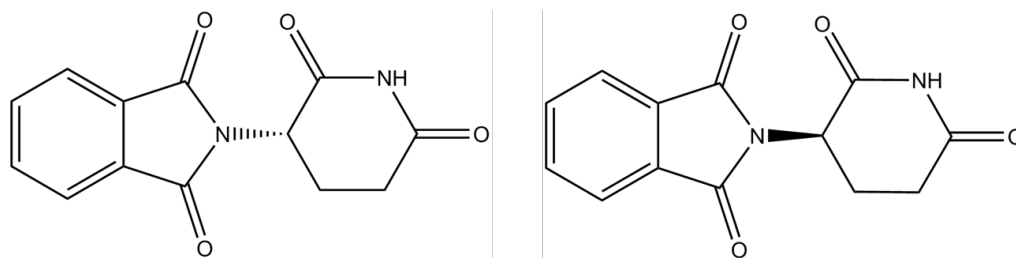


Figure 1.9: S-Thalidomide (left) and R-Thalidomide (right) enantiomers.

Our understanding of chirality has grown considerably over the years and has since been applied to nanomaterials where it is envisaged to play an important role in nanotechnology. Over the last few years a range of new chiral nanomaterials have been developed, including quantum nanostructures,<sup>111-114</sup> metal oxides<sup>115-117</sup> and metal nanoparticles.<sup>118-121</sup> The interest in chiral nanomaterials is continuously growing due to their unique properties and the range of poten-

tial applications offered by these materials such as chiral sensing,<sup>122–126</sup> asymmetric catalysis<sup>127–130</sup> and biotechnology.<sup>131,132</sup>

The origin of chirality in chiral nanomaterials can be grouped into three categories: intrinsic chirality, ligand induced chirality and structural chirality. Since chiral nanomaterials typically exhibit chiroptical activity (ie. the preferential absorbance of left or right handed circular polarised light) circular dichroism (CD) spectroscopy is used to elucidate the presence and handedness of chiral nanomaterials. CD spectroscopy is outlined in more detail in chapter 2, section 2.2.2. Over the next few sections we will discuss the different forms of chirality and highlight the significance of chiral and achiral ligands on inducing chirality in nanomaterials.

### 1.5.1 Intrinsic chirality

Intrinsic chirality is chirality that originates from the symmetry breaking of a nanocrystals lattice structure or chiral distortion of its surface atoms. This phenomenon is most notably seen in the case of Au and Ag metal nanoclusters composed of only a few atoms.<sup>133,134</sup> In these cases chiral metal cores are produced using achiral ligands. An example of this was demonstrated by Janzinsky *et al.*<sup>135</sup> using p-

mercaptobenzoic acid as a capping agent on Au clusters composed of 102 Au atoms. Through X-ray crystallography it was found that the observed chirality by these Au clusters was due to the formation of a chiral pattern from SR-Au-SR "staple" motifs on the surface of the cluster. This chiral distortion on metal clusters was similarly seen for Au<sub>28</sub>,<sup>136</sup> Au<sub>38</sub><sup>137</sup> and Au<sub>144</sub><sup>138</sup> clusters capped with achiral thiols.

Examples of intrinsic chirality expressed by larger nanomaterials (5-100 nm) however is rare. A prominent example of this was demonstrated by Mukhina *et al.*<sup>139</sup> with the synthesis of a racemic mixture (50:50 of L and D) of intrinsically chiral CdSe/ZnS quantum dots and rods. In this particular case the authors attribute the intrinsic chirality to the formation left and right handed screw dislocations in the lattice of the nanocrystal (Figure 1.10). The authors also remarkably achieved chiral resolution of these nanocrystals via phase transfer process using L-cysteine. Furthermore intrinsically chiral nanomaterials have also been achieved using nanocrystals with chiral lattice structures such as  $\alpha$ -HgS.<sup>140</sup>

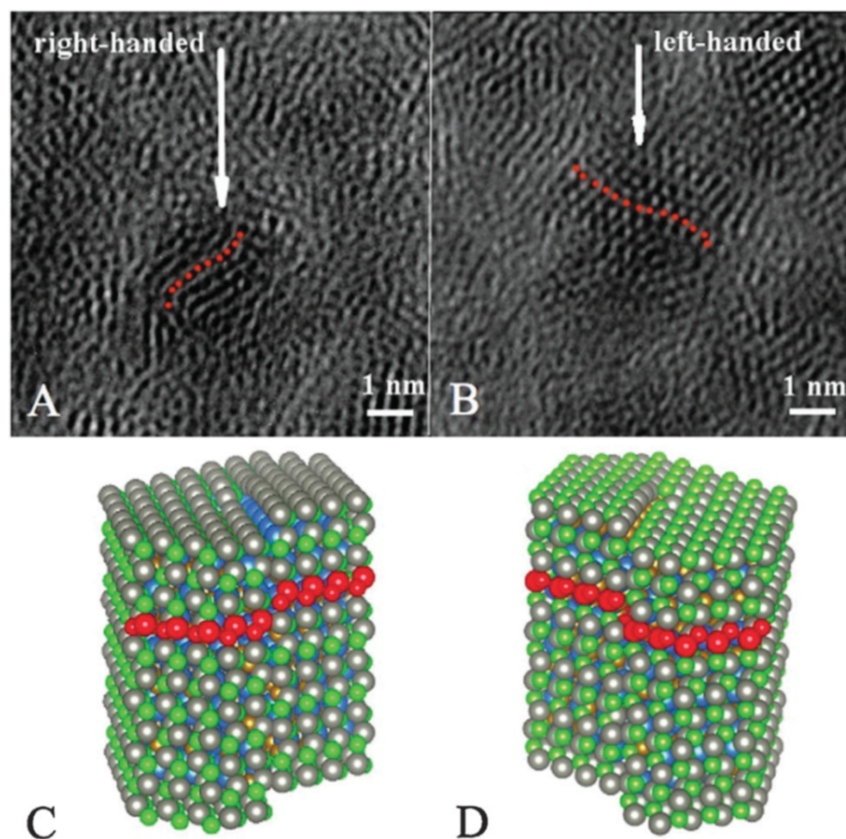


Figure 1.10: TEM images (A and B) and atomistic models of right (C) and Left (D) screw dislocations. Image reproduced from ref 134.

### 1.5.2 Ligand induced chirality

Ligand induced chirality involves the interaction of chiral molecules typically with achiral nanomaterials. Synthetically, ligand induced chirality can be achieved either during synthesis using chiral capping agents or via post synthesis ligand exchange. The use of chiral modifiers as capping agents during synthesis is perhaps the most common method. Chiral amino acids particularly pencilamine and cysteine are

among the most extensively used chiral capping agents. For example due to the strong affinity between S-Au and S-Ag, pencilamine and cysteine are routinely used as capping agents in the synthesis of chiral Au and Ag nanoparticles.<sup>141-146</sup> In addition, work done by our group in particular has also demonstrated use of pencilamine as a capping agent for the synthesis of a variety of chiral luminescent semiconductor nanomaterials.<sup>111-113,147</sup> Other capping agents such as the chiral phosphine BINAP, which expresses axial chirality, has also been effectively used to synthesize chiral Au, Pd and Rh nanoparticles.<sup>130,148</sup>

The origin of chirality in this ligand induced case was initially modelled using the dissymmetric field model in which the chiral electronic state of the chiral molecule mixes with the electronic state of the nanomaterial,<sup>149</sup> however it was since found to be a more complex phenomenon. Through density functional calculations Garzon and co workers<sup>150</sup> showed that the observed chirality in the case of glutathione capped Au clusters was due to a combination of chiral distortion of surface atoms and from the presence of the chiral molecule. Our group has demonstrated that nanomaterials can exhibit a chiral memory effect in which chiroptical activity is still expressed by the nanomaterial even after the removal of the chiral capping agent, due to the presence of chiral defects on the surface.<sup>112</sup> This was similarly shown by Nakashima *et al.*<sup>151</sup> in which CdTe quantum dots remained chiral fol-



lowing a ligand exchange of cysteine methylester hydrochloride with 1-dodecanethiol (Figure 1.11). The use of chiral imprinting has since been realised as effective method for producing chiral surfaces for potential chiral recognition applications.<sup>152</sup>

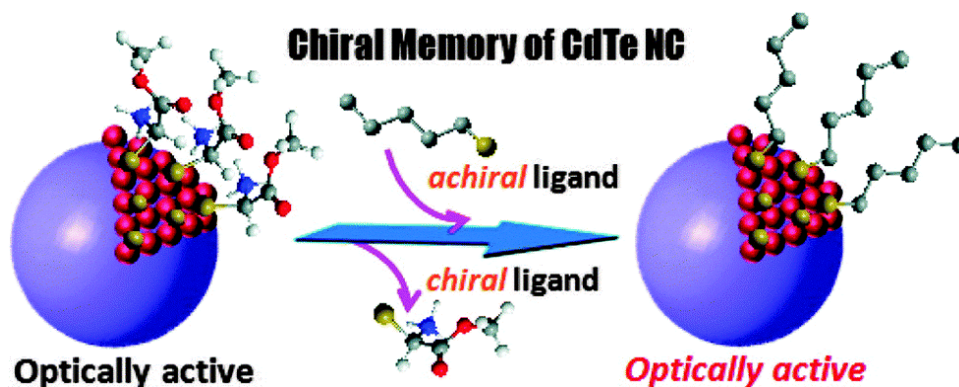


Figure 1.11: Chiral memory effect for CdTs nanocrystals. Image reproduced from ref 146.

In relation to 1D nanomaterials specifically, cysteine capped Au nanorods are the most common example.<sup>153</sup> To the best of our knowledge, ligand induced chiral modification of NWs is rare. One of the most prominent examples of this was demonstrated by Erathodiyil *et al.*<sup>154</sup> in which a cinchonidine alkaloids adsorbed onto the surface of ultrathin Pt NWs. It was found that the Aromatic moiety of the cinchonidine acts as an anchor on the Pt surface while the chiral centre acts as an enantioselective site (Figure 1.12 ).

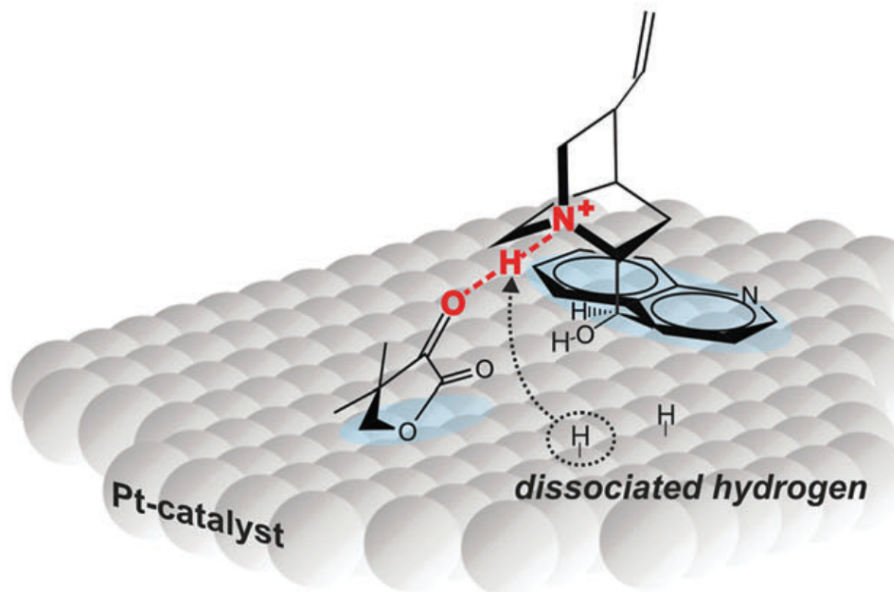


Figure 1.12: proposed confirmation of cinchonidine on a Pt surface. Image reproduced from ref 149.

Regarding the ligand exchange method, this involves the post synthetic replacement of an achiral capping agent with a chiral ligand. For instance citrate capped Au nanoparticles have been made chiral via a direct ligand exchange with cysteine.<sup>155</sup> Typically ligand exchange is achieved using a phase transfer approach in which chiral molecules are used as the phase transfer agent.<sup>156,157</sup>

### 1.5.3 Structural chirality

Finally, the last source of chirality is from nanomaterials that have chiral shapes and morphologies. Typically chiral architectures such

as helices and twisted structures have been produced using the chiral scaffold of biomolecules like DNA and peptides as templates.<sup>158–161</sup> For example helical self-assemblies of Au and Ag nanoparticles with specifically left or right handed chirality have been produced via in situ growth on these bio-templates.<sup>158,162,163</sup> The chiroptical activity of chiral structures such as self assemblies, depends on the helice pitch and radius, and the number of nanoparticles. The versatility of this templating method was highlighted by Lan *et al.*<sup>164</sup> with the controlled design of helical Au nanorod self-assemblies. The authors show that by varying Au nanorod to DNA ratio it was possible to produce entirely left or right handed helices composed of 9, 4 or 2 Au nanorods (Figure 1.13). It was further highlighted that the CD response for the larger Au nanorod assemblies was the greatest.

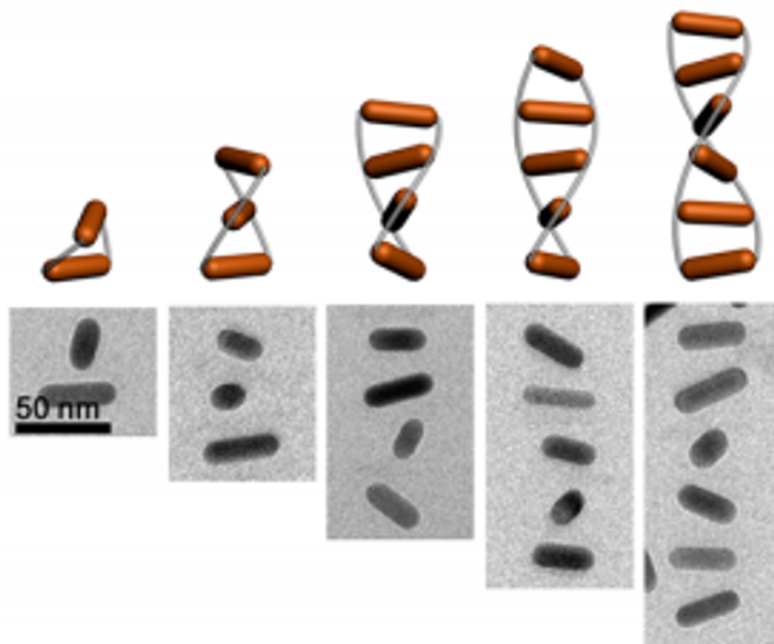


Figure 1.13: Helical self assemblies of Au nanorods. Image reproduced from ref 159.

More wet chemical based methods involving NWs are beginning to emerge, in which surface strain induced by the deposition of metals onto the NWs causes the NWs to adopt helical morphologies.<sup>165,166</sup> Unfortunately these methods do not control the resulting handedness of the helices and are chiroptically inactive. While controlled wet chemical methods remain a challenge, recent work by Nakagawa and coworkers<sup>167</sup> have demonstrated the synthesis of left and right handed ultrathin Au NW double helices (Figure 1.14) using 2 organogelators. The function of one organogelolator was to form a chiral soft template nanoribbon while other organogelator acted as a stabilizer to help form the ultrathin NWs.

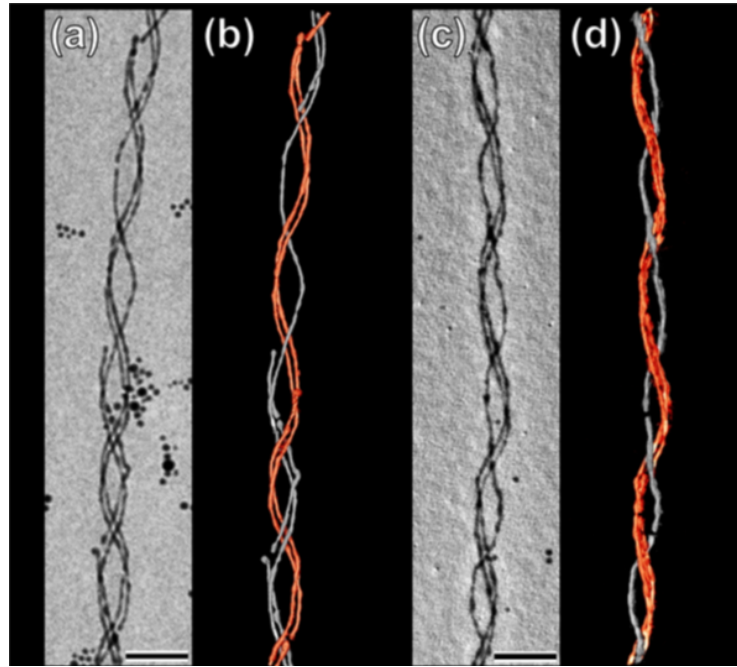


Figure 1.14: TEM (A,C) and corresponding TEM tomography images (B,D) of Au NWs prepared from left and right handed templates respectively. Image reproduced from ref 162.

## 1.6 Fuel cells

The development of direct fuels cells has long been recognised as important step in overcoming our fuel crisis. While the direct fuel cell was first reported in 1839, inefficient technology (ie. poor and/or costly catalysts), transport and infrastructure issues have hindered their large scale commercialization. However significant developments in nanotechnology and the use of fuels like alcohols has significantly

progressed fuel cell research.<sup>168-170</sup> The basic principle of an alcohol fuel cell is outlined in Figure 1.15. A fuel cell is composed of an anodic compartment and a cathodic compartment separated by a polyelectrolyte membrane. At the anode the fuel is oxidised resulting in an electrical out-put and protons being exchanged across the polyelectrolyte membrane. These protons are subsequently involved in the oxygen reduction reaction at the cathode to produce water.

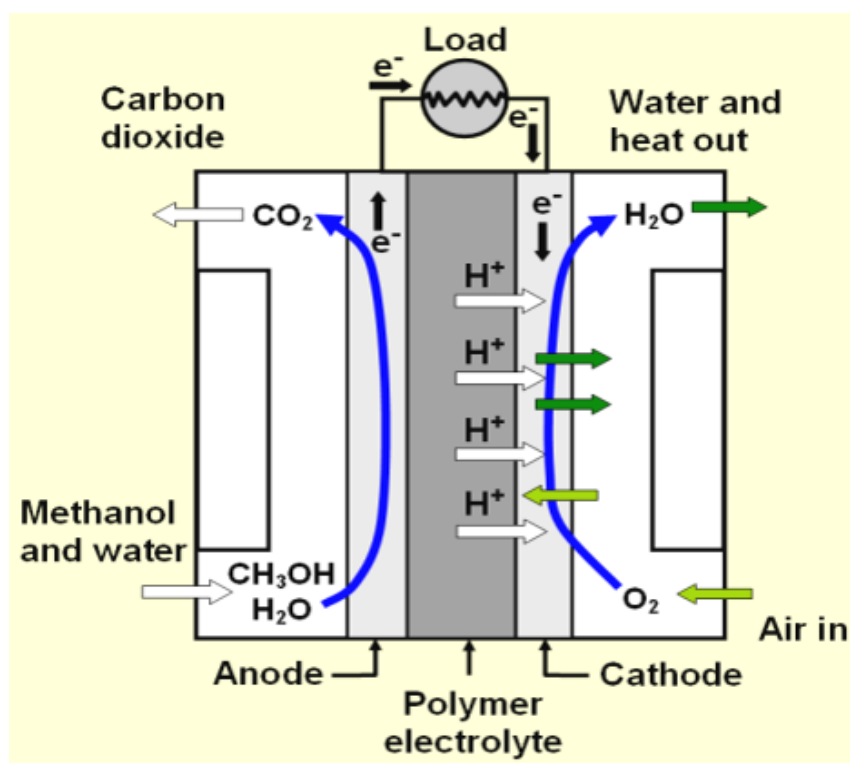
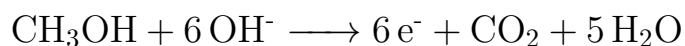


Figure 1.15: Basic principle of a direct methanol fuel cell. Image reproduced from ref 167.<sup>171</sup>

### 1.6.1 Anode compartment

As mentioned previously the anode is where the alcohol (the fuel) is oxidized. Methanol in particular has become one of the most extensively studied fuels for a number of reasons: it offers large energy densities, can be produced from natural gases and is relatively safe and easy to transport and store.<sup>172</sup> The half-cell equation for the complete oxidation of methanol is detail below.



Regarding the mechanism for the oxidation of methanol, a dual reaction pathway has been generally accepted.<sup>168,173–176</sup> In one pathway the adsorbed methanol on the catalyst surface forms adsorbed CO which is further oxidised to CO<sub>2</sub>, while the other pathway involves the oxidation of adsorbed carbon intermediates (Figure 1.16). The presence of adsorbed oxygen species such as OH from the dissociation of water has been found to play a critical role in the oxidation of the adsorbed intermediates. Furthermore, strongly adsorbed species like CO are the main cause of catalytic poisoning. This results in inefficiencies like slow oxidation kinetics, as catalytic sites are blocked and higher overpotentials. In addition, a further drawback to using small

fuels like methanol, is that it has a high tendency to cross over the polyelectrolyte membrane and poison the cathode thus hampering the performance of the fuel cell.<sup>177,178</sup>

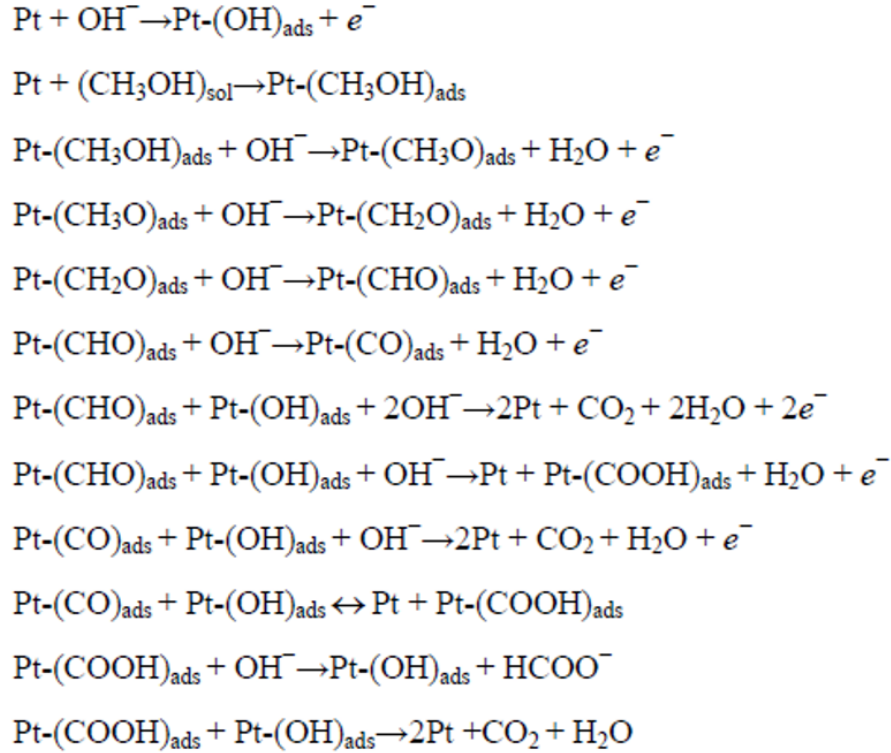


Figure 1.16: Proposed mechanisms for the electro-oxidation of methanol. Image reproduced from ref 172.

In more recent years researchers have moved towards the use of ethylene glycol (EG) as a fuel.<sup>179–182</sup> EG offers a higher energy density and due to its size is less likely to cause crossover poisoning. More importantly EG is already produced on a large scale from the car industry thus the potential infrastructure is already present. Unlike methanol which is the one of the simplest fuels, having no C-C bonds, the



oxidation of EG is more complex. Matsouka *et al.*<sup>183</sup> proposed that oxidation of EG in alkaline medium occurs via a poisoning and non-poisoning pathway as shown in Figure 1.17. In the non-poisoning route EG is oxidised to oxalate while in the poisoning route EG forms formate which subsequently oxidises to form CO poisoning species. A down side to EG oxidation process however is the formation of partially oxidized products such as glycolaldehyde, glyoxal, glycolic acid, glyoxylic acid. Wang *et al.*<sup>184</sup> further proposed that a "desorption–re-adsorption–further oxidation" mechanism accounts for the oxidation of the C<sub>2</sub> species ( ie. intermediate species containing 2 carbons).

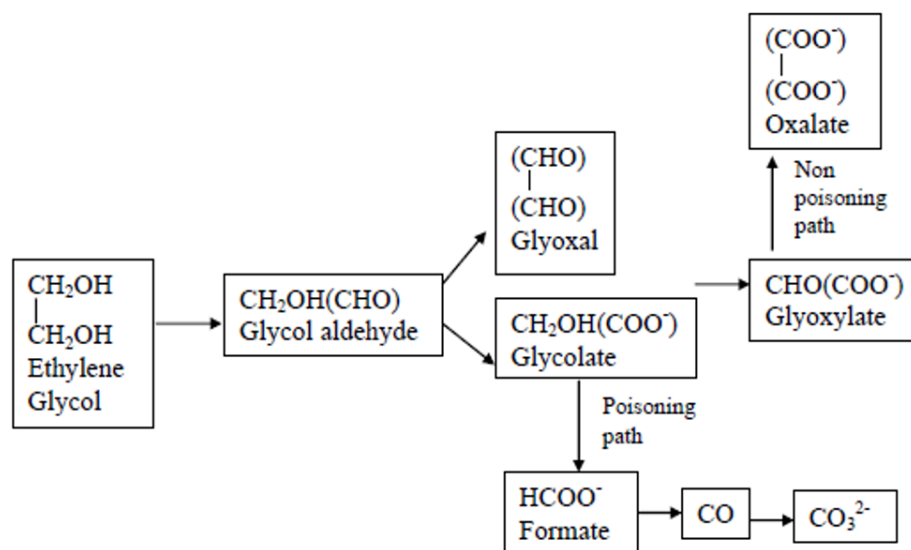


Figure 1.17: Proposed mechanisms for the electro-oxidation of EG. Image reproduced from ref 180.

### 1.6.2 Cathode compartment

As mentioned earlier the cathodic compartment is where oxygen is reduced to form water. Oxygen reduction can occur via 2 pathways: a direct 4 electron transfer or by a 2 electron transfer involving a  $\text{H}_2\text{O}_2$  intermediate. Several mechanisms have been proposed for this reduction process, these include the 1) direct dissociation of adsorbed  $\text{O}_2$ , 2) dissociation of adsorbed OOH species, and 3) the dissociation of  $\text{H}_2\text{O}_2$ .<sup>133,176,185</sup> In the direct dissociation of oxygen route, the adsorbed  $\text{O}_2$  dissociates to form 2 oxygen atoms which subsequently react with adsorbed H to form  $\text{H}_2\text{O}$ . In mechanism 2) the adsorbed oxygen first reacts with adsorbed H to form a OOH species. The OOH species then dissociates to form O and OH. This OH subsequently reacts with adsorbed H to form water. In the final proposed mechanism, the adsorbed oxygen reacts with 2 adsorbed H atoms forming  $\text{H}_2\text{O}_2$ . The  $\text{H}_2\text{O}_2$  then dissociates into 2 adsorbed OH species which then react with adsorbed H atoms to form water. These reaction mechanisms are summarised in Figure 1.18.

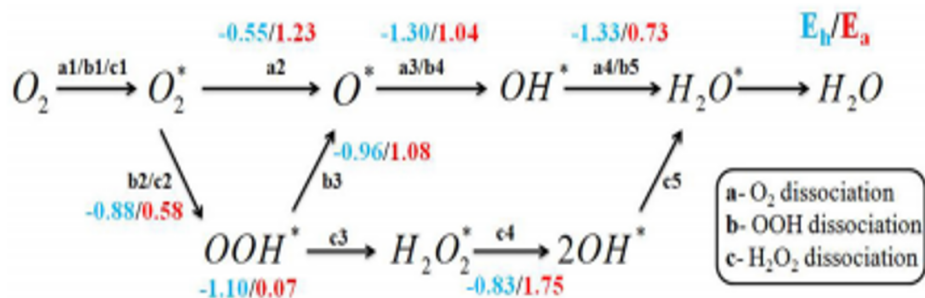
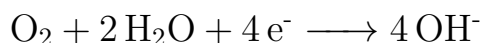


Figure 1.18: Proposed mechanisms for the oxygen reduction reaction. Asterix denotes an adsorbed species. Image reproduced from ref 182.

The reduction of oxygen is given by the half equation below.



### 1.6.3 1D nanomaterials as Anodic catalyst

The overall performance of polyelectrolyte fuel cells depends strongly on the anodic and cathodic catalysts. For the purpose of this work we will only focus on the anodic catalyst. Pt in particular is the most extensively used catalyst for fuel cell applications as it is effective at C-C bond breaking. However Pt is highly expensive and also susceptible to poisoning from oxidized intermediates.<sup>168</sup> Over the last few years researchers have focused on improving catalyst design, particularly on

aspects such as catalyst morphology and composition.<sup>186–189</sup>

As mentioned earlier (section 1.3) ultrathin NWs have become widely used in fuel cells offering remarkable catalytic performances compared to their 0D counterparts. For instance, Xia *et al.*<sup>55</sup> showed that ultrathin Pt NWs not only offer greater current out-puts compared to Pt nanoparticles but they are also significantly more durable. Among some other examples include PtRuFe,<sup>190</sup> PtPdFe<sup>191</sup> and PtSn<sup>192</sup> ultrathin NWs each exhibiting striking activities as anodic catalysts. Alloying has notably become an efficient means of improving catalysts. Alloying has a 2-fold effect: it reduces the loading of expensive metals and can enhance catalytic performance due to synergistic effects from the alloying metals. These synergistic effects typically involve changes in the electronic structure of the alloyed metal and/or geometric effects such as segregation and arrangement of the surface atoms of each metal in the alloy.<sup>193</sup> For example, in order to mitigate the issue of catalytic poisoning researchers have looked to alloying Pt with more oxophilic metals such as Ru, Sn, Rh, Ni.<sup>193</sup> In the case of PtRu ultrathin nanomaterials,<sup>194,195</sup> the enhanced catalytic performance has been attributed to Ru actively promoting the formation of adsorbed OH species and from the downward shift of the Pt d-band resulting in weaker bonding with adsorbed CO.

## 1.7 Aims of the project

In light of our review of the current literature it is apparent that the NWs, particularly ultrathin metallic NWs are highly versatile and promising nanomaterials, with field rapidly growing each year. However there are many issues that still need to be addressed. Firstly, there is lack of synthetic protocols for tunable aqueous based synthesis of ultrathin NWs. In addition, Te ultrathin NWs are the most used sacrificial templates however there are very few studies performed using alternative ultrathin NWs as sacrificial templates. Finally, to the best of our knowledge there are no examples of ligand induced chirality on ultrathin NWs. In keeping with the topic of chirality, preliminary results in our group has shown that mechanical influences such as stirring can induce chirality in large aspect ratio Ag NWs and this may be used as templates for the controlled synthesis of chiral self assemblies.

Since the synthesis of ultrathin Au NWs and the chiral modification of Au based nanomaterials are well established, the focus of this work will be on developing tunable water soluble synthesis of ultrathin Au based NWs, exploring their chiral modification and their use as sacrificial templates. In summary the aims of this work are as follows:

- To develop a tunable water soluble synthesis of ultrathin Au based NWs

- To explore chiral ligand induced methods to make the ultrathin Au based NWs chiral
- To investigate these ultrathin Au based NWs are sacrificial templates for the synthesis of various new 1D nanomaterials and to test their catalytic activities for potential fuel cell applications
- To continue preliminary studies done in our group studying the effect of stirring induced chirality on large aspect ratio Ag NWs and to further explore this induced chirality for the synthesis of new chiral self-assemblies

# References

- (1) Pokropivny, V. V.; Skorokhod, V. V. *Materials Science and Engineering C* **2007**, *27*, 990–993.
- (2) Sofiah, A. G.; Samykano, M.; Kadirgama, K.; Mohan, R. V.; Lah, N. A. *Applied Materials Today* **2018**, *11*, 320–337.
- (3) Khanarian, G.; Joo, J.; Liu, X. Q.; Eastman, P.; Werner, D.; O’Connell, K.; Trefonas, P. *Journal of Applied Physics* **2013**, *114*, 024302.
- (4) Agrawal, B. K.; Agrawal, S; Singh, S *Journal of Nanoscience and Nanotechnology* **2005**, *5*, 635–640.
- (5) Lajvardi, M.; Eshghi, H.; Ghazi, M. E.; Izadifard, M.; Goodarzi, A. *Materials Science in Semiconductor Processing* **2015**, *40*, 556–563.
- (6) Gong, S.; Cheng, W. *Advanced Electronic Materials* **2017**, *3*, 1600314.
- (7) Niu, W.; Zhang, L.; Xu, G. *Nanoscale* **2013**, *5*, 3172–3181.

- (8) Gole, A.; Murphy, C. J. *Chemistry of Materials* **2004**, *16*, 3633–3640.
- (9) Lee, E. J.; Ribeiro, C.; Longo, E.; Leite, E. R. *Journal of Physical Chemistry B* **2005**, *109*, 20842–20846.
- (10) Lv, W.; He, W.; Wang, X.; Niu, Y.; Cao, H.; Dickerson, J. H.; Wang, Z. *Nanoscale* **2014**, *6*, 2531–2547.
- (11) Hochbaum, A. I.; Fan, R.; He, R.; Yang, P. *Nano Letters* **2005**, *5*, 457–460.
- (12) Kamins, T. I.; Li, X.; Williams, R. S.; Liu, X. *Nano Letters* **2004**, *4*, 503–506.
- (13) Hu, Y.; Liu, X.; Zhang, X.; Wan, N.; Pan, D.; Li, X.; Bai, Y.; Zhang, W. *Electrochimica Acta* **2016**, *190*, 33–39.
- (14) Chang, W. Y.; Wu, J. T.; Lin, K. H.; Yang, S. Y.; Lee, K. L.; Wei, P. K. *Microelectronic Engineering* **2011**, *88*, 909–913.
- (15) Maleak, N.; Potpattanapol, P.; Bao, N. N.; Ding, J.; Wongkokuo, W.; Tang, I. M.; Thongmee, S. *Journal of Magnetism and Magnetic Materials* **2014**, *354*, 262–266.
- (16) Wilson, N. R.; Macpherson, J. V. *Nano Letters* **2003**, *3*, 1365–1369.
- (17) Kitaura, R.; Imazu, N.; Kobayashi, K.; Shinohara, H. *Nano Letters* **2008**, *8*, 693–699.



- (18) Han, Y. J.; Kim, J. M.; Stucky, G. D. *Chemistry of Materials* **2000**, *12*, 2068–2069.
- (19) Huang, M. H.; Choudrey, A.; Yang, P. *Chemical Communications* **2000**, 1063–1064.
- (20) Cui, J.; Wu, Y.; Wang, Y.; Zheng, H.; Xu, G.; Zhang, X. *Applied Surface Science* **2012**, *258*, 5305–5311.
- (21) Xu, H.; Qin, D. H.; Yang, Z.; Li, H. L. *Materials Chemistry and Physics* **2003**, *80*, 524–528.
- (22) Wang, X.; Wang, X.; Huang, W.; Sebastian, P. J.; Gamboa, S. *Journal of Power Sources* **2005**, *140*, 211–215.
- (23) Liu, X. M.; Zhou, Y. C. *Applied Physics A: Materials Science and Processing* **2005**, *81*, 685–689.
- (24) Liu, T.; Burger, C.; Chu, B. *Progress in Polymer Science (Oxford)* **2003**, *28*, 5–26.
- (25) Thurn-Albrecht, T.; Schotter, J.; Kästle, G. a.; Emley, N.; Shibauchi, T.; Krusin-Elbaum, L.; Guarini, K.; Black, C. T.; Tuominen, M. T.; Russell, T. P. *Science* **2000**, *290*, 2126–2129.
- (26) Hassanien, R.; Al-Said, S. A.; Šiller, L.; Little, R.; Wright, N. G.; Houlton, A.; Horrocks, B. R. *Nanotechnology* **2012**, *23*, 075601.
- (27) Kundu, S.; Liang, H. *Langmuir* **2008**, *24*, 9668–9674.
- (28) Slocik, J. M.; Kim, S. N.; Whitehead, T. A.; Clark, D. S.; Naik, R. R. *Small* **2009**, *5*, 2038–2042.

- (29) Song, Y.; Garcia, R. M.; Dorin, R. M.; Wang, H.; Qiu, Y.; Coker, E. N.; Steen, W. A.; Miller, J. E.; Shelnut, J. A. *Nano Letters* **2007**, *7*, 3650–3655.
- (30) Wang, D. P.; Sun, D. B.; Yu, H. Y.; Qiu, Z. G.; Meng, H. M. *Materials Chemistry and Physics* **2009**, *113*, 227–232.
- (31) Ksar, F.; Surendran, G.; Ramos, L.; Keita, B.; Nadjò, L.; Prouzet, E.; Beaunier, P.; Hagège, A.; Audonnet, F.; Remita, H. *Chemistry of Materials* **2009**, *21*, 1612–1617.
- (32) Wang, C.; Chen, M.; Zhu, G.; Lin, Z. *Journal of Colloid and Interface Science* **2001**, *243*, 362–364.
- (33) Li, Y.; Yang, X. Y.; Feng, Y.; Yuan, Z. Y.; Su, B. L. *Critical Reviews in Solid State and Materials Sciences* **2012**, *37*, 1–74.
- (34) Vigderman, L.; Khanal, B. P.; Zubarev, E. R. *Advanced Materials* **2012**, *24*, 4811–4841.
- (35) Pérez-Juste, J.; Pastoriza-Santos, I.; Liz-Marzán, L. M.; Mulvaney, P. *Coordination Chemistry Reviews* **2005**, *249*, 1870–1901.
- (36) Shibu, E. S.; Varkentina, N.; Cognet, L.; Lounis, B. *Advanced Science* **2017**, *4*, 1–5.
- (37) Vigderman, L.; Zubarev, E. R. *Chemistry of Materials* **2013**, *25*, 1450–1457.

- (38) Park, K.; Hsiao, M. S.; Yi, Y. J.; Izor, S.; Koerner, H.; Jawaid, A.; Vaia, R. A. *ACS Applied Materials and Interfaces* **2017**, *9*, 26363–26371.
- (39) Sun, Y.; Xia, Y. *Advanced Materials* **2002**, *14*, 833–837.
- (40) Li, S.; Zhang, H. *Advanced Materials Research* **2014**, *881-883*, 940–943.
- (41) Wang, G. H.; Zhu, J. J.; Kan, C. X.; Wan, J. G.; Han, M. *Journal of Nanomaterials* **2011**, *2011*, 1–7.
- (42) Jiu, J.; Araki, T.; Wang, J.; Nogi, M.; Sugahara, T.; Nagao, S.; Koga, H.; Suganuma, K.; Nakazawa, E.; Hara, M.; Uchida, H.; Shinozaki, K. *Journal of Materials Chemistry A* **2014**, *2*, 6326–6330.
- (43) Sun, Y.; Mayers, B.; Herricks, T.; Xia, Y. *Nano Letters* **2003**, *3*, 955–960.
- (44) Zhang, J.; Liu, H.; Wang, Z.; Ming, N. *Advanced Functional Materials* **2007**, *17*, 3295–3303.
- (45) Xia, Y.; Xia, X.; Peng, H. C. *Journal of the American Chemical Society* **2015**, *137*, 7947–7966.
- (46) Teng, X.; Han, W. Q.; Ku, W.; Hücker, M. *Angewandte Chemie - International Edition* **2008**, *47*, 2055–2058.
- (47) Wang, C.; Hou, Y.; Kim, J.; Sun, S. *Angewandte Chemie - International Edition* **2007**, *46*, 6333–6335.

- (48) Pascual, J. I.; Mendez, J.; Barb, A. M.; Garcia, N. *Science* **1995**, *267*.
- (49) Bezryadin, A.; Lau, C. N.; Tinkham, M. *Nature* **2000**, *404*, 971–974.
- (50) Cui, F.; Yu, Y.; Dou, L.; Sun, J.; Yang, Q.; Schildknecht, C.; Schierle-Arndt, K.; Yang, P. *Nano Letters* **2015**, *15*, 7610–7615.
- (51) Sun, S.; Jaouen, F.; Dodelet, J. P. *Advanced Materials* **2008**, *20*, 3900–3904.
- (52) Wang, C.; Sun, S. *Chemistry - An Asian Journal* **2009**, *4*, 1028–1034.
- (53) Fu, X.; Wang, Y.; Wu, N.; Gui, L.; Tang, Y. *Journal of Materials Chemistry* **2003**, *13*, 1192–1195.
- (54) Liu, Y.; Chen, Y.; Shi, R.; Cao, L.; Wang, Z.; Sun, T.; Lin, J.; Liu, J.; Huang, W. *RSC Advances* **2017**, *7*, 4891–4895.
- (55) Xia, B. Y.; Wu, H. B.; Yan, Y.; Lou, X. W.; Wang, X. *Journal of the American Chemical Society* **2013**, *135*, 9480–9485.
- (56) Zhao, Y.; Sun, B.; Zhang, S.; Wang, L.; Gao, X.; Liu, Q.; Mu, S.; Zhang, M.; Hu, S.; Huo, Z. *Nanoscale* **2017**, *9*, 12830–12834.
- (57) Liu, B. J.-W.; Zheng, J.; Wang, J.-L.; Xu, J.; Li, H.-H.; Yu, S.-H. *Nano Letters* **2013**, *13*, 3589–3593.

- (58) Xi, G.; Ouyang, S.; Li, P.; Ye, J.; Ma, Q.; Su, N.; Bai, H.; Wang, C. *Angewandte Chemie International Edition* **2012**, *51*, 2395–2399.
- (59) Yu, X. F.; Liu, J. W.; Cong, H. P.; Xue, L.; Arshad, M. N.; Albar, H. A.; Sobahi, T. R.; Gao, Q.; Yu, S. H. *Chemical Science* **2015**, *6*, 2511–2515.
- (60) Zhang, Z.; Murayama, T.; Sadakane, M.; Ariga, H.; Yasuda, N.; Sakaguchi, N.; Asakura, K.; Ueda, W. *Nature Communications* **2015**, *6*, 1–10.
- (61) Liu, Z.; Xu, J.; Chen, D.; Shen, G. *Chemical Society Reviews* **2015**, *44*, 161–192.
- (62) Zhang, Q. G.; Deng, C.; Soyekwo, F.; Liu, Q. L.; Zhu, A. M. *Advanced Functional Materials* **2016**, *26*, 792–800.
- (63) Zhou, K.; He, Y.; Xu, Q.; Zhang, Q.; Zhou, A.; Lu, Z.; Yang, L. K.; Jiang, Y.; Ge, D.; Liu, X. Y.; Bai, H. *ACS Nano* **2018**, *12*, 5888–5894.
- (64) Romanov, S. *Journal of Physics: Condensed Matter* **1993**, *5*, 1081–1090.
- (65) Byung Hee Hong; Sung Chul Bae; Lee, C. W.; Jeong, S.; Kim, K. S. *Science* **2001**, *294*, 348–351.
- (66) Silica, M. *Communications* **2000**, *2*, 3107–3110.

- (67) Coleman, N. R.; O'Sullivan, N.; Ryan, K. M.; Crowley, T. A.; Morris, M. A.; Spalding, T. R.; Steytler, D. C.; Holmes, J. D. *Journal of the American Chemical Society* **2001**, *123*, 7010–7016.
- (68) Crowley, T. A.; Ziegler, K. J.; Lyons, D. M.; Erts, D.; Olin, H.; Morris, M. A.; Holmes, J. D. *Chemistry of Materials* **2003**, *15*, 3518–3522.
- (69) Voloskiy, B.; Niwa, K.; Chen, Y.; Zhao, Z.; Weiss, N. O.; Zhong, X.; Ding, M.; Lee, C.; Huang, Y.; Duan, X. *ACS Nano* **2015**, *9*, 3044–3049.
- (70) Wang, K.; Xi, D.; Zhou, C.; Shi, Z.; Xia, H.; Liu, G.; Qiao, G. *Journal of Materials Chemistry A* **2015**, *3*, 9415–9420.
- (71) Moon, G. D.; Ko, S.; Min, Y.; Zeng, J.; Xia, Y.; Jeong, U. *Nano Today* **2011**, *6*, 186–203.
- (72) Lu, C.; Kong, W.; Zhang, H.; Song, B.; Wang, Z. *Journal of Power Sources* **2015**, *296*, 102–108.
- (73) Cobley, C. M.; Xia, Y. *Materials Science and Engineering R: Reports* **2010**, *70*, 44–62.
- (74) Ma, S. Y.; Li, H. H.; Hu, B. C.; Cheng, X.; Fu, Q. Q.; Yu, S. H. *Journal of the American Chemical Society* **2017**, *139*, 5890–5895.

- (75) Hong, W.; Wang, J.; Wang, E. *Nano Research* **2015**, *8*, 2308–2316.
- (76) Li, H. H.; Zhao, S.; Gong, M.; Cui, C. H.; He, D.; Liang, H. W.; Wu, L.; Yu, S. H. *Angewandte Chemie - International Edition* **2013**, *52*, 7472–7476.
- (77) Hong, W.; Wang, J.; Wang, E. *Journal of Power Sources* **2014**, *272*, 940–945.
- (78) Hai-Wei, L.; Shuo, L.; Jun-Yan, G.; Shang-Bing, W.; Lei, W.; Shu-Hong, Y. *Advanced Materials* **2009**, *21*, 1850–1854.
- (79) Hong, W.; Wang, J.; Wang, E. *Small* **2014**, *10*, 3262–3265.
- (80) Wang, L.; Chen, H.; Chen, M. *Materials Research Bulletin* **2014**, *53*, 185–189.
- (81) Luo, M.; Zhou, M.; Da Silva, R. R.; Tao, J.; Figueroa-Cosme, L.; Gilroy, K. D.; Peng, H. C.; He, Z.; Xia, Y. *ChemNanoMat* **2017**, *3*, 190–195.
- (82) Zhang, L.; Li, N.; Gao, F.; Hou, L.; Xu, Z. *Journal of the American Chemical Society* **2012**, *134*, 11326–11329.
- (83) Kura, H.; Ogawa, T. *Journal of Applied Physics* **2010**, *107*, 074310.
- (84) Halder, A.; Ravishankar, N. *Advanced Materials* **2007**, *19*, 1854–1858.

- (85) Pazos-Pérez, N.; Baranov, D.; Irsen, S.; Hilgendorff, M.; Liz-Marzán, L. M.; Giersig, M. *Langmuir* **2008**, *24*, 9855–9860.
- (86) Hong, X.; Wang, D.; Yu, R.; Yan, H.; Sun, Y.; He, L.; Niu, Z.; Peng, Q.; Li, Y. *Chemical Communications* **2011**, *47*, 5160.
- (87) Lu, X.; Yavuz, M. S.; Tuan, H.-y.; Korgel, B. A.; Xia, Y. **2008**, 3–5.
- (88) Science, M.; Di, V; Berkeley, L. **2008**, 2–5.
- (89) Pud, S.; Kisner, A.; Heggen, M.; Belaineh, D.; Temirov, R.; Simon, U.; Offenhäusser, A.; Mourzina, Y.; Vitusevich, S. *Small* **2013**, *9*, 846–852.
- (90) Lu, X.; Yavuz, M. S.; Tuan, H.-y.; Korgel, B. A.; Xia, Y. **2008**, 3–5.
- (91) Kim, Y.; Kim, H. J.; Kim, Y. S.; Choi, S. M.; Seo, M. H.; Kim, W. B. *Journal of Physical Chemistry C* **2012**, *116*, 18093–18100.
- (92) Trung, T. N.; Arepalli, V. K.; Gudala, R.; Kim, E. T. *Materials Letters* **2017**, *194*, 66–69.
- (93) Gonzalez-Garcia, L.; Maurer, J. H. M.; Reiser, B.; Kanelidis, I.; Kraus, T. *Procedia Engineering* **2016**, *141*, 152–156.
- (94) Gong, S.; Schwalb, W.; Wang, Y.; Chen, Y.; Tang, Y.; Si, J.; Shirinzadeh, B.; Cheng, W. *Nature Communications* **2014**, *5*, 1–8.



- (95) N, L. *Journal of Material Science & Engineering* **2016**, *05*, 1000241.
- (96) Hong, X.; Tan, C.; Liu, J.; Yang, J.; Wu, X. J.; Fan, Z.; Luo, Z.; Chen, J.; Zhang, X.; Chen, B.; Zhang, H. *Journal of the American Chemical Society* **2015**, *137*, 1444–1447.
- (97) Guo, X.; Qiu, M.; Bao, J.; Wiley, B. J.; Yang, Q.; Zhang, X.; Yaoguang, M.; Yu, H.; Tong, L. *Nano Letters* **2009**, *9*, 4515–4519.
- (98) Wang, A. X.; Kong, X. *Materials* **2015**, *8*, 3024–3052.
- (99) Vo-Dinh, T.; Dhawan, A.; Norton, S. J.; Khoury, C. G.; Wang, H. N.; Misra, V.; Gerhold, M. D. *Journal of Physical Chemistry C* **2010**, *114*, 7480–7488.
- (100) Zhang, Q.; Lima, D. Q.; Lee, I.; Zaera, F.; Chi, M.; Yin, Y. *Angewandte Chemie - International Edition* **2011**, *50*, 7088–7092.
- (101) Sousa-Castillo, A.; Comesaña-Hermo, M.; Rodríguez-González, B.; Pérez-Lorenzo, M.; Wang, Z.; Kong, X. T.; Govorov, A. O.; Correa-Duarte, M. A. *Journal of Physical Chemistry C* **2016**, *120*, 11690–11699.
- (102) Kelly, K. L.; Coronado, E.; Zhao, L. L.; Schatz, G. C. *Journal of Physical Chemistry B* **2003**, *107*, 668–677.

- (103) Ma, Z. Y.; Xia, H. X.; Liu, Y. P.; Liu, B.; Chen, W.; Zhao, Y. D. *Chinese Science Bulletin* **2013**, *58*, 2530–2536.
- (104) Zhang, Y.; Wang, G.; Yang, L.; Wang, F.; Liu, A. *Coordination Chemistry Reviews* **2018**, *370*, 1–21.
- (105) Ding, H.; Yong, K. T.; Roy, I.; Pudavar, H. E.; Law, W. C.; Bergey, E. J.; Prasad, P. N. *Journal of Physical Chemistry C* **2007**, *111*, 12552–12557.
- (106) Lal, S.; Link, S.; Halas, N. J. *Nature Photonics* **2007**, *1*, 641–648.
- (107) Lee, H.; Kim, M.; Kim, I.; Lee, H. *Advanced Materials* **2016**, *28*, 4541–4548.
- (108) Fang, Y.; Li, Z.; Huang, Y.; Zhang, S.; Nordlander, P.; Halas, N. J.; Xu, H. *Nano Letters* **2010**, *10*, 1950–1954.
- (109) Van De Groep, J.; Spinelli, P.; Polman, A. *Nano Letters* **2012**, *12*, 3138–3144.
- (110) Kang, M. G.; Xu, T.; Park, H. J.; Luo, X.; Guo, L. J. *Advanced Materials* **2010**, *22*, 4378–4383.
- (111) Moloney, M. P.; Gun'ko, Y. K.; Kelly, J. M. *Chemical Communications* **2007**, *7345*, 3900–3902.
- (112) Elliott, S. D.; Moloney, M. P.; Gun'ko, Y. K. *Nano Letters* **2008**, *8*, 2452–2457.

- (113) Gallagher, S. A.; Moloney, M. P.; Wojdyla, M.; Quinn, S. J.; Kelly, J. M.; Gun'Ko, Y. K. *Journal of Materials Chemistry* **2010**, *20*, 8350–8355.
- (114) Wojdyla, M.; Gallagher, S. A.; Moloney, M. P.; Gunko, Y. K.; Kelly, J. M.; Magno, L. M.; Quinn, S. J.; Clark, I. P.; Greetham, G. M.; Towrie, M. *Journal of Physical Chemistry C* **2012**, *116*, 16226–16232.
- (115) Harada, T.; Simeon, F.; Vander Sande, J. B.; Hatton, T. A. *Physical Chemistry Chemical Physics* **2010**, *12*, 11938–11943.
- (116) Cleary, O.; Purcell-Milton, F.; Vandekerckhove, A.; Gun'ko, Y. K. *Advanced Optical Materials* **2017**, *5*, 1–5.
- (117) Gao, P. X.; Ding, Y.; Mai, W.; Hughes, W. L. *Science* **2005**, *309*, 1700–1705.
- (118) Guerrero-Martínez, A.; Alonso-Gómez, J. L.; Auguie, B.; Cid, M. M.; Liz-Marzán, L. M. *Nano Today* **2011**, *6*, 381–400.
- (119) Gérard, V. A.; Gun'Ko, Y. K.; Defrancq, E.; Govorov, A. O. *Chemical Communications* **2011**, *47*, 7383–7385.
- (120) Mark, A. G.; Gibbs, J. G.; Lee, T. C.; Fischer, P. *Nature Materials* **2013**, *12*, 802–807.
- (121) Jin, X.; Jiang, J.; Liu, M. *ACS Nano* **2016**, *10*, 11179–11186.

- (122) Jeong, H. H.; Mark, A. G.; Alarcón-Correa, M.; Kim, I.; Oswald, P.; Lee, T. C.; Fischer, P. *Nature Communications* **2016**, *7*, 11331.
- (123) Matuschek, M.; Singh, D. P.; Jeong, H. H.; Nesterov, M.; Weiss, T.; Fischer, P.; Neubrech, F.; Liu, N. *Small* **2018**, *14*, 1–7.
- (124) Li, W.; Zhang, H.; Zhang, J.; Fu, Y. *Analytical Methods* **2015**, *7*, 4464–4471.
- (125) Nan, J.; Yan, X. P. *Chemistry - A European Journal* **2010**, *16*, 423–427.
- (126) Han, B.; Hou, X.; Xiang, R.; He, G. *Analytical Methods* **2017**, *9*, 4028–4032.
- (127) Gellman, A. J.; Tysoe, W. T.; Zaera, F. *Catalysis Letters* **2015**, *145*, 220–232.
- (128) Yasukawa, T.; Miyamura, H.; Kobayashi, S. *ACS Catalysis* **2016**, *6*, 7979–7988.
- (129) Tamura, M.; Fujihara, H. *Journal of the American Chemical Society* **2003**, *125*, 15742–15743.
- (130) Tamura, M.; Fujihara, H. *Journal of the American Chemical Society* **2003**, *125*, 15742–15743.
- (131) Luo, Z.; Zhang, S. *Chemical Society Reviews* **2012**, *41*, 4736–4754.

- (132) Wen, A. M.; Steinmetz, N. F. *Chemical Society Reviews* **2016**, *45*, 4074–4126.
- (133) Yang, Y.; Dai, C.; Fisher, A.; Shen, Y. **2017**.
- (134) Zeng, C.; Jin, R. *Chemistry - An Asian Journal* **2017**, *12*, 1839–1850.
- (135) Hoffman, a. S. et al. *Science* **2007**, 430–433.
- (136) Zeng, C.; Li, T.; Das, A.; Rosi, N. L.; Jin, R. *Journal of the American Chemical Society* **2013**, *135*, 10011–10013.
- (137) Qian, H.; Eckenhoff, W. T.; Zhu, Y.; Pintauer, T.; Jin, R. *Journal of the American Chemical Society* **2010**, *132*, 8280–8281.
- (138) Lopez-Acevedo, O; Akola, J.; Whetten, R. *The Journal of* **2009**, *113*, 5035–5038.
- (139) Mukhina, M. V.; Maslov, V. G.; Baranov, A. V.; Fedorov, A. V.; Orlova, A. O.; Purcell-Milton, F.; Govan, J.; Gun'Ko, Y. K. *Nano Letters* **2015**, *15*, 2844–2851.
- (140) Ben-Moshe, A.; Govorov, A. O.; Markovich, G. *Angewandte Chemie - International Edition* **2013**, *52*, 1275–1279.
- (141) Bürgi, T. *Nanoscale* **2015**, *7*, 15553–15567.
- (142) Monti, S.; Carravetta, V.; Ågren, H. *Nanoscale* **2016**, *8*, 12929–12938.
- (143) Tielens, F.; Santos, E. *Distribution* **2010**, 9444–9452.

- (144) Perni, S.; Hakala, V.; Prokopovich, P. *Colloids and Surfaces A: Physicochemical and Engineering Aspects* **2013**, *460*, 219–224.
- (145) Panhwar, S.; Hassan, S. S.; Mahar, R. B.; Canlier, A.; Sirajuddin; Arain, M. *Journal of Inorganic and Organometallic Polymers and Materials* **2018**, *28*, 863–870.
- (146) Ock, K. S.; Dembereldorj, U.; Park, J.; Ganbold, E. O.; Kim, S.; Shin, H. C.; Joo, S. W. *Spectrochimica Acta - Part A: Molecular and Biomolecular Spectroscopy* **2013**, *102*, 419–424.
- (147) Martynenko, I. V.; Kuznetsova, V. A.; Litvinov, I. K.; Orlova, A. O.; Maslov, V. G.; Fedorov, A. V.; Dubavik, A.; Purcell-Milton, F.; Gun'ko, Y. K.; Baranov, A. V. *Nanotechnology* **2016**, *27*, 75102.
- (148) Han, D.; Li, X.; Zhang, H.; Liu, Z.; Hu, G.; Li, C. *Journal of Molecular Catalysis A: Chemical* **2008**, *283*, 15–22.
- (149) Goldsmith, M. R.; George, C. B.; Zuber, G.; Naaman, R.; Waldeck, D. H.; Wipf, P.; Beratan, D. N. *Physical Chemistry Chemical Physics* **2006**, *8*, 63–67.
- (150) Sánchez-Castillo, A.; Noguez, C.; Garzón, I. L. *Journal of the American Chemical Society* **2010**, *132*, 1504–1505.
- (151) Nakashima, T.; Kobayashi, Y.; Kawai, T. *Journal of the American Chemical Society* **2009**, *131*, 10342–10343.

- (152) Wattanakit, C.; Côme, Y. B. S.; Lapeyre, V.; Bopp, P. A.; Heim, M.; Yadnum, S.; Nokbin, S.; Warakulwit, C.; Limtrakul, J.; Kuhn, A. *Nature Communications* **2014**, *5*, 1–8.
- (153) Hou, S.; Wen, T.; Zhang, H.; Liu, W.; Hu, X.; Wang, R.; Hu, Z.; Wu, X. *Nano Research* **2014**, *7*, 1699–1705.
- (154) Erathodiyil, N.; Gu, H.; Shao, H.; Jiang, J.; Ying, J. Y. *Green Chemistry* **2011**, *13*, 3070–3074.
- (155) Gautier, C.; Bürgi, T. *ChemPhysChem* **2009**, *10*, 483–492.
- (156) Knoppe, S.; Wong, O. A.; Malola, S.; Häkkinen, H.; Bürgi, T.; Verbiest, T.; Ackerson, C. J. *Journal of the American Chemical Society* **2014**, *136*, 4129–4132.
- (157) Tohgha, U.; Varga, K.; Balaz, M. *Chemical Communications* **2013**, *49*, 1844–1846.
- (158) Chen, C.-l.; Zhang, P.; Rosi, N. L. *Water* **2008**, 1–15.
- (159) Merg, A. D.; Boatz, J. C.; Mandal, A.; Zhao, G.; Mokashi-Punekar, S.; Liu, C.; Wang, X.; Zhang, P.; Van Der Wel, P. C.; Rosi, N. L. *Journal of the American Chemical Society* **2016**, *138*, 13655–13663.
- (160) Mokashi-Punekar, S.; Merg, A. D.; Rosi, N. L. *Journal of the American Chemical Society* **2017**, *139*, 15043–15048.
- (161) Singh, G.; Chan, H.; Baskin, A.; Gelman, E.; Repnin, N.; Král, P.; Klajn, R. *Science* **2014**, *345*, 1149–1153.

- (162) Shemer, G.; Krichevski, O.; Markovich, G.; Molotsky, T.; Lubitz, I.; Kotlyar, A. B. *Journal of the American Chemical Society* **2006**, *128*, 11006–11007.
- (163) Zhou, C.; Duan, X.; Liu, N. *Accounts of Chemical Research* **2017**, *50*, 2906–2914.
- (164) Lan, X.; Lu, X.; Shen, C.; Ke, Y.; Ni, W.; Wang, Q. *Journal of the American Chemical Society* **2015**, *137*, 457–462.
- (165) Lu, Y.; Yang, S.; Xu, J.; Liu, Z.; Wang, H.; Lin, M.; Wang, Y.; Chen, H. *Small* **2018**, *1801925*, 1801925.
- (166) Wang, Y.; Wang, Q.; Sun, H.; Zhang, W.; Chen, G.; Wang, Y.; Shen, X.; Han, Y.; Lu, X.; Chen, H. *Journal of the American Chemical Society* **2011**, *133*, 20060–20063.
- (167) Nakagawa, M.; Kawai, T. *Journal of the American Chemical Society* **2018**, *140*, 4991–4994.
- (168) Zhao, X.; Yin, M.; Ma, L.; Liang, L.; Liu, C.; Liao, J.; Lu, T.; Xing, W. *Energy & Environmental Science* **2011**, *4*, 2736.
- (169) June, C.; Page, S. E.E. L.; Kammen, D. M. *Science* **2006**, *311*, 506–509.
- (170) Wang, Y.; Zou, S.; Cai, W.-B. *Catalysts* **2015**, *5*, 1507–1534.
- (171) NCFRC: Fuel Cells Explained: Fuel Cell Types.
- (172) Aricò, A. S.; Srinivasan, S.; Antonucci, V. *Fuel Cells* **2001**, *1*, 133–161.



- (173) Jusys, Z.; Kaiser, J.; Behm, R. J. *Langmuir* **2003**, *19*, 6759–6769.
- (174) Herrero, E.; Chrzanowski, W.; Wieckowski, A. *Journal of Physical Chemistry* **1995**, *99*, 10423–10424.
- (175) Iwasita, T. *Electrochimica Acta* **2002**, *47*, 3663–3674.
- (176) Yu, E. H.; Krewer, U.; Scott, K. *Energies* **2010**, *3*, 1499–1528.
- (177) Tamaki, T.; Yamauchi, A.; Ito, T.; Ohashi, H.; Yamaguchi, T. *Fuel Cells* **2011**, *11*, 394–403.
- (178) Pethaiah, S. S.; Arunkumar, J.; Ramos, M.; Al-Jumaily, A.; Manivannan, N. *Bulletin of Materials Science* **2016**, *39*, 273–278.
- (179) Serov, A.; Kwak, C. *Applied Catalysis B: Environmental* **2010**, *97*, 1–12.
- (180) An, L.; Zhao, T. S.; Shen, S. Y.; Wu, Q. X.; Chen, R. *International Journal of Hydrogen Energy* **2010**, *35*, 4329–4335.
- (181) Xu, H.; Yan, B.; Yang, J.; Li, S.; Wang, J.; Du, Y.; Ren, F. *International Journal of Hydrogen Energy* **2018**, *43*, 1489–1496.
- (182) Xu, H.; Yan, B.; Zhang, K.; Wang, J.; Li, S.; Wang, C.; Xiong, Z.; Shiraishi, Y.; Du, Y. *ChemElectroChem* **2017**, *4*, 2527–2534.
- (183) Matsuoka, K.; Iriyama, Y.; Abe, T.; Matsuoka, M.; Ogumi, Z. *Journal of The Electrochemical Society* **2005**, *152*, A729.

- (184) Wang, H.; Jusys, Z.; Behm, R. J. *Electrochimica Acta* **2009**, *54*, 6484–6498.
- (185) Singh, R. N.; Awasthi, R.; Sharma, C. S. *Int. J. Electrochem. Sci* **2014**, *9*, 5607–5639.
- (186) Balan, B. K.; Sathe, B. R. *Journal of Nanoscience and Nanotechnology* **2012**, *12*, 8994–8998.
- (187) Pei, J.; Mao, J.; Liang, X.; Zhuang, Z.; Chen, C.; Peng, Q.; Wang, D.; Li, Y. *ACS Sustainable Chemistry and Engineering* **2018**, *6*, 77–81.
- (188) Liu, D.; Xie, M.; Wang, C.; Liao, L.; Qiu, L.; Ma, J.; Huang, H.; Long, R.; Jiang, J.; Xiong, Y. *Nano Research* **2016**, *9*, 1590–1599.
- (189) Lai, J.; Luque, R.; Xu, G. *ChemCatChem* **2015**, *7*, 3206–3228.
- (190) Scofield, M. E.; Koenigsmann, C.; Wang, L.; Liu, H.; Wong, S. S. *Energy and Environmental Science* **2015**, *8*, 350–363.
- (191) Guo, S.; Zhang, S.; Sun, X.; Sun, S. **2011**, 1–4.
- (192) Li, L.; Liu, H.; Qin, C.; Liang, Z.; Scida, A.; Yue, S.; Tong, X.; Adzic, R. R.; Wong, S. S. *ACS Applied Nano Materials* **2018**, *1*, 1104–1115.
- (193) Demirci, U. B. *Journal of Power Sources* **2007**, *173*, 11–18.
- (194) Lu, S.; Eid, K.; Ge, D.; Guo, J.; Wang, L.; Wang, H.; Gu, H. *Nanoscale* **2017**, *9*, 1033–1039.

- (195) Xu, C.; Wang, L.; Mu, X.; Ding, Y. *Langmuir* **2010**, *26*, 7437–7443.

# Chapter 2

## Experimental methods

### 2.1 Chemicals and general materials

All chemical starting materials were purchased from Sigma Aldrich and Acros Organic and were used as received. The millipore water was obtained using a milliQ filtration system operating at 18  $\Omega$ M.

Centrifugation was done using Hermle Z233 M-2 for smaller volume samples and a Hettich Zentrifugen Universal 32 for large volume samples.

TEM grids were purchased from TED PELLA.

SEM aluminium stubs and carbon tabs were purchased from TED PELLA.

Glassy Carbon electrodes (3 mm diameter), Pt wire reference electrode and the electrode polishing kit were purchased from CH Instruments Inc.

## 2.2 Instrumentation and Preparation

### 2.2.1 UV-Vis absorbance spectroscopy

In this technique the sample is irradiated with light within the UV-visible region of the electromagnetic spectrum (290 – 900 nm). Typically a UV-Vis spectrometer uses an incandescent white light source which passes through a monochromator such as a prism or grating which in turn splits the white light into its various wavelengths. A samples absorbance is governed by the Beer-Lambert law:

$$A = \epsilon Cl$$

Where A is the absorbance,  $\epsilon$  is the molar extinction coefficient (ie. a constant that defines the absorbance of the sample at given wavelength), C is the sample concentration and L is the pathlength that the light passes through. Thus the absorbance of a sample depends

directly on its concentration.

All UV-Vis absorbance spectra were recorded on a Perkin Elmer LAMBDA 1050 UV/vis/NIR spectrometer. All measurements were done in a quartz cuvette with a 10 mm path length.

### 2.2.2 Circular Dichroism (CD)

Circular dichroism is an absorbance technique that studies a chiral samples preferential absorbance of left or right handed circularly polarised light, as detailed in the following equation.

$$\Delta A = A_{(\text{left})} - A_{(\text{right})}$$

In this technique the sample is irradiated with a combination of both left and right handed circularly polarised light. Since a chiral sample absorbs a preferential handedness of circularly polarised light, the transmitted light contains more of one hand over another and thus the detected light is elliptical. For this reason a circular dichroism spectrum is typically expressed in terms of absorbance or ellipticity in units of millidegrees (mdeg).

All Circular dichroism analysis was performed on a Jasco J-815 and Jasco J-810 spectrometer. All scans were done in a quartz cuvette

with a 10 mm path length.

### 2.2.3 Attenuated total reflectance Infra-red spectroscopy (ATR-IR)

Attenuated total reflectance (ATR) is an IR technique that involves the total internal reflection of IR waves through a crystal of high refractive index. This total internal reflection produces evanescent waves on the surface of the crystal and into a sample held in contact with the crystal (refer to figure 2.1 below).

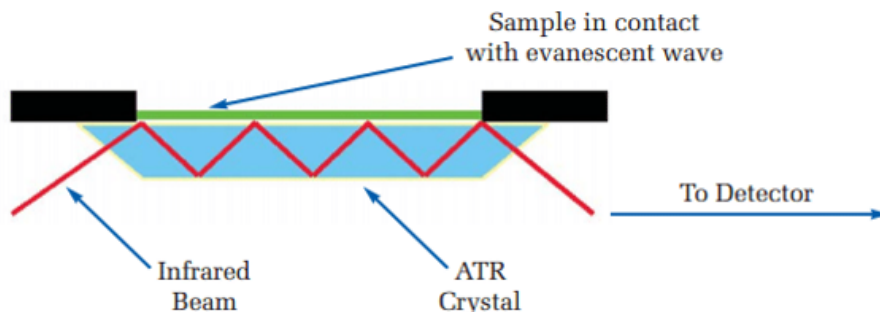


Figure 2.1: Principle of ATR-IR. Image reproduced from reference 1<sup>1</sup>

Absorption of IR radiation by the sample results in an attenuation of the evanescent waves. The attenuated energy is passed back into the IR beam, which then passes through the crystal and exits the opposite end of the crystal where it is detected. Unlike conventional IR

techniques which requires the sample to be in a matrix such as KBr, ATR-IR only requires the solid sample to be in direct contact with the crystal.

All IR spectra were recorded on a Bruker Tensor II with an ATR accessory. All samples were dried under vacuum prior to analysis. All measurements were done over the range of 4000 - 200  $\text{cm}^{-1}$

#### **2.2.4 X-Ray powder diffraction (XRD)**

XRD is a non-destructive technique that uses X-rays to characterise crystalline materials. A material is defined as crystalline if it has a regular and periodic arrangement of its atoms. This technique involves the formation of diffraction patterns by interacting X-rays with crystal planes in a sample. In order to simplify the system reflection is used to describe the diffraction events that occur from a given plane. This is further simplified by using miller indices which convert the reflecting planes into points defined by coordinates (h,k,l). In order for a diffraction pattern to be observed constructive interference from the diffracted waves must occur. This constructive interference occurs when Braggs law is satisfied (refer to the following equation).

$$n\lambda = 2d\sin(\theta)$$



where  $n$  is an integer number,  $\lambda$  is the wavelength of the incident beam,  $d$  is the distance between parallel planes and  $\sin(\theta)$  is the angle of incidence.

All XRD analysis was performed on a Bruker D2 Phaser diffractometer. All samples were dried under vacuum prior to analysis.

### 2.2.5 Scanning Electron Microscopy (SEM)

Scanning electron microscopy (SEM) is a form of electron microscopy which uses accelerated electrons as the illumination source. These electrons are generated from an electron gun typically by heating a tungsten tip. The electrons are then accelerated by an anode under a vacuum and pass through condenser lenses which control the intensity and size of the beam. Objective lenses then focus the beam onto the sample while scanning coils deflected the beam horizontally and vertically over the surface of the sample. The basic set up of the SEM is shown in Figure 2.2.

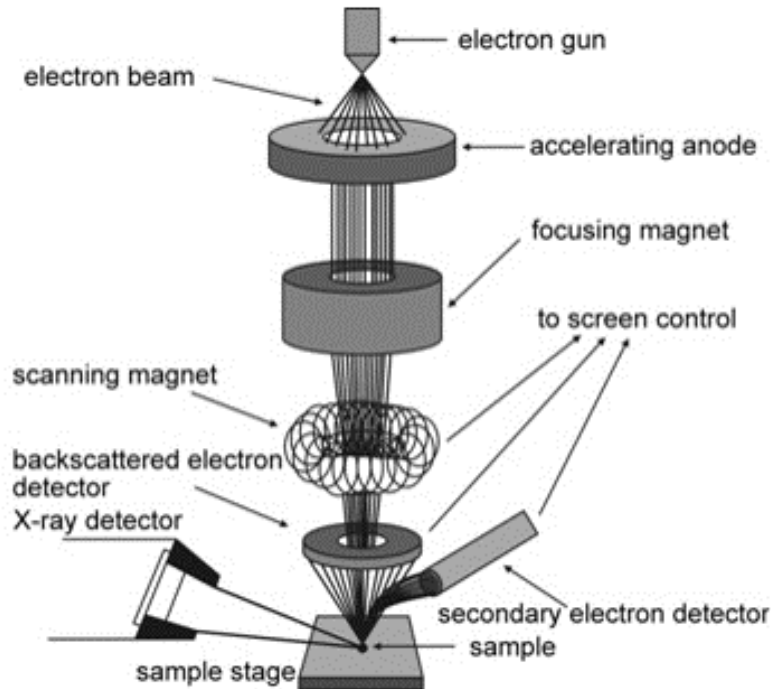


Figure 2.2: Basic set-up of a scanning electron microscope. image reproduced from ref 2<sup>2</sup>.

The bombardment of the sample by the electron beam results in electrons being ejected from the sample. This generates secondary electrons and backscattered electrons. Secondary electrons are due to emission from valence electrons from the surface atoms of the sample. Since these electrons are generated only from the surface, they provide information about the samples surface topology. Backscattered electrons are produced from deeper inside the sample than the secondary electrons and provide information about the surface topology and composition of the sample. In addition X-rays can also be generated following the excitation and relaxation of inner shell electrons

from the constituent atoms of the sample. This allows for elemental analysis of the sample. X-ray elemental analysis is discussed in more detail section 2.2.8. SEM thus can provide a variety information about the samples morphology, surface topology and composition.

SEM Analysis was performed on an Zeiss Ultra Plus SEM. Samples were prepared by drop-casting the sample onto a carbon tab on a aluminium stub and allowing to dry overnight.

### **2.2.6 Transmission Electron Microscopy (TEM)**

Transmission electron microscopy (TEM) is another form of electron microscopy. Similar to SEM, the electron beam is generated from an electron gun and accelerated by an applied voltage in a vacuum. The TEM uses a complex condenser lens set up composed of at least 2 lenses to focus the electron beam onto the sample. Apertures are further used to control the spot size and intensity of beam on the sample. Unlike SEM which detects secondary and backscattered electrons, TEM uses only thin samples and thus detects electrons that are transmitted through the sample. The transmitted beam then passes through an objective lens and aperture to further fine focus the beam onto the detector. Typically a CCD detector is used to produce the final image. Regarding high-resolution (HR)-TEM, this offers signif-

icantly enhanced spatial resolution of up to 0.2 nm. As a result HR-TEM can provide more detailed information about the sample such as crystal orientation due to the formation of lattice fringes. The basic principle of a TEM is shown in Figure 2.3

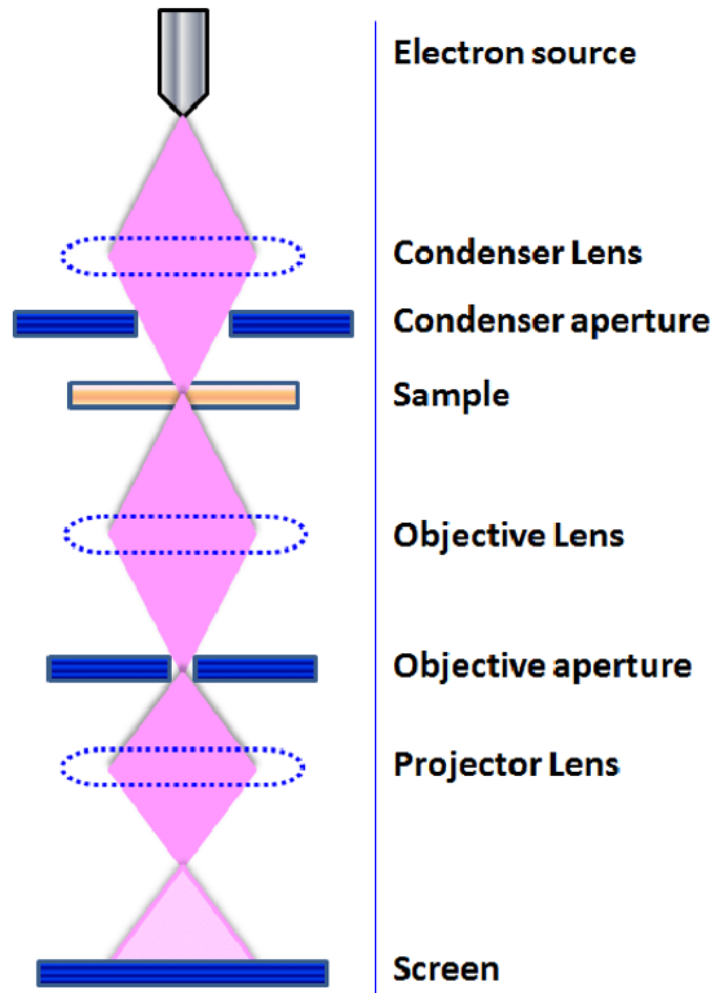


Figure 2.3: Basic set-up of a Transmission electron microscope. Image reproduced from ref 3.<sup>3</sup>

All low resolution Transmission Electron Microscopy (TEM) and high

resolution TEM analysis was performed on a JOEL 2100 and a FEI-Titan respectively. The samples were prepared by drop-casting the sample onto 300 mesh lacy carbon copper grids and allowing to dry overnight. Low resolution TEM was performed using a 200 KeV acceleration voltage from a Lanthanum Hexborise emission source. High resolution TEM was performed using an acceleration voltage of at least 300 KeV.

### **2.2.7 Scanning Transmission Electron Microscopy (STEM)**

Scanning transmission electron microscopy (STEM) is a highly versatile form of electron microscopy for characterising and analysing nanomaterials. This microscopy works on the same principle as SEM however thin samples are used, which allows for transmission modes of imaging as seen in TEM also to be used. Thus STEM combines the benefits of TEM and SEM. Similar to SEM, STEM produces secondary electrons and backscattered electrons, however the signal levels are higher and greater spatial resolution can be achieved by STEM by detecting the transmitted electrons. Multiple detectors can be used in STEM to provide different but complimentary information about the sample. The typical detectors include the bright field detector (BF) which detects electrons directly from the transmitted electron beam and the annular dark field (ADF) detector, that surrounds the

transmitted beam and detects the scattered electrons. The ADF detector is typically angled out side of the incident transmitted beam to optimize the collection of scattered electrons. Since the scattering of electrons depends on the atomic number ( $Z$ ) this is often referred to as  $Z$ -contrast or High angle annular dark field (HAADF) imaging. The basic principle of STEM is presented in Figure 2.4.

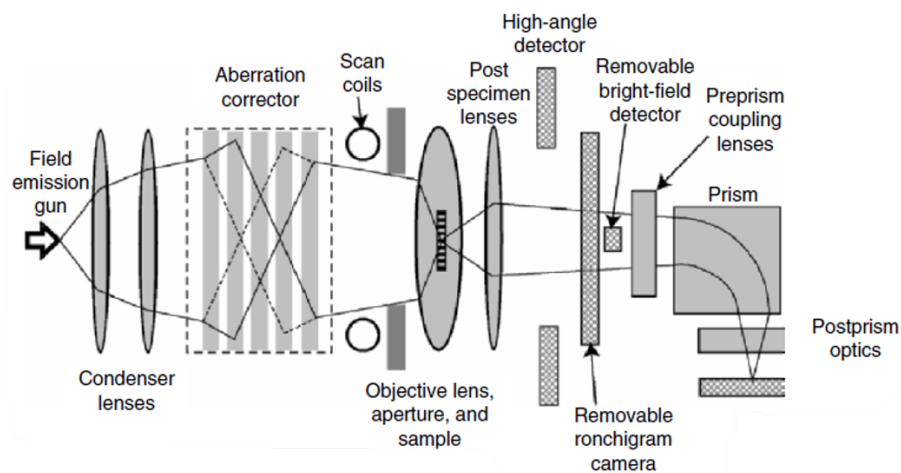


Figure 2.4: Basic set-up for scanning transmission electron microscope. Image reproduced from ref 4.<sup>4</sup>

STEM was performed by using the High angle annular dark field STEM detector on an FEI-Titan. The Samples were prepared by drop-casting the sample onto 300 mesh lacy carbon copper grids and allowing to dry overnight.

### 2.2.8 Energy dispersive X-ray Spectroscopy (EDX)

Energy dispersive X-ray analysis is a technique used for identifying and quantifying elements present in a sample. All EDX analysis was performed by using the EDX detector on the Jeol 2100, FEI-Titan and Zeiss Ultra Plus SEM. EDX mapping was performed by Dr. Sarah McCarty and Dr. Finn Purcell-Milton.

Briefly, in this technique electrons are ejected out from the inner shell of an atom following irradiation from a high energy electron beam. An electron from an outer shell then relaxes to fill the vacancy of the ejected electron. The relaxation of the outer electron results in the emission of X-ray photons. Since the energy difference between each shell is characteristic of that atom it is possible to identify elements.

Characteristic X-rays are labeled depending on the shell from which the ionisation and relaxation process occurs. The shells are termed K, L, M and N with K being the closest to the nucleus. If for example ionization occurs from the K shell and the relaxing electron is from the L shell, the emitted X-ray is termed  $K\alpha$  (as L is one shell away from the K shell). If relaxation from M to K occurs this is termed  $K\beta$  (as M is two shells away from K). Figure 2.5 below details the principle of EDX spectroscopy.

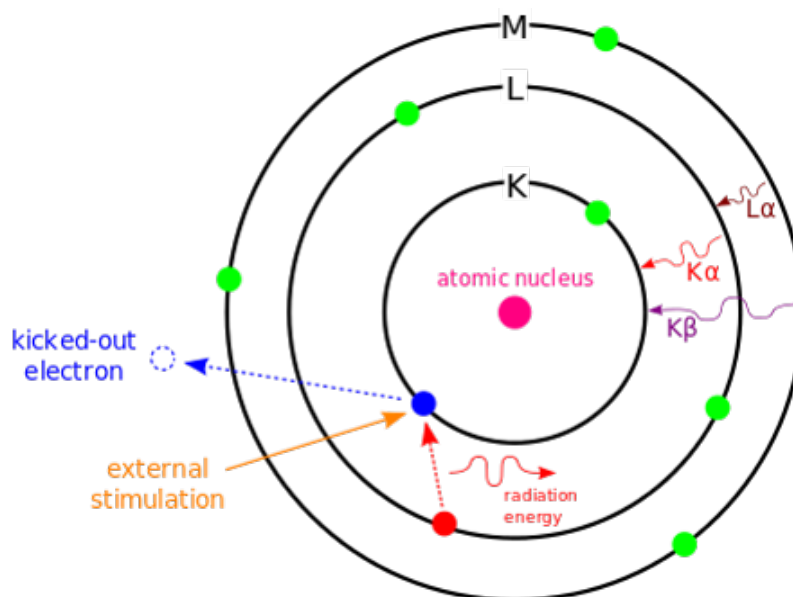


Figure 2.5: Basic principle of EDX. Image reproduced from ref 5.<sup>5</sup>

### 2.2.9 Electrochemistry

Electrochemistry is the study of electron transfer processes between an electrode surface and molecules either bound to the electrode or in solution near the electrode.<sup>6</sup> Electrochemical analysis is done in an electrochemical cell which consists of a working electrode, reference electrode and a counter electrode. The working electrode provides the surface where the electron transfer process(es) occur. This surface needs to be pristine prior to any surface modification, in our case with nanomaterials in order to achieve optimal performance. In the case of the reference electrode, this has a well defined and stable equilibrium



potential. It is used as a reference point against which the potential of other electrodes can be measured in the electrochemical cell. Common examples include the saturated Calomel electrode and the Ag/AgCl electrode. Finally the purpose of the counter electrode is to complete the electrical circuit in the cell. Since the current in the cell flows from the working electrode to the counter electrode, the counter electrode needs to be chemically inert within the potential window being studied. In addition a suitable electrolyte solution is also needed to reduce solution resistance. A typical electrochemical cell set up is shown in Figure 2.6.

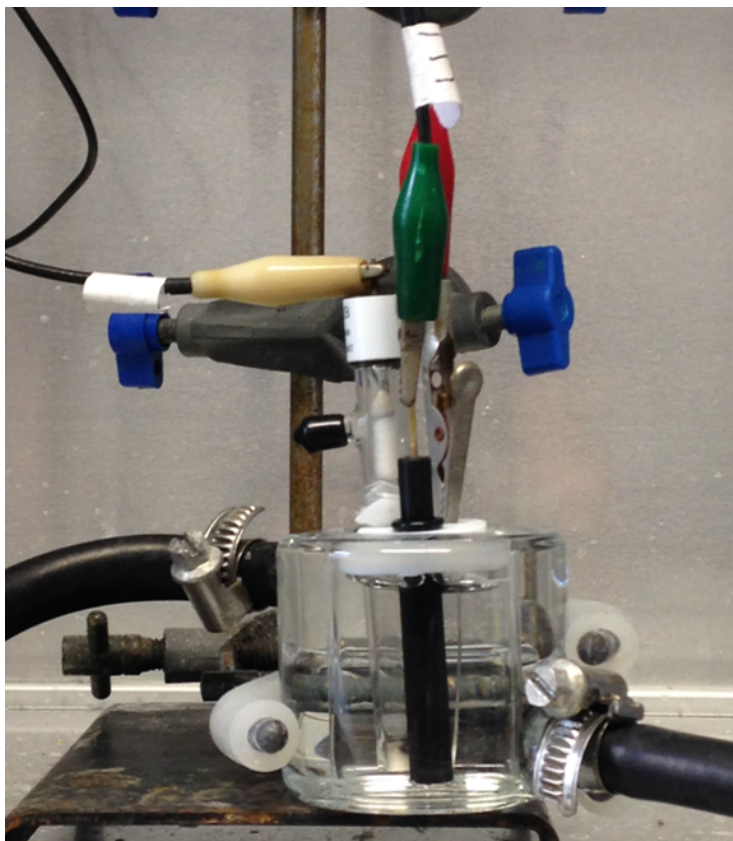


Figure 2.6: Electrochemical cell set up with working electrode (green), reference electrode (white) and counter electrode (red).

Electrochemistry offers a multitude of analytical techniques, with cyclic voltammetry (CV) in particular being one of the most commonly used techniques. CV involves sweeping the electrode potential between 2 potential limits  $E_1$  and  $E_2$  at known scan rate. Upon reaching  $E_2$  the sweep is then reversed to  $E_1$  thus forming a cyclic scan. CV plots current against potential and indicates the potentials where redox process occur. Oxidation process occur in the forward scan ( $E_1$  to  $E_2$ ) by applying a positive potential ramp. This causes the electroactive species to lose electrons at the electrode and results in an

anodic current peak at a given potential. Reduction process typically occur in the reverse scan ( $E_2$  to  $E_1$ ) by applying a negative potential ramp. The reduction of the analyte results in a cathodic current peak at a given potential.

CV is a highly versatile electroanalytical tool, as by varying the scan rate it is also possible to probe the mechanism of an electrochemical process. The relationship between scan rate and the peak current for a reversible and quasi-reversible reaction is given by Randles-Sevciks equation:

$$i_p = 0.4463nFA C \left( \frac{n\nu F D}{RT} \right)^{\frac{1}{2}}$$

Where  $i_p$  is the peak current,  $n$  is the number of electrons involved in the electron transfer process,  $F$  is the Faradic constant,  $A$  is the geometric surface area of the electrode,  $C$  is the concentration,  $\nu$  is the scan rate,  $D$  is the diffusion coefficient,  $R$  is the gas constant and  $T$  is temperature. Since the current response in CV depends on the amount of analyte being oxidized/reduced at the electrode surface, this is effected by the diffusion of the species to the electrode. This diffusion process further depends on the concentration gradient at the electrode. As the voltage changes the concentration of the species near the electrode changes thus at slow scan rates the diffusion layer

thickness is large resulting in smaller peak current, while for fast scan rates the diffusion layer thickness is small hence the peak current is large. In keeping with the Randles-Sevcik's equation a plot of the peak current versus the square root of the scan rate is linear for diffusion controlled processes.

Cyclic voltammetry (CV) was recorded on a CH Instruments electrochemical workstation. All electrocatalytic studies were performed using a standard three electrode cell at room temperature (24 ± 1 °C) controlled by a Julabo F-12. The cell was placed inside a Faraday cage for all measurements. Glassy carbon electrodes (GCE) 3 mm in diameter were used as the working electrode, Pt wire was used as the counter electrode and Ag/AgCl or saturated calomel as the reference electrode. All solutions were degassed by bubbling nitrogen through them for at least 25 minutes. All glassware was thoroughly rinsed with HCl and millipore water prior to use. The electrode surface was cleaned and renewed after each measurement, by rinsing the electrode in HCl and water and sequentially polishing the surface with 1, 0.3 and 0.05 μm alumina powder.

## 2.3 Experimental protocols

## 2.4 Experimental protocols of chapter 3

### 2.4.1 Synthesis of ultrathin AuAg nanowires

PVP (1 mL, 500 mM),  $\text{HAuCl}_3 \cdot 3\text{H}_2\text{O}$  (200  $\mu\text{L}$ , 50 mM) and  $\text{AgNO}_3$  (200  $\mu\text{L}$ , 50 mM) were dissolved in DMF (8 mL). The solution was vortexed for 2 minutes and an aqueous solution of ascorbic acid (1 mL, 400 mM) was then injected into the solution. The mixture was vortexed for a further 30 s and then left standing for 1 day (for 8 nm nanowires) or 3 days (for 3 nm nanowires) at room temperature. After aging, the solution was then diluted by a factor of 20 with water. The resulting grey solution was then centrifuged twice (9000 rpm, 35 mins) and the precipitate was redispersed in water.

### 2.4.2 Synthesis of ultrathin AuAg nano-necklaces

PVP (1 mL, 500 mM),  $\text{HAuCl}_3 \cdot 3\text{H}_2\text{O}$  (200  $\mu\text{L}$ , 50 mM) and  $\text{AgNO}_3$  (200  $\mu\text{L}$ , 50 mM) were dissolved in DMF (8 mL). The solution was vortexed for 2 minutes and ascorbic acid (1 mL, 400 mM) was then injected into the solution. The mixture was vortexed for a fur-

ther 30 s and then left standing for 18 hrs day at 35 °C. After aging, the solution was then diluted by a factor of 20 with water. The resulting grey solution was then centrifuged twice (9000 rpm, 35 mins) and the precipitate was redispersed in water.

### **2.4.3 Catalytic reduction of 4-nitrophenol using Ultrathin AuAg nanowires**

4-Nitrophenol (500  $\mu\text{L}$ , 4 mM) was dissolved in millipore water (9 mL).  $\text{NaBH}_4$  (500  $\mu\text{L}$ , 0.2 M) was then added and the resulting dark yellow solution was stirred for 10 minutes at room temperature. The AuAg NWs (500  $\mu\text{L}$ , 0.45 mg/mL) were then added to the solution and 2.5 mL of this mixture was transferred into a quartz cuvette. The formation of the nitrophenolate anion was then monitored by UV-Vis analysis by taking measurements every 1 minute until completion of the reaction.

### **2.4.4 Ultrathin AuAg nanowires as anodic catalyst for ethylene glycol oxidation**

The glassy carbon working electrode (3 mm diameter) was modified with 9 or 3.6 nm ultrathin AuAg NWs by drop casting from stock

solutions and allowing to dry in air. Typically 10  $\mu\text{g}$  of catalyst in each case was used. Nafion (25  $\mu\text{L}$ ) 1 wt % was then drop cast onto the modified electrode and allowed to air dry. The cyclic voltammograms (CVs) were obtained in nitrogen-saturated solutions and the potential was scanned from -0.8 to 0.8 V (saturated camel electrode) at 50  $\text{mV s}^{-1}$ . All measurements were carried out using a solution of 0.5 M ethylene glycol with 1 M KOH as the electrolyte. The scan was repeated several times to ensure that a stable and reproducible cyclic voltammetry (CV) curve was obtained.

#### **2.4.5 AuAg nano-necklaces as anodic catalysts for ethylene glycol oxidation**

The glassy carbon working electrode (3 mm diameter) was modified with ultrathin AuAg NNL by drop casting from stock solutions and allowing to dry in air. Typically 10  $\mu\text{g}$  of catalyst in each case was used. Nafion (25  $\mu\text{L}$ ) 1 wt % was then drop cast onto the modified electrode and allowed to air dry. The cyclic voltammograms (CVs) were obtained in nitrogen-saturated solutions and the potential was scanned from -0.8 to 0.8 V (saturated camel electrode) at 50  $\text{mV s}^{-1}$ . All measurements were carried out using a solution of 0.5 M ethylene glycol with 1 M KOH as the electrolyte. The scan was repeated several times to ensure that a stable and reproducible cyclic voltammetry

(CV) curve was obtained.

#### **2.4.6 Experimental protocols of chapter 4**

#### **2.4.7 Chiral modification of 1D ultrathin AuAg nanomaterials**

Chiral modification was performed by using a ligand exchange using thiol containing amino acids. Typically chiral ligand (120  $\mu\text{L}$ , 1 mM) was added to 1D Ultrathin AuAg nanomaterials (500  $\mu\text{L}$ ) in water (1.5 mL). The sample was then purified by centrifugation (15000 rpm, 20 mins) and the precipitate was redispersed in water.

#### **2.4.8 Experimental protocols of chapter 5**

#### **2.4.9 Templated synthesis of RhPt dendritic nanowires**

PVP (30.3 mg , 55000 wt) was dissolved in water (14 mL). Ultrathin AuAg NWs (1 mL, 0.35 mg/mL) were then added and the solution was heated to 80 °C.  $\text{RhCl}_3$  (270  $\mu\text{L}$ , 19 mM) and  $\text{H}_2\text{PtCl}_4$  (2.7 mL, 5 mM) were added sequentially and the solution was stirred for 1 min. An aqueous solution of ascorbic acid (1 mL, 1 mM ) was then added and the solution was left heating at 80 °C for 1 hour. The solution



was then cooled to room temperature and Acetone was added. The solution was then centrifuged three times (9000 rpm, 30 mins) and the precipitate was the redispersed in water.

#### **2.4.10 Templated synthesis of Pt dendritic nanowires**

In the case of 1D Pt assemblies the procedure was repeated as detailed in 7.3.1 only 2 equivalents of  $\text{H}_2\text{PtCl}_4$  (5.4 mL, 5 mM) were added.

#### **2.4.11 1D Pt and RhPt assemblies for electrocatalytic oxidation of methanol, ethanol and formic acid**

The working electrode was modified with the Pt or RhPt assemblies by drop casting from stock solutions and allowing to dry in air. Typically 4.9  $\mu\text{g}$  of catalyst in each case was used. Nafion (5  $\mu\text{L}$ ) 0.1 wt % was then drop cast onto the modified electrode and allowed to air dry. In the case of methanol perchloric acid was used as the electrolyte. While for formic acid oxidation,  $\text{H}_2\text{SO}_4$  was used as the electrolyte. The cyclic voltammograms (CVs) were obtained in nitrogen-saturated solutions. and the potential was scanned from -0.25 to 1.05 V (Ag/AgCl) at a scan rate 50  $\text{mV s}^{-1}$  in all cases. Voltammogram measurements for the oxidation of each substance were carried out in a solution of 1 M methanol or 0.5 M formic acid with a 0.5 M of electrolyte both

cases. The scan was repeated several times to ensure that a stable cyclic voltammetry (CV) curve was obtained.

#### **2.4.12 Synthesis of AuAg nanowires@ Rh nanoparticle hybrid structures**

PVP (30.3 mg , 55000 wt) was dissolved in water (14 mL). Ultrathin AuAg NWs(1 mL, 0.35 mg/mL) were then added and the solution was heated to 80 °C. RhCl<sub>3</sub> (540 μL, 19 mM) was then added and the solution was stirred for 1 min. Ascorbic acid (1 mL, 1 mM ) was then added and the solution was left heating at 80 °C for 1 hour. The solution was then cooled to room temperature and Acetone was added. The solution was then centrifuged three times (9000 rpm, 30 mins) and the precipitate was then redispersed in water.

## **2.5 Experimental protocols of chapter 6**

### **2.5.1 Synthesis of ultra-long Ag nanowires**

Ag NWs were synthesized using a typical polyol synthesis.<sup>7</sup> Briefly PVP (0.2 g, 55000 wt) was added to ethylene glycol (25 mL) and

sonicated until completely dissolved.  $\text{AgNO}_3$  (0.25 g) was then added into the PVP solution and sonicated for 30 s. Finally 3.5 g of a  $\text{FeCl}_3$  solution (600  $\mu\text{M}$ ) dissolved in ethylene glycol was then added into the above solution. The resulting mixture was then added into a pre-heated reaction vessel at 130 °C and heated for 5 hours. The solution was then allowed to cool to room temperature and washed with acetone and ethanol followed by centrifugation (9000 rpm, 30 min) three times. The precipitated nanowires were then re-dispersed in ethanol.

### **2.5.2 Synthesis of Ag nanowire@ quantum dot hybrid structures**

Prior to the synthesis of the hybrid structures the QDs were transferred into ethanol following centrifugation (and washing twice more with ethanol). The concentration of the QDs in ethanol was then adjusted to the required concentration using UV-vis absorbance spectroscopy (typically an absorbance of 0.6 a.u @ 500 nm was used). The hybrid structures were then synthesized by adding quantum dots (1 mL, ab 500 nm = 0.6 a.u) into ethanol (1.75 mL) while stirring at 960 rpm. Ultra-long Ag NWs (1 mL, 0.525 mg/mL) were then added and the mixture was then stirred counter-clock wise for 10 mins at 960 rpm. The solution was then allowed to age at 4° C for up to 8 days.

After aging the mixture was centrifuged ( 9000 rpm, 10 mins) and the precipitate was redispersed in ethanol.

# References

- (1) ATR-FTIR —The Bernasek Lab website, accessed 20-11-18.
- (2) TECHNOORG - LINDA website, accessed 26-10 -18.
- (3) Bobji, M TRANSMISSION ELECTRON MICROSCOPE, image page 4, accessed 26-10-18., Ph.D. Thesis.
- (4) De Jonge, N.; Sougrat, R.; Northan, B. M.; Pennycook, S. J. *Microscopy and Microanalysis* **2010**, *16*, 54–63.
- (5) Wikipedia Energy-dispersive X-ray spectroscopy image, accessed 29-9-18.
- (6) Elgrishi, N.; Rountree, K. J.; McCarthy, B. D.; Rountree, E. S.; Eisenhart, T. T.; Dempsey, J. L. *Journal of Chemical Education* **2018**, *95*, 197–206.
- (7) Jiu, J.; Araki, T.; Wang, J.; Nogi, M.; Sugahara, T.; Nagao, S.; Koga, H.; Suganuma, K.; Nakazawa, E.; Hara, M.; Uchida, H.; Shinozaki, K. *Journal of Materials Chemistry A* **2014**, *2*, 6326–6330.

# Chapter 3

## Ultrathin AuAg nanowires

### 3.1 Introduction

The synthesis of ultrathin Au nanowires (NWs) has been extensively developed over the last decade, with these materials finding a range of applications from sensing<sup>1-3</sup> and catalysis<sup>4-6</sup> to electronics.<sup>7-9</sup> Typically organic reagents such as oleylamine (Oam) and oleic acid are used in their synthesis, as these reagents can function not only as a solvent but also as reducing and capping agents.<sup>10-15</sup> This multi-functional role helps to restrict the growth of the material to the ultrathin domain (<10 nm). While organic solvents offer uniformity they do however have the disadvantages of toxicity, difficulty in further processing and costly large scale production. Thus in order for this field to expand water soluble Au based NWs are necessary.

Recently, work by Hui *et al*<sup>16</sup> demonstrated that the use of the amine based dendrimer polyamidoamine (PAMM) results in 1.3 nm diameter water soluble ultrathin Au NWs. The NWs produced were highly uniform however extensive dialysis was needed to remove excess of dendrimer. Additional wet chemical methods such as that shown by Ai-Jun *et al*<sup>17</sup> in which  $\text{HAuCl}_4$  was reduced by  $\text{NaBH}_4$  in the presence of L-Glutamic acid (in low concentration) proved effective in producing non-uniform Au NW networks. Similarly Lui *et al*<sup>18</sup> also showed that reduction of  $\text{HAuCl}_4$  by ascorbic acid in the presence of citric acid also produces non-uniform Au NWs. In both these case a low concentration of capping agent was necessary to allow the growth of the seeds into a NW structure. In addition using a method more typical for Au nanorod synthesis, Li *et al*.<sup>19</sup> showed that adding toluene can change the cylindrical micelle of CTAB into a sandwich like micelle which helps to facilitate the growth of ultrathin Au NWs. While methods are emerging for water soluble synthesis of ultrathin Au NWs the field is progressing quite slowly.

Furthermore the synthesis of ultrathin Au based NW alloys is an area also still in its infancy. While the use of ultrathin Au NWs has been established, the potential of ultrathin Au NW alloys has not yet been fully realised due to the scarcity in synthetic methods. AuAg alloys in particular are one of the most extensively studied nano alloys as they

are highly compatible and present promising plasmonic and catalytic properties. Recent examples of 1D alloys include work by Hui *et al.*<sup>16</sup>, who showed that by using the PAMM dendrimer it is also possible to produce a water soluble ultrathin AuAg NW alloy however the NWs are very poly-disperse. Wang *et al.*<sup>20</sup> has also produced highly uniform 3 nm AuAg NW alloy by reduction of Au and Ag salts with Ascorbic acid under vortex mixing and allowing to age. The draw back to this synthesis however is the extended aging time of 10 days.

The aim of this part of the project was to develop the synthesis for water stable ultrathin AuAg NWs and investigate their properties. Here we detail our results on a new synthesis of ultrathin AuAg NWs with tunable diameters of 9 nm and 3 nm. In addition we report the synthesis of a novel AuAg ultrathin nano-necklace structure. Finally we explore the application of these materials as anodic catalysts for ethylene glycol oxidation and for the catalytic reduction of 4-nitrophenol.



## 3.2 Synthesis and characterisation of Ultrathin AuAg nanowires

Water soluble ultrathin AuAg nanowires were synthesised by modifying the protocol developed by Wang *et al.*<sup>20</sup> Briefly, H<sub>2</sub>AuCl<sub>4</sub> and AgNO<sub>3</sub> were reduced (1:1) in dimethylformamide (DMF) under vortex stirring using ascorbic acid (AA) as a reducing agent and polyvinylpyrrolidone (PVP) as a stabiliser. After reduction the solution was then left standing at room temperature. By allowing the solution to age for up to 4 days and diluting a 1 mL aliquot from the reaction mixture by a factor of 20 (with water) after aging each day, it was possible to tune the resulting NW diameter. TEM analysis is presented in Figure 3.1 below.

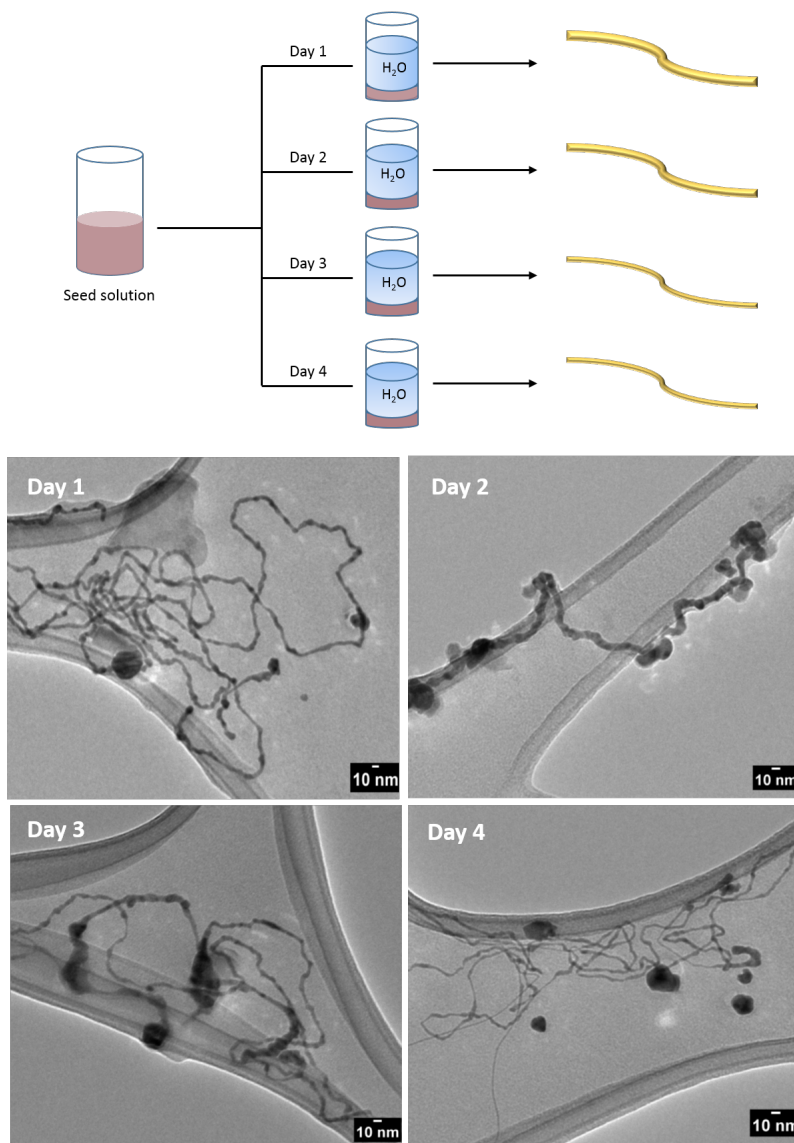


Figure 3.1: Schematic presentation of the preparation of AuAg NWs (top) and TEM images (bottom) of NWs produced following dilution with water after various days of aging.

As shown by our TEM analysis after aging the reaction mixture for 18-24 hours (day 1) and diluting the mixture by a factor of 20 with water, resulted in non-uniform ultrathin NWs with an average diameter of 8 nm and ranging up to microns in length. As the reaction mixture was

aged longer the resulting NWs following dilution became on average thinner, going from 8 nm after day 1 to on average 3 nm by days 3 and 4. The reproducibility of this synthesis is shown in Figure A1. It must be noted that while the diameters significantly changed over time, the products also became more poly-disperse. UV-Vis analysis (Figure 3.2) of the NWs produced after each day shows broad plasmonic bands around 370 and a shoulder at 500 nm. A similar observation was also reported by Wang et al.<sup>20</sup> These 2 plasmonic bands may be due to the longitudinal and transverse plasmonic modes arising from the non-uniformity of the NWs. Regarding the broadness of the peaks this is most likely due to the poly-dispersity of the products particularly for days 2-4 and also the non-uniformity of the NWs. The peak at 500 nm is a common plasmon for Au NWs<sup>16,18</sup> and its peak position remains unchanged after each day. The peak centred around 370 nm is more typically seen in Ag nanomaterials<sup>21,22</sup> and also remains relatively unchanged after each day. A more detailed study of this peak is discussed later (section 3.3). Extending the UV-Vis analysis into the near-IR region (1000 nm), showed no additional peaks.

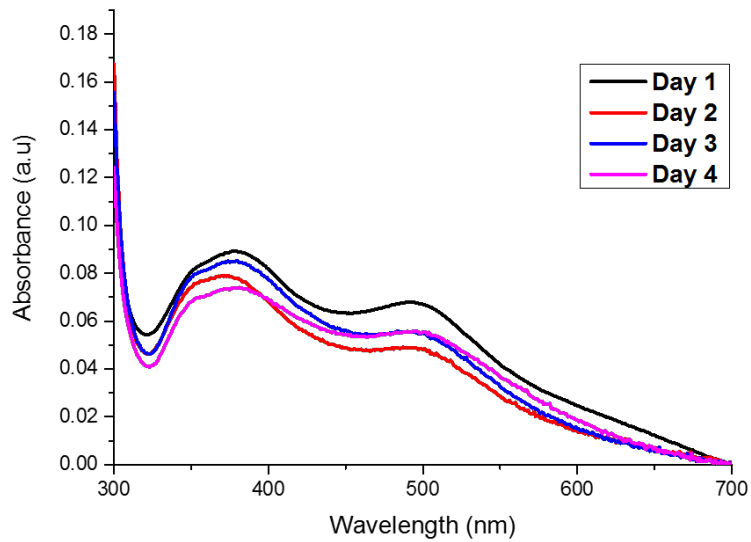


Figure 3.2: UV-vis spectra of NWs produced following dilution after each day of aging.

Since the NWs produced after day 1 were the most monodisperse we performed extensive characterisation only on these NWs. Figure 3.3 presents the High-resolution Transition electron microscopy (HR-TEM) of the NWs produced after 1 day of aging.

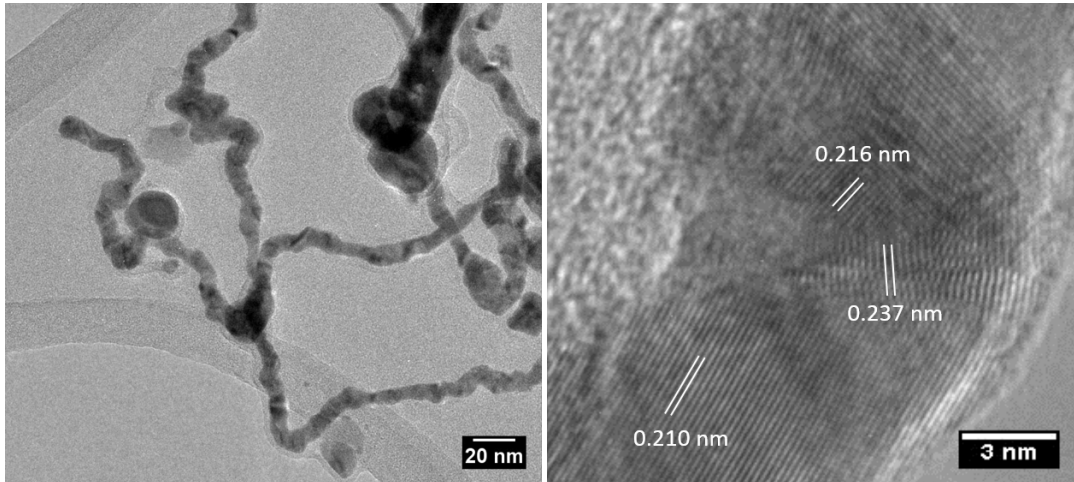


Figure 3.3: HR-TEM images of NWs produced following dilution after 1 day of aging

From our HR-TEM analysis the NWs are poly-crystalline showing multiple lattice fringes with d-spacing of  $0.210 \pm 0.017$  and  $0.237 \pm 0.027$  nm corresponding to the (111) and (200) of FCC Au and Ag.

X-ray diffraction (XRD) was performed to further investigate the crystal structure of the NWs (Figure 3.4).

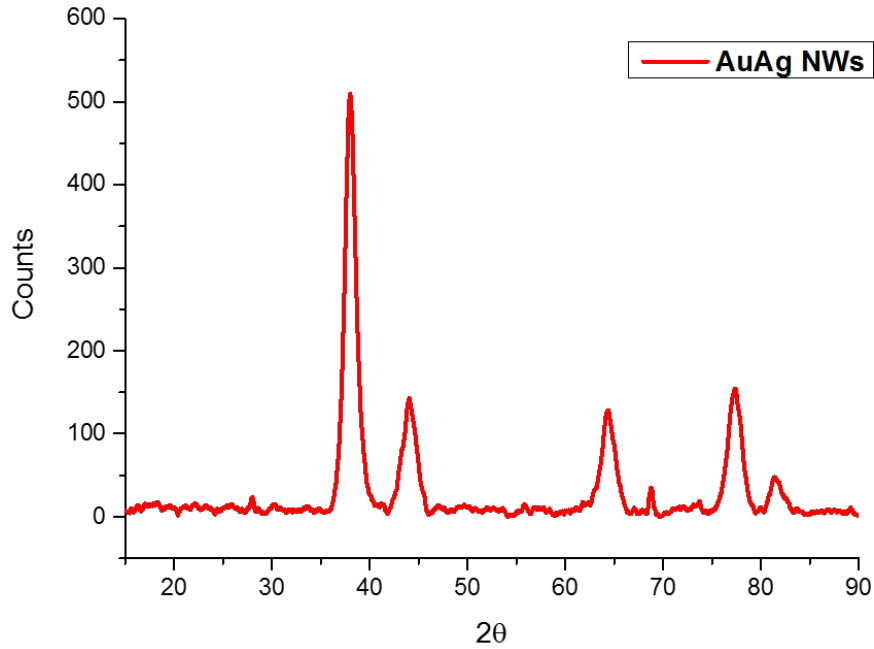


Figure 3.4: XRD pattern for AuAg ultrathin nanowires.

The XRD analysis shows that the NWs have a high degree of crystallinity with diffraction peaks at  $2\theta$  values of 38.2 , 43.9, 64.37, 77.3 and 81.5 ° corresponding to the (111), (200), (220), (311) and (222) planes respectively for both FCC Au ( JCPDS-01-117) and Ag (JCPDS-01-1164). This observation is typical for noble metal nanomaterials of this kind. Furthermore texture coefficient (TC) analysis (table 3.1) shows that the (111) plane has the highest coefficient. This analysis indicates that the NWs preferentially grow along the (111) plane.

Table 3.1: Texture coefficient analysis of AuAg ultrathin NWs produced after 1 day of aging

<b>Facet</b>	<b>I<sub>0</sub> (counts)</b>	<b>I (counts)</b>	<b>TC* of sample</b>
111	453.3	510	1.13
200	208.5	143.4	0.67
220	117	133.2	1.07
311	136.6	150.5	1.10

\* refer to appendix for TC equation. Reference 05-8482 was used for this analysis.

High angle annular dark field Scanning transmission electron microscopy (HAADF-STEM) was also performed on the NWs to study their surface topology (Figure 3.5). The HAADF-STEM analysis shows that the NWs present a smooth surface topology. In addition a uniform z-contrast along the length of the NWs was also noted, indicating that there is a homogeneous distribution of metals present in the NWs.

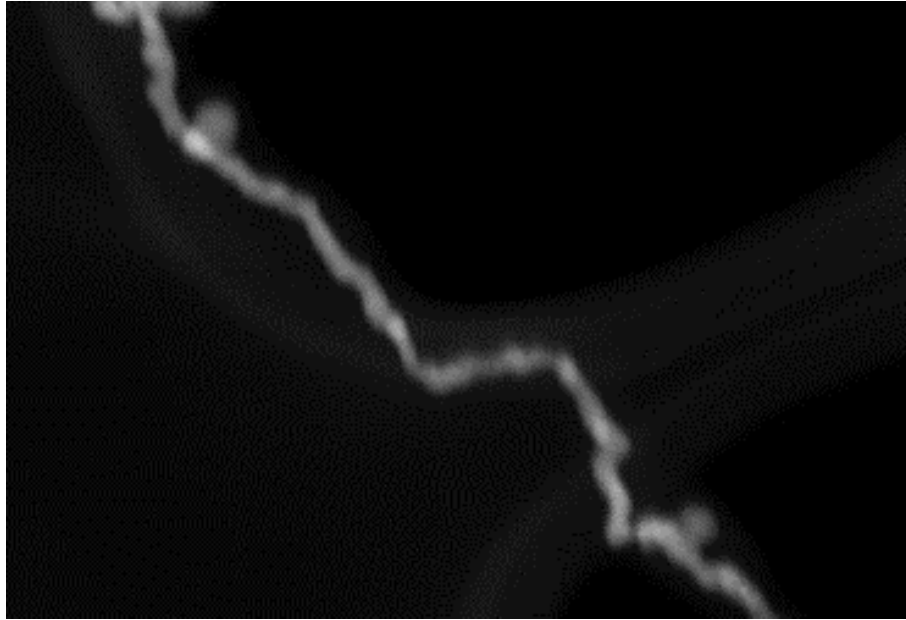


Figure 3.5: STEM analysis of AuAg nanowires produced following dilution after 1 day of aging.

In order to confirm the elemental composition and distribution of metals in the NWs HAADF-STEM energy-dispersive X-ray (HAADF-STEM EDX) mapping was performed (Figure 3.6).



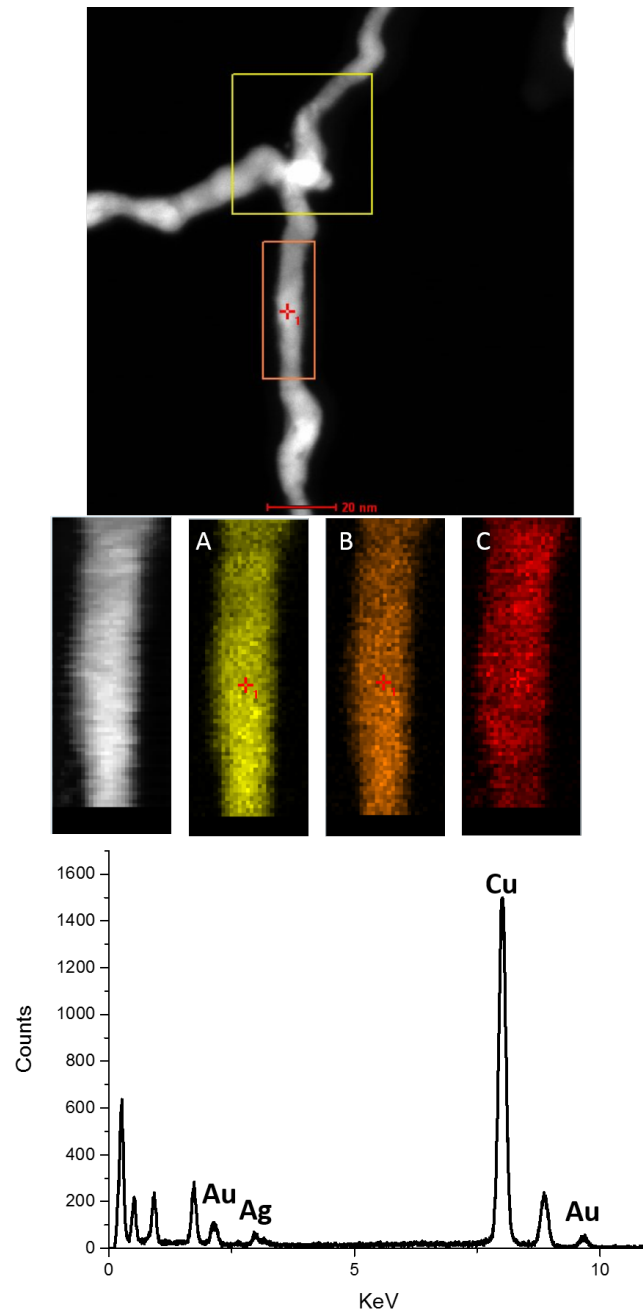


Figure 3.6: STEM-EDX map (top) of AuAg nanowires where A and B denotes the L- and K- lines of Au and C denotes the L- line of Ag and the associated EDX spectrum (bottom).

The elemental analysis confirms that the NWs are an alloy of Au

and Ag with a Au:Ag ratio of 60:40. The EDX spectrum shows the characteristic L and M peaks of Au at 9.7 and 2.1 KeV respectively and the L peak of Ag at 3.1 KeV respectively. The additional peaks present are due to the Cu from the TEM grids used for this analysis. HAADF-STEM EDX mapping further confirms that both metals are uniformly distributed along the NW. This result also accounts for the uniform contrast observed in our STEM analysis.

### **3.3 Analysis of the pre-diluted solution**

Analysis of the pre-diluted solution was crucial for understanding the formation of these NWs. After aging the reaction mixture for 18-20 hrs, we analysed the resulting solution with TEM, STEM and UV-Vis (Figure 3.7).

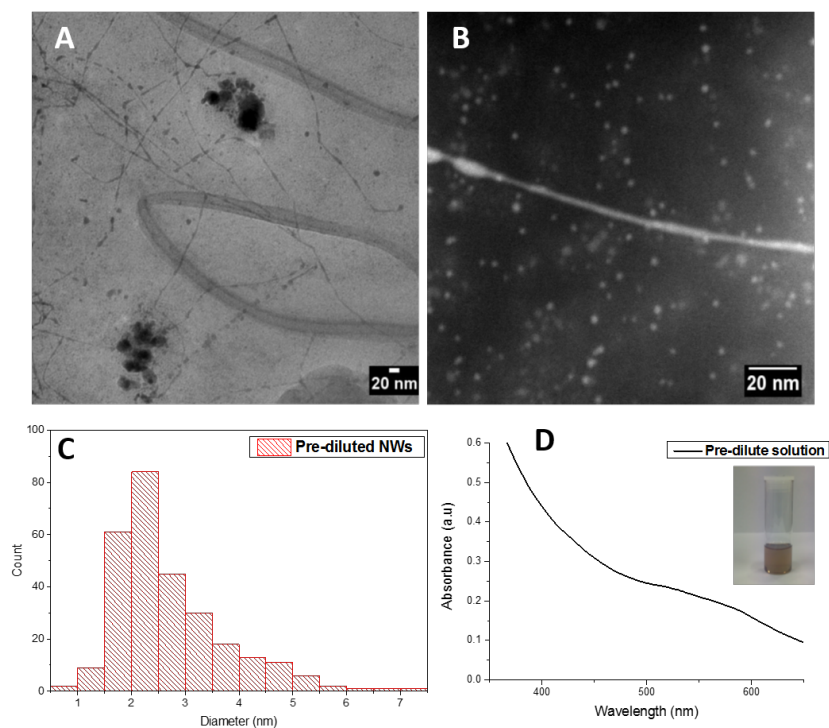


Figure 3.7: TEM image (A), STEM image (B), size distribution (C) and UV-Vis spectrum (D) (with photograph inset of solution ) of pre-diluted solution.

The TEM image displays the presence of ultrathin NWs with an average diameter of 3.1 nm as shown by the size distribution. These NWs are similar to those produced by Wang *et al.*<sup>20</sup> as expected. The UV-Vis shows a broad absorbance profile with a broad absorbance band with an on-set at 500 nm. In addition STEM analysis shows a similar uniform contrast as seen by the post dilution NWs and also highlights the presence of seed nanoparticles. These NWs were notably very fragile and dissociated under a short exposure time by the electron beam. We further characterised these NWs by EDX analysis (Figure 3.8).

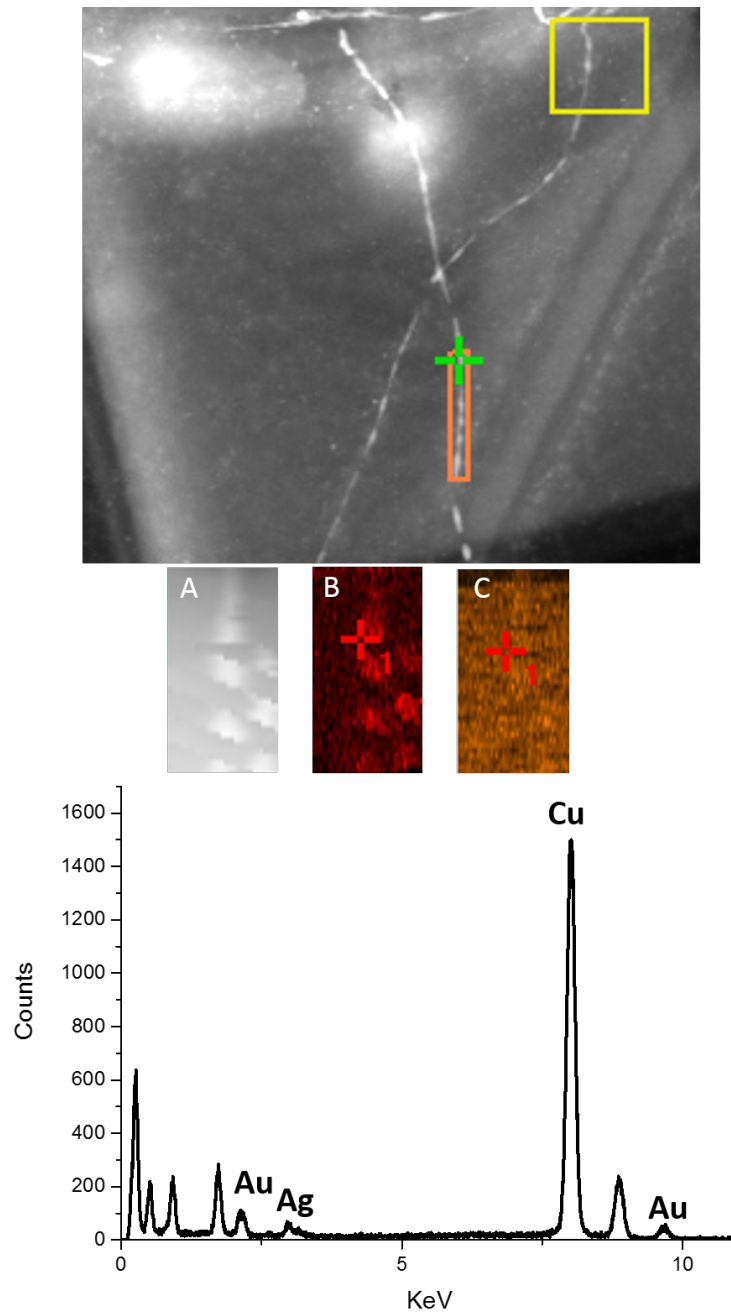


Figure 3.8: HAADF STEM (A) and EDX map of pre-diluted AuAg NWs were and B and C denotes the L- line of Ag and M- line of Au respectively. The associated EDX spectrum (bottom) is also detailed.

Our EDX analysis shows that these NWs are also composed of Au and

Ag as noted by the L and M lines of Au and Ag as detailed in section 3.2. The peaks due to copper is a result of using copper TEM grids as a substrate. A more detailed STEM-HAADF EDX mapping study showed that both metals are also uniformly distributed along the NWs.

### **3.4 Monitoring the formation of ultrathin AuAg nanowires following dilution**

To further understand the mechanism and formation of these NWs we took aliquot from the reaction mixture prior to dilution (after aging for 18-20 hrs) and at various times intervals following dilution and prepared them quickly on lacy carbon TEM grids for TEM analysis. The TEM images are shown in Figure 3.9.

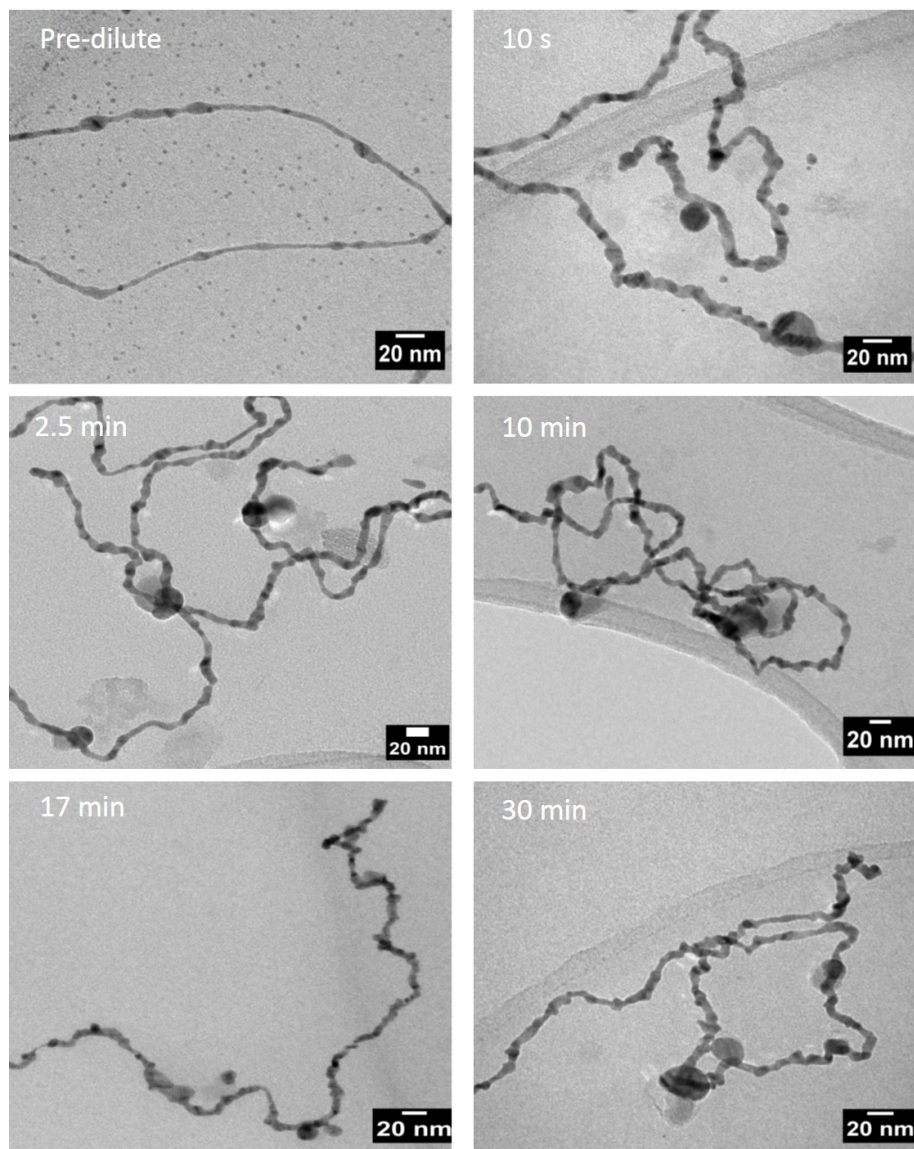


Figure 3.9: TEM analysis monitoring the growth of AuAg nanowires following dilution with water

Our TEM analysis showed that prior to dilution, the aging of the solution resulted in ultrathin NWs with an average diameter of 2-3 nm. The presence of excess seeds was also observed. Following the dilution process we can see that within 10 s thicker NWs are formed.

These resulting NWs become on average 2.5 times thicker than the initial NWs prior to dilution. Comparison of NWs produced at different stages over the duration of the study showed no significant size difference. This implies that the growth process is not immediately stopped when dropped onto the TEM grid. We also performed UV-Vis analysis in tandem with our TEM preparation (refer to Figure 3.10).

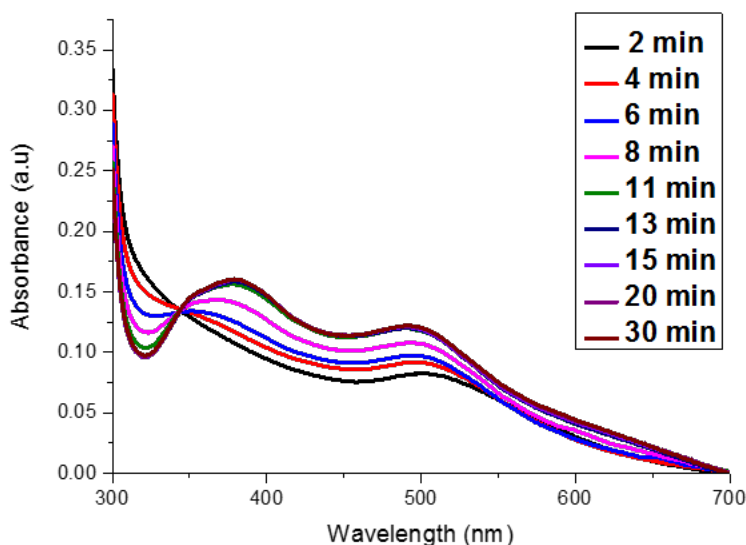


Figure 3.10: UV-Vis analysis monitoring the growth of AuAg nanowires following dilution with water.

UV-Vis analysis shows a single broad absorbance band initially at 500 nm and over time we see the development of the second peak at 370 nm. This second peak is associated with the formation of a new surface as the NWs become thicker.

Thus from these results we propose that the NWs are produced via a 2 step templated mechanism; firstly, the seeds produced from the reduction process undergo an orientated attachment during the aging period to form ultrathin NWs. Secondly in the dilution step, the excess seeds in solution fuse with the NW templates to form the resulting thicker NWs. This fusion process was similarly reported by Al-Wang *et al.*<sup>17</sup> in which a low concentration of capping agent facilitated the growth of Au NW networks. In our case the dilution step, disperses the PVP resulting in poorly passivated seeds. This promotes inter-particle attractive forces such as Van Der Waals, dipole-dipole and hydrogen bonding between the seeds and template NWs which offer large surface areas. The seeds subsequently undergo fusion and wetting onto the surface of the templates. This mechanism supports our earlier observation in which aging the solution for 2-4 days prior to dilution resulted in NWs with a thinner average diameters, as during the aging, more seeds form templates. Thus during the dilution step there are fewer seeds to fuse with the template NWs so the resulting diameters stay on average smaller. Furthermore the random fusion of the seeds with the template also explains the polycrystallinity of the resulting NWs observed in our HR-TEM analysis.



### **3.5 Control study - investigating the role of Ag and Au in the formation of the nanowires**

To further understand the formation of these NWs the role of Au and Ag were studied individually. Control experiments were performed by using either only  $\text{H}_2\text{AuCl}_4$  or  $\text{AgNO}_3$  for the synthesis. The concentration of the metals was kept the same in both cases (2.2 mM) and the samples were monitored after days 1 and 3. These 2 days were chosen as they mark the most distinct changes for the AuAg NWs. Our TEM and UV-vis analysis for the Ag control is shown in Figure 3.11.

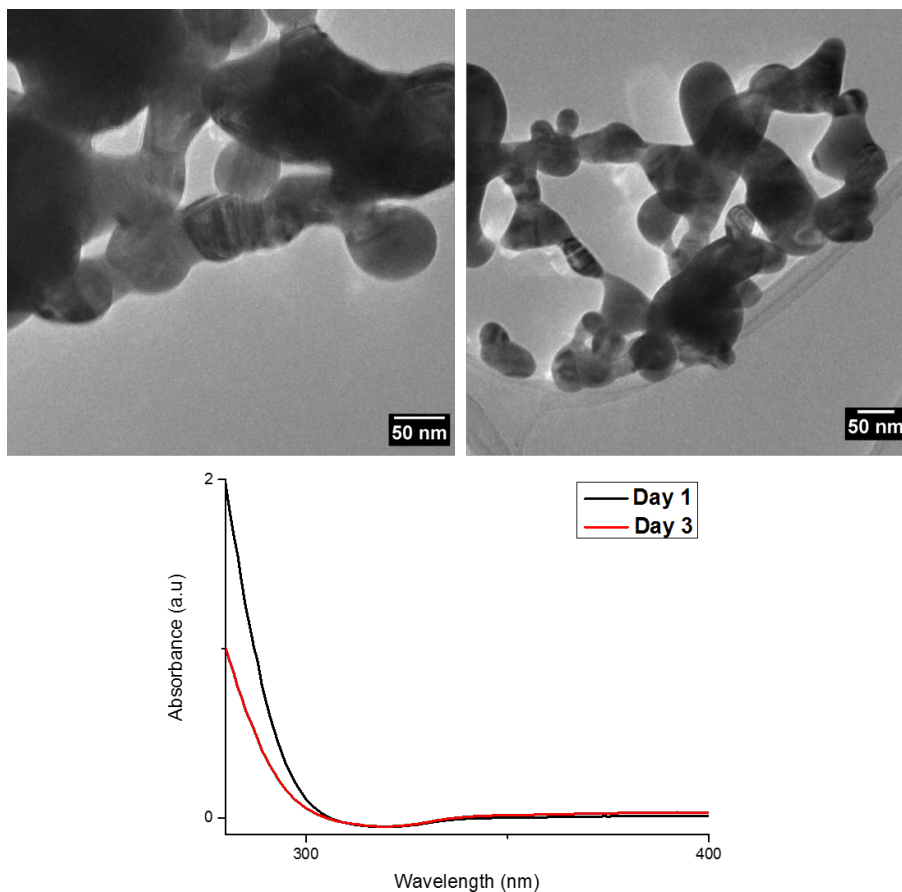


Figure 3.11: TEM images of Ag control after 1 (A) and 3 (B) days aging following dilution and UV-Vis spectra of products produced following dilution after each day.

Interestingly, TEM analysis clearly shows that following dilution Ag nanoparticles undergo a fusion and aggregation process. The fusion of the nanoparticles appears to show 1D anisotropic growth after both days. Since the aging process did not show any significant improvement in the products after day 3, aging the solution longer did not warrant further investigation. In addition the UV-Vis analysis shows a broad absorbance profile with a shoulder at 340 nm after both days. This absorbance feature is common in 1D Ag nanomaterials<sup>23,24</sup> and

the broadness of the absorption profile also compliments the aggregation observed in our TEM. Regarding the Au control, TEM and UV-Vis analysis (Figure 3.12) show a dramatic difference in behaviour compared to the Ag control.

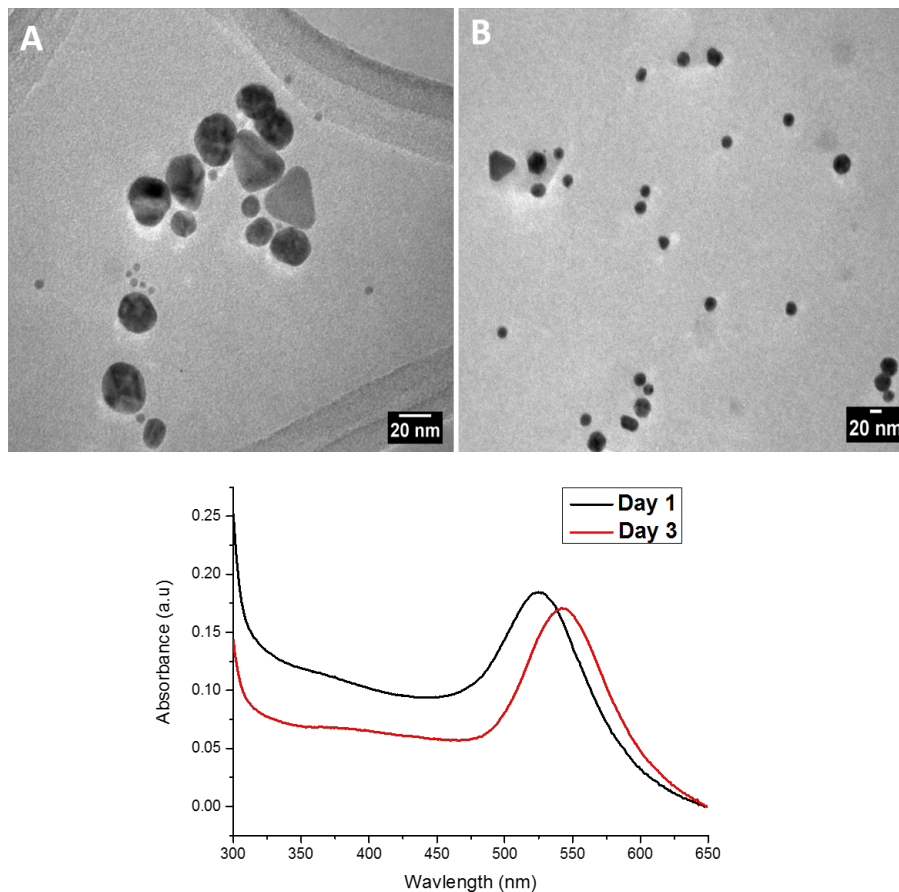


Figure 3.12: TEM image of Au control after 1 (A) and 3 (B) days aging following dilution and UV-Vis spectra of products produced following dilution after each day.

From the TEM (Figure 3.12) only Au nanoparticles of various sizes and shapes were formed following dilution. Furthermore these parti-

cles did not show any fusion and only minor aggregation after both days. The UV-Vis analysis shows a peak at 520 nm after day 1 and 550 nm after day 3 which is typical for Au nanoparticles.<sup>25</sup> The red shift of peaks is indicative of larger particle sizes after day 3.

Thus from our study both metals are required to yield ultrathin NWs. This result is not too surprising as the use of Ag has been well established to promote 1D growth in Au-based nanomaterials.<sup>26,27</sup> The anisotropic fusion seen for the Ag control also supports our proposed mechanism and that perhaps the presence of the Ag component in the alloy helps to facilitate this process.

### **3.6 Study on the effect of various solvents on nanowire formation**

In light of our mechanistic study it was also important to investigate the influence of various solvents for the dilution process. To carry out this study we have chosen 3 alcohols; methanol, ethanol and isopropanol (as they are miscible with both DMF and water and vary in polarity) and diluted 1 ml aliquots from the reaction after each day of aging with water and with each of our chosen alcohols. A dilution factor of 20 was used in all cases and the study was carried out over 3

days. The dilution process was monitored by UV-Vis and the products were analysed by TEM (Figure 3.13- 3.15).

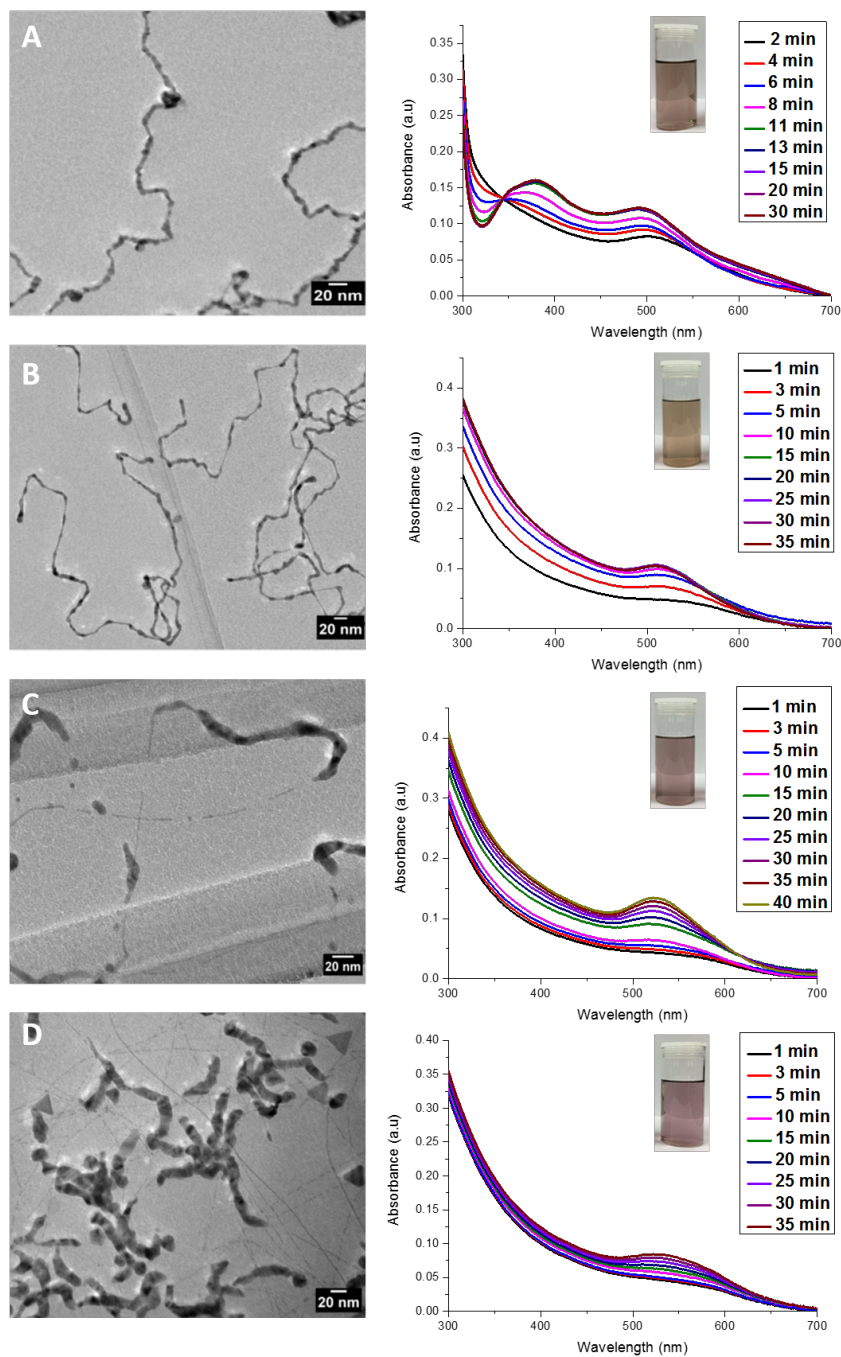


Figure 3.13: TEM (left) and UV-Vis(right) analysis of nanowires produced following dilution with water (A), methanol (B), ethanol (C) and isopropanol (D) after 1 day of aging. Photograph inset of final solution.

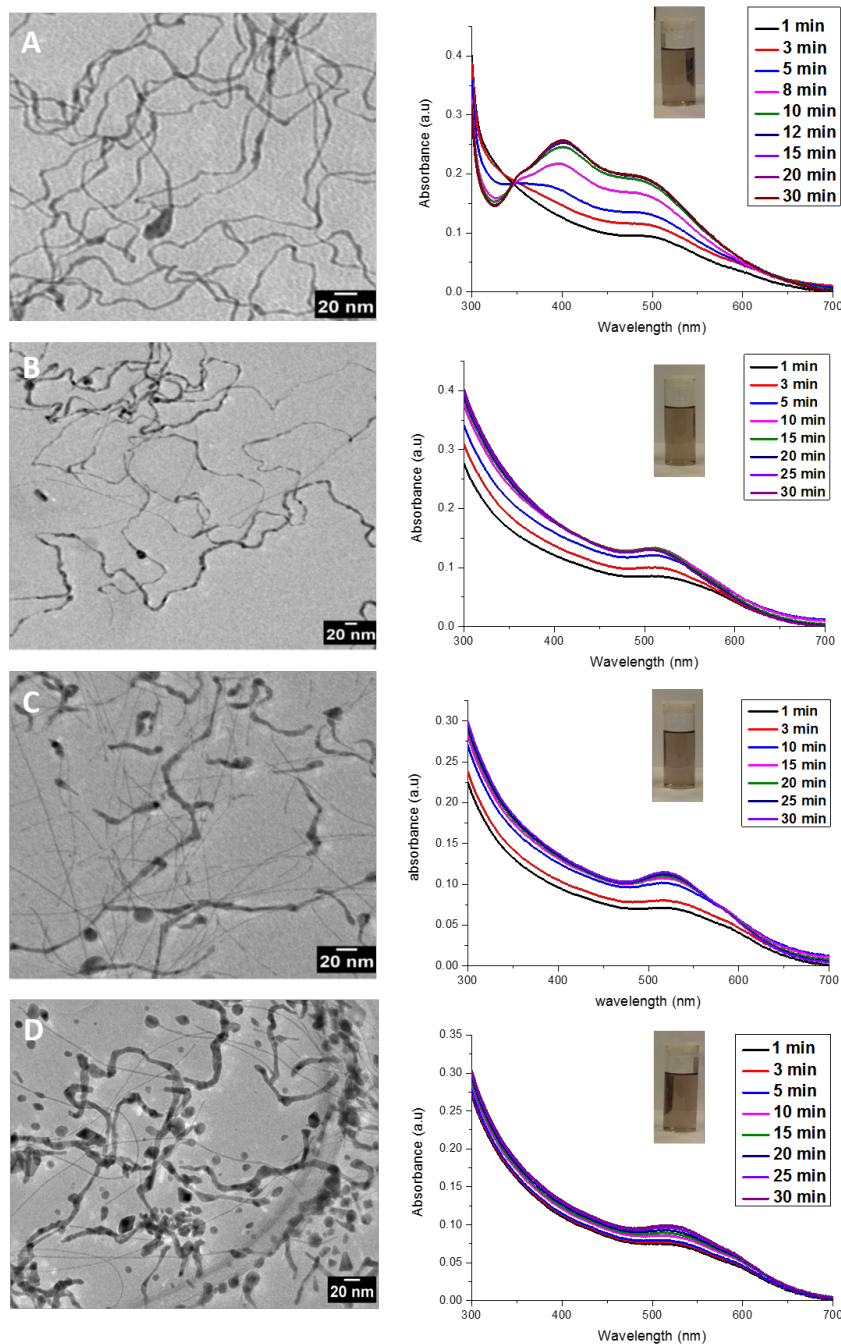


Figure 3.14: TEM (left) and UV-vis(right) analysis of nanowires produced following dilution with water (A), methanol (B), ethanol (C) and isopropanol (D) after 2 day of aging. Photograph inset of final solution.

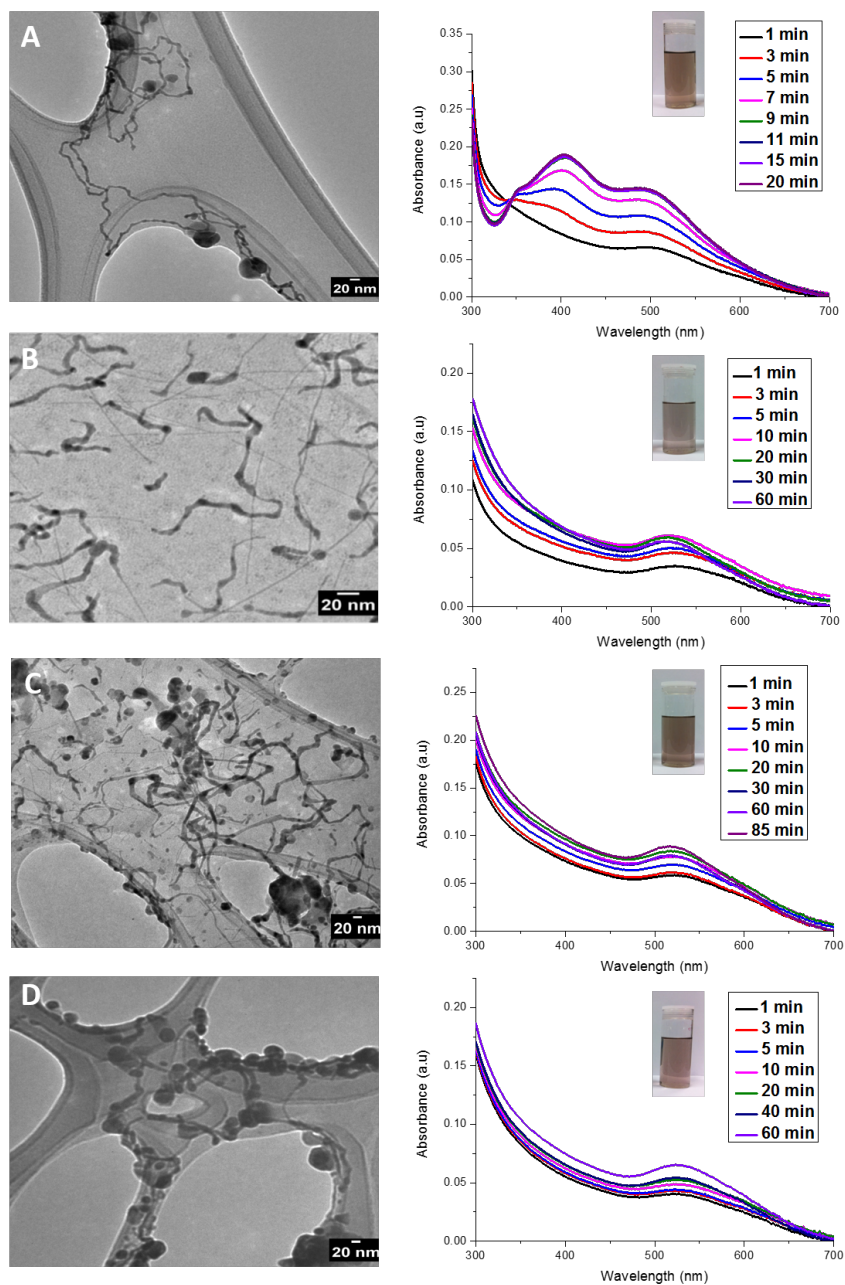


Figure 3.15: TEM (left) and UV-vis(right) analysis of nanowires produced following dilution with water (A), methanol (B), ethanol (C) and isopropanol (D) after 3 days of aging. Photograph inset of final solution.

As expected, the choice of solvent used for the dilution step has a significant effect on the morphology of the resulting NWs. In the case



of ethanol and isopropanol our TEM analysis after each day, showed highly poly-disperse products. These products included nanoparticles of various sizes and a broad distribution of NWs. This result was seen after each day showing that aging did not influence the resulting NWs for both these solvents. This is a marked difference in behaviour and morphology compared to those produced by water, which were non-uniform along the length of NW and gradually became thinner by day 3. Methanol proved most interesting, forming NWs similar in morphology to water but slightly thinner (6 nm) after 1 day of aging. After the second day of aging, the methanol products became more poly disperse showing NWs with average diameters ranging from 3.7 to 5.5 nm. It must be noted that these NWs still resembled those produced by water. By day 3 the resulting methanol products were similar to that seen by ethanol and isopropanol and were highly poly-disperse.

We propose that the difference in polarity of each solvent plays a major role in changing the resulting morphology. It is well known that PVP mainly binds through oxygen of the pyrrolidone ring. Through the use of DFT calculations Al-Saidi *et al.*<sup>28</sup> determined that Van Der Waals forces in particular play an important role in the binding and configuration of this capping agent. Thus the PVP-solvent interaction has a pronounced influence on the binding ability of PVP, with

alcohols favoring hydrophobic interactions as highlight by Kedia *et al.*<sup>29</sup> Furthermore the solvent mediated self-assembly of noble metal nanomaterials is also well documented, with lower polarity solvents favouring aggregation.<sup>30</sup> In our case, ethanol and isopropanol showed a tendency to form nanoparticle aggregates while water and methanol produced NWs of similar morphology.

UV-Vis analysis (Figure 3.13-3.15) further shows a pronounced difference between water and the 3 chosen alcohols. While 2 peaks are noted in the case of water (as detailed earlier), only a single broad peak was observed for all the alcohols. Furthermore a blue shift was noted in all cases as detailed in Table 3.2. The reason for this may be due the formation of thin 1D morphologies and small nanoparticle aggregates.<sup>31,32</sup> This shifting was also most apparent on day 1 perhaps due to an excess of seeds present in solution which undergo aggregation following dilution.

Table 3.2: Change in peak position following dilution with various alcohols

Solvent	Day 1 (nm)	Day 2 (nm)	Day 3 (nm)
Methanol	15	12	8
Ethanol	23	14	5
Isopropanol	21	6	5

### 3.7 Effect of dilution factor on nanowire formation

Another key point of interest was the effect of the dilution factor on the resulting NWs. We performed the dilution step using a smaller dilution factors of 5 and 10 on a solution after 1 day of aging. These were monitored by UV-Vis and the products analysed by TEM (Figure 3.16).

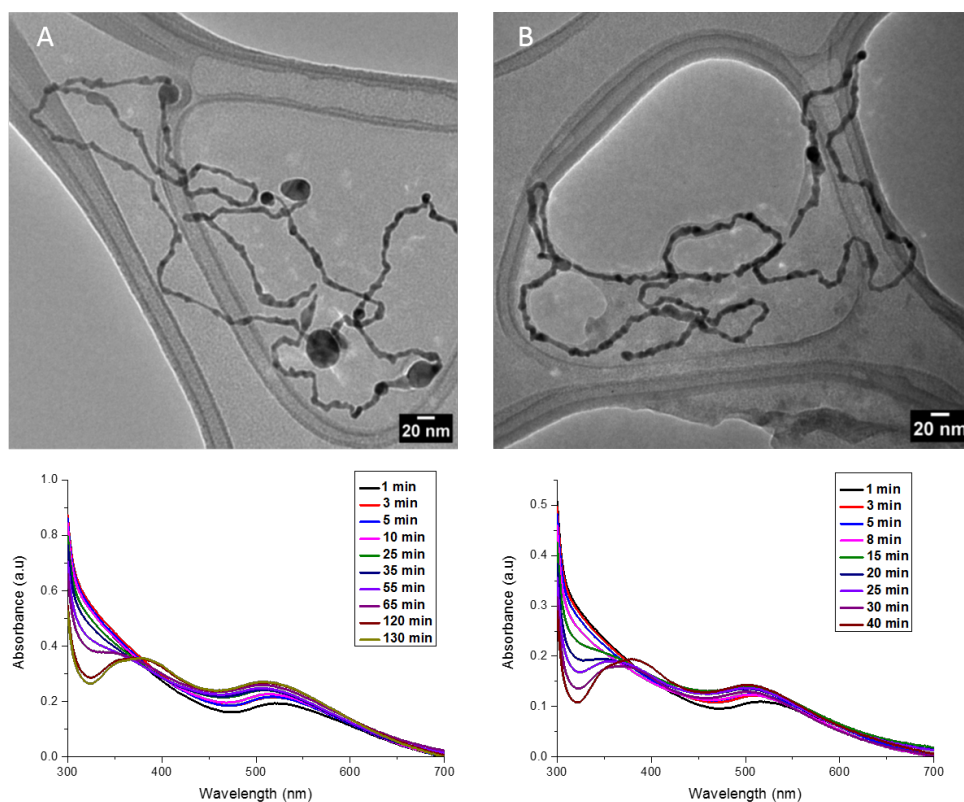


Figure 3.16: TEM images and UV-Vis spectra studying the effect of 5 ml (left) and 10 ml (right) dilution factors on nanowire growth.

As seen in our UV-Vis analysis (Figure 3.16) the dilution factor had a profound effect on the rate of formation of the NWs, with a dilution factor of 5 taking 3.25 times longer to reach completion than a dilution factor of 10. To further understand the kinetics of this process further we done a kinetic curve for the on-set of the second peak at 324 nm (Figure 3.17 ).

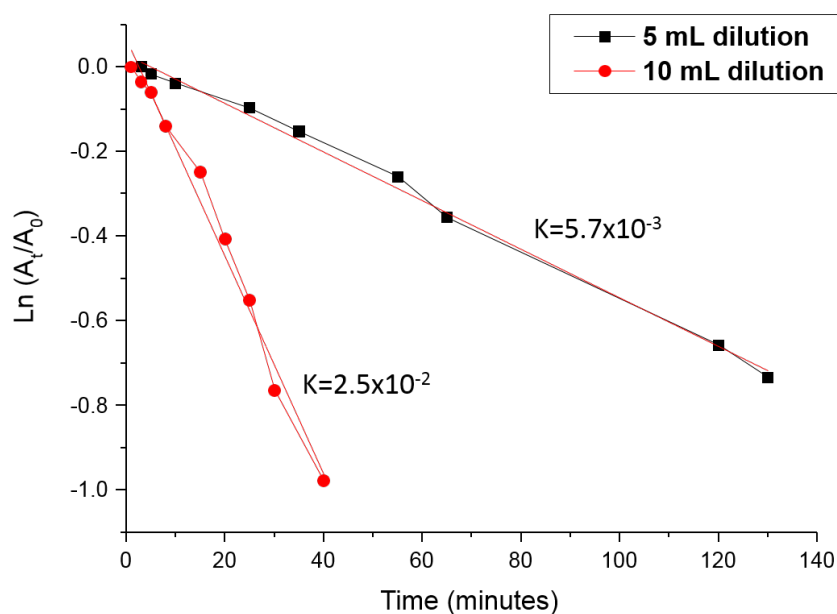


Figure 3.17: Kinetic curves for rate of formation of AuAg nanowires following dilution with 5 and 10 mL at 324 nm.

The kinetic curve shows a linear relationship in both cases with a 5 mL dilution producing a rate constant of  $k=0.0057 \text{ min}^{-1}$  and a 10 mL dilution producing a rate constant of  $k=0.025 \text{ min}^{-1}$ . Thus we propose that a smaller dilution factor does not disperse the PVP in solution as effective as a larger dilution factor. Consequently the seeds

are not as poorly passivated so the growth of the resulting NWs is a more gradual process. Interestingly TEM analysis showed no distinct difference between the NWs produced in either case (refer to Figure A3 and A4 for size distribution analysis). This indicates that wetting of the seeds on the template NWs occurs to the same extent until lowest energy surface is produced.

### **3.8 Influence of different molecular weight PVP on nanowire synthesis**

Our next step was to minimize the polydispersity of our NWs particularly after 3 days of aging. It is well known that the capping agent plays a crucial role in controlling the shape of nanomaterials by preferentially binding onto different facets of nanocrystals. Recently, the molecular weight (MW) of PVP has proved to play important role in defining the quality of NW products.<sup>33-35</sup> While these results were focused predominantly on Ag NWs, we have shown that the Ag component of our alloy has a major influence on the formation of these NWs. Thus we investigated the effect of various PVPs with MWs of 29K, 55K and 360K. These were compared to the 40K PVP typically used for this synthesis. The samples were analysed following dilution after 1 and 3 days of aging. A fixed concentration of 500 mM of PVP

was used in all cases. TEM and UV-Vis analysis of samples produced after 1 day are shown in Figure 3.18.

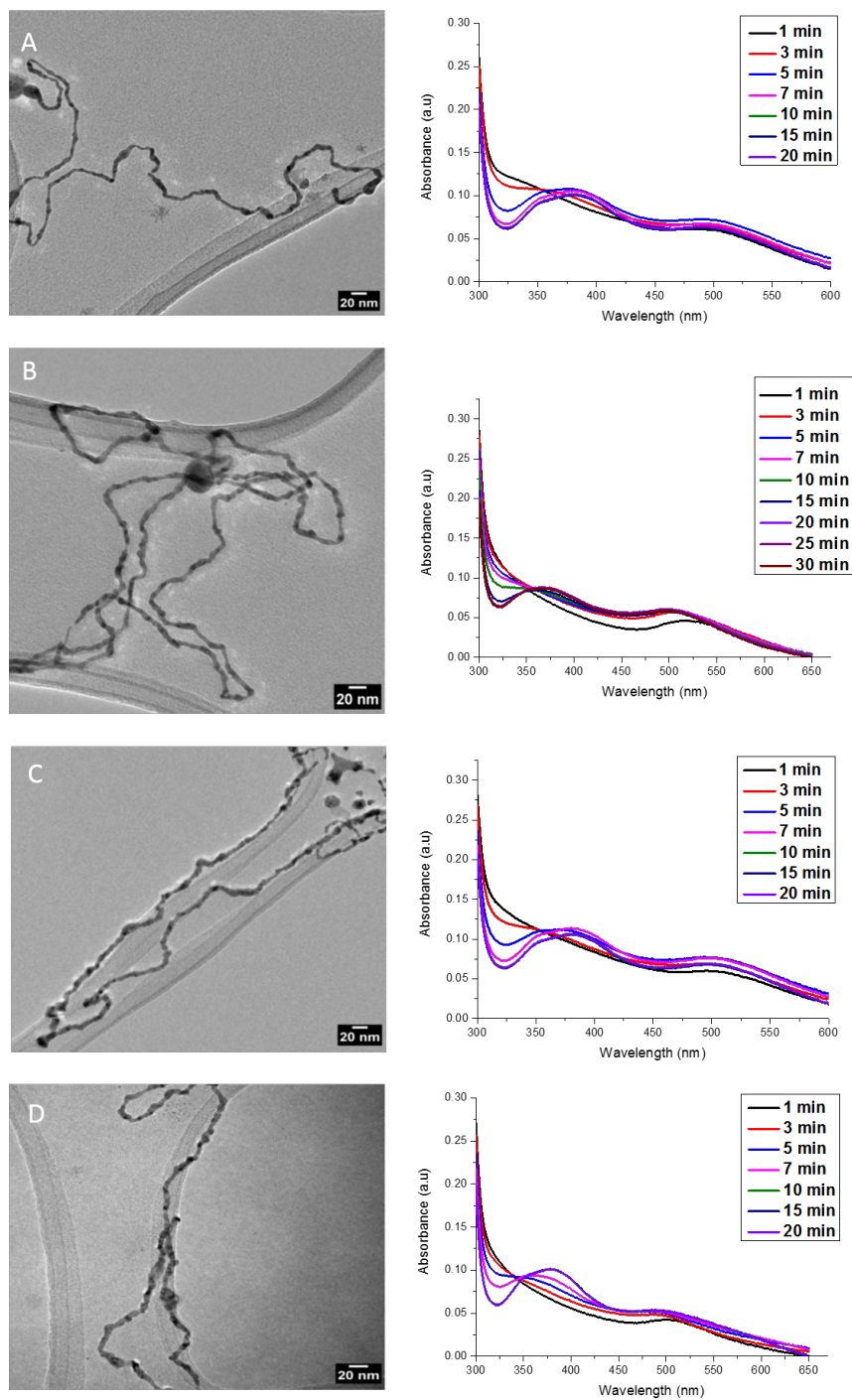


Figure 3.18: TEM (left) and UV-Vis spectra (right) studying the effect of 29K (A), 40K (B), 55K (C) and 360K (D) PVP on nanowire growth following dilution after 1 day of aging.

After 1 day of aging TEM analysis, Figure 3.18 revealed that all of the chosen PVPs did not improve the quality of our products after dilution. Compared to the use of 40K PVP which is typically used for this synthesis, the NWs were more polydisperse. It was noted that the NWs produced using the 29K PVP were on average thinner ranging from 4-6 nm while the products from the 55K and 360K PVP tended to be larger with average diameters 7.5 and 9.2 nm respectively (refer to Figure A5-7 for size distribution analysis). This may be explained by the fact that PVP can also act as a reducing agent due to the presence of its hydroxyl end groups.<sup>36-39</sup> It is generally accepted that shorter MW PVPs are stronger reducing agents. In keeping with our proposed mechanism, the rapid production of seeds by the shorter MW PVP consequently results in some PVP adsorbing to the seeds and loss of its reducing power.<sup>37</sup> In the case of heavier MW PVPs the slower reduction produces a larger number of seeds over the 18 hr aging period.<sup>39,40</sup> Therefore following dilution this results in thicker NWs. UV-Vis of all samples shows a typical absorbance profile for these NWs with a shoulder at 500 nm and broad peak at 370 nm. In addition the dilution process was completed within 30 min in all cases.

Regarding the 3 day aged samples, it can be seen from Figure 3.19 that the products remain polydisperse after dilution. UV-Vis analysis of these samples also reflects the polydispersity noted in the TEM



analysis with the presence of broad absorption profiles with 360K PVP capped sample in particular showing 2 pronounced peaks at 500 and 380 nm.

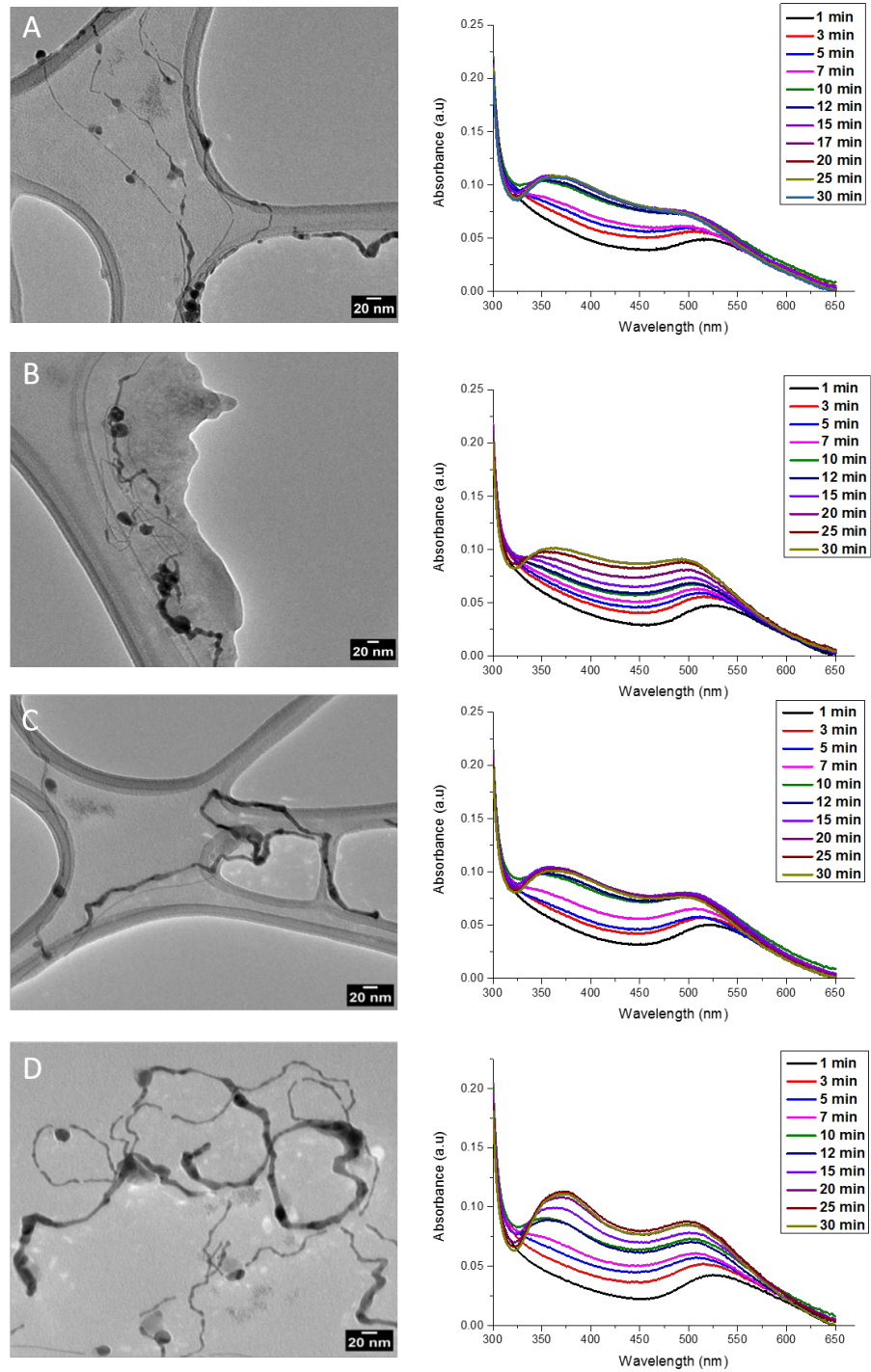


Figure 3.19: TEM images (left) and UV-Vis spectra (right) studying the effect of 29K (A), 40K (B), 55K (C) and 360K (D) PVP on nanowire growth following dilution after 3 days of aging.

While the PVPs in this study did not improve our protocol they did however highlight the impact of the MW. Thus the use of heavier or lighter PVPs may potentially be employed to further tune this synthesis by producing larger or smaller diameter NWs respectively.

### **3.9 Effect of temperature on nanowire synthesis**

In an attempt to improve on our protocol we focused further on trying to minimize the polydispersity of our products and aimed for shorter reaction times. We found that the biggest disadvantage to aging the reaction mixture at room temperature over 4 days was the variation in temperature from day to day and between day and night. To solve this issue we performed a temperature controlled study by aging the reaction mixture at 20, 25, 30, 35 and 40 °C for 18 hrs. In addition to studying the synthesis with AuAg we also looked at the effect on using only Au or Ag for the synthesis as a control. The solutions were then diluted by a factor of 20 with water and the products were analysed by TEM (Figure 3.20)

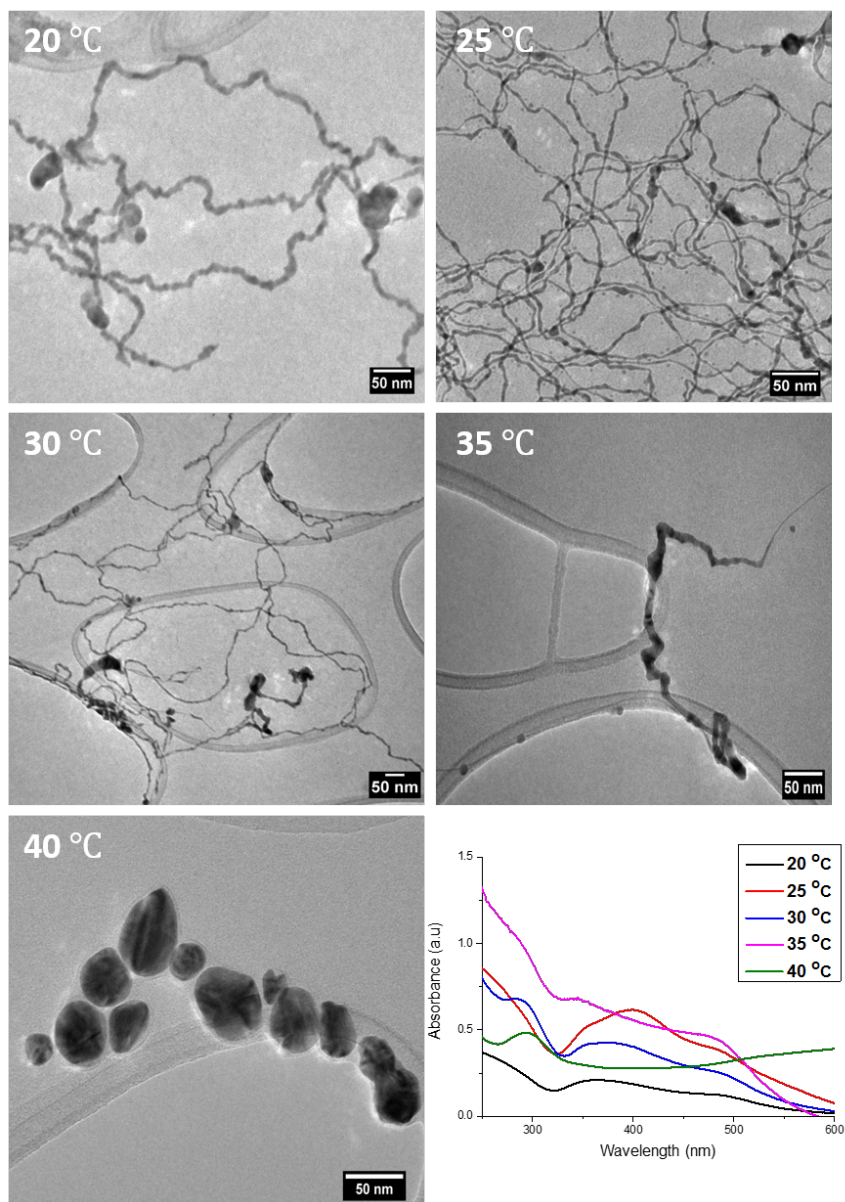


Figure 3.20: TEM and UV-Vis analysis of products following dilution after aging at various temperatures for 18 hrs.

Our TEM analysis shows a significant difference in the resulting nanostructures size and morphology between each temperature. At 20 °C the resulting non-uniform NWs following dilution were on average 9.2 nm in diameter and were monodisperse. Interestingly after aging at

25 °C the average diameter of the post dilution NWs was 3.6 nm and they were also highly monodisperse. This is a striking improvement on our protocol as the not only was the product quality enhanced we also achieved NWs typically seen after 3-4 days after only 18 hrs of aging. This difference in results after a small temperature change of 5°C further highlights how sensitive this synthesis is to temperature. Regarding the sample aged at 30 °C, it was noted that the products became polydisperse. We observed that 2 types of NWs emerged; one which was similar in size and morphology to the 25 °C aged sample while the other type appeared more necklace like containing bead like shapes along the length of the NW. In the case of the 35 °C aged sample a complete morphology change had occurred with the presence of only ultrathin nano-necklace structures. A detailed characterisation of this structures is discussed in section 3.11. Thus aging at 30 °C marked a transition point in the morphology of the resulting NWs. Finally, aging at 40 °C proved to be detrimental as only anisotropic nanoparticles of various shapes and sizes were formed. UV-Vis analysis (Figure 3.20) of all the products from this study shows peaks at 500 and 370 nm in all cases except for the 40°C aged sample which shows a peak a broad absorption band with an on-set at 600 nm. The results of this study are schematically presented in Figure 3.21. The reproducibility of the 20, 25 and 35°C synthesis is shown in Figure A8.

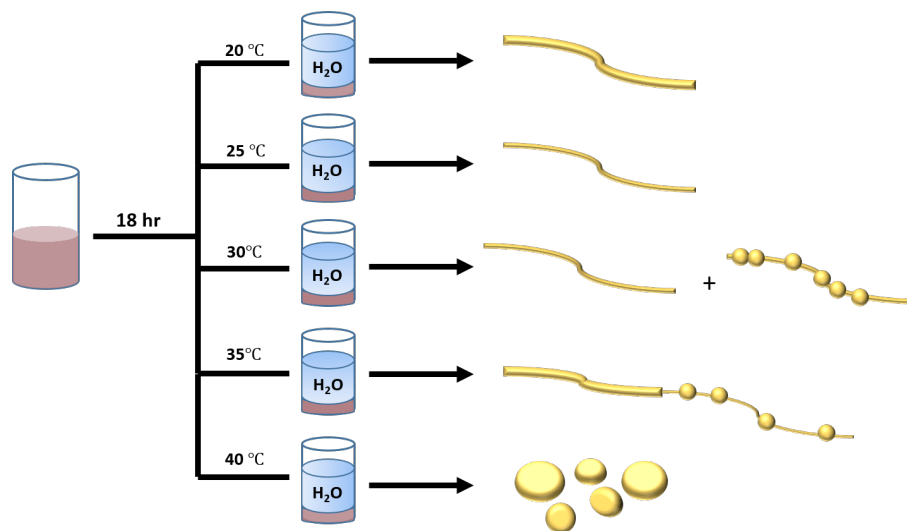


Figure 3.21: Reaction presentation summarizing the products produced following dilution after aging at various temperatures for 18 hrs.

Regarding the Au and Ag control, the samples were aged at only 20 and 25 °C as TEM analysis (Figure 3.22) revealed no improvement or change in behaviour compared to our earlier control study (section 3.5) at these temperatures.

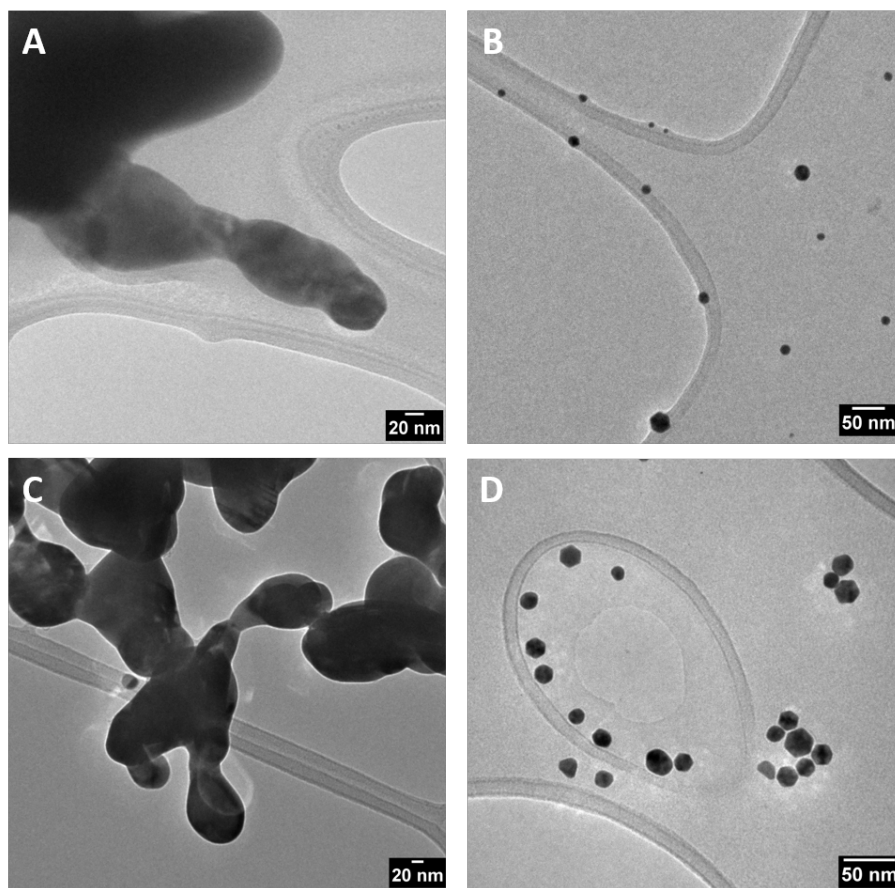


Figure 3.22: TEM images of Ag and Au control produced following dilution after aging at 20°C (A and B) and 25°C (C and D).

Thus keeping the reaction mixture at a fixed temperature served to accelerate the nucleation and growth processes. In addition the polydispersity of the products was notably reduced as the growth kinetics were not altered due to temperature fluctuations during the aging period.

### 3.10 Characterisation of AuAg nanowires synthesised by aging at 25°C

Following the temperature controlled study we conducted a detailed characterisation of the AuAg NWs produced following dilution after aging at 25°C. HR-TEM analysis (Figure 3.23) as expected are polycrystalline, similar to the larger NWs produced after 1 day of aging. In addition these NW were on average 3.6 nm in diameter (refer to Figure A9 for size distribution analysis). These NWs exhibit multiple lattice fringes with  $d$  values of  $0.216 \pm 0.014$  nm and  $0.246 \pm 0.025$  nm corresponding to the (111) and (200) of FCC Au and Ag.

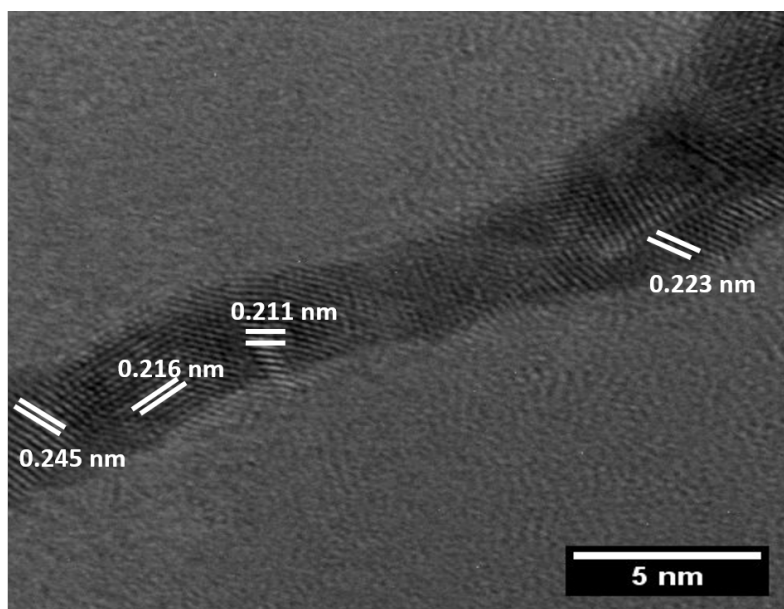


Figure 3.23: HR-TEM image of AuAg NWs produced following dilution after aging at 25°C for 18 hrs.

EDX line map analysis further confirms that the NWs are an alloy of



Au and Ag. The EDX spectrum shows the characteristic L and M peaks of Au at 9.7 and 2.1 KeV respectively and the L peak of Ag at 3.1 KeV respectively. The additional peaks present are due to the Cu from the TEM grids used for this analysis. Comparison of the L line produced from each metal indicates that the NWs are predominantly made of Au as similarly seen for our previous AuAg NWs (section 3.24).

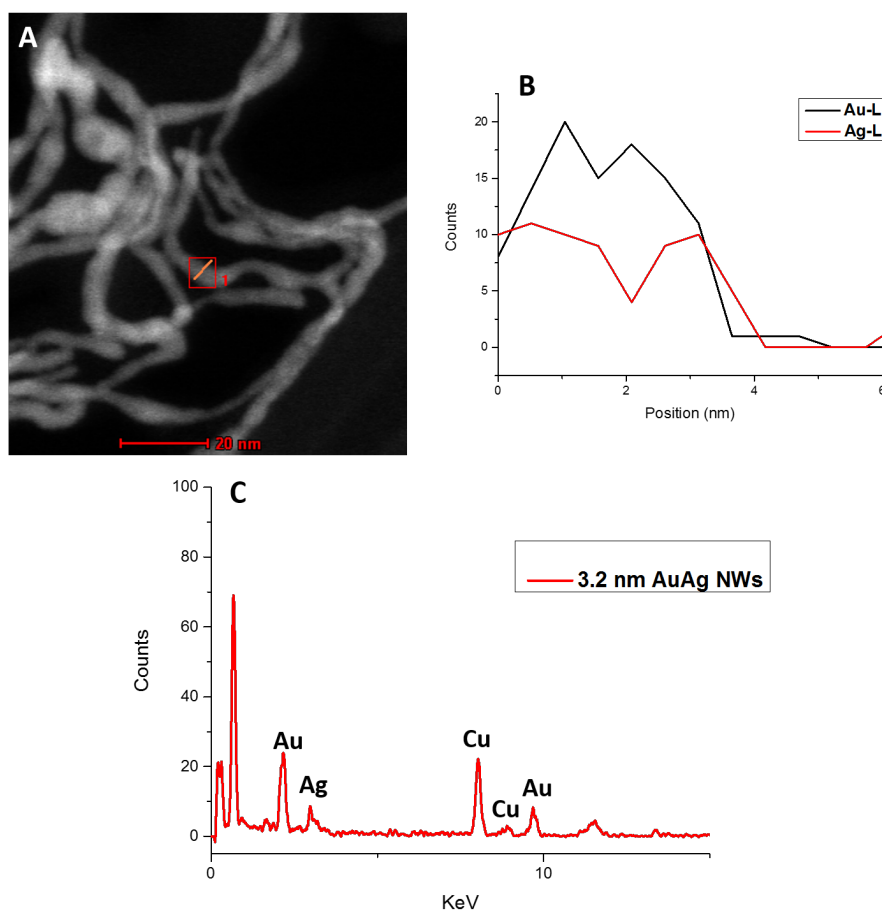


Figure 3.24: HAADF STEM image (A), EDX line profile (B) and EDX spectrum (C) of AuAg NWs produced following dilution after aging at 25 °C .

XRD analysis was used to assess the crystal structure of these NWs (Figure 3.25)

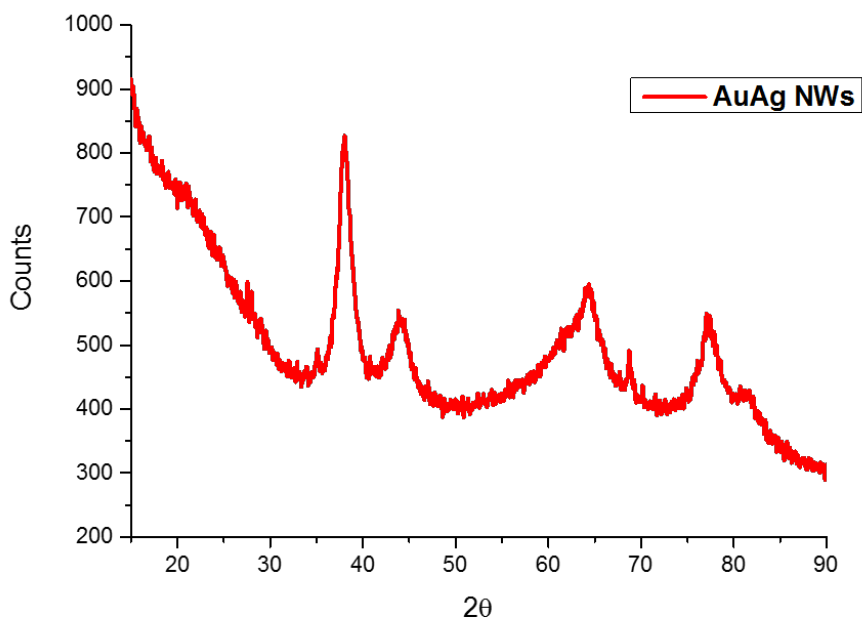


Figure 3.25: XRD pattern of AuAg NWs produced following dilution after aging at 25 °C .

The XRD analysis shows the expected pattern with diffraction peaks at  $2\theta$  values of 38.2 , 43.9, 64.37, 77.3 and 81.5 ° corresponding to the (111), (200), (220), (311) and (222) planes, respectively, for both FCC Au (JCPDS-01-117) and Ag (JCPDS-01-1164). Furthermore from our texture coefficient analysis the (111) plane was found to be to be the most dominant (refer to table 3.3). This analysis indicates that the NWs preferentially grow along the (111) plane as seen

with our previous NWs (section 3.2).

Table 3.3: Texture coefficient analysis of AuAg ultrathin NWs produced after 25°C

Facet	$I_0$ (counts)	I (counts)	TC* of sample
111	609	555.6	1.15
200	508.4	423.6	0.91
220	510.1	456.7	0.98
311	480	520.5	1.05
222	371.3	406	0.977

\* refer to appendix for TC equation. Reference 05-8482 was used for this analysis.

### 3.11 AuAg nano-necklaces

In light of the temperature study, we produced a novel AuAg nano-necklace (NNL) structure. NNLs represent an interesting class of hybrid material combining the advantages of 1D and 0D nanomaterials. This makes them promising candidates for potential catalytic, sensing and electronics applications. Current methods to producing such materials however are synthetically challenging requiring the use of intensive techniques such as chemical vapour deposition<sup>41</sup> (CVD) and

laser aberration<sup>42</sup>, while more wet-chemical approaches rely heavily on templates.<sup>43,44</sup> Nevertheless recent work by Huang *et al.*<sup>45</sup> in particular, has demonstrated the use of Te NWs as effective templates in the synthesis of Pd-Au NNLs. Further to this Huang and co-workers outline how the Au bead-to-bead distances and bead size can be tuned by varying the amount reducing agent and Au precursor respectively. In addition Jia *et al.*<sup>46</sup> also showed that Ag/AgCl NNLs can be achieved through an interesting oxidation method. By employing poly-crystalline Ag NWs as a template Jia details how FeCl<sub>3</sub> (the oxidant) can promote the growth of AgCl beads at grain boundaries in the template. While interesting methods are emerging, the field is still at an early stage. In this section we present a detailed characterisation of AuAg NNLs produced via a low temperature, template-free synthesis.

TEM analysis of our NNLs is detailed in Figure 3.26 below.

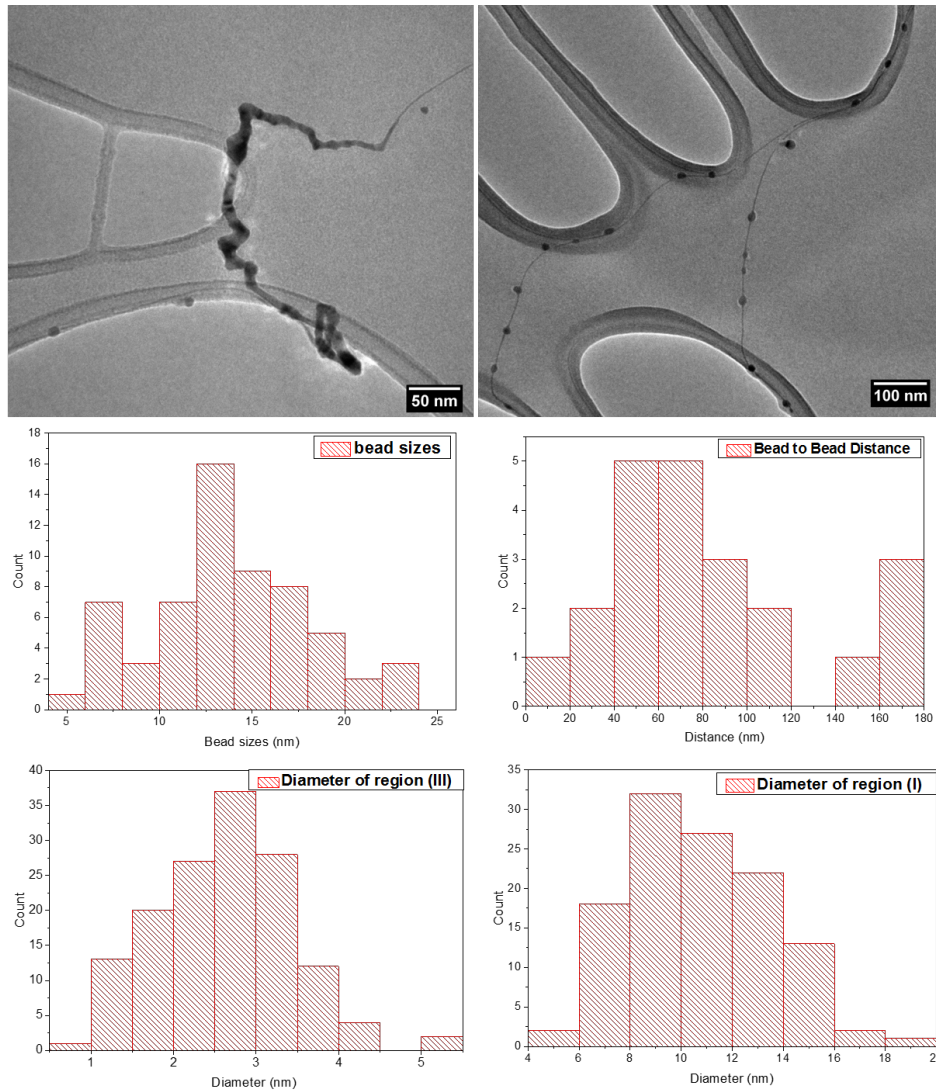


Figure 3.26: TEM images and size distributions of the various regions of the AuAg NNLs.

As can be seen in Figure 3.26 the NNLs present a complex morphology with 4 distinct regions: a thick NW region (I) which goes into a tapered region (II), ultimately forming a thinner NW region (III) with beads (IV) along its the length. The complexity of this structure is not common in NL structures and is most likely a result of ther-

mal atomic diffusion during the synthesis. Size distribution analysis (Figure 3.26) further shows that region (I) is on average 10 nm and can be up to microns in length. The thinnest part of this structure, region (III) is on average 2.5 nm in diameter with a very narrow size distribution. Interestingly the beads (region IV) have a varied bead-to-bead distance ranging from 14.4 nm to 175 nm. In addition the bead sizes also vary, but are on average 13 nm. Regarding the tapered region (II), this marks the transition point between (I) and (III) and its length tended to differ between NNLs.

UV-Vis analysis (Figure 3.27) of our NNLs shows a peak at 370 nm and a shoulder at 490 nm. This absorption profile is commonly observed for our AuAg 1D structures as highlighted earlier. Further extension of the UV-Vis into the near-IR (1000 nm) also shows no additional peaks associated with the longitudinal mode due to the large aspect ratio of these structures.

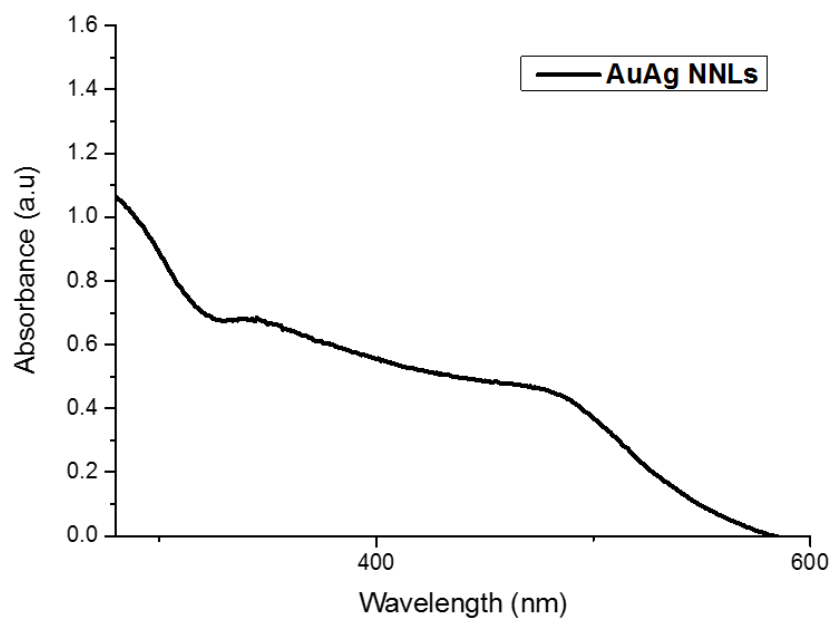


Figure 3.27: UV-Vis spectrum of AuAg NNLs

HR-TEM was used to further study the components of this structure in more detail (Figure 3.28).

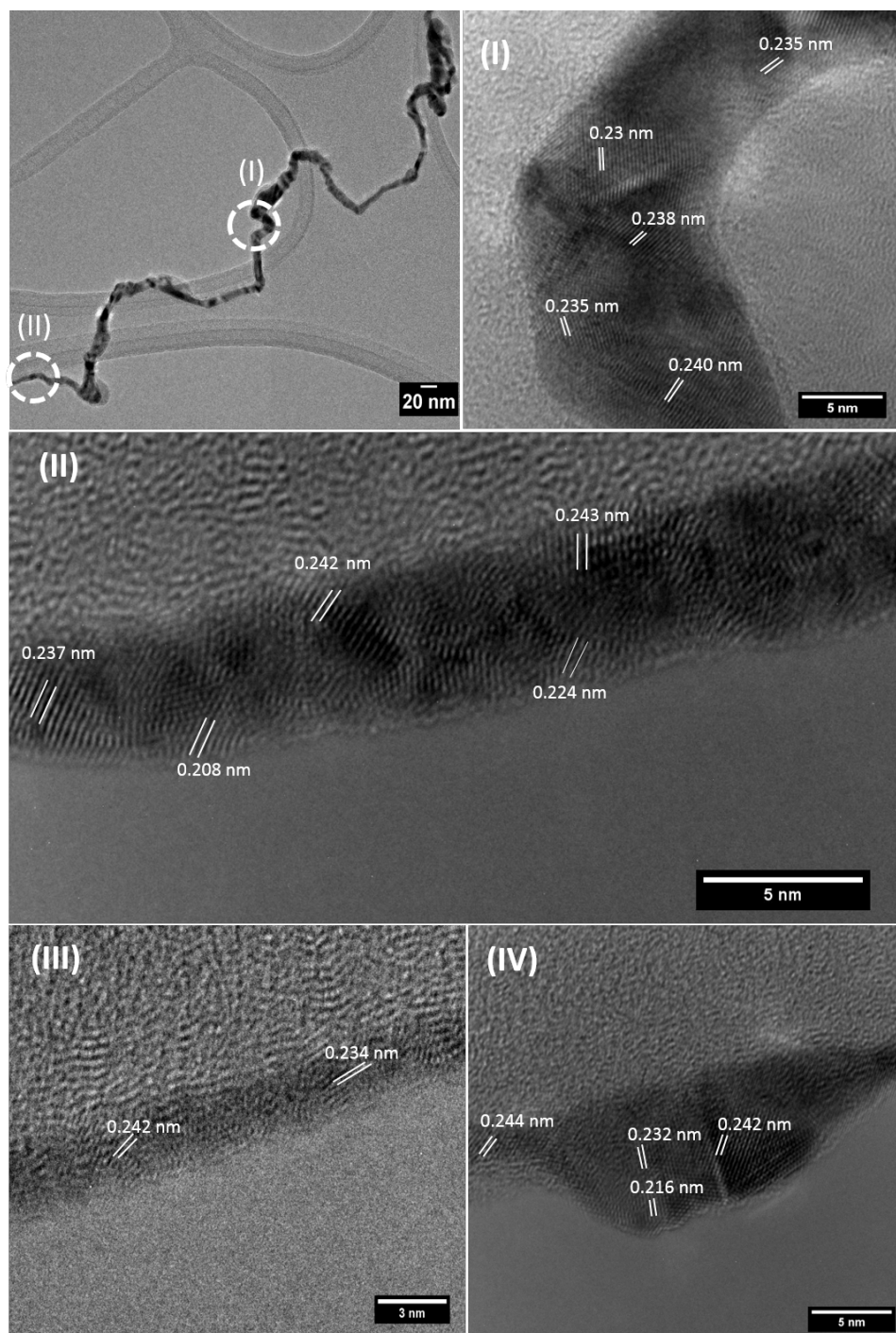


Figure 3.28: HR-TEM analysis of the various regions of the AuAg NNs

Our HR-TEM analysis shows that these NNs are polycrystalline pre-



senting multiple different lattice spacings. The  $d$  values observed for each region are detailed in table 3.4.

Table 3.4:  $d$  spacing values in each region of the AuAg NNLs

<b>Region on NNL</b>	<b><math>d</math> values (nm)</b>
I	$0.237 \pm 0.017$ , $0.241 \pm 0.010$
II	$0.208 \pm 0.007$ , $0.224 \pm 0.029$ , $0.243 \pm 0.013$
III	$0.234 \pm 0.037$ , $0.242 \pm 0.023$
IV	$0.216 \pm 0.013$ , $0.232 \pm 0.009$ , $0.242 \pm 0.011$

The  $d$  values are typical of the FCC materials with values of 0.20 and 0.23 nm corresponding to the 111 and 200 planes of FCC Au and Ag.

STEM analysis (Figure 3.29) further revealed that the NNLs have a smooth surface topology. In addition there is a Z-contrast between the beads and the adjoining NW. This is to be expected given the difference in thickness between both these 2 regions.

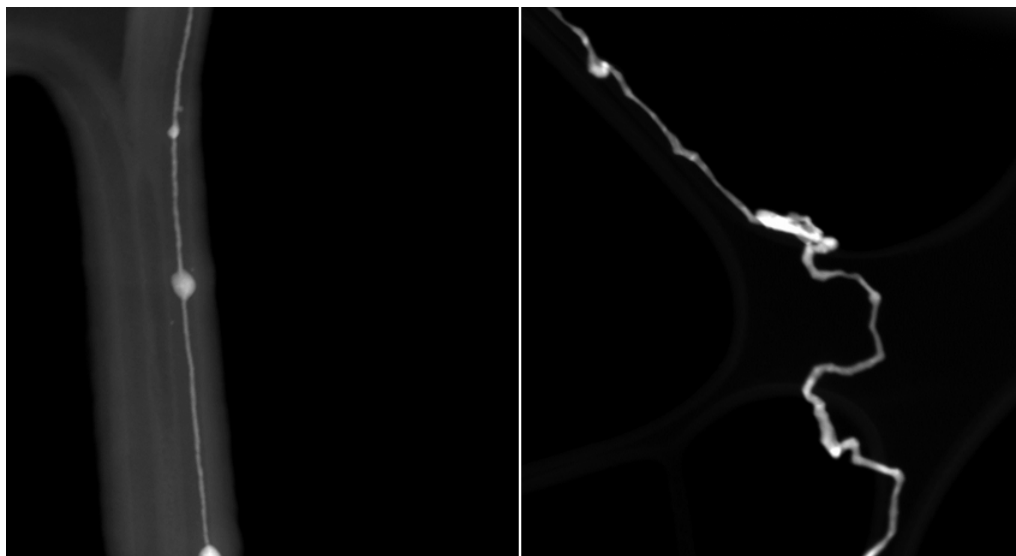


Figure 3.29: STEM analysis of AuAg NNs.

XRD analysis was used to investigate the crystal structure of the NNs (Figure 3.30 ).

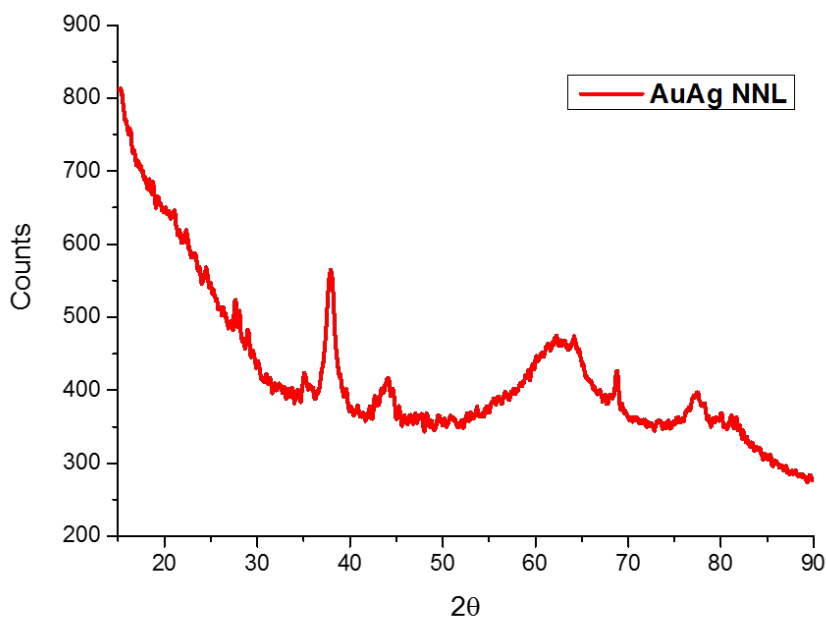


Figure 3.30: XRD pattern of ultrathin AuAg NNLs.

The XRD analysis shows that the NNLs have diffraction peaks at  $2\theta$  values of 37.9, 44.1, 62.6, 77.4 and 81.5 ° corresponding to the (111), (200), (220), (311) planes respectively for both FCC Au ( JCPDS-01-117 ) and Ag (JCPDS-01-1164). In addition TC analysis shows that the (111) has the highest coefficient value (refer to table 3.5). This analysis further indicates that the NWs preferentially grow along the (111) plane.

Table 3.5: Texture coefficient analysis of AuAg NNL

<b>Facet</b>	<b>I<sub>0</sub> (counts)</b>	<b>I (counts)</b>	<b>TC* of sample</b>
111	511.8	554.9	1.07
200	417	423.6	0.99
220	430.2	456.7	1.04
311	372.8	328.9	0.87

\* refer to appendix for TC equation. Reference 05-8482 was used for this analysis.

In order to understand the elemental composition and distribution of the NNLs HAADF-STEM EDX line mapping studies (Figure 3.31) were performed.

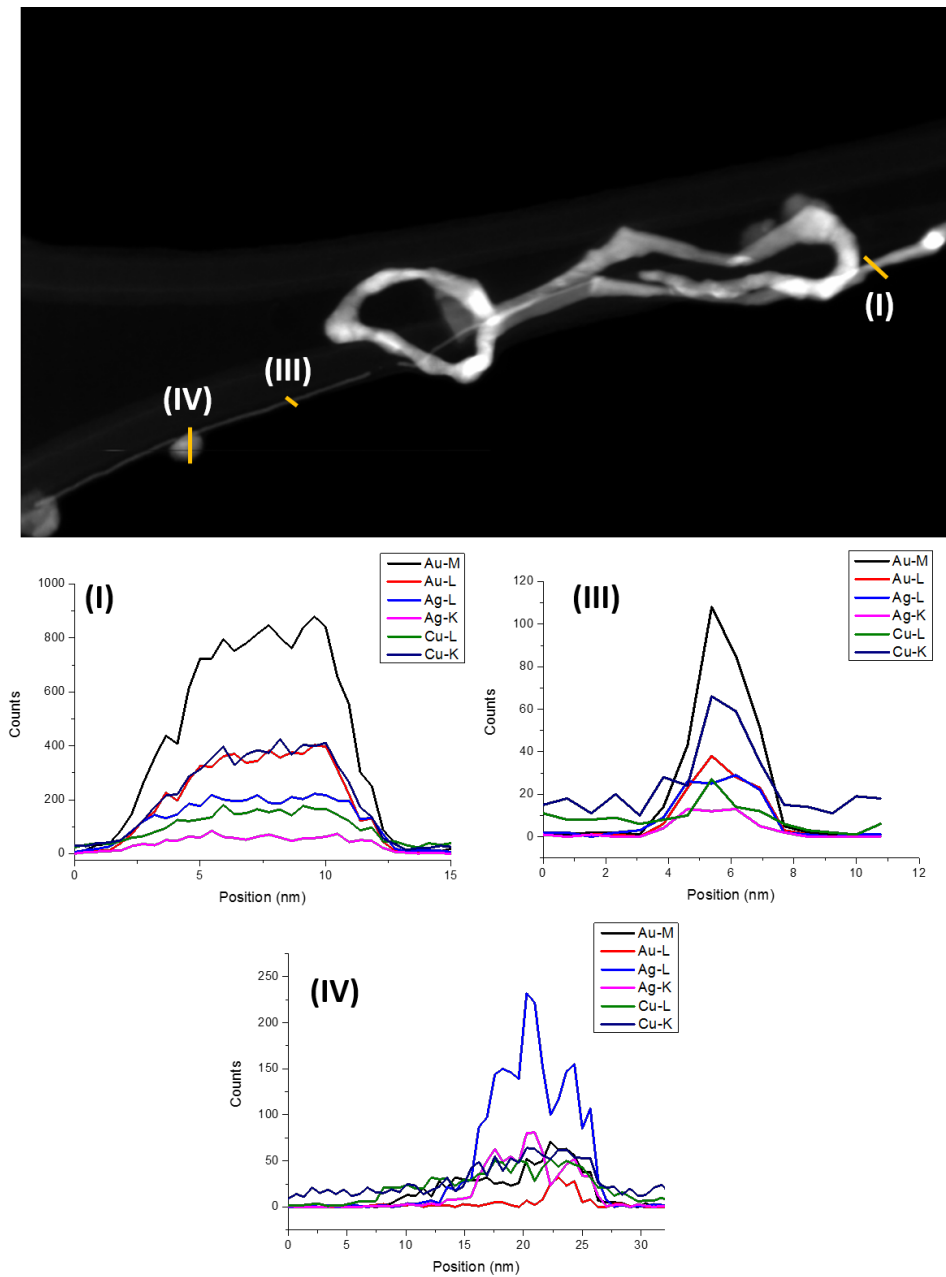


Figure 3.31: EDX line map analysis of AuAg NNLS.

The elemental analysis shows that in regions (I) and (III) there is a higher Au composition compared to Ag as indicated by the greater

intensity from the Au L-line in both cases. Interestingly the beads (region IV) are more richer in Ag than Au. This variation in the metal composition in the different regions of the NNL may be due to the difference in atomic diffusion between Au and Ag,<sup>47,48</sup> however a detailed study of the formation of these NNL is needed to fully understand this composition variation.

The sample aged at 35°C was also assessed by TEM prior to the dilution step. Interestingly TEM analysis (Figure 3.32) shows the presence of NNL. This strongly indicates that the NNL structures are formed during the aging process rather than from the dilution step.

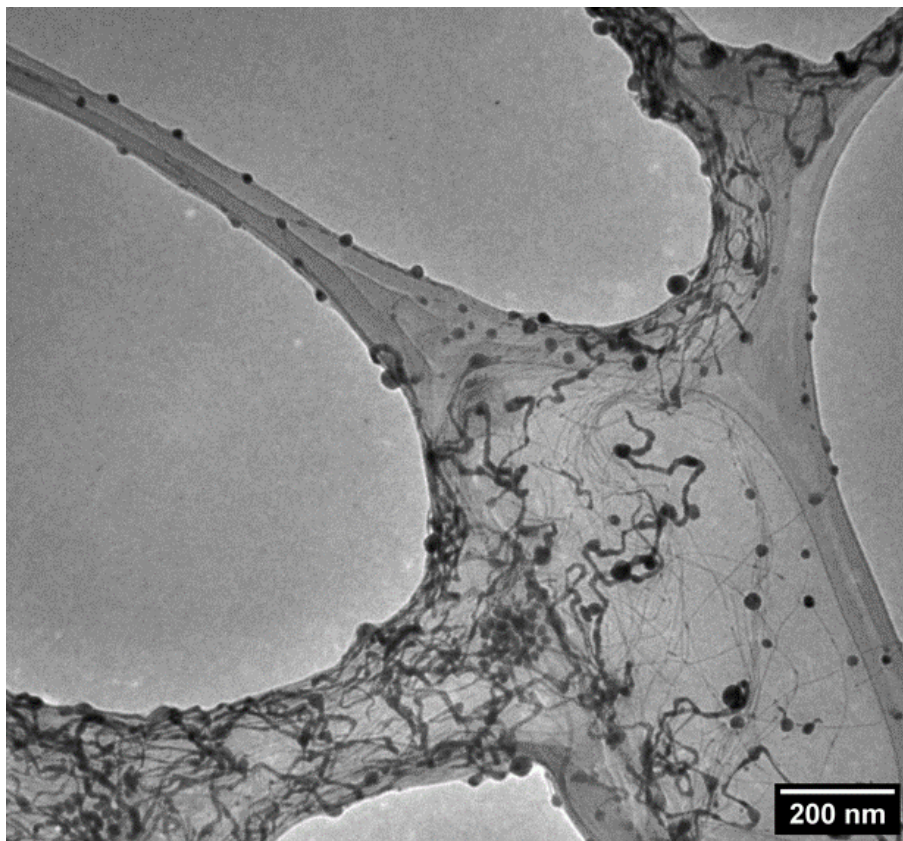


Figure 3.32: TEM image of 35°C aged solution prior to dilution.

### 3.12 Ultrathin AuAg nanowires for the catalytic reduction of 4-Nitro-phenol

4-Nitrophenol is an organic pollutant produced by industrial and agricultural activities. It is highly hazardous to the environment and toxic, with exposure causing serious damage to the liver and central nervous system. However the conversion of 4-nitrophenol to its amino

acid, 4-aminophenol by hydrogenation has been realised as a solution to this issue. The production of an aminophenol is not only a remedy for this pollutant but can also be employed for a range of applications such as in corrosion inhibitors,<sup>49</sup> production of anti-pyretic drugs<sup>50</sup> and in photograph developers. As originally demonstrated by Pal *et al.*,<sup>51</sup> sodium borohydride when used with a nanomaterial catalyst can serve as effective hydrogen source for this conversion process. This method has since been established as a model reaction for testing the catalytic behaviour of nanomaterials.

The performance of nanomaterials, particularly those containing Au and Ag shows a strong size and morphology dependence, with larger surface area materials offering potentially greater activity.<sup>52-54</sup> This field has notably been dominated by the use of nanoparticle catalysts on various supports such as on metal oxides<sup>55,56</sup>, ionic<sup>57,58</sup> and organic<sup>59-61</sup> polymers. While supports can enhance the performance of these catalyst, their use however involves additional steps in the material preparation. Thus the use of ultrathin 1D materials would undoubtedly remove the need for supports as they inherently offer large surface areas and they do not tend to aggregate. In this section we detail the catalytic results of our ultrathin NWs produced following dilution after 1 and 3 days of aging. UV-Vis analysis as shown in Figure 3.33 was used to monitor this catalytic reduction process.



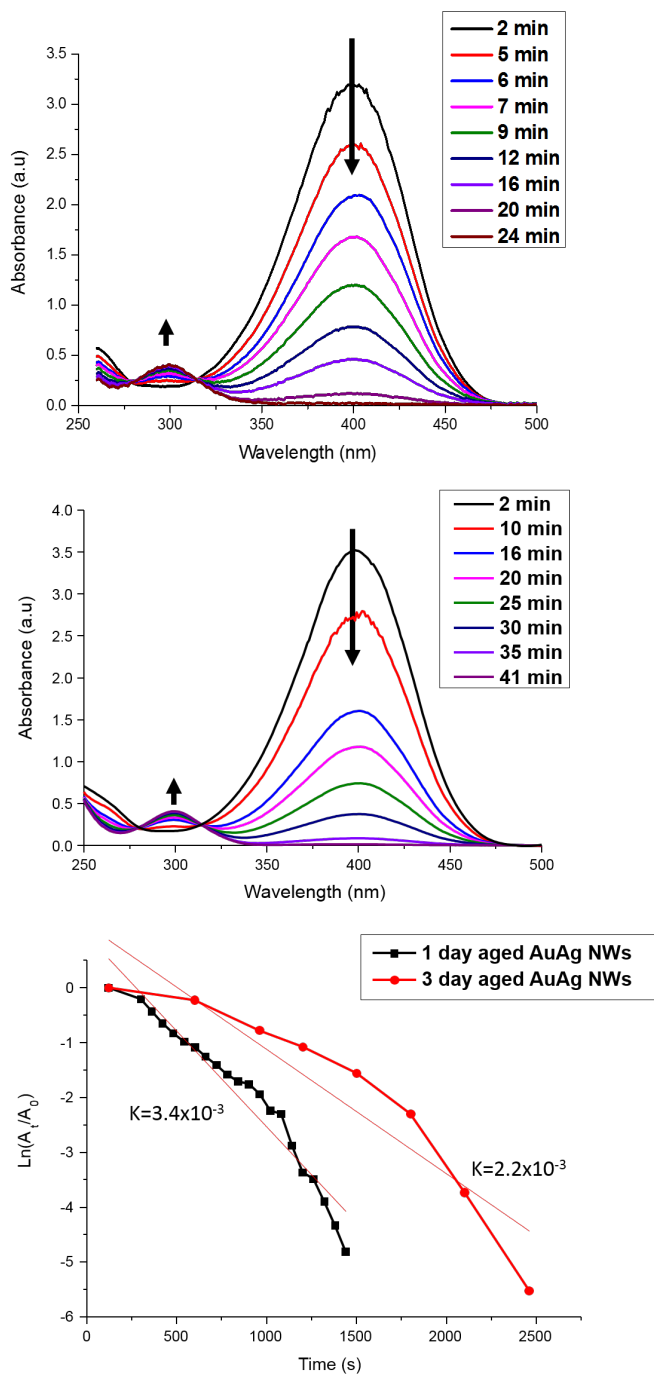


Figure 3.33: UV-Vis analysis monitoring the catalytic reduction of 4-nitrophenol using ultrathin AuAg nanowires produced after 1 day( top) and 3 days (middle) and kinetic curves for the rate of reduction (bottom) at 400 nm

UV-Vis analysis shows the characteristic decrease of the 4-nitrophenolate peak at 400 nm and the increase of the product peak at 300 nm. Interestingly the larger NWs (produced after day 1) exhibited a greater catalytic activity, completing the reaction within 24 mins compared to the thinner NWs which took 41 mins. Applying the typical pseudo first order kinetics for this reaction a plot of  $\ln (A_t/A_0)$  (where  $A_t$  is the absorbance at a given time and  $A_0$  is initial absorbance) with respect to time further shows that day 1 aged NWs have a rate constant of  $k= 3.4 \times 10^{-3} \text{ s}^{-1}$  and the day 3 aged NWs have a rate constant of  $k= 2.2 \times 10^{-3} \text{ s}^{-1}$ . While the thinner, larger surface area NWs (day 3) were expected to perform better, their under-performance may be due to degradation during the reaction, as these NWs are significantly fragile.<sup>62,63</sup> Also, it must be noted that we were unable to recover the nanowires used in both cases after the reaction. It is commonly accepted that the catalytic reduction of 4-nitrophenol occurs via the Langmuir-Hinshelwood (LH) mechanism<sup>58,64</sup> (i.e. adsorption of both reactants onto the surface of the catalyst, then reaction on the surface followed by desorption of the products). Thus, in order to rationalize these results further we propose that in the initial adsorption steps of the reactants, the thinnest regions of the smaller non-uniform NWs are susceptible to dissociation following to the removal of PVP by hydride stripping.<sup>65</sup> Another main contributor to the lower rate constant for the thinner NWs is most likely due to the inhibition of active

catalytic sites.<sup>66,67</sup> In addition it has been shown that as metallic nanomaterials become thinner they behave less like metals.<sup>68,69</sup> This would significantly affect, not only the affinity of the product and reactants with the catalyst surface,<sup>70,71</sup> but also the electron transfer process, which is critical for the reduction step in this reaction to occur.<sup>72-74</sup> Furthermore it is well documented that larger diameter NWs exhibit greater charge transport properties compared to their smaller diameter counterparts.<sup>3,75,76</sup> 60 The plot for this reaction for the thinner NWs shows a deviation from linearity ( $R^2 = 0.85$ ) and thus may not be strictly following LH behaviour. Nevertheless, comparison of our NWs with other ultrathin and noble metal nanomaterials (Table 3.6) shows that the NWs produced after day 1 provide good catalytic activity with rate constants comparable to that of notable Pt containing catalysts and can also significantly out-perform both supported and unsupported nanoparticle catalysts.

Table 3.6: Catalytic reduction of 4-Nitrophenol by various noble metal nanomaterials

Catalyst	rate constant ( $10^{-3} \text{ s}^{-1}$ )	Catalyst loading
Ag NW @ Au np <sup>77</sup>	1.4	0.5 mg mL <sup>-1</sup>
Au NWs (2 nm) on alumina beads <sup>78</sup>	8.8	2.28 $\mu\text{g}$
Pt <sub>93</sub> Bi <sub>7</sub> NW <sup>79</sup> (4.1 nm)	0.46	15 $\mu\text{g}$
Pt <sub>92</sub> Bi <sub>8</sub> NWs <sup>79</sup> (4.7 nm)	2.3	15 $\mu\text{g}$
Pt <sub>55</sub> Pd <sub>38</sub> Bi <sub>7</sub> NWs <sup>79</sup> (4.4 nm)	4.3	15 $\mu\text{g}$
Pt <sub>92</sub> Bi <sub>8</sub> NWs <sup>79</sup> (4.7 nm)	2.3	15 $\mu\text{g}$
Ag NWs <sup>77</sup> (30 nm)	0.47	0.45 mg
Au NP@ Tween 80 (14 nm) <sup>80</sup>	1.5	1 mmol L <sup>-1</sup>
Ag NP@ SiO <sub>2</sub> nanorattles <sup>81</sup>	3.3	4 mg
AuAg NWs (8 nm) (This work)	3.4	0.45 mg mL <sup>-1</sup>
AuAg NWs (3 nm) (This work)	2.2	0.45 mg mL <sup>-1</sup>

### 3.13 Electro-oxidation of ethylene glycol using Ultrathin AuAg nanowires as anodic catalysts

In the face of the energy crisis the need and demand for alternative fuel

sources has become ever more important. Over the last few decades the use of alcohols such as methanol and ethanol have been extensively studied in poly-electrolyte fuel cells.<sup>82-84</sup> While these alcohols provide good energy densities they have significant disadvantages; methanol has a low boiling point and is toxic while ethanol which is produced from biomass requires a vast amount of land and infrastructure. In addition both these fuels have a high tendency to cross over the poly-electrolyte membrane and poison the cathode thus hampering the performance of these fuel cells.<sup>85,86</sup> In more recent years researchers have moved towards the use of ethylene glycol (EG) as a fuel.<sup>87,88</sup> EG offers higher energy density and due to its size is less likely to cause crossover poisoning. More importantly EG is already produced on a large scale from the car industry thus the potential infrastructure is already present.

While Pt and Pd based nanomaterials have commonly been used as catalysts there is a major effort to move to more cost efficient materials. Au based nanomaterials in particular have emerged as effective catalyst for the EG oxidation reaction (EGOR).<sup>89,90</sup> Work by Li and co workers<sup>91</sup> demonstrated that Au nanostars suffer little poisoning and can produce a current density of 26 mA mg<sup>-1</sup>. In addition to morphology effects, Au and Ag are plasmonic. This makes them potentially multi-functional materials as highlighted by Xu *et al.*,<sup>92</sup> with

white light irradiation of AuAg nanobowls amplifying their performance for EGOR. Furthermore the use of 1D Pt and Pd materials alloyed or decorated with Au have shown significant catalytic activity owing to synergistic effects and large surface areas.<sup>93-96</sup> In this section we present for the first time the use of AuAg ultrathin NWs as anodic catalyst for the electro-oxidation of EG.

The electro-catalytic activities of 9.2 and 3.6 nm diameter NWs produced from our temperature controlled study following aging at 20 and 25 °C respectively, were assessed by cyclic voltammetry (CV) in a 1 M KOH solution containing 0.5 M EG (Figure 3.34).

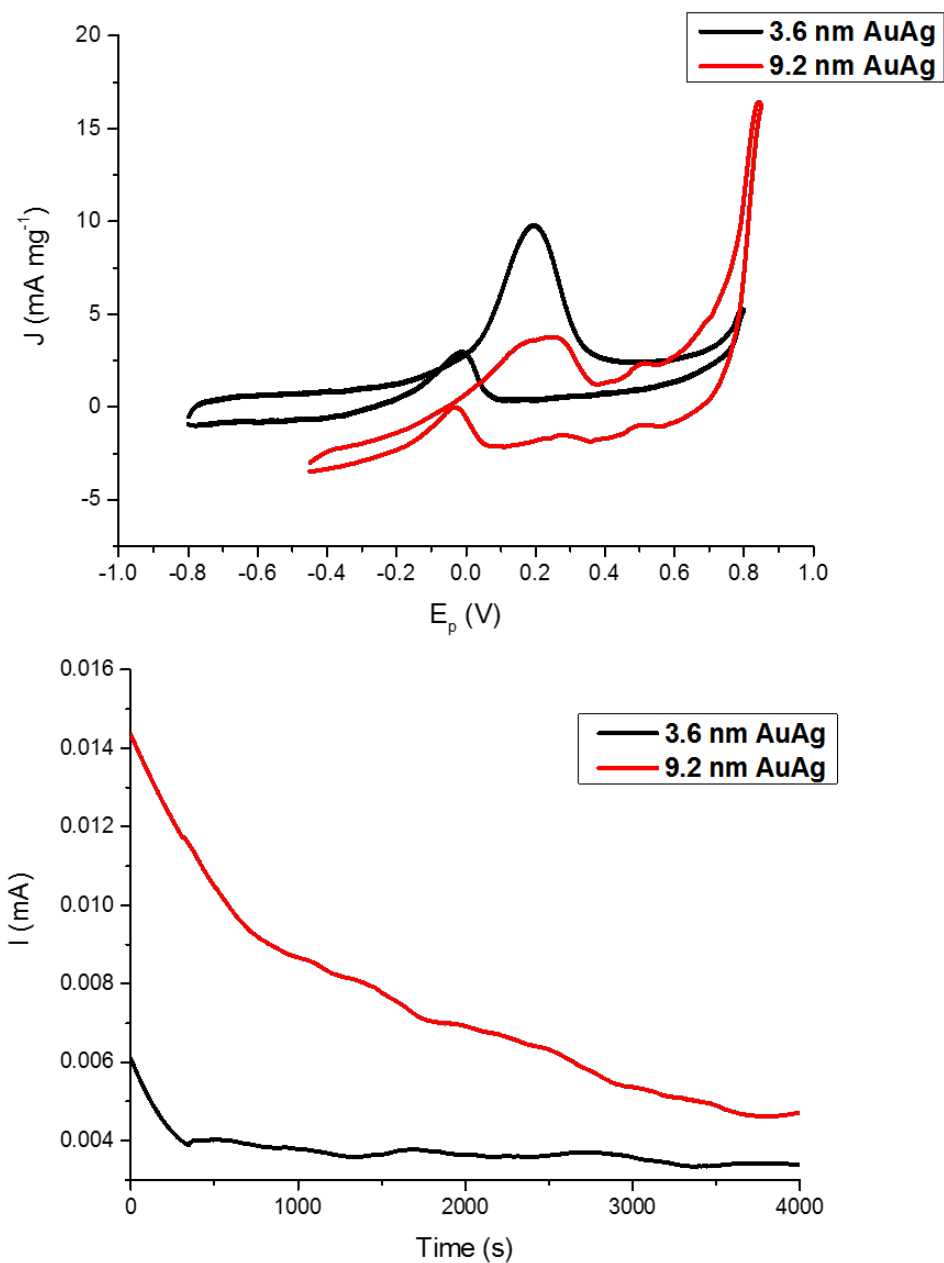


Figure 3.34: CV curves (top) at  $50 \text{ mV s}^{-1}$  and  $i$ - $t$  curves over 4000 s at 0.2 V (bottom) for 3.6 and 9.2 nm AuAg NWs versus saturated Calomel electrode in a 1 M KOH solution containing 0.5 M EG.

As shown in Figure 3.34 the 3.6 nm NWs produce a larger current density ( $9.6 \text{ mA mg}^{-1}$ ) compared to that of the thicker NWs ( $4.1 \text{ mA mg}^{-1}$ ). Furthermore the peak potential of these thinner NWs was slightly more negative (0.193 V) than the thicker NWs which have a peak potential at 0.22 V. These results highlight the influence of the NW diameter on catalytic performance, with thinner NWs benefiting from larger surface areas and more active sites. In addition, both catalyst produce 2 peaks. Since the oxidation of EG is complex, the peak in the forward scan has been attribute to the partial oxidation of adsorbed EG to its possible  $\text{C}_2$  product(s) such as glyoxal or glycolate. In the reverse scan reduction of surface poison occurs producing active sites which allows complete oxidation of the  $\text{C}_2$  product(s) resulting in the second peak. The larger the ratio of the forward peak ( $J_f$ ) to the reverse peak ( $J_b$ ) the greater the electrodes poison-resistance ability. In our case  $J_f/J_b$  for the 3.6 and 9.2 nm NWs was found to be 3.2 and 1.7 respectively. Compared with other catalyst (Table 3.7) our NWs particularly the 3.6 nm diameter NWs, have a remarkable catalytic performance. Using chrono-amperimetric *i-t* curves over a 4000 s period, it was further found that the thicker NWs were more durable than the thinner NWs.



Table 3.7: Electro-oxidation of EG by various Au based catalysts in alkaline medium

Catalyst	$E_p$ (V)	$J_f/J_b$
Au nanostars <sup>91</sup>	0.2	3.71
AuPd@Pd nanocrystals <sup>97</sup>	<i>ca.</i> -0.7	2.41
Au nanocrystals <sup>97</sup>	<i>ca.</i> 0.3	2.31
AuPd NW networks <sup>98</sup>	<i>ca.</i> 0.025	<i>ca.</i> 0.8
AuPd Nanoflowers <sup>99</sup>	<i>ca.</i> -0.01	<i>ca.</i> 0.75

We next investigated the mechanism for this electro-oxidation process by varying scan rate in our CV analysis. Scan rates of 35, 50, 75 and 90 mV s<sup>-1</sup> were used as outlined in Figure 3.35.

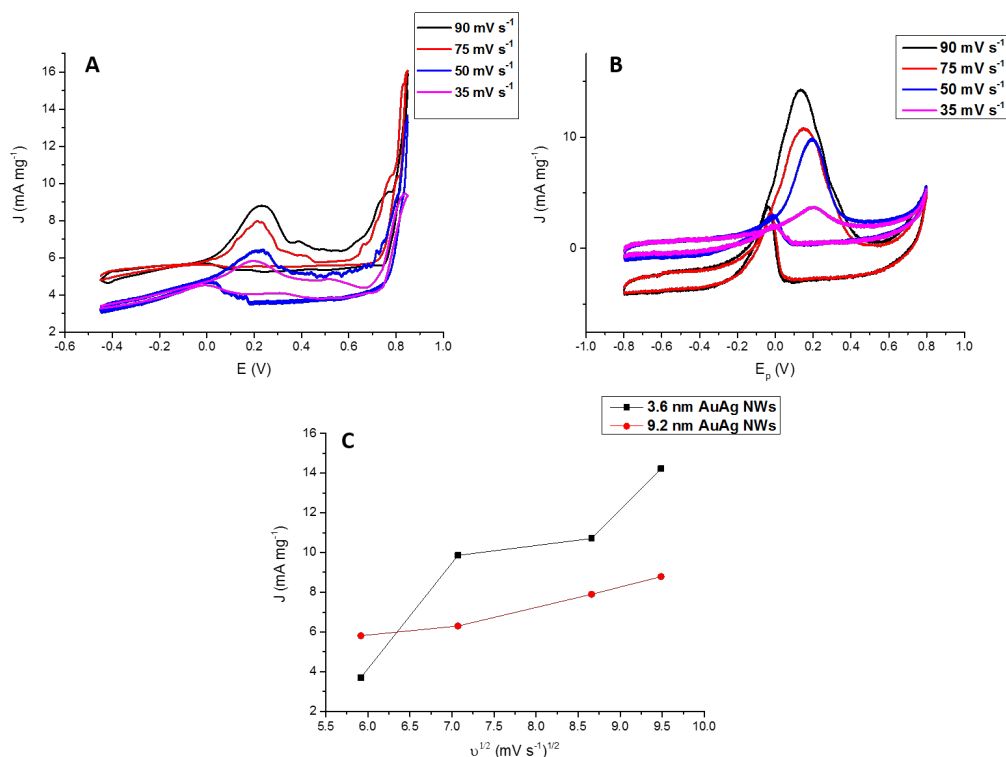


Figure 3.35: CV analysis at scan rates of 35, 50, 75 and 90 mV s<sup>-1</sup> for 9.2 (A) and 3.6 nm (B) AuAg NW versus saturated Calomel reference electrode and corresponding plot of current density vs square root of scan rate (C) in a 1 M KOH solution containing 0.5 M EG.

In both cases, increasing the scan rate resulted in an increase in the current density of the forward scan. A linear relationship between the peak current density and the square root of the scan rate was further observed in both cases which is typical behaviour for a diffusion limited process.

### 3.14 Electro-oxidation of ethylene glycol using AuAg nano-necklaces as anodic catalysts

As a continuation to our previous work (Section 3.14) we investigated the use of our AuAg NNLs as anodic catalyst for the EGOR. The use of hybrid nanomaterials is becoming increasingly more popular as catalysts for fuel cell applications.<sup>100–102</sup> These heterostructured materials provide complex morphologies offering large surface areas and interesting synergistic effects particularly from hetero-interfaces. Typically, templates such as graphene<sup>103–106</sup> and various metal oxides<sup>100,107</sup> have been used a starting point on which catalytic nanoparticles are grown. Recently Lutz *et al.*<sup>108</sup> outlined how combining techniques such as templating and galvanic replacement can be an effective route to producing hybrid materials. More specific to this work, while NNL have not, to the best of our knowledge, been employed for fuel cell catalysis they have shown significant performance in Li ion batteries.<sup>109</sup> Thus they could prove promising for fuel cells. Herein we present the catalytic results of our novel AuAg NNLs for the EGOR.

The electro-catalytic activity of AuAg NNLs was evaluated using CV over a range - 0.8 - 0.8 V in a 1M KOH + 0.5 M EG solution (Figure 3.36).

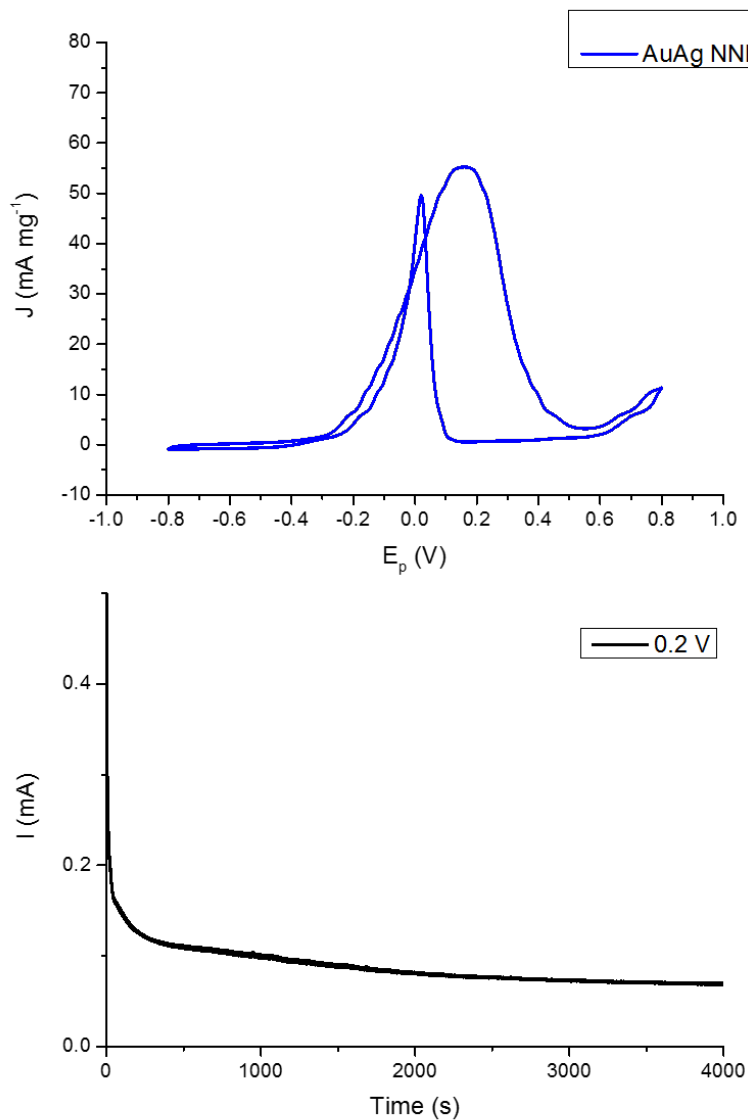


Figure 3.36: CV analysis (top) at  $50 \text{ mV s}^{-1}$  and  $i$ - $t$  curve over 4000 s at 0.2 V (bottom) for AuAg NNLs versus saturated Calomel electrode in a 1 M KOH solution containing 0.5 M EG.

The CV (Figure 3.36) shows a peak at 0.2 V in the forward scan, which is associated with the oxidation of EG and a peak at 0.02 V in the

reverse scan associated with the oxidation of poisons on the surface of the catalyst. The peak current density (at a  $50 \text{ mV s}^{-1}$  scan rate) was  $55.7 \text{ mA mg}^{-1}$  and an appreciable poison resistance of  $J_f/J_b = 1.1$ . In addition, chronoamperometric analysis also shows that the NNLs exhibit good catalytic durability over an extended period of time (4000 s) at peak potential. Compared with our previous 9.2 and 3.6 nm AuAg NWs, the current density produced by the NNLs are 15 and 5.6 times greater, respectively. This marked enhancement in performance is most likely a result of the complex morphology of the hybrid material.

We further investigated the effect of varying the scan rate in our CV analysis. Scan rates of 25, 35, 50, 75 and  $90 \text{ mV s}^{-1}$  were used as detailed in Figure 3.37.

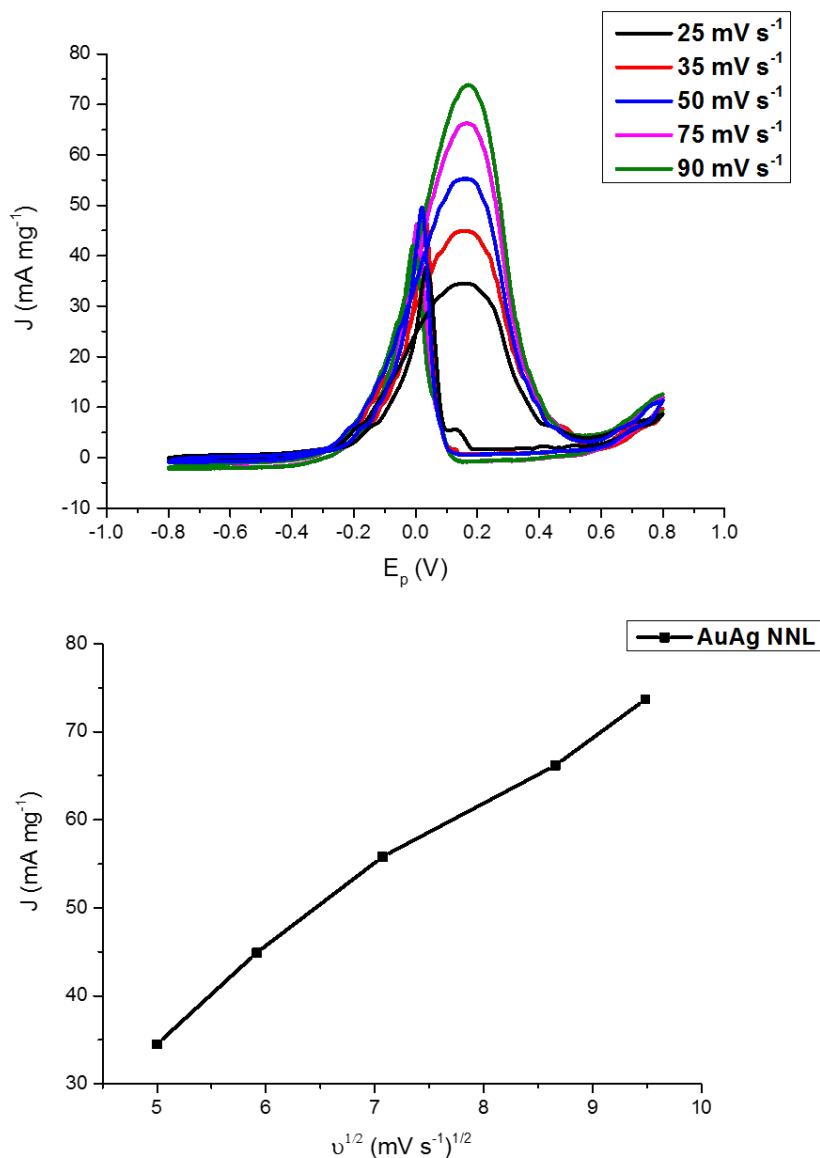


Figure 3.37: CV analysis (top) at scan rates of 25, 35, 50, 75 and 90 mV s<sup>-1</sup> versus saturated Calomel electrode and plot of current density vs square root of scan rate (bottom) for AuAg NNLs in a 1 M KOH solution containing 0.5 M EG.

As shown in Figure 3.37 as the scan rate is increased the peak current densities also increases. A plot of the peak current density with re-

spect to square root of the scan rate shows a linear relationship. This indicates that this reaction diffusion rate limited.

### 3.15 Conclusion and future work

In conclusion we developed a facile and tunable synthesis for water soluble ultrathin AuAg NWs. Through the use of TEM analysis we demonstrated that these NWs are produced through a novel 2 step mechanism involving the formation of NW templates during an aging period and the subsequent formation of thicker NWs by a solvent driven fusion and wetting following the dilution step. It was found that Ag plays an important role in the NW formation process with control studies showing that Ag tends to undergo 1D anisotropic aggregation when diluted. Furthermore the dilution factor has a marked influence on the rate of the NW formation, with a dilution factor of 5 taking 3.25 times longer than a dilution factor of 10. Interestingly the resulting NW thickness was the same in both cases indicating that the aggregation and wetting process occurs to the same extent. In addition the choice of solvent for the dilution process also has a pronounced effect on the resulting NWs. We demonstrated that lower polarity solvents such as isopropanol and ethanol produced highly poly-disperse products after each day of aging while water and methanol performed similarly, producing NWs of the same morphology particularly after

days 1 and 2. This highlighted the significance of the PVP-solvent interaction and its potential use for manipulating crystal growth in future nanomaterial synthesis. Regarding the choice of PVP, we found that while larger (360K and 55K) and smaller (29K) MWs did not improve the quality of our products after aging, we did note that we could potentially tune the average NW diameter from 9.2 nm to 6.3 nm (after 1 day of aging) by using larger (360K) or smaller (29K) MW PVP.

We further improved our protocol by reducing the poly-dispersity of the products and shortened the reaction time from 3 days to just 18 hrs. This was achieved through the use temperature controlled aging of the reaction mixture. We produced non-uniform NWs with an average diameter of 9.2 and 3.6 nm following dilution by aging the reaction at 20 and 25°C respectively. Interestingly aging the reaction at 35°C resulted in novel ultrathin AuAg NNLs with a complex morphology. We further demonstrated that at 40 °C NWs are no longer produced.

Finally we explored the use of AuAg NWs and NNLs for various catalytic applications. We found that larger AuAg NWs (8 nm av. diameter ) performed better than thinner NWs (produced after 3 days of aging) for the catalytic reduction of 4-nitrophenol. We proposed that the larger NWs are more robust and do not degrade as easily as the



thinner NWs in the  $\text{NaBH}_4$  solution. The use of 9.2 and 3.6 nm AuAg NWs (produced from our temperature controlled synthesis) showed remarkable catalytic activity as anodic catalyst for the EGOR. It was noted that the thinner NWs had lower peak potentials and higher current densities compared to the larger NWs as a result of their larger surface area. Furthermore our ultrathin AuAg NNL also exhibited outstanding catalytic activity for the EGOR. This hybrid material out performed both the 9.2 and 3.6 nm AuAg NWs with even lower peak potential (0.16 V) and significantly higher current densities.

For our future work we plan to investigating the formation mechanism of our NNL structures and the plasmon-enhanced catalytic activity of our AuAg nanostructures for the EGOR using an appropriate light irradiation. The use of photo-responsive plasmonic metal nanomaterials for fuel cells is gaining increasing interest and stands a potential remedy to the energy crisis.<sup>92,110</sup> In the next chapters we explore the chiral modification of these 1D nanomaterials and demonstrate the use of AuAg NWs as templates for producing other novel 1D nanomaterials.

## References

- (1) Feng, H.; Yang, Y.; You, Y.; Li, G.; Guo, J.; Yu, T.; Shen, Z.; Wu, T.; Xing, B. *Chemical Communications* **2009**, 1984.
- (2) Gong, S.; Schwalb, W.; Wang, Y.; Chen, Y.; Tang, Y.; Si, J.; Shirinzadeh, B.; Cheng, W. *Nature Communications* **2014**, *5*, 1–8.
- (3) Muratova, I. S.; Mikhelson, K. N.; Ermolenko, Y. E.; Offenhäusser, A.; Mourzina, Y. *Sensors and Actuators, B: Chemical* **2016**, *232*, 420–427.
- (4) Lu, Y.; Tu, J.-p.; Gu, C.-d.; Xia, X.-h.; Wang, X.-l.; Mao, S. X. *Journal of Materials Chemistry* **2011**, *21*, 4843.
- (5) Zhu, W.; Zhang, Y.-J.; Zhang, H.; Lv, H.; Li, Q.; Michalsky, R.; Peterson, A. A.; Sun, S. *Journal of the American Chemical Society* **2014**, *136*, 16132–16135.
- (6) Hu, L.; Cao, X.; Yang, J.; Li, M.; Hong, H.; Xu, Q.; Ge, J.; Wang, L.; Lu, J.; Chen, L.; Gu, H. *Chemical Communications* **2011**, *47*, 1303–1305.

- (7) Pud, S.; Kisner, A.; Heggen, M.; Belaineh, D.; Temirov, R.; Simon, U.; Offenhäusser, A.; Mourzina, Y.; Vitusevich, S. *Small* **2013**, *9*, 846–852.
- (8) Adachi, M.; Mori, K.; Sato, Y.; Pei, L. *Journal of Chemical Engineering of Japan* **2004**, *37*, 604–608.
- (9) Gonzalez-Garcia, L.; Maurer, J. H. M.; Reiser, B.; Kanelidis, I.; Kraus, T. *Procedia Engineering* **2016**, *141*, 152–156.
- (10) Kura, H.; Ogawa, T. *Journal of Applied Physics* **2010**, *107*, 074310.
- (11) Halder, A.; Ravishankar, N. *Advanced Materials* **2007**, *19*, 1854–1858.
- (12) Pazos-Pérez, N.; Baranov, D.; Irsen, S.; Hilgendorff, M.; Liz-Marzán, L. M.; Giersig, M. *Langmuir* **2008**, *24*, 9855–9860.
- (13) Hong, X.; Wang, D.; Yu, R.; Yan, H.; Sun, Y.; He, L.; Niu, Z.; Peng, Q.; Li, Y. *Chemical Communications* **2011**, *47*, 5160.
- (14) Lu, X.; Yavuz, M. S.; Tuan, H.-y.; Korgel, B. A.; Xia, Y. **2008**, 3–5.
- (15) Science, M.; Di, V; Berkeley, L. **2008**, 2–5.
- (16) Liu, H.; Cao, X.; Yang, J.; Gong, X. Q.; Shi, X. *Scientific Reports* **2013**, *3*, 1–6.
- (17) Wang, A.-J.; Lv, J.-J.; Zhou, D.-L.; Weng, X.; Qin, S.-F.; Feng, J.-J. *New Journal of Chemistry* **2014**, *38*, 3395.

- (18) Pei, L.; Mori, K.; Adachi, M. *Langmuir* **2004**, *20*, 7837–7843.
- (19) Li, B.; Jiang, B.; Tang, H.; Lin, Z. *Chem. Sci.* **2015**, *6*, 6349–6354.
- (20) Wang, Y.; Wang, Q.; Sun, H.; Zhang, W.; Chen, G.; Wang, Y.; Shen, X.; Han, Y.; Lu, X.; Chen, H. *Journal of the American Chemical Society* **2011**, *133*, 20060–20063.
- (21) Jang, H. W.; Kim, Y. H.; Lee, K. W.; Kim, Y. M.; Kim, J. Y. *APL Materials* **2017**, *5*, 080701.
- (22) Devarajan, S.; Vimalan, B.; Sampath, S. *Journal of Colloid and Interface Science* **2004**, *278*, 126–132.
- (23) Mirzaei, A.; Janghorban, K.; Hashemi, B.; Bonyani, M.; Leonardi, S. G.; Neri, G. *Journal of Nanostructure in Chemistry* **2017**, *7*, 37–46.
- (24) Kumar, M.; Devi, P.; Kumar, A. *Journal of Materials Science: Materials in Electronics* **2017**, *28*, 5014–5020.
- (25) Dhumale, V. A.; Gangwar, R. K.; Datar, S. S.; Sharma, R. B. *Materials Express* **2012**, *2*, 311–318.
- (26) Liu, M.; Guyot-Sionnest, P. *Journal of Physical Chemistry B* **2005**, *109*, 22192–22200.
- (27) Jessl, S.; Tebbe, M.; Guerrini, L.; Fery, A.; Alvarez-Puebla, R. A.; Pazos-Perez, N. *Small* **2018**, *14*, 1–12.

- (28) Saidi, W. A.; Feng, H.; Fichtorn, K. A. *Journal of Physical Chemistry C* **2013**, *117*, 1163–1171.
- (29) Kedia, A.; Kumar, P. S. *Journal of Physical Chemistry C* **2012**, *116*, 23721–23728.
- (30) Tilaki, R. M.; Zad, A. I.; Mahdavi, S. M. *Journal of Nanoparticle Research* **2007**, *9*, 853–860.
- (31) Dhara, S.; Giri, P. *Nanoscale Research Letters* **2011**, *6*, 320.
- (32) Yang, Y. H.; Chen, X. Y.; Feng, Y.; Yang, G. W. *Nano Letters* **2007**, *7*, 3879–3883.
- (33) Tsuji, M.; Nishizawa, Y.; Matsumoto, K.; Kubokawa, M.; Miyamae, N.; Tsuji, T. *Materials Letters* **2006**, *60*, 834–838.
- (34) Wang, M.; Song, Y.-j.; Wang, M.; Zhang, X.-y.; Wu, J.-y.; Zhang, T. *Nanoscale Research Letters* **2014**, *9:17*, 1–8.
- (35) Zeng, X.; Zhou, B.; Gao, Y.; Wang, C.; Li, S.; Yeung, C. Y.; Wen, W. J. *Nanotechnology* **2014**, *25*, 495601.
- (36) Pastoriza-Santos, I.; Liz-Marzán, L. M. *Nano Letters* **2002**, *2*, 903–905.
- (37) Washio, I.; Xiong, Y.; Yin, Y.; Xia, Y. *Advanced Materials* **2006**, *18*, 1745–1749.
- (38) Ah, C. S.; Yun, Y. J.; Park, H. J.; Kim, W. J.; Ha, D. H.; Yun, W. S. *Chemistry of Materials* **2005**, *17*, 5558–5561.

- (39) Zhang, J.; Liu, H.; Wang, Z.; Ming, N. *Advanced Functional Materials* **2007**, *17*, 3295–3303.
- (40) Xiong, Y.; Washio, I.; Chen, J.; Cai, H.; Li, Z. Y.; Xia, Y. *Langmuir* **2006**, *22*, 8563–8570.
- (41) Okuno, H.; Grivei, E.; Fabry, F.; Gruenberger, T. M.; Gonzalez-Aguilar, J.; Palnichenko, A.; Fulcheri, L.; Probst, N.; Charlier, J. C. *Carbon* **2004**, *42*, 2543–2549.
- (42) Jafarkhani, P.; Torkamany, M. J.; Dadras, S.; Chehrghani, A.; Sabbaghzadeh, J. *Nanotechnology* **2011**, *22*, 235703.
- (43) Fukuoka, A.; Higuchi, T.; Ohtake, T.; Oshio, T.; Kimura, J. I.; Sakamoto, Y.; Shimomura, N.; Inagaki, S.; Ichikawa, M. *Chemistry of Materials* **2006**, *18*, 337–343.
- (44) Li, X.; Zhang, X.; Jia, C.; Matras-Postolek, K.; Yang, P. *ChemPlusChem* **2015**, *80*, 865–870.
- (45) Huang, Z.; Cai, K.; Zhang, H.; Hong, Z.; Yuan, Z.; Han, H. *CrystEngComm* **2017**, *19*, 5686–5691.
- (46) Jia, C.; Yang, P.; Huang, B. *ChemCatChem* **2014**, *6*, 611–617.
- (47) Gao, F.; Yin, Q.; Wang, J.; Zhou, G.; Gu, Z. *Proceedings - Electronic Components and Technology Conference* **2016**, *2016-Augus*, 2329–2334.
- (48) Bukaluk, A. **1983**, 20–27.
- (49) Naik, U.; Shah, N. *ECS Transactions* **2017**, *77*, 705–722.

- (50) Yadav, M. R.; Nimekar, D. M.; Ananthakrishnan, A.; Brahmshatriya, P. S.; Shirude, S. T.; Giridhar, R.; Parmar, A.; Balaraman, R. *Bioorganic and Medicinal Chemistry* **2006**, *14*, 8701–8706.
- (51) Pradhan, N.; Pal, A.; Pal, T. *Colloids and Surfaces A: Physicochemical and Engineering Aspects* **2002**, *196*, 247–257.
- (52) Suchomel, P.; Kvitek, L.; Pucek, R.; Panacek, A.; Halder, A.; Vajda, S.; Zboril, R. *Scientific Reports* **2018**, *8*, 1–11.
- (53) De Oliveira, F.; Nascimento, L.; Calado, C.; Meneghetti, M.; da Silva, M. *Catalysts* **2016**, *6*, 215.
- (54) Jiang, D.; Xie, J.; Chen, M.; Li, D.; Zhu, J.; Qin, H. *Journal of Alloys and Compounds* **2011**, *509*, 1975–1979.
- (55) Chang, Y. C.; Chen, D. H. *Journal of Hazardous Materials* **2009**, *165*, 664–669.
- (56) Xiong, R.; Wang, Y.; Zhang, X.; Lu, C.; Lan, L. *RSC Advances* **2014**, *4*, 6454–6462.
- (57) Dotzauer, D. M.; Dai, J.; Sun, L.; Bruening, M. L. *Nano Letters* **2006**, *6*, 2268–2272.
- (58) Gu, S.; Wunder, S.; Lu, Y.; Ballauff, M.; Fenger, R.; Rademann, K.; Jaquet, B.; Zaccone, A. *Journal of Physical Chemistry C* **2014**, *118*, 18618–18625.

- (59) Seo, E.; Kim, J.; Hong, Y.; Kim, Y. S.; Lee, D.; Kim, B. S. *Journal of Physical Chemistry C* **2013**, *117*, 11686–11693.
- (60) Xiao, C.; Chen, S.; Zhang, L.; Zhou, S.; Wu, W. *Chemical Communications* **2012**, *48*, 11751–11753.
- (61) Dai, Y.; Yu, P.; Zhang, X.; Zhuo, R. *Journal of Catalysis* **2016**, *337*, 65–71.
- (62) Kundu, S.; Leelavathi, A.; Madras, G.; Ravishankar, N. *Langmuir* **2014**, *30*, 12690–12695.
- (63) Chatterjee, D.; Shetty, S.; Müller-Caspary, K.; Grieb, T.; Krause, F. F.; Schowalter, M.; Rosenauer, A.; Ravishankar, N. *Nano Letters* **2018**, *18*, 1903–1907.
- (64) Wunder, S.; Lu, Y.; Albrecht, M.; Ballauff, M. *ACS Catalysis* **2011**, *1*, 908–916.
- (65) Ansar, S. M.; Ameer, F. S.; Hu, W.; Zou, S.; Pittman, C. U.; Zhang, D. *Nano Letters* **2013**, *13*, 1226–1229.
- (66) Ikhsan, N. I.; Rameshkumar, P.; Huang, N. M. *Electrochimica Acta* **2016**, *192*, 392–399.
- (67) Liu, Z.; Du, J.; Qiu, C.; Huang, L.; Ma, H.; Shen, D.; Ding, Y. *Electrochemistry Communications* **2009**, *11*, 1365–1368.
- (68) Laoufi, I.; Saint-Lager, M. C.; Lazzari, R.; Jupille, J.; Robach, O.; Garaudée, S.; Cabailh, G.; Dolle, P.; Cruguel, H.; Bailly, A. *Journal of Physical Chemistry C* **2011**, *115*, 4673–4679.



- (69) Roy, A.; Pandey, T.; Ravishankar, N.; Singh, A. K. *J. Phys. Chem. C* **2014**, *118*, 46.
- (70) Kisner, A.; Heggen, M.; Mayer, D.; Simon, U.; Offenhäusser, A.; Offenhäusser, O.; Mourzina, Y. *Nanoscale* **2014**, *6*, 5146.
- (71) Shi, P.; Zhang, J.; Lin, H.-Y.; Bohn, P. W. **2010**, DOI: 10.1002/smll.201001295.
- (72) Ansar, S. M.; Kitchens, C. L. *ACS Catalysis* **2016**, *6*, 5553–5560.
- (73) Lin, C.; Tao, K.; Hua, D.; Ma, Z.; Zhou, S. *Molecules (Basel, Switzerland)* **2013**, *18*, 12609–12620.
- (74) Ciganda, R.; Li, N.; Deraedt, C.; Gatard, S.; Zhao, P.; Salmon, L.; Hernández, R.; Ruiz, J.; Astruc, D. *Chem. Commun.* **2014**, *50*, 10126–10129.
- (75) Wang, C.; Hu, Y.; Lieber, C. M.; Sun, S. *Journal of the American Chemical Society* **2008**, *130*, 8902–8903.
- (76) Bergin, S. M.; Chen, Y.-H.; Rathmell, A. R.; Charbonneau, P.; Li, Z.-Y.; Wiley, B. J. *Nanoscale* **2012**, *4*, 1996–2004.
- (77) Fu, H.; Yang, X.; Jiang, X.; Yu, A. *Langmuir : the ACS journal of surfaces and colloids* **2013**, *29*, 7134–42.
- (78) Kundu, S.; Leelavathi, A.; Madras, G.; Ravishankar, N. *Langmuir* **2014**, *30*, 12690–12695.

- (79) Shen, Y. Y.; Sun, Y.; Zhou, L. N.; Li, Y. J.; Yeung, E. S. *Journal of Materials Chemistry A* **2014**, *2*, 2977–2984.
- (80) Suchomel, P.; Kvitek, L.; Pucek, R.; Panacek, A.; Halder, A.; Vajda, S.; Zboril, R. *Scientific Reports* **2018**, *8*, 4589.
- (81) Hou, J.; Yu, B.; Liu, E.-g.; Dong, W.-b.; Lu, P.-c.; Wang, Z.; Yang, V. C.; Gong, J.-b. *RSC Advances* **2016**, *6*, 95263–95272.
- (82) Zhao, X.; Yin, M.; Ma, L.; Liang, L.; Liu, C.; Liao, J.; Lu, T.; Xing, W. *Energy & Environmental Science* **2011**, *4*, 2736.
- (83) June, C.; Page, S. E.E. L.; Kammen, D. M. *Science* **2006**, *311*, 506–509.
- (84) Wang, Y.; Zou, S.; Cai, W.-B. *Catalysts* **2015**, *5*, 1507–1534.
- (85) Tamaki, T.; Yamauchi, A.; Ito, T.; Ohashi, H.; Yamaguchi, T. *Fuel Cells* **2011**, *11*, 394–403.
- (86) Pethaiah, S. S.; Arunkumar, J.; Ramos, M.; Al-Jumaily, A.; Manivannan, N. *Bulletin of Materials Science* **2016**, *39*, 273–278.
- (87) Serov, A.; Kwak, C. *Applied Catalysis B: Environmental* **2010**, *97*, 1–12.
- (88) An, L; Zhao, T. S.; Shen, S. Y.; Wu, Q. X.; Chen, R. *International Journal of Hydrogen Energy* **2010**, *35*, 4329–4335.

- (89) Li, Y. F.; Lv, J. J.; Wang, A. J.; Zhang, M.; Wang, R. Z.; Feng, J. J. *Journal of Solid State Electrochemistry* **2015**, *19*, 3185–3193.
- (90) Xu, H.; Ren, F.; Yan, B.; Wang, J.; Li, S.; Du, Y. *Journal of Electroanalytical Chemistry* **2018**, *811*, 37–45.
- (91) Li, A.; Chen, Y.; Duan, W.; Wang, C.; Zhuo, K. *RSC Advances* **2017**, *7*, 19694–19700.
- (92) Xu, H.; Song, P.; Yan, B.; Wang, J.; Guo, J.; Du, Y. *ACS Sustainable Chemistry and Engineering* **2018**, *6*, 4138–4146.
- (93) Cai, K.; Liao, Y.; Zhang, H.; Liu, J.; Lu, Z.; Huang, Z.; Chen, S.; Han, H. *ACS Applied Materials and Interfaces* **2016**, *8*, 12792–12797.
- (94) Xin, L.; Zhang, Z.; Qi, J.; Chadderdon, D.; Li, W. *Applied Catalysis B: Environmental* **2012**, *125*, 85–94.
- (95) Ottoni, C. A.; da Silva, S. G.; De Souza, R. F.; Neto, A. O. *Ionics* **2016**, *22*, 1167–1175.
- (96) Hong, W.; Wang, J.; Wang, E. *ACS Applied Materials and Interfaces* **2014**, *6*, 9481–9487.
- (97) Liu, Q.; Xu, Y. R.; Wang, A. J.; Feng, J. J. *International Journal of Hydrogen Energy* **2016**, *41*, 2547–2553.

- (98) Xu, H.; Yan, B.; Zhang, K.; Wang, C.; Zhong, J.; Li, S.; Du, Y.; Yang, P. *Colloids and Surfaces A: Physicochemical and Engineering Aspects* **2017**, *522*, 335–345.
- (99) Xu, H.; Yan, B.; Zhang, K.; Wang, J.; Li, S.; Wang, C.; Xiong, Z.; Shiraishi, Y.; Du, Y. *ChemElectroChem* **2017**, *4*, 2527–2534.
- (100) Hoseini, S. J.; Bahrami, M.; Roushani, M. *RSC Advances* **2014**, *4*, 46992–46999.
- (101) Guo, S.; Fang, Y.; Dong, S.; Wang, E. *Journal of Physical Chemistry C* **2007**, *111*, 17104–17109.
- (102) Wang, Y.; Du, C.; Sun, Y.; Han, G.; Kong, F.; Yin, G.; Gao, Y.; Song, Y. *Electrochimica Acta* **2017**, *254*, 36–43.
- (103) Wang, C.; Li, N.; Wang, Q.; Tang, Z. *Nanoscale Research Letters* **2016**, *11*, 0–6.
- (104) Zhu, C.; Dong, S. *Nanoscale* **2013**, *5*, 10765–10775.
- (105) Yang, S.; Shen, C.; Lu, X.; Tong, H.; Zhu, J.; Zhang, X.; Gao, H. J. *Electrochimica Acta* **2012**, *62*, 242–249.
- (106) Yang, S.; Zhang, F.; Gao, C.; Xia, J.; Lu, L.; Wang, Z. *Journal of Electroanalytical Chemistry* **2017**, *802*, 27–32.
- (107) Karuppasamy, L.; Chen, C. Y.; Anandan, S.; Wu, J. J. *Electrochimica Acta* **2017**, *246*, 75–88.
- (108) Lutz, P. S.; Bae, I. T.; Maye, M. M. *Nanoscale* **2015**, *7*, 15748–15756.

- (109) Pawlitzek, F.; Pampel, J.; Schmuck, M.; Althues, H.; Schumm, B.; Kaskel, S. *Journal of Power Sources* **2016**, *325*, 1–6.
- (110) Arulmani, D. V.; Eastcott, J. I.; Mavilla, S. G.; Easton, E. B. *Journal of Power Sources* **2014**, *247*, 890–895.

# Chapter 4

## Chiral modification of 1D ultrathin AuAg nanostructures

### 4.1 Introduction

Over the last few years there has been a significant focus on the development and functionalisation of nanomaterials with chiral modifiers. Chiral nanomaterials have a broad range of applications such as asymmetric catalysis<sup>1,2</sup>, sensing<sup>3-7</sup> and in nanotherapeutics.<sup>8,9</sup> Synthetically there are 2 main routes to producing ligand induced chirality in nanomaterials, namely during synthesis as a capping agent or post synthesis via ligand exchange. The use of chiral modifiers as capping agent during synthesis is perhaps the most common method. Previous work in our group has demonstrated the use of pencillamine and cysteine as capping agents in the synthesis of various chiral luminescent

semi-conducting quantum dots.<sup>7,10-13</sup> Interestingly it has been further shown that the binding of the chiral capping agent can lead to chiral defects on the surface of materials.<sup>7</sup> Our group has also recently reported the synthesis of chiroptically active TiO<sub>2</sub> nanorods<sup>14</sup> with 3-4 nm diameters through the use of (1R,2R)-(+)-1,2-diphenylethylene diamine (or 1S,2S)-(-)-1,2-diphenylethylenediamine) as a capping agent during synthesis. These nanorods exhibited interesting luminescence properties with quantum yields of up to 3.5 %. Other chiral capping agents such as BINAP which express axial chirality have been shown to produce ultrafine Au and Pd nanoparticles with excellent selectivity for asymmetric Suzuki reactions.<sup>15,16</sup> Also the cinchonidine-Pt system in particular has been shown to be highly efficient for selective hydrogenation of activated ketones.<sup>17,18</sup> In this system the aromatic moiety of the cinchonidine acts as an anchor on the Pt surface while the chiral centre acts as an enantioselective site.

Regarding the ligand exchange approach, this involves the post synthetic replacement of an achiral capping agent with an a chiral ligand.<sup>19,20</sup> This method has been of particular interest in nanotherapeutic applications for potential drug delivery. This was recently reported by Hong *et al.*<sup>21</sup> who showed that by introducing Au nanoparticles capped with the cationic ligand tetra(ethylene glycol)-lyated (TTMA) and a thiolated Bodipy dye, HSBDP, a ligand exchange occurs due to the

high concentration of glutathione present in the cytoplasm of cells. This replacement of the dye with glutathione resulted in an increase in luminescence in the cells. While still in its early stages this ligand exchange method shows much promise.

To the best of our knowledge there are no current reports on the chiral modification of ultrathin nanowires (NWs). Thus the focus of this part of the project was to study the chiral modification of 1D ultrathin AuAg nanostructures namely; AuAg NWs with 9 nm and 3.6 nm average diameters and nano-necklace structures (NNL). A facile ligand exchange approach was employed in all cases using thiolated amino acids as the chiral modifiers. Through the use of circular dichroism (CD) and attenuated total reflectance infra-red (ATR-IR) spectroscopy we study the resulting optical activity and binding interaction of these ligands with our nanomaterials.

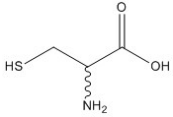
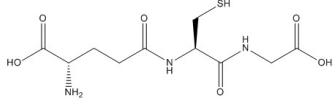
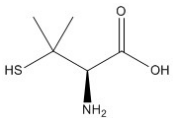
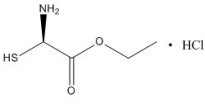
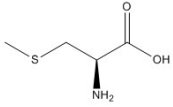
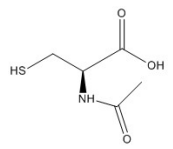
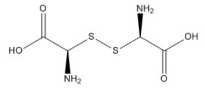
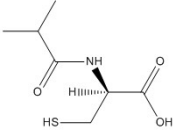
## **4.2 Chiral modification and characterisation of 1D AuAg nanostructures**

Chiral thiolated amino acids were chosen for this study as thiols are known to form strong bonds with Au and Ag. A simple ligand ex-



change method was used in which the chiral modifier was added in excess to an aqueous solution containing our AuAg nanomaterials capped with PVP. Table 4.1 below details the results from the various chiral modifiers used only on the AuAg NWs (9 nm diameter).

Table 4.1: Chiral modification of ultrathin AuAg nanowires

chiral modifier	stereochemistry	Chiral signal position
D/L-cysteine		360 nm
L-glutathione		360 nm
D-pencillamine		-
L-cysteine ethyl ester		-
L-methionine		-
N-acetyl cysteine		-
L-cystine		-
N-isobutryl-L-cysteine		-

Interestingly only cysteine (Cys) and L-glutathione (Glu) induced chiroptical activity in these AuAg NWs. We propose that the accessibility of the thiol group plays an important role in this ligand exchange process. For instance L-cystine and L-methionine do not have a thiol available for binding to the metal surface, while in the case of pencillamine, the thiol is adjacent to 2 methyl groups which may sterically prevent it binding to the NWs. The binding of L-Glu and not the various analogous of cysteine (L-cysteine ethyl ester, N-acetyl cysteine and N-isobutryl -L-cysteine) may suggest that steric hindrance and perhaps the conformation and interaction of the chiral modifiers with each other on the surface of the NWs are also significant factors in this chiral modification.

CD analysis (Figure 4.1) shows mirror image signals at 360 nm for D- and L- Cys capped NWs. These CD signals are distinctly in the plasmonic region of the NWs confirming that its a ligand induced phenomenon,<sup>22</sup> as the unbound Cys signal is much lower at 220 nm. As shown by our TEM analysis (Figure 4.1) the chiral modification did not change the topology of the NWs.

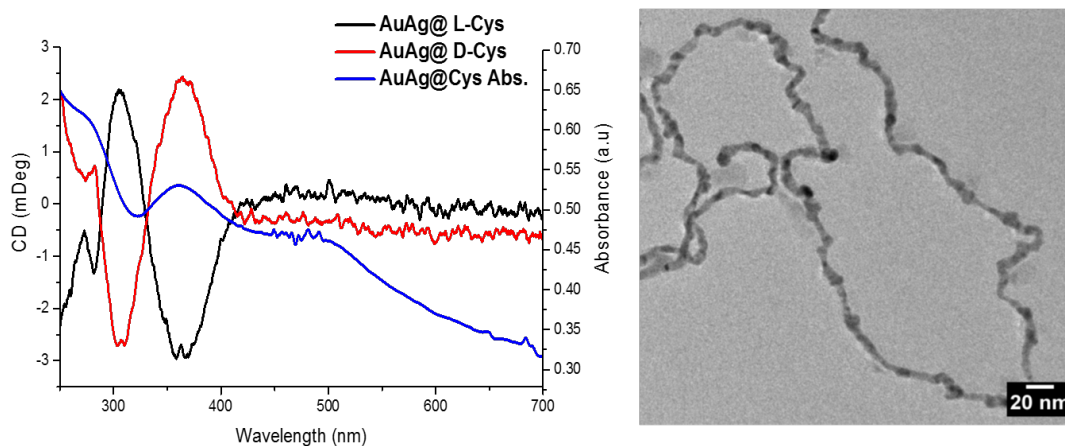


Figure 4.1: CD and UV-Vis spectra (left) for D and L- Cys capped AuAg NWs and TEM image (right) of L-Cys capped AuAg nanowires.

IR spectroscopy was also carried to further confirm the binding of the Cys to the NWs (Figure 4.2).

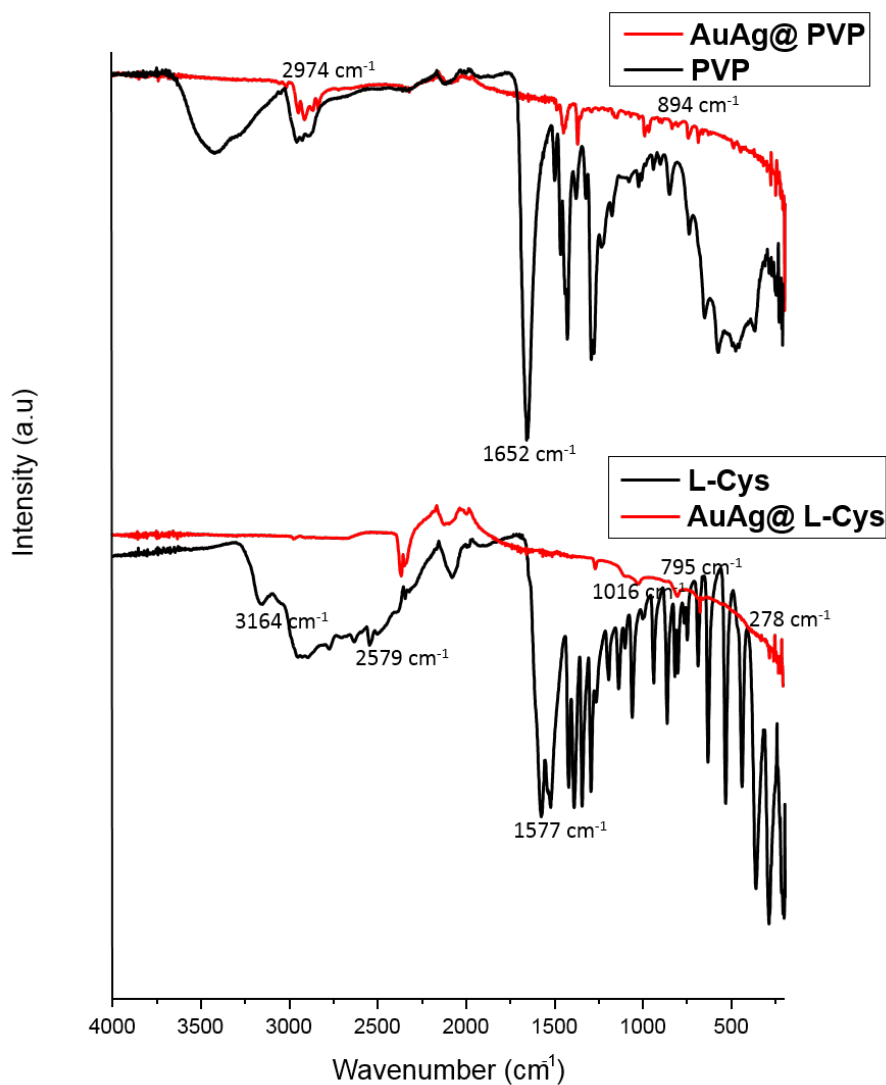


Figure 4.2: IR spectra of PVP and PVP capped AuAg NWs (top) and L-Cys and L-Cys capped AuAg NWs (bottom).

As shown by our IR analysis (Figure 4.2, top) the NWs initially exhibits vibrational bands consistent with PVP.<sup>23–25</sup> These include the vibrational breathing mode of the pyrrolidone ring (894 cm<sup>-1</sup>) and CH<sub>2</sub> asymmetric stretching (2974 cm<sup>-1</sup>) from the polymer backbone. Following the ligand exchange we see a distinct change in the vibrational

bands expressed by the NWs (Figure 4.2 bottom). Firstly, the unbound "free" Cys shows typical carboxylic acid bands at 1645 and 1389  $\text{cm}^{-1}$  associated with the  $\text{COO}^-$  asymmetric and symmetric stretches respectively. Bands related to  $\text{NH}_3^+$  group are noted at 3164 and 1577  $\text{cm}^{-1}$  corresponding to symmetric stretch and asymmetric bend respectively. Finally the SH stretching vibrational mode is noted at 2579  $\text{cm}^{-1}$ . Compared to the bound Cys, we observe no bands due to SH, indicating the cleavage of this bond and the formation of a new bond with the NW surface.<sup>26-28</sup> Bands typically associated with the carboxylic acid and amino group are also detailed at 795 and 278  $\text{cm}^{-1}$  respectively. We also noted a new peak emerge at 1016  $\text{cm}^{-1}$ . This result was similarly reported by Aryal *et al.*<sup>29</sup> for Cys capped Au nanoparticles, who proposed that it may be due to the combination of different vibrational modes of the amino group into one mode. However the exact origin of this peak is still unclear and requires further investigation. In addition further comparison of the IR spectra from the PVP and Cys capped NWs with ascorbic acid (Figure A10 ) shows no peaks in both cases contributing from ascorbic acid. While the binding of Cys via the thiol is expected the exact binding mode, understanding the role of the amino and carboxylic acid groups is an on going field of research. Computational modeling by Di Fecile<sup>30</sup> and Gronbeck<sup>31</sup> showed that it is favourable for the amino group to also coordinate to the surface and that the thiol binds at a bridge site be-

tween 2 atoms however this is still in question.

Regarding L-glu, the CD signal was expressed at 350 nm confirming that the chiroptical activity is also ligand induced. Interestingly the ligand exchange occurred instantly in the case of Cys however an induction period was required for the functionalization of L-Glu to occur. A more detailed study of this is discussed later in section 4.3. TEM analysis of the L-Glu modified NWs shows that NWs were etched by the chiral ligand (Figure 4.3). This accounts for the change in the absorbance and the shift in the CD signal compared to the Cys capped NWs. L-Glu which is a tripeptide composed of glutamic acid, Cys and glycine has  $Pk_a$  values of  $PK1 = 2.12$  (COOH of Glutamic acid);  $PK2 = 3.59$  (COOH of Glycine);  $PK3 = 8.75$  ( $NH_3^+$ );  $PK4 = 9.65$  (SH). Thus the etching we observed may be due to the acidity of this ligand.

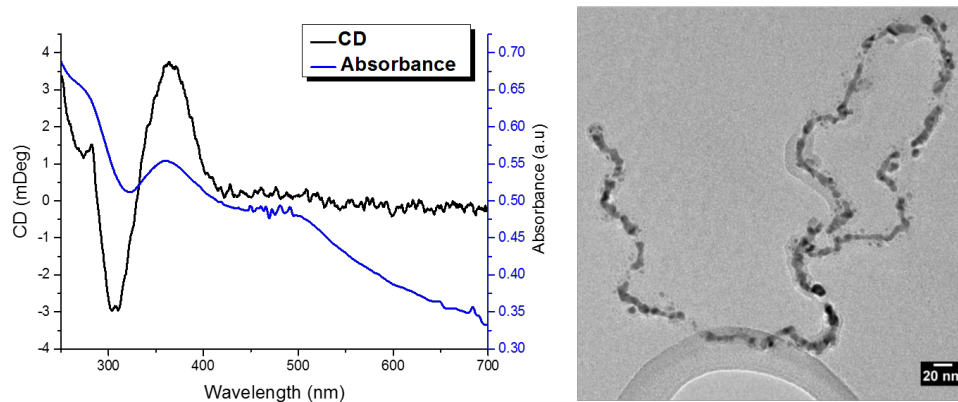


Figure 4.3: CD and UV-Vis spectra (left) and TEM image (right) of AuAg nanowires modified with L-Glutathione.

We used IR spectroscopy to investigate the binding of L-Glu to the NWs (Figure 4.4).



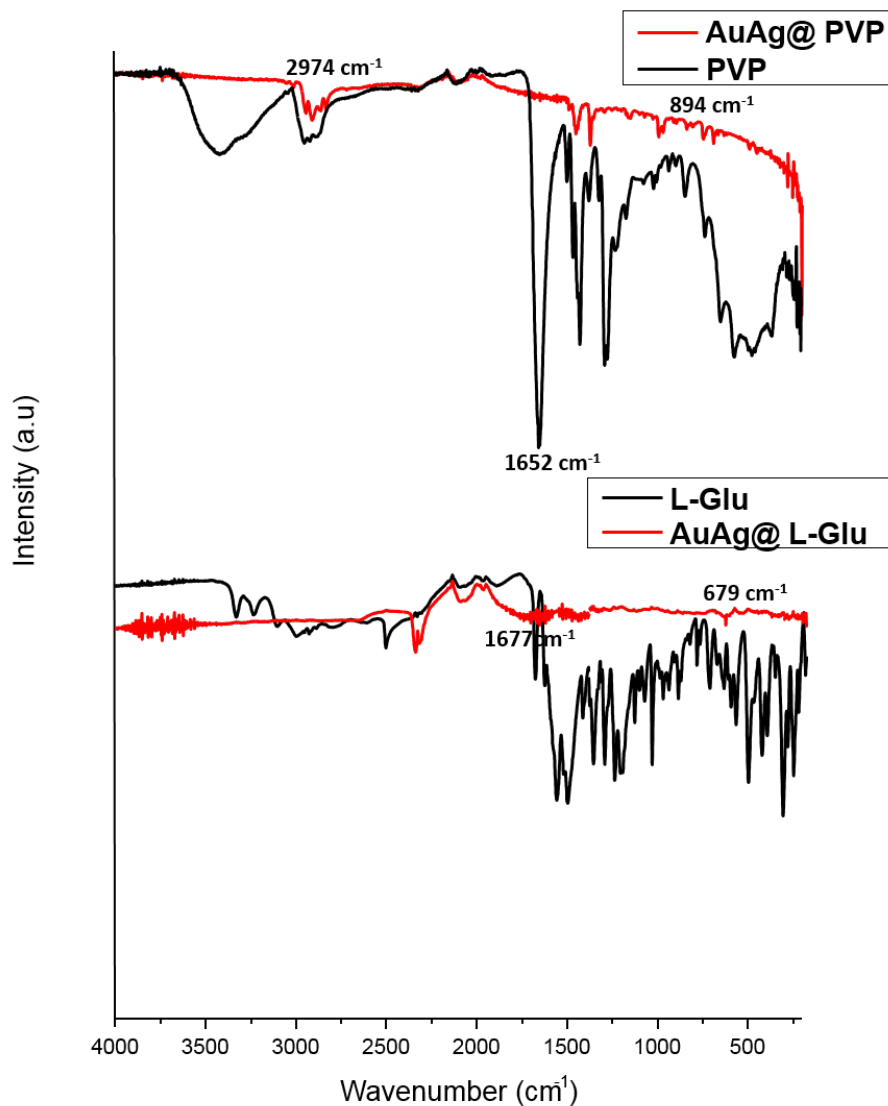


Figure 4.4: IR spectra of PVP and PVP capped AuAg NWs (top) and L-Glu and L-Glu capped AuAg NWs (bottom).

Our IR analysis confirms that the ligand exchange has occurred as noted by the marked difference in spectra between the PVP capped NWs (top) and L-Glu capped NWs (bottom). As expected the bound L-Glu shows no bands associated with the S-H mode indicating that

molecule is binding via the thiol. The bands at 1677 and 679  $\text{cm}^{-1}$  were assigned to carbonyl and C-S vibrational modes respectively.

In light of this work on the 9 nm diameter AuAg NWs we performed a ligand exchange with our PVP capped 3.6 nm AuAg NWs and NNL structures with only Cys and L-Glu as these ligands proved most successful. The resulting CD spectra are shown in Figure 4.5 below.

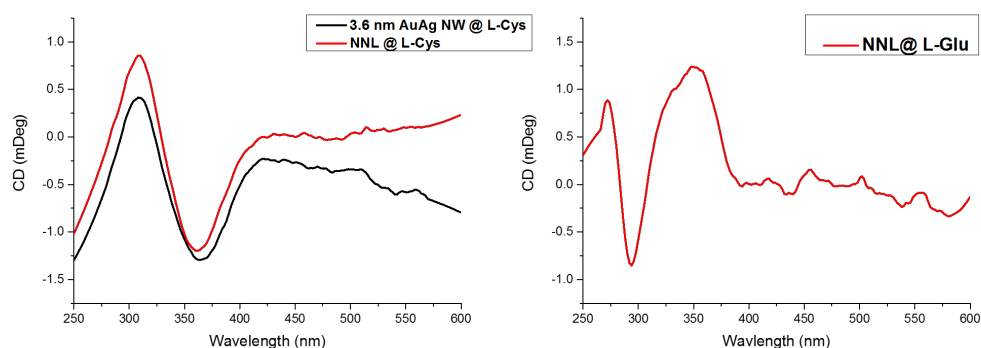


Figure 4.5: CD spectra of NNL and AuAg NWs (3.6 nm av.diameter) modified with L-Cys (left) and L-Glu capped NNL (right).

Both 3.6 nm NWs and the NNLs were functionalized with Cys producing CD signals at 360 nm as expected (Figure 4.6). The CD signals in both cases were notably smaller than that for larger NWs. Interestingly only the NNL became functionalized with L-Glu and a lengthy induction period was also similarly noted in this case. Time monitored CD analysis of this ligand exchange is discussed in section 4.3. Further TEM analysis (Figure 4.6) also revealed that both these materials are

damaged by etching. In the case of the NNLs only the thinnest region (2.7 nm average diameter) was severely etched while the 3.6 nm AuAg NWs showed only minor etching mostly at the thinnest parts of these non-uniform NWs.

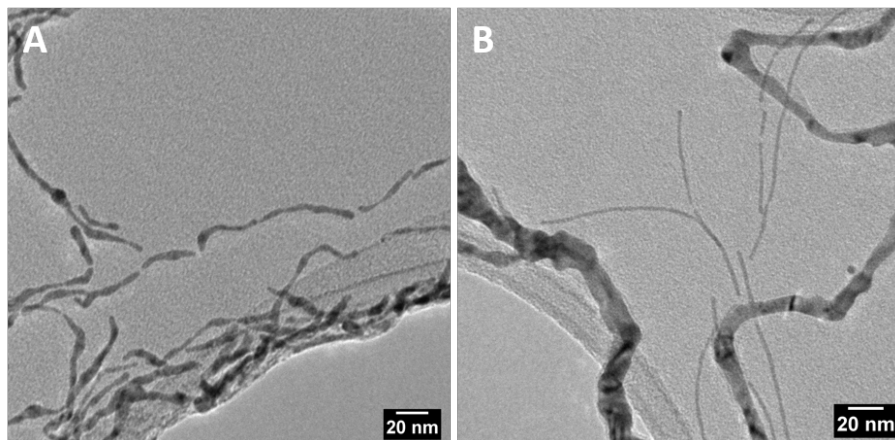


Figure 4.6: TEM images of 3.6 nm AuAg nanowires (A) and NNLs (B) modified with L-Cys.

### 4.3 Time Monitored CD analysis of L-Glutathione modification

As mentioned earlier the ligand exchange process takes notably longer to occur for L-Glu than for Cys for both the AuAg NWs (9 nm diameter) and the NNL. We investigated this further by performing a time determined CD study to monitor the development of the induced chiroptical activity. L-Glu was added in excess to each material and

scans were acquired every 75 seconds for 80 mins. Figure 4.7 details the change in the CD signal over time for NWs.

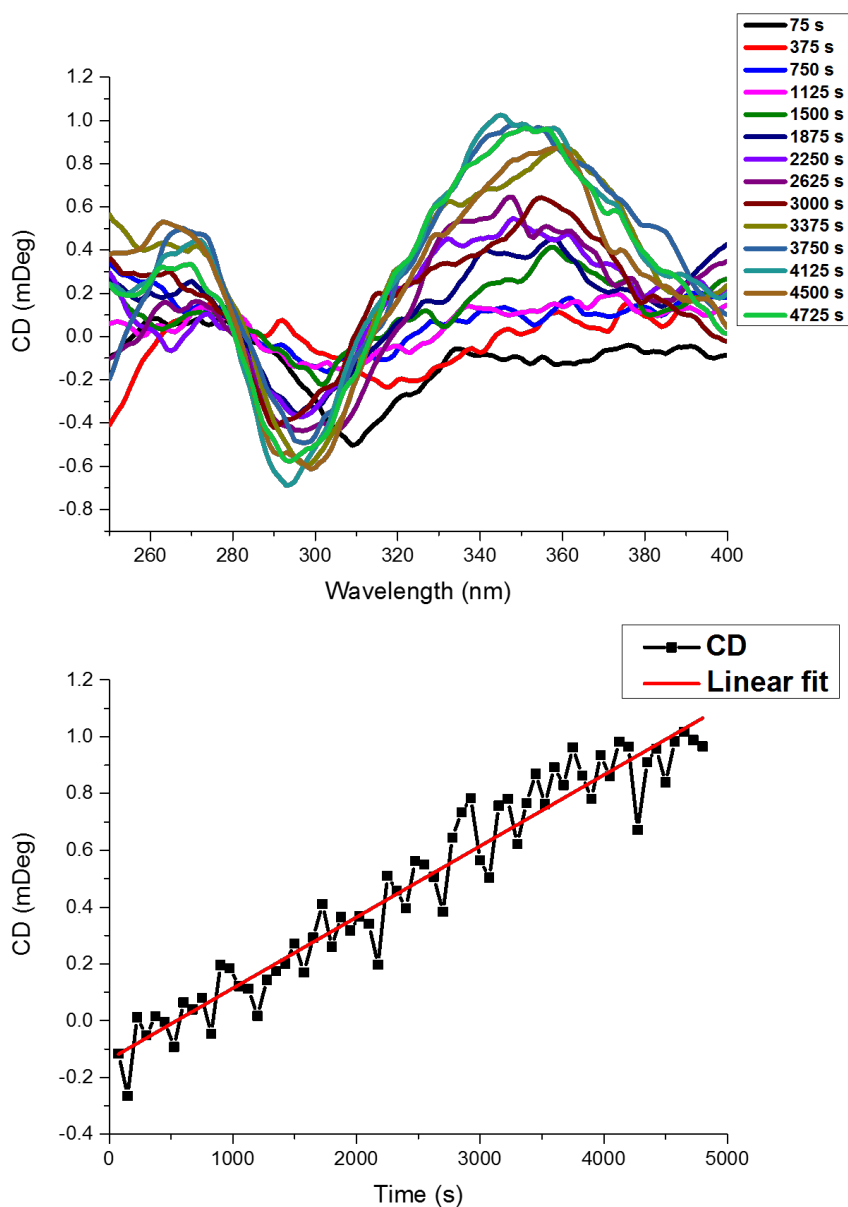


Figure 4.7: Time monitored CD analysis (top) and plot of CD signal with respect to time at 350 nm (bottom) for L-Glu ligand exchange with AuAg NWs.

As shown in Figure 4.7 the CD signal at 350 nm gradually increases over time reaching completion by 75 mins. A linear plot of the change of the CD signal over time at 350 nm further highlights the increase in CD signal over time. The slope of this plot was determined to be  $2.5 \times 10^{-4}$  mDeg  $s^{-1}$ . Regarding the NNL the time monitored CD analysis is detailed in Figure 4.8.

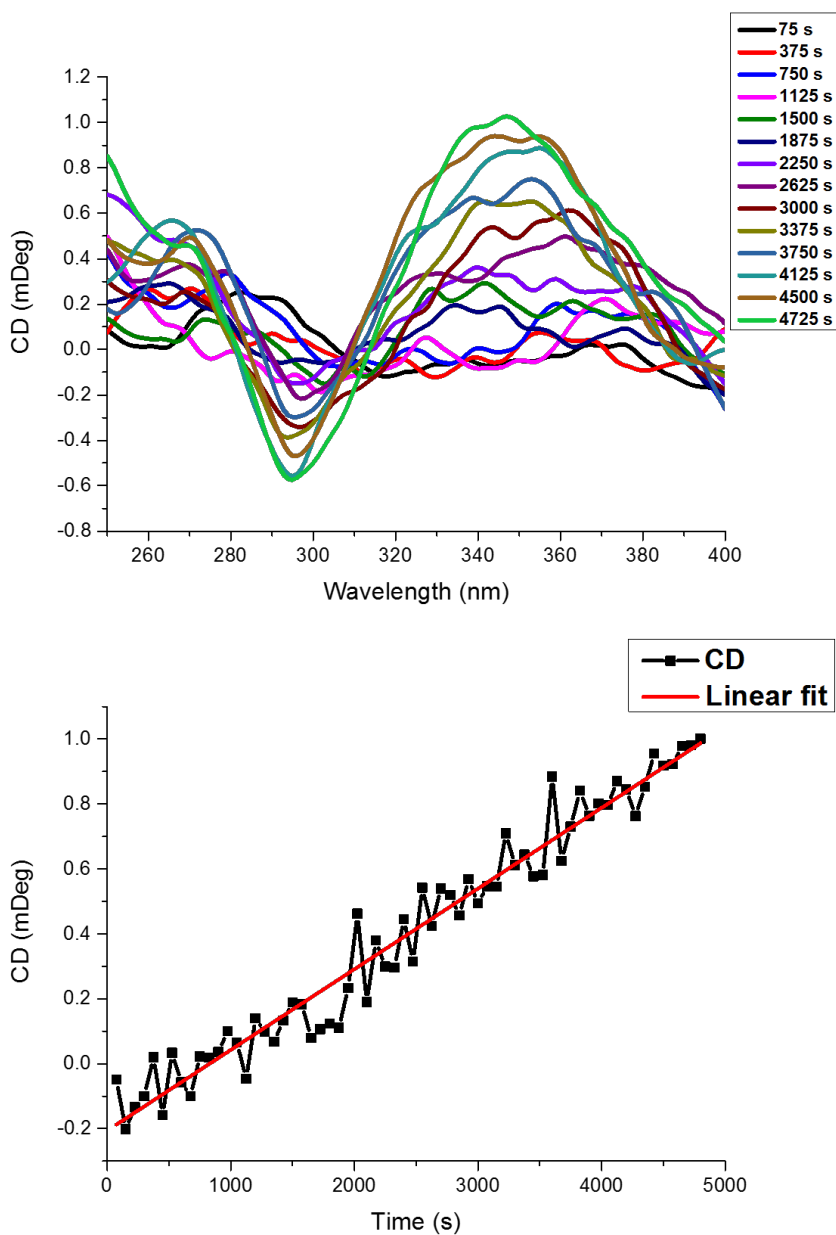


Figure 4.8: Time monitored CD analysis (top) and plot of CD signal with respect to time at 350 nm (bottom) for L-Glu ligand exchange with AuAg NNLS.

Interestingly we see the same trend as in the previous case with a gradual increase in chiroptical activity at 350 nm. The process simi-

larly reaches completion by 75 mins. In addition the linear plot of the change of the CD signal over time at 350 nm shows the increase in CD signal with time and a slope of  $2.5 \times 10^{-4}$  mDeg  $s^{-1}$  was also determined. We propose that this slow ligand exchange process is due to the complexity and bulky size of L-Glu ligand.

#### **4.4 Investigating the influence of thiol accessibility on ligand exchange**

In order to further investigate the influence of the thiol accessibility on the ligand exchange process we used thioglycic acid (TGA). This achiral molecule has only a thiol and carboxylic acid functional group and closely resembles Cys, making it an ideal ligand for this study (Figure 4.9). We used only the 9 nm AuAg NWs and elucidated the binding of TGA with NWs using IR spectroscopy (Figure 4.9).

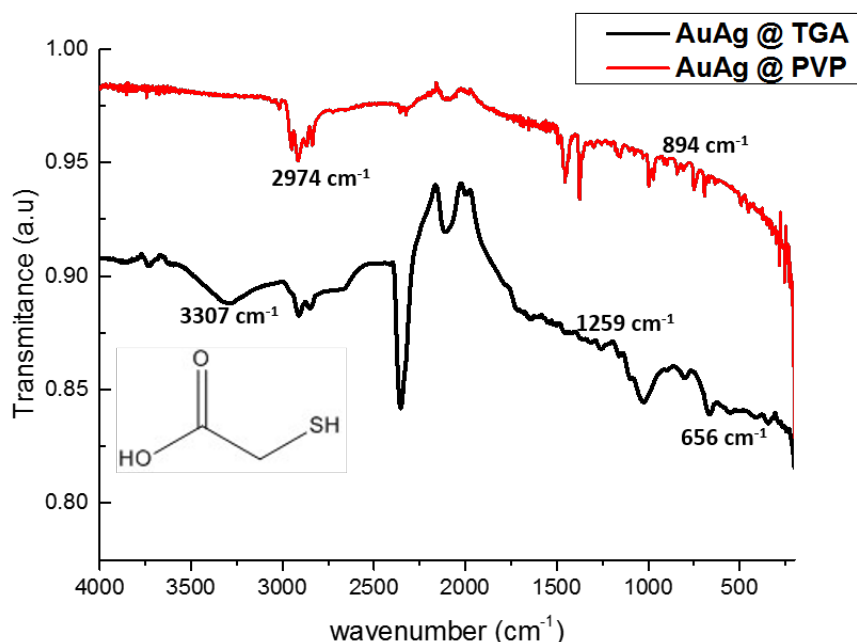


Figure 4.9: IR spectra of PVP and TGA capped AuAg NWs with structure of TGA inset.

IR analysis confirms that TGA is bound to the NWs as noted by the difference in spectra compared to the PVP capped NWs. The IR spectrum of TGA capped NWs shows peaks at 3307, 1259, 656 cm<sup>-1</sup> associated with the hydroxyl, carbonyl and CH vibrational modes respectively. The absence of SH bands also indicates that TGA is deprotonated and bound to the NWs through the thiol as expected. TEM analysis (Figure 4.10) further shows that TGA modification also does not change or damage the topology of the NWs.



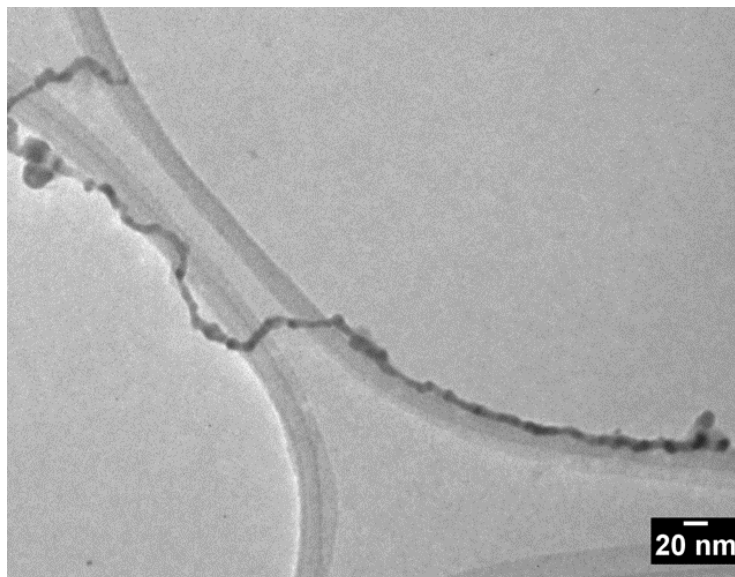


Figure 4.10: TEM image of AuAg NWs capped with TGA.

Thus these result highlights that the accessibility of the ligands' binding group (in this case the thiol) plays an important role in ligand exchange. In order to understand this further computational analysis is required.

## 4.5 Conclusion and future work

In conclusion we demonstrated for the first time the chiral modification of various 1D ultrathin AuAg nanomaterials via a facile ligand exchange method. Our CD analysis shows chiroptical activity in the plasmonic region of each nanomaterial confirming that it is ligand induced chirality. IR analysis further confirms the binding of the chiral

ligands on our nanomaterials with the absence of SH stretches in all cases indicating binding via the thiol as expected. We also observed that thinner materials are more susceptible to etching as noted from our TEM analysis. In addition by monitoring the evolution of chiroptical activity with time monitored CD analysis we found that the L-Glu ligand exchange occurs gradually requiring 75 mins to reach completion for both NWs and>NNLs while Cys binds instantly. This is mostly likely due to the size and complexity of this tripeptide. Finally, using TGA we further demonstrated, that ligand size and the accessibility of its binding group(s) are crucial in this ligand exchange.

For our future work we plan on performing computational model studies to better understand the binding modes of the chiral modifiers on our nanomaterials. This field is still in its early stages and while much work has been done for simple thiols little is known about the binding of more complex molecules like L-Glu. In addition through computational analysis we plan to further investigate the steric effects of the ligands in more detail. Finally, we also aim to explore the use of our chiral modified materials for sensing applications particularly for direct glucose sensing. The focus of this work will be to study the influence of chirality on the limit of detection for D-glucose.

# References

- (1) Gellman, A. J.; Tysoe, W. T.; Zaera, F. *Catalysis Letters* **2015**, *145*, 220–232.
- (2) Yasukawa, T.; Miyamura, H.; Kobayashi, S. *ACS Catalysis* **2016**, *6*, 7979–7988.
- (3) Li, W.; Zhang, H.; Zhang, J.; Fu, Y. *Analytical Methods* **2015**, *7*, 4464–4471.
- (4) Nan, J.; Yan, X. P. *Chemistry - A European Journal* **2010**, *16*, 423–427.
- (5) Han, B.; Hou, X.; Xiang, R.; He, G. *Analytical Methods* **2017**, *9*, 4028–4032.
- (6) Delgado-Pérez, T.; Bouchet, L. M.; De La Guardia, M.; Galian, R. E.; Pérez-Prieto, J. *Chemistry - A European Journal* **2013**, *19*, 11068–11076.
- (7) Mukhina, M. V.; Korsakov, I. V.; Maslov, V. G.; Purcell-Milton, F.; Govan, J.; Baranov, A. V.; Fedorov, A. V.; Gun'Ko, Y. K. *Scientific Reports* **2016**, *6*, 2–7.

- (8) Zhang, Y.; Li, J.; Jiang, H.; Zhao, C.; Wang, X. *RSC Advances* **2016**, *6*, 63331–63337.
- (9) Du, T.; Liang, J.; Dong, N.; Lu, J.; Fu, Y.; Fang, L.; Xiao, S.; Han, H. *ACS Applied Materials and Interfaces* **2018**, *10*, 4369–4378.
- (10) Elliott, S. D.; Moloney, M. P.; Gun'ko, Y. K. *Nano Letters* **2008**, *8*, 2452–2457.
- (11) Martynenko, I. V.; Kuznetsova, V. A.; Litvinov, I. K.; Orlova, A. O.; Maslov, V. G.; Fedorov, A. V.; Dubavik, A.; Purcell-Milton, F.; Gun'ko, Y. K.; Baranov, A. V. *Nanotechnology* **2016**, *27*, 75102.
- (12) Gallagher, S. A.; Moloney, M. P.; Wojdyla, M.; Quinn, S. J.; Kelly, J. M.; Gun'ko, Y. K. *Journal of Materials Chemistry* **2010**, *20*, 8350–8355.
- (13) Moloney, M. P.; Gun'ko, Y. K.; Kelly, J. M. *Chemical Communications* **2007**, *7345*, 3900–3902.
- (14) Cleary, O.; Purcell-Milton, F.; Vandekerckhove, A.; Gun'ko, Y. K. *Advanced Optical Materials* **2017**, *5*, 1–5.
- (15) Tamura, M.; Fujihara, H. *Journal of the American Chemical Society* **2003**, *125*, 15742–15743.
- (16) Tamura, M.; Fujihara, H. *Journal of the American Chemical Society* **2003**, *125*, 15742–15743.

- (17) Baiker, A. *Chemical Society Reviews* **2015**, *44*, 7449–7464.
- (18) Maeda, N.; Hungerbühler, K.; Baiker, A. *Journal of the American Chemical Society* **2011**, *133*, 19567–19569.
- (19) Knoppe, S.; Wong, O. A.; Malola, S.; Häkkinen, H.; Bürgi, T.; Verbiest, T.; Ackerson, C. J. *Journal of the American Chemical Society* **2014**, *136*, 4129–4132.
- (20) Tohgha, U.; Varga, K.; Balaz, M. *Chemical Communications* **2013**, *49*, 1844–1846.
- (21) Hong, R.; Han, G.; Fernández, J. M.; Kim, B. J.; Forbes, N. S.; Rotello, V. M. *Journal of the American Chemical Society* **2006**, *128*, 1078–1079.
- (22) Ben-Moshe, A.; Teitelboim, A.; Oron, D.; Markovich, G. *Nano Letters* **2016**, *16*, 7467–7473.
- (23) Christine H. Moran Matthew Rycenga, Q. Z.; Xia, Y. *Phys Chem C Nanomater Interfaces* **2011**, *115*, 21852–21857.
- (24) Verma, M.; Kedia, A.; Newmai, M. B.; Kumar, P. S. *RSC Advances* **2016**, *6*, 80342–80353.
- (25) Koczur, K. M.; Mourdikoudis, S.; Polavarapu, L.; Skrabalak, S. E. *Dalton Transactions* **2015**, *44*, 17883–17905.
- (26) Bürgi, T. *Nanoscale* **2015**, *7*, 15553–15567.
- (27) Knoppe, S.; Bürgi, T. *Accounts of Chemical Research* **2014**, *47*, 1318–1326.

- 
- (28) Tielens, F.; Santos, E. *Distribution* **2010**, 9444–9452.
- (29) Aryal, S.; Remant, B. K. C.; Dharmaraj, N.; Bhattarai, N.; Kim, C. H.; Kim, H. Y. *Spectrochimica Acta - Part A: Molecular and Biomolecular Spectroscopy* **2006**, *63*, 160–163.
- (30) Di Felice, R.; Selloni, A. *Journal of Chemical Physics* **2004**, *120*, 4906–4914.
- (31) Gronbeck, H.; Curioni, A.; Andreoni, W. *Journal of the American Chemical Society* **2000**, *122*, 3839–3842.

# Chapter 5

## Ultrathin AuAg nanowires as templates

### 5.1 Introduction

Over the last few years there has been a considerable drive to develop methods to synthetically control the morphology of nanomaterials. It is well accepted that the size and morphology of nanomaterials can have a significant effect on their catalytic and optical properties.<sup>1-3</sup> One of the most effective methods for achieving control in nanomaterial design is via template based synthesis. Typical examples include the use soft templates such as DNA<sup>4,5</sup> and hard templates such as aluminium oxide.<sup>6-8</sup> A major disadvantage to this approach however is the removal of the template after synthesis. Recently sacrificial templating has been realized as route to overcoming this problem.<sup>9,10</sup>

This method relies on the galvanic replacement of the metal template, resulting in dissociation of the template and its (e.g 1D) morphology being preserved in the product.<sup>11,12</sup> Work by Liang *et al.*<sup>13</sup> demonstrated the use of ultrathin Te NWs as sacrificial templates for the synthesis of ultrathin Pt nanotubes (NTs) and Pd NWs. The authors showed that the valency of the metal precursor has a significant impact on the product with  $\text{Pt}^{2+}$  producing NTs and  $\text{Pt}^{4+}$  producing NWs. Ultrathin Te NWs have since been used as templates in the synthesis of a variety of novel 1D nanomaterials such as; ultrathin PtCu NWs<sup>14</sup>, AuPt NTs<sup>11</sup>, PtAgTe NWs<sup>15</sup> and PtPdRuTe NTs<sup>16</sup> with each of these nanomaterials exhibiting interesting catalytic performances particularly for fuel cell applications.

Ag NWs have also widely been used as sacrificial templates in the synthesis of Pt based nanomaterials, most notably producing hollow NT structures.<sup>17,18</sup> Chen *et al.*<sup>19</sup> demonstrated the synthesis of double walled AuPt hollow NTs through a 2 step process. Firstly Au undergoes a galvanic reaction with the Ag NWs to afford hollow Au NTs with a thin sheath of Ag on the surface, these subsequently undergo a further galvanic reaction with Pt producing AuPt hollow NTs. Interestingly the inner wall of these NT was made of Au while the outer wall was made up of Pt. This multi-step approach highlights the versatility of templating as a controlled way of producing complex



nanostructures.

In addition to Ag NWs, ultrathin Au NWs have recently emerged as interesting sacrificial templates. Hong *et al.*<sup>20</sup> showed that these NWs can be used to produce dendritic NWs composed of AuPt and AuPtCu with considerable catalytic activity for methanol oxidation. While the cost of the template material is still of concern particularly for large scale applications, researchers have employed Cu NWs as a cheaper alternative for sacrificial templating. This has seen the development of various alloys such as AuCu<sup>21,22</sup>, PtCu<sup>21,23</sup> and AuPtCu NTs.<sup>24</sup>

The aim of this part of the project was to investigate the use of our ultrathin AuAg NWs as templates in the synthesis of novel 1D nanomaterials. We focused on the development of Pt, Rh and RhPt based materials. These were chosen for 2 reasons; firstly the redox potential of our NW templates are relatively high ( $\text{Au}^0/\text{Au}^{1+} = -1.4 \text{ V}$  and  $\text{Ag}^0/\text{Ag}^{1+} = -0.8 \text{ V}$ ) compared to the Pt ( $\text{Pt}^{4+}/\text{Pt}^0 = 0.755 \text{ V}$ ) and Rh ( $\text{Rh}^{3+}/\text{Rh}^0 = 0.758 \text{ V}$ ) and secondly, the importance of these metals for catalysis is well established. Herein we detail the synthesis of novel Pt and RhPt dendritic NWs through the use of AuAg ultrathin NWs as sacrificial templates. We further demonstrate in the case of Rh, a tunable synthesis of AuAg NW@ Rh nanoparticle hybrid structures. Finally we present the application of our Pt and RhPt dendritic NWs

as anodic catalysts for methanol and formic acid electro-oxidation.

## 5.2 Synthesis and characterisation of Pt and RhPt dendritic nanowires

Pt and RhPt dendritic NWs were synthesised using ultrathin AuAg NWs as templates. Briefly PVP (55K molecular weight) and the ultrathin AuAg NWs (produced after following 1 day of aging) were added together in water and heated to 80 °C. In the case of the RhPt dendritic NWs, RhCl<sub>3</sub> and H<sub>2</sub>PtCl<sub>4</sub> were added sequentially (1:1), while for Pt dendritic NWs only H<sub>2</sub>PtCl<sub>4</sub> (2 eq.) was added. Ascorbic acid was then added after 1 min and the mixture was left heating at 80 °C for 1 hour. TEM analysis of both products is shown in Figure 5.1.

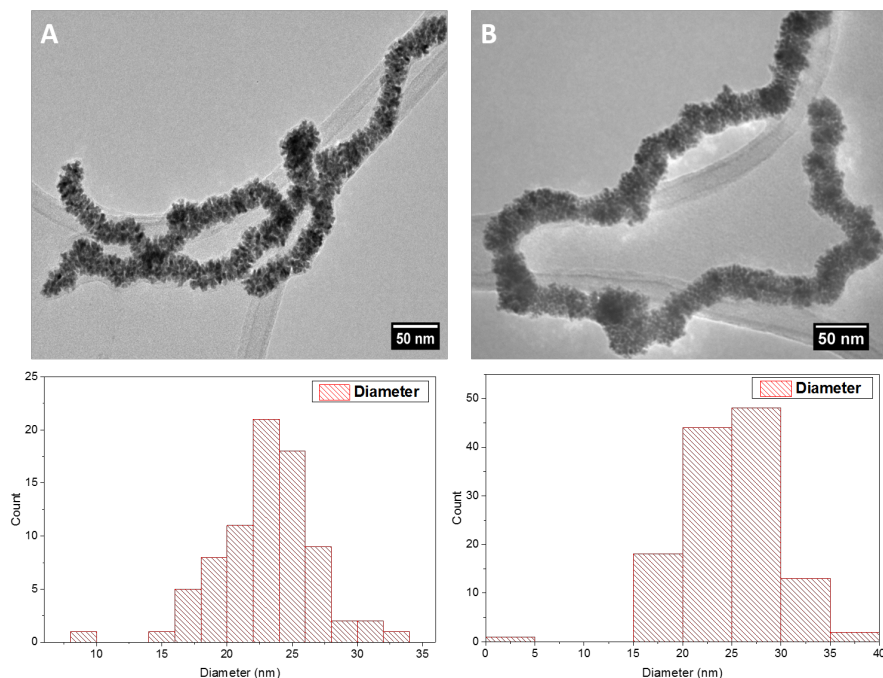


Figure 5.1: TEM images of Pt (A) and RhPt (B) dendritic nanowires and associated size distributions.

Our TEM analysis shows that the ultrathin AuAg NWs performed as effective templates producing high yields of product in both cases. The resulting structures consist of an assembly of anisotropic nanoparticles with a NW formation. The reproducibility of this synthesis is shown in Figure A10. These structures closely resemble the AuPt and AuPtCu dendritic NWs produced by Hong *et al.*<sup>20</sup> using ultrathin Au NWs as templates. It must be noted that when this reaction is performed using only  $\text{RhCl}_3$  as the metal precursor a different behaviour is observed, this will be discussed in more detail in section 5.5. Size distribution analysis shows that both products are of similar size rang-

ing up to microns in length and with average diameters of 23.7 and 24.7 nm for the Pt and RhPt dendritic NWs respectively. UV-Vis spectra (Figure 5.2) further show broad absorbance profiles in both cases with Pt in particular exhibiting a peak 290 nm which is typical for these nanoparticles.<sup>25</sup>

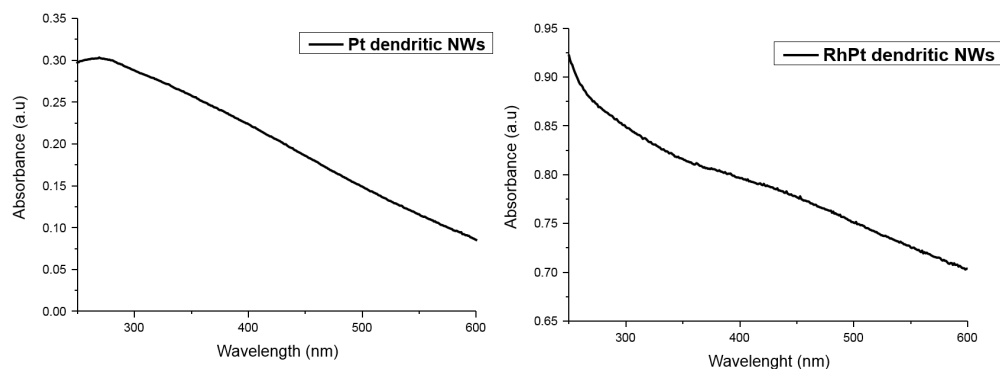


Figure 5.2: UV-Vis spectra of Pt (left) and RhPt (right) dendritic nanowires.

HR-TEM analysis (Figure 5.3) shows that the Pt dendritic NWs have d spacing values of  $0.235 \pm 0.009$  nm and  $0.232 \pm 0.019$  nm which correlates with the 111 and 200 planes of FCC Pt respectively. In the case of the RhPt dendritic NWs, HR-TEM revealed similar d-spacing values of  $0.195 \pm 0.018$  nm and  $0.228 \pm 0.015$  nm which correlates with the 111 and 200 planes of FCC Rh and Pt. The size of the nanoparticles in these dendritic structures was found to range from 2 to 8 nm for both the Pt and RhPt dendritic NWs.

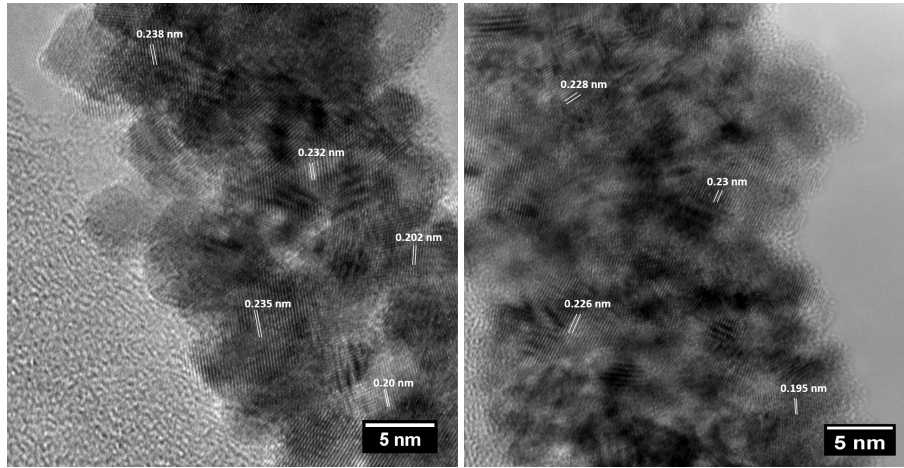


Figure 5.3: HR-TEM images of Pt dendritic nanowires (left) and RhPt dendritic nanowires (right).

HAADF-STEM (Figure 5.4) further highlights the complex assembly of anisotropic nanoparticles that make these structures. The Z-contrast noted between the nanoparticles may also indicate a porous nature of these dendritic NWs.

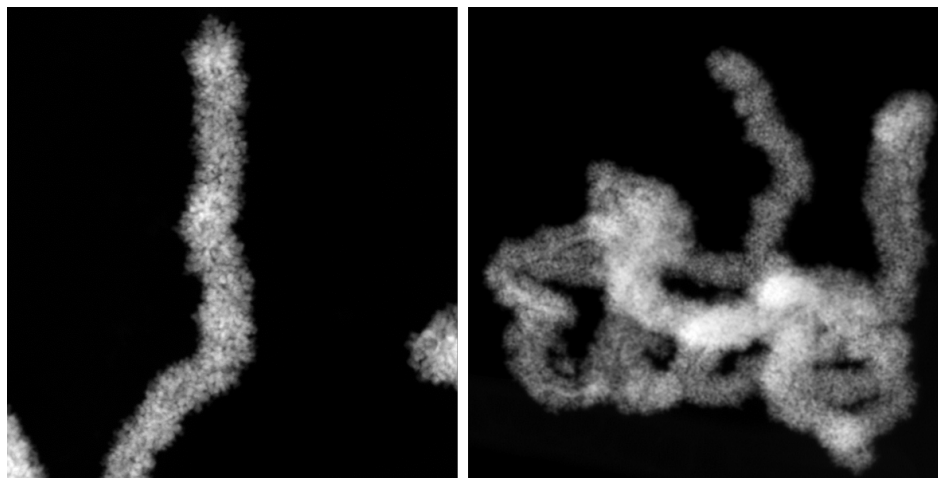


Figure 5.4: HAADF STEM image of Pt (left) and RhPt (right) dendritic nanowires.

Both dendritic NW samples were further investigated using XRD analysis (Figure 5.5).

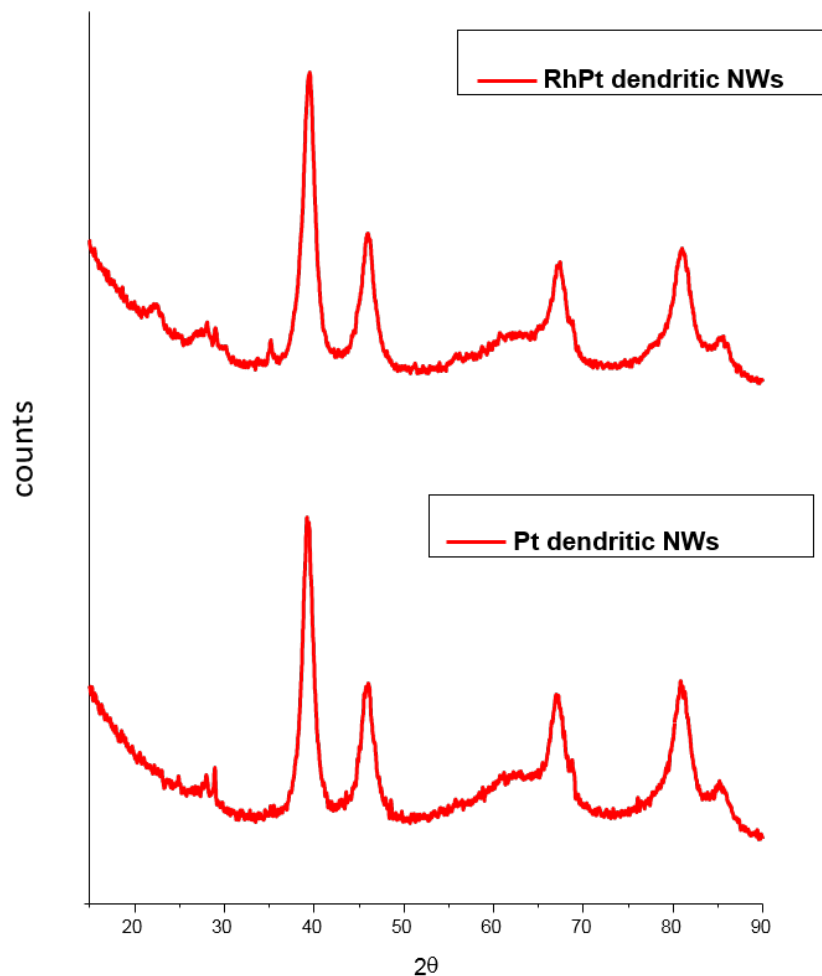


Figure 5.5: XRD analysis of Pt (bottom) and RhPt (top) of dendritic nanowires.

The XRD patterns of both dendritic NWs are very similar with Pt exhibiting diffraction peaks at  $2\theta$  values of 39.19, 45.96, 66.9, 80.7 and 85.13° while in the case of RhPt there is only minor difference in the peaks with values of 39.5, 45.9, 67.04, 80.98 and 85.24°. These peaks corresponding to the (111), (200), (220), (311) and (222) planes respectively for FCC Pt (JCPDS-01-117). This observation is common for noble metal nanomaterials of this kind. Furthermore TC

analysis for just the Pt dendritic NWs, shows that the (111) facet is the most dominant (refer to table 5.1) . This analysis indicates that the dendritic NWs preferentially grow along the (111) plane. This is to be expected as we previously demonstrated (chapter 3, section 3.2) that the (111) facet of our AuAg NWs is predominant.

Table 5.1: Texture coefficient analysis of Pt dendritic NWs

<b>Facet</b>	<b>I<sub>0</sub> (counts)</b>	<b>I (counts)</b>	<b>TC* of sample</b>
111	799.9	964.1	1.05
200	569.3	599.2	0.918
220	510.37	584.2	0.997
311	503.86	617.9	1.03

\* refer to appendix for TC equation. Reference 04-0802 was used for this analysis.

In order to understand the elemental composition and distribution of both our dendritic NWs HAADF-STEM EDX analysis was performed. Figure 5.6 details the EDX analysis of the RhPt dendritic NWs.



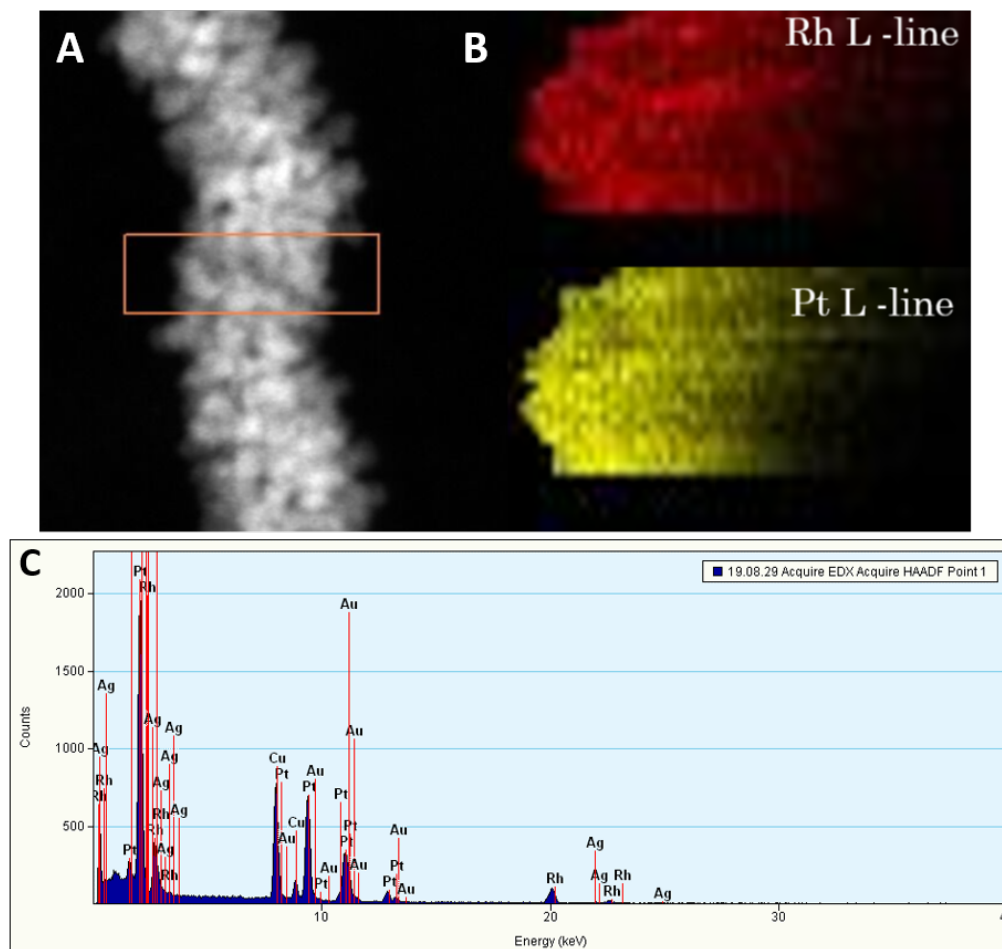


Figure 5.6: HAADF STEM image (A), EDX maps of Pt and Rh L lines (B) and EDX spectrum (C) of RhPt dendritic NWs. The red lines in the spectrum highlight the absence of Ag and Au peaks.

The elemental analysis of the RhPt dendritic NWs confirms that they are alloy of Rh and Pt with a Pt:Rh ratio of 90:10. The EDX spectrum shows the characteristic L and M peaks of Pt at 9.44 and 2.04 KeV respectively and the L peak of Rh at 2.69 KeV. The additional peaks present are due to the Cu from the TEM grids used for this analysis. Our EDX analysis further indicates that the alloy is mainly composed

of Pt. This may account for the minor difference noted in the XRD analysis between the two products.

The HAADF-STEM EDX analysis of the Pt dendritic NWs is presented in Figure 5.7.

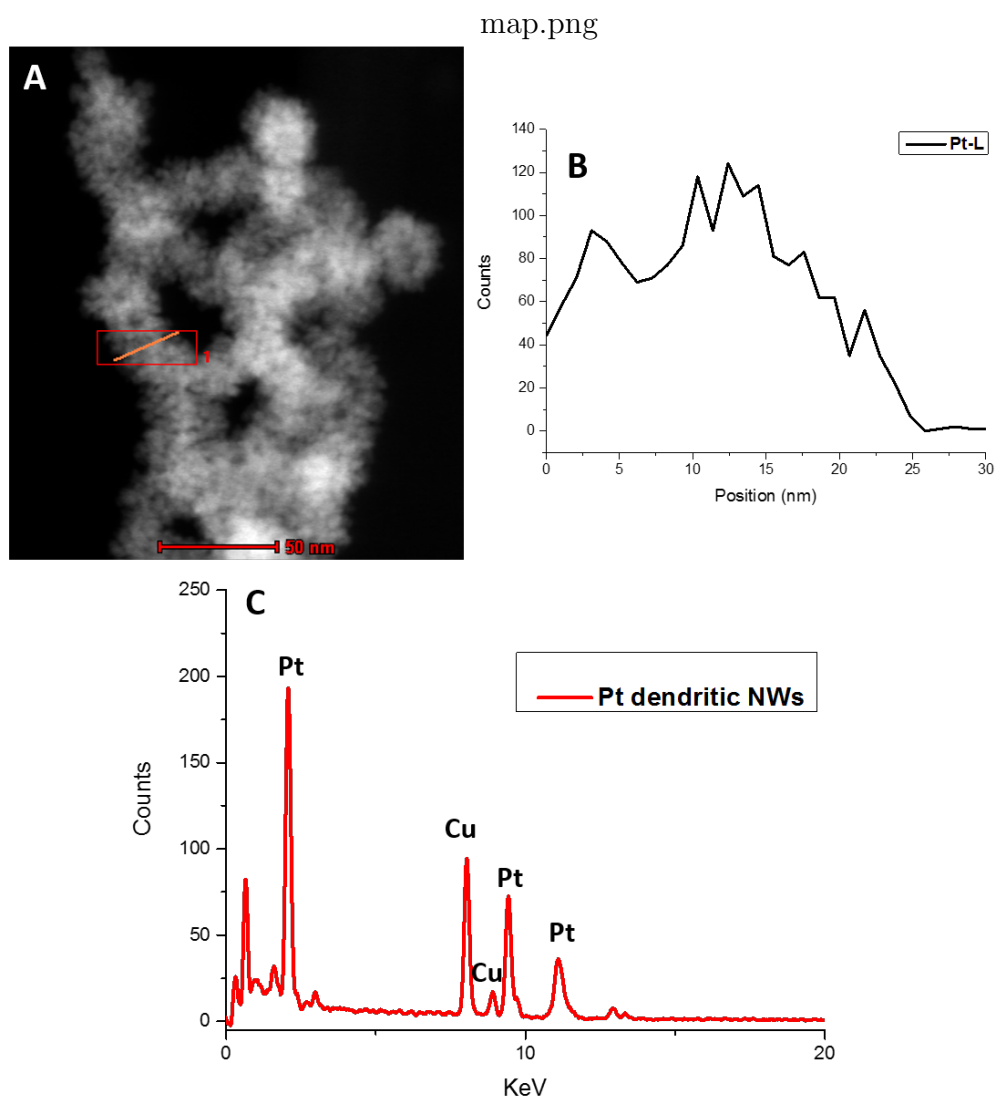


Figure 5.7: HAADF STEM image (A), EDX line profile (B) and EDX spectrum (C) of Pt dendritic NWs.

The elemental analysis of the Pt dendritic NWs confirms that the structure is composed entirely of Pt. The EDX spectrum shows the characteristic L and M peaks of Pt at 9.44 and 2.04 KeV respectively. The additional peaks present are due to the Cu from the TEM grids used for this analysis. Most importantly in both cases our elemental analysis did not show the presence of any Au or Ag from the template in either nanostructure. This confirms that the NWs are performing as sacrificial templates and are completely dissociated during the synthesis. This is a striking result as unlike in the case of Hong *et al.*<sup>20</sup>, where Au from the Au NW template remains in the final product in our case it does not. The reason for this may be due to the presence of Ag in our AuAg NW alloy facilitating the complete dissociation of the template following the galvanic reaction replacement with the metal precursors.

### 5.3 Monitoring dendritic nanowire formation

We investigated the formation of the dendritic NWs by taking aliquots from the reaction mixture at various times intervals, following the addition of ascorbic acid, and prepared them quickly on lacy carbon TEM grids for TEM analysis. This was done only in the case of the RhPt dendritic NWs. The TEM analysis is detailed in Figure 5.8.

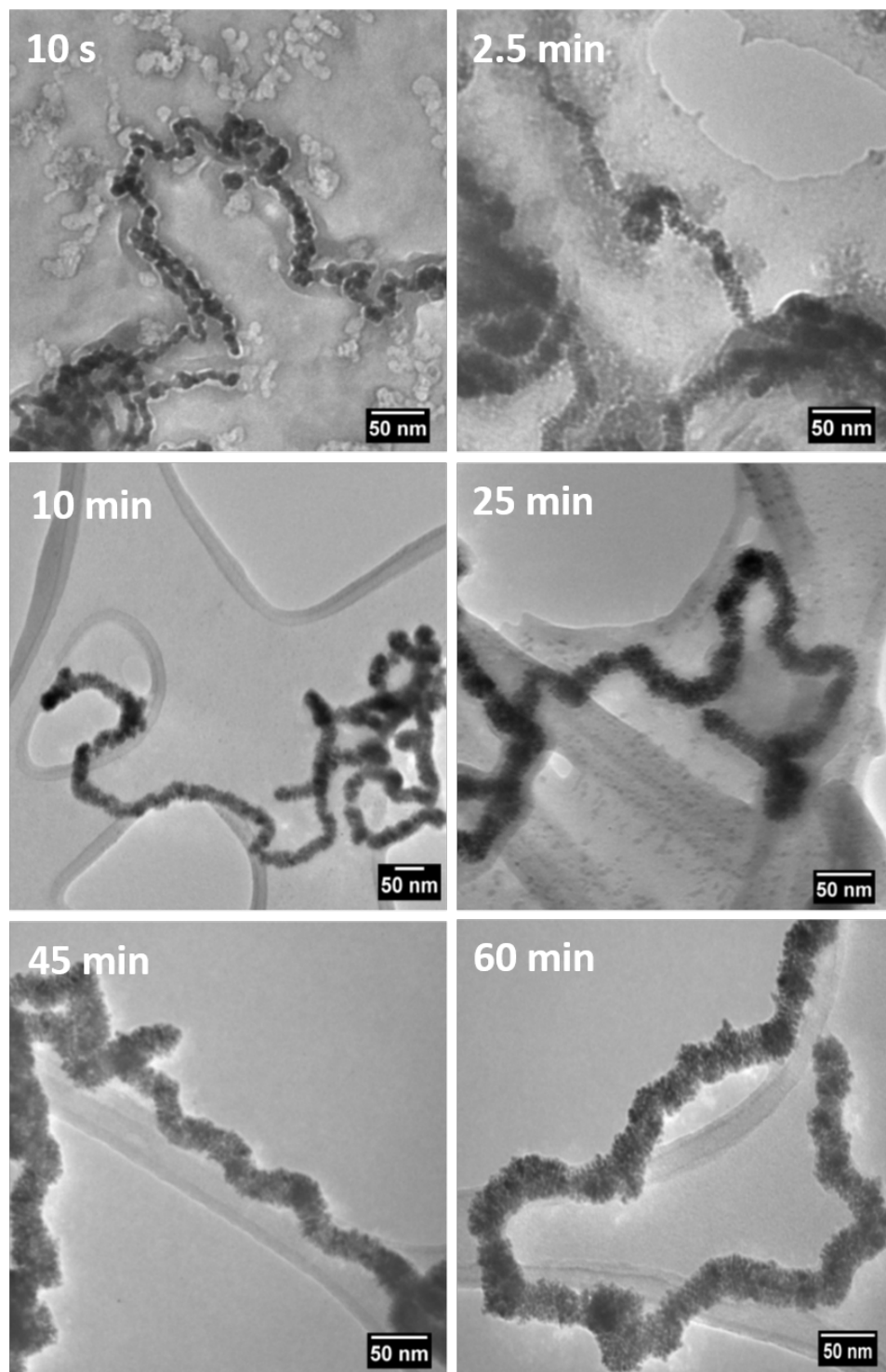


Figure 5.8: TEM images monitoring the formation of RhPt dendritic nanowires over time.

Our TEM analysis clearly shows that within 10 s of adding ascorbic acid the dendritic NWs begin to form, as noted by the nanoparticle aggregates present on the template. By 2.5 mins we see complete formation of dendritic NWs with an average diameters of 15.1 nm. After 10 mins the dendritic NWs remain of a similar size with an average diameter of 15.6 nm. The dendritic NWs gradually increase in thickness reaching a diameter of typically 25 nm after 25 mins (refer to Figure A11 -A14. The diameter remains unchanged upon completion of the reaction at 60 mins. In addition to TEM, we also performed UV-Vis analysis to monitor the evolution of the structure (Figure 5.9).

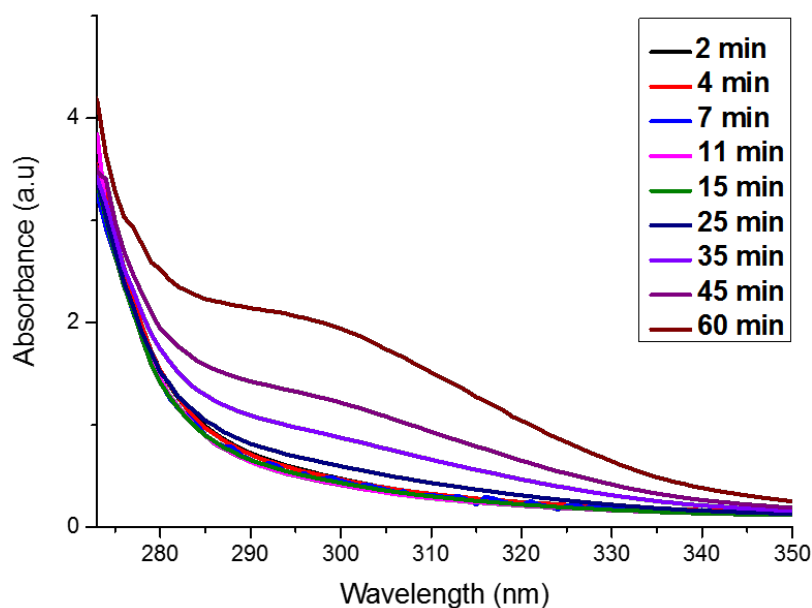


Figure 5.9: UV-Vis spectra monitoring the formation of RhPt dendritic nanowires over time.

UV-Vis analysis shows the gradual formation of a broad absorbance band centred around 300 nm over the course of the reaction. This absorbance profile matches that of RhPt dendritic NWs, as detailed in Figure 5.2. Thus from our mechanistic study, the initial galvanic reaction between the template and the metal precursors occurs rapidly resulting in dendritic NWs forming in the early stages of the reaction. These NWs subsequently undergo gradual increase in thickness over the course of the reaction, reaching a complete thickness by 25 mins.

## 5.4 Investigating the role of the template

In order to confirm the role of the template in this synthesis we also performed a control study with Rh, Pt and RhPt in the absence of the AuAg NW template. The concentration of the metal precursors was kept the same in all cases and the products were analysed by TEM and UV-Vis spectroscopy as detailed in Figure 5.10.

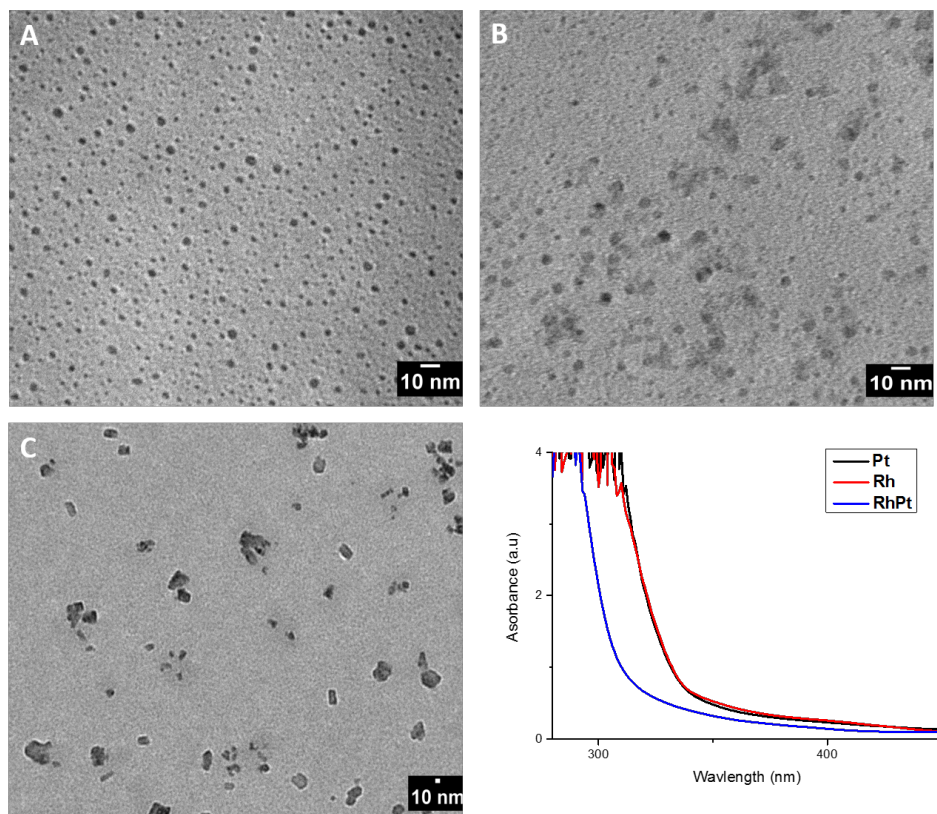


Figure 5.10: TEM images of Rh, Pt and RhPt controls in the absence of templates and associate UV-Vis spectra.

As expected, in the absence of the AuAg NW templates no dendritic NWs are formed. In all cases only nanoparticles were produced from each control. The average diameters were 2.3, 2.42 and 22.7 nm for the Pt, Rh and RhPt nanoparticles respectively. This result was similarly observed by Tu *et al.*<sup>26</sup> in case of Pt and Rh and by Lee *et al.*<sup>27</sup> for RhPt. In addition no aggregation was observed by these nanoparticles. Interestingly, recent work by Gacem *et al.*<sup>28</sup> demonstrated the controlled synthesis of spherical aggregates of PVP capped Rh nanopar-

ticles using similar reaction condition to ours, only using sodium borohydride as the reducing agent. The authors further showed that the aggregation is driven by the hydrophobic interaction between water and the PVP capping the nanoparticles. This result could have potential implication in our work. While the template is needed to form the dendritic NWs the choice of capping agent and solvent may also be used to further tune the morphology of our products. Regarding the UV-Vis analysis, each control shows broad absorbance bands centred at 300 nm, which is common for these nanoparticles. Thus our control study clearly confirms that the AuAg NWs are performing as templates and are necessary to produce the dendritic NWs.

## **5.5 Synthesis and characterisation of AuAg@Rh hybrid nanostructures**

AuAg NW@Rh nanoparticle hybrid nanostructures were synthesised using ultrathin AuAg NWs as a template. These structures were produced using the same protocol as detailed for Pt and RhPt dendritic NWs (section 5.1) using only  $\text{RhCl}_3$  as the metal precursor. The development of similar Au@Rh core-shell hybrid nanostructures has become area of interest to researchers in recent years.<sup>29-31</sup> By coupling the well established catalytic behaviour of Rh with the plasmonic and catalytic properties of nano scale Au, these hybrid materials make interesting



candidates for potential photocatalytic applications.<sup>32</sup> However the synthesis of such hybrid nanomaterials is synthetically challenging due to the lattice mismatch between Au and Rh (Au 0.408 nm versus Rh 0.380 nm) and the large difference in their surface energy density (Au  $1.6 \text{ J m}^{-2}$  versus Rh  $2.8 \text{ J m}^{-2}$ ), as a result there are very few reports in the literature.<sup>33</sup> One of the most prominent examples of this work was done by Kang *et al.*,<sup>34</sup> with the in situ synthesis of Au nanoparticle cores with atomically thin Rh plate like shells, which exhibited a photocatalytic enhancement of hydrogen generated from hydrazine. In this section we present for the first time a detailed characterisation of our novel AuAgNW@Rh nanoparticle hybrid nanomaterial.

HR-TEM images of our AuAg@Rh hybrid is shown in Figure 5.11.

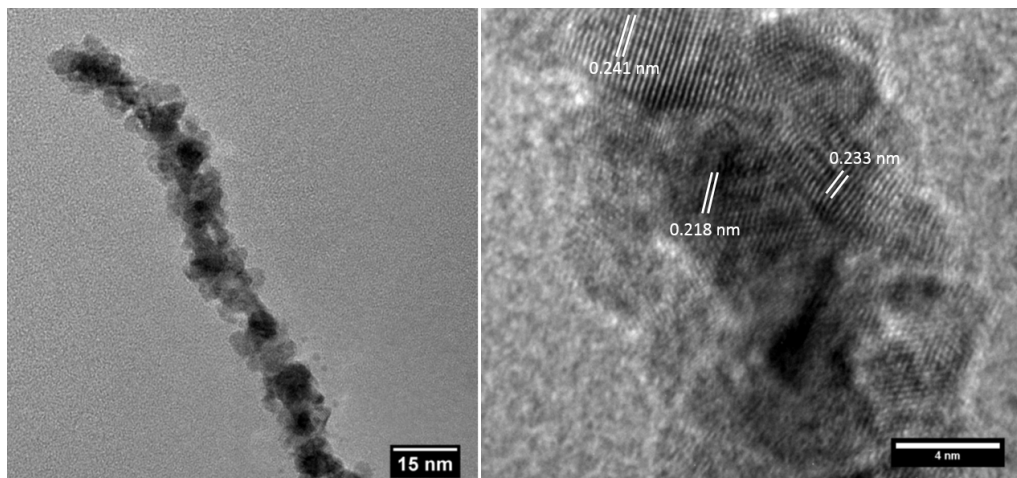


Figure 5.11: HR-TEM images of AuAg@Rh hybrid structure

Our HR-TEM clearly shows that the AuAg NWs are completely covered by ultrafine anisotropic Rh nanoparticles, resulting in a core-shell like hybrid structure. This is a striking difference in behaviour compared to the use Pt and RhPt, in which the AuAg NWs perform a more sacrificial role due to galvanic replacement, while in this case heteroepitaxial growth occurs on the AuAg NW templates. The reproducibility of this synthesis is shown in Figure A15. The d spacing values were determined to be  $0.220 \pm 0.041$  nm and  $0.237 \pm 0.009$  nm which correspond to the 200 and 111 facet of FCC Rh respectively. UV-Vis analysis of this hybrid structure (Figure 5.12) shows that the distinct surface plasmon peaks of the AuAg template at 370 and 500 nm are completely lost upon formation of the new structure with only a broad absorbance profile been noted.

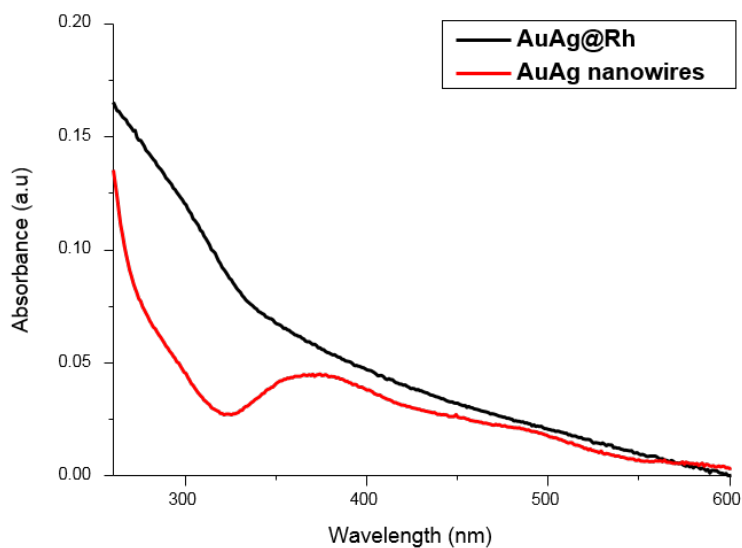


Figure 5.12: UV-Vis spectra of AuAg NWs and AuAg@Rh hybrid structure.

HAADF-STEM analysis (Figure 5.13) further highlights the presence of the Rh nanoparticles on the NW templates. The size of these nanoparticles was found to be on average 4.2 nm.

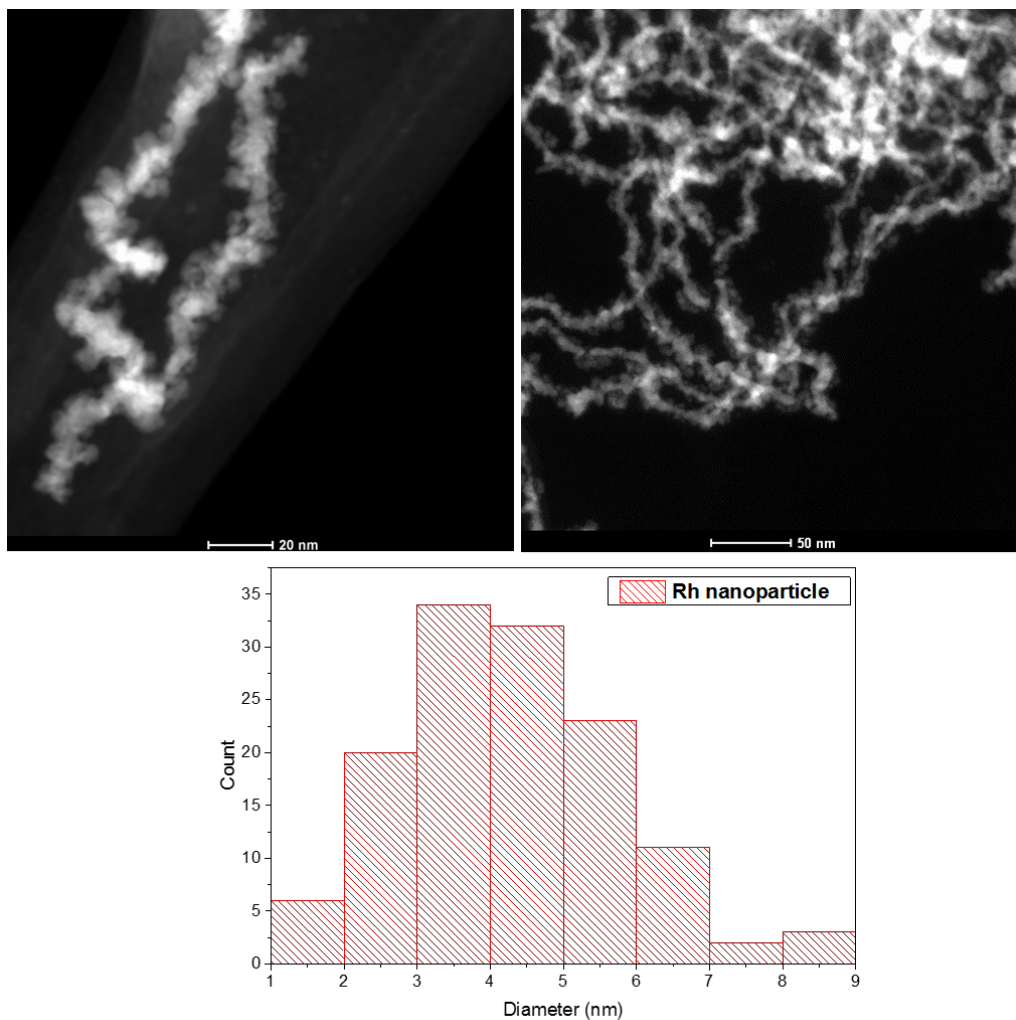


Figure 5.13: STEM images of AuAg@Rh hybrid nanostructure (top) and size distribution of Rh nanoparticles (bottom).

The crystallinity of our hybrid nanostructure was further investigated using XRD analysis (Figure 5.14)

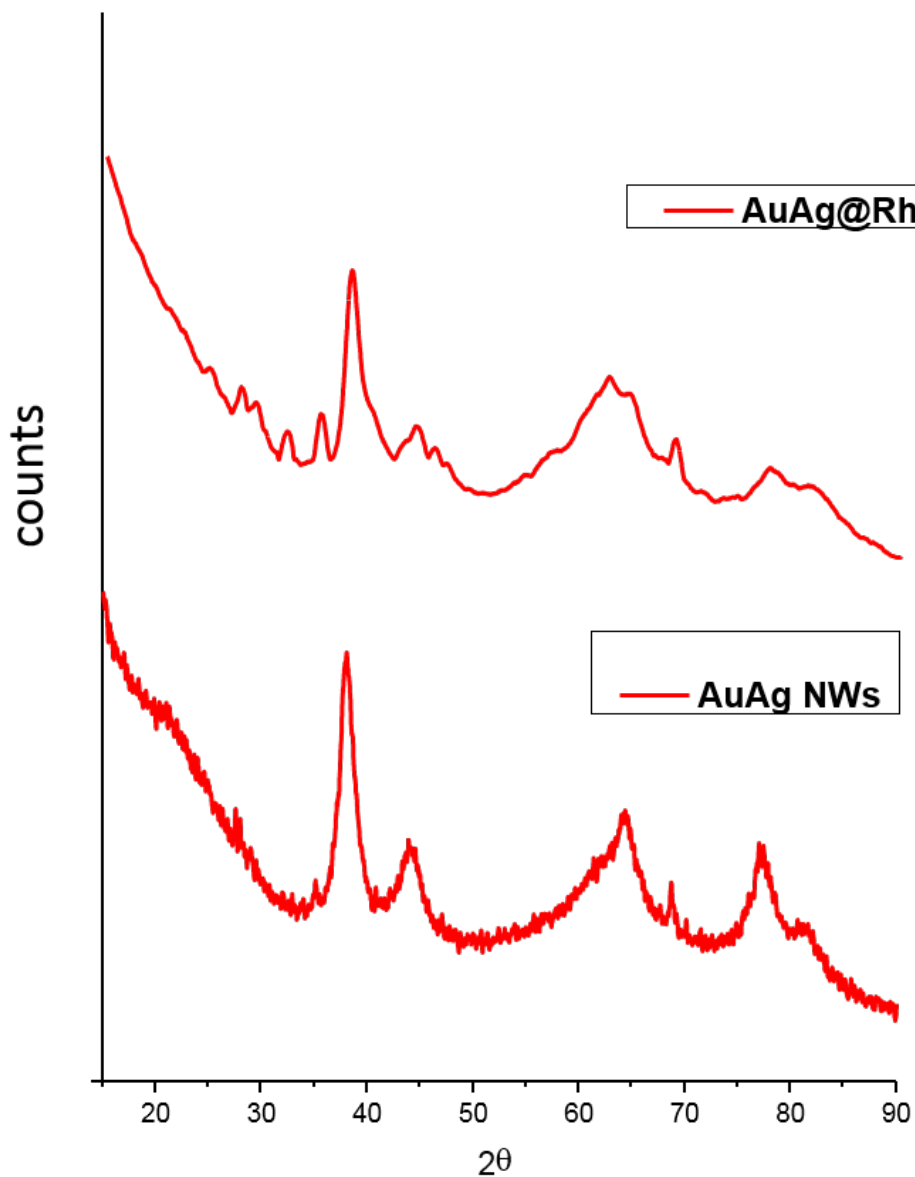


Figure 5.14: XRD analysis of AuAg NWs (bottom) and AuAg@Rh hybrid structure (top).

The XRD pattern of the AuAg NW@Rh hybrid shows  $2\theta$  values of 38, 44, 64, 77.5 and 81.2° corresponding to the (111), (200), (220), (311) and (222) planes respectively of the FCC AuAg NW template

and at 47 and 69° corresponding to the (200) and (220) planes of FCC Rh (01-071-4657).

HAADF-STEM EDX line map analysis (Figure 5.15) further confirms that the hybrid structure is composed of Au, Ag and Rh. The EDX spectrum (Figure 5.15C) shows the characteristic L and M peaks of Au at 9.7 and 2.1 KeV respectively, the L peak of Ag at 3.1 KeV and the K line of Rh at 20 KeV. The additional peaks present are due to the Cu from the TEM grids used for this analysis.

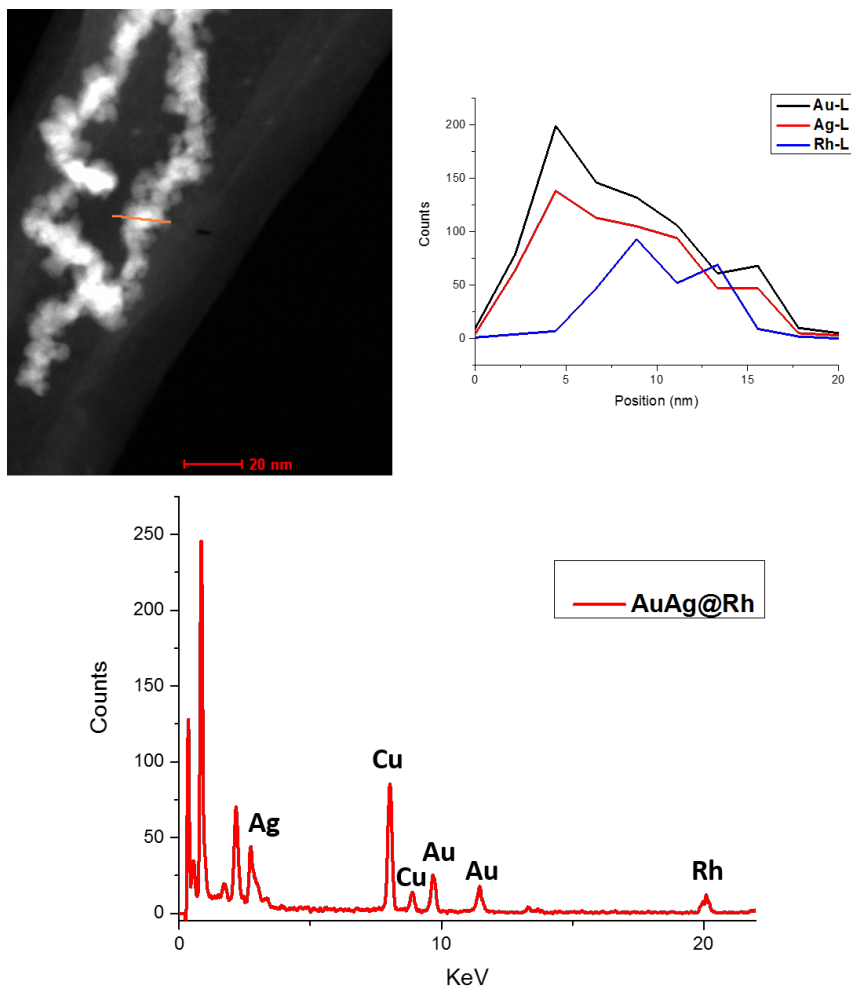


Figure 5.15: HAADF STEM image (A), EDX line profile (B) and EDX spectrum (C) of AuAg NWs@Rh hybrid structure.

## 5.6 Monitoring of AuAg@Rh hybrid formation

In order to understand formation of these core-shell hybrid structures we monitored the progress of the reaction by taking aliquot from the reaction mixture at various times intervals, following the addition of ascorbic acid, and prepared them instantly on lacy carbon TEM grids

for TEM analysis. The TEM analysis is detailed in Figure 5.16

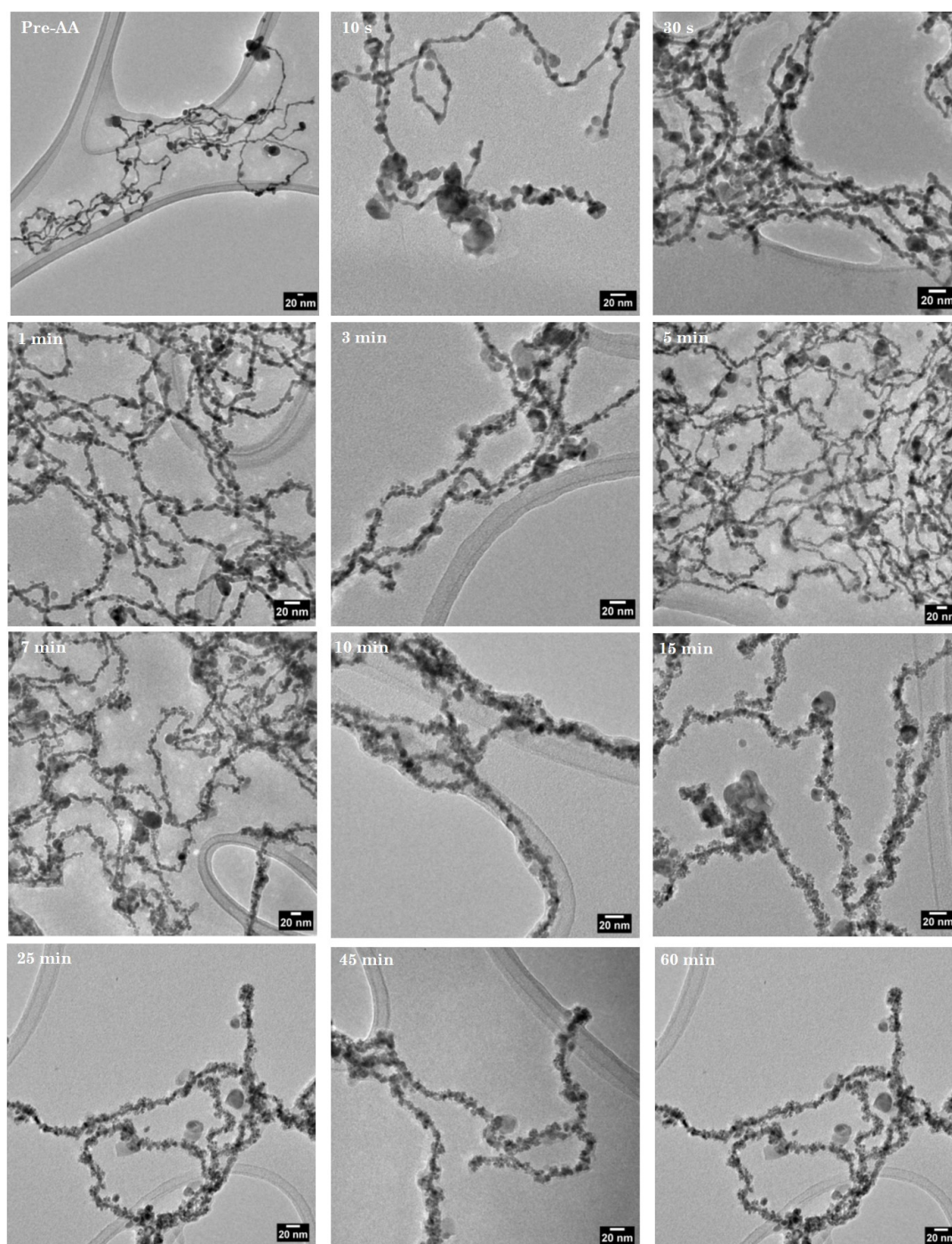


Figure 5.16: TEM images monitoring the growth of AuAg@Rh hybrid structure over time.



Our TEM analysis shows that prior to the addition of ascorbic acid only AuAg NW without Rh NPs are present. Within 10 s of the reaction we see the formation of Rh nanoparticles on the AuAg template. By 30 s an appreciable coverage of Rh nanoparticles was noted on some of the templates. The coverage of Rh gradually increases over the course of the reaction with a complete coverage noted after 25 mins. In addition to TEM, we also monitored the progress of the reaction by UV-Vis spectroscopy (Figure 5.17).

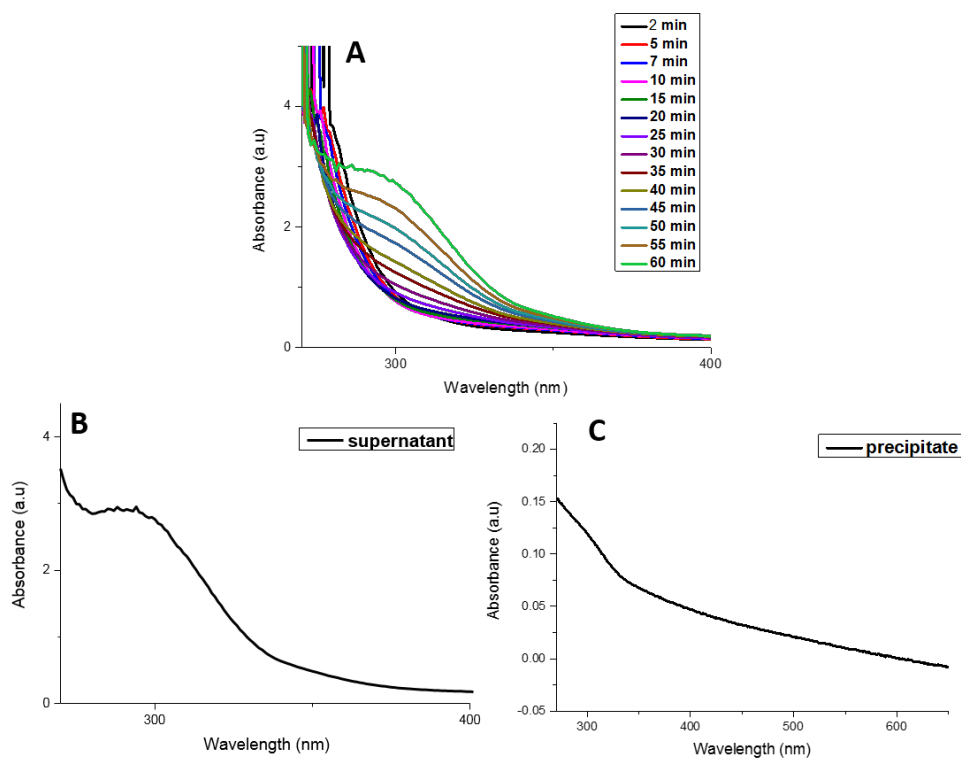


Figure 5.17: UV-Vis analysis monitoring the formation of AuAg@Rh hybrid structure over time (A) and UV-Vis spectra of the final supernatant (B) and purified precipitate (C).

Our UV-Vis analysis also shows a gradual change over the duration of the reaction with formation of a broad absorbance band at 290 nm. Comparison of the UV-Vis spectra from the purified sample (precipitate) and the supernatant, reveals that the peak from the time monitored study closely resembles the supernatant. TEM analysis (Figure 5.18) of the supernatant shows only Rh nanoparticles. Thus the gradual change in the absorbance spectra during the reaction is associated with the reduction of our Rh precursor and the growth of Rh nanoparticles. This mechanistic study shows that the initial deposition of Rh onto the AuAg NW occurs rapidly however the growth of the Rh nanoparticles and coverage of templates is gradual. This trend was similarly observed by Kang *et al.*<sup>34</sup> for the synthesis of Au nanoparticle @Rh sheet hybrid structures and for our RhPt dendritic NWs.

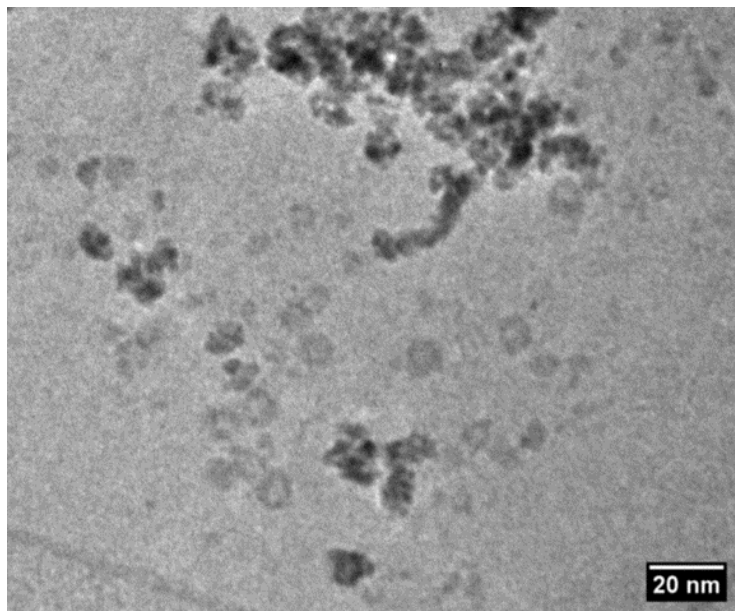


Figure 5.18: TEM image of supernatant from the time monitored study of AuAg@Rh formation.

## 5.7 Effect of Rh concentration on the template coverage

We next focused on controlling the coverage of Rh on the template NWs. Heterostructured nanomaterials which are composed of distinctly different morphologies, in our case 0D on a 1D nanomaterial, represent an interesting class of hybrid material with unique catalytic properties.<sup>35</sup> In recent years many researchers have focused on controlling various parameters such as the shape, size and relative position of each component of these nanomaterials in an attempt to improve their

catalytic performance.<sup>36,37</sup> In keeping with our work the most common method to producing these hybrid materials is through the use of templates, onto which another material(s) is grown or deposited. This has seen the use of a variety of different templates such as graphene,<sup>38-41</sup> metal oxides,<sup>42-44</sup> metal nanorods,<sup>45</sup> and NWs.<sup>46-48</sup> Recent work by Cai *et al.*<sup>49</sup> in particular demonstrated how the concentration of Au islands on Pd nanotubes has a significant influence on the catalytic performance for ethanol electro-oxidation. The authors highlight that this is due to the concentration of exposed heterojunctions between the Au and Pd and that an optimal concentration of these heterojunctions is required for the best performance. Thus we performed our study by using various Rh concentrations of; 0.68, 0.34, 0.17, 0.108, 0.085 and 0.068 mM in the reaction. TEM analysis of each sample is detailed in Figure 5.19.

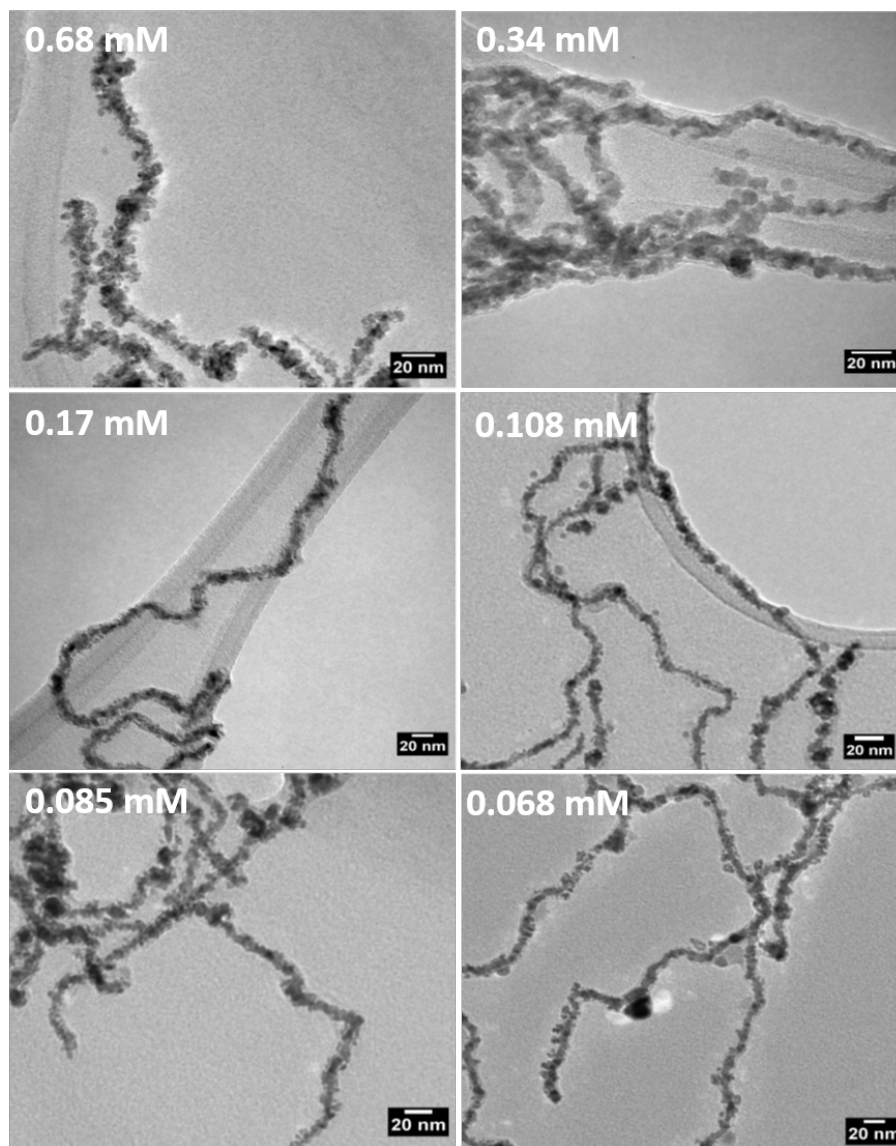


Figure 5.19: TEM analysis detailing the variation in Rh coverage on AuAg NWs with a change in Rh concentration

As expected, our TEM analysis shows that lowering the Rh concentration in the reaction effects the resulting coverage on the NW template. At 0.68 and 0.34 mM the resulting structure is a core-shell with Rh nanoparticles completely covering the templates. As the concentra-

tion is lowered, the Rh nanoparticles become notably more sparse along the AuAg NWs with a concentration of 0.068 mM showing the least coverage of Rh. We propose a scheme in Figure 5.20 to highlight this variation in coverage with a change in concentration. It must be noted however, that as the concentration of Rh is lowered, fewer templates become modified. Nevertheless we demonstrated that by varying the Rh concentration it is possible to tune the coverage on the NW template.

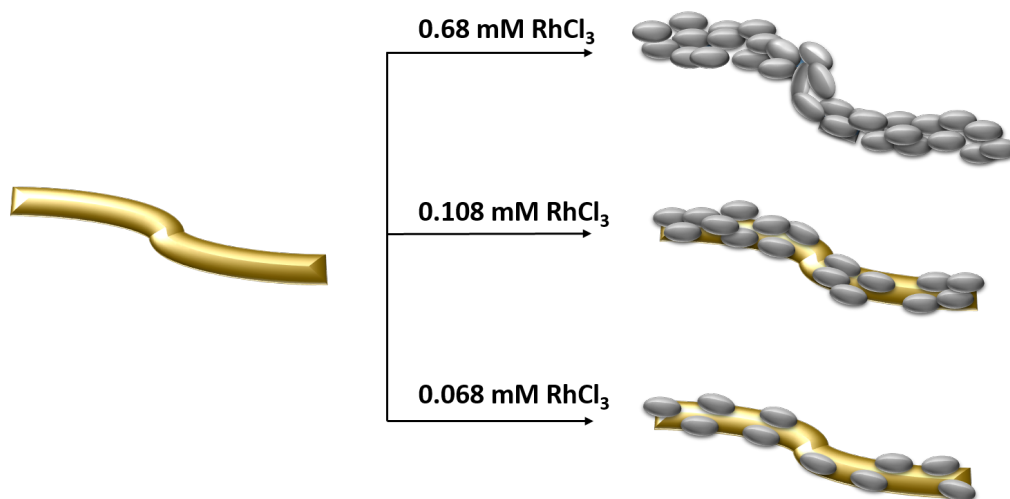


Figure 5.20: Reaction scheme detailing the change in coverage associated with a change in Rh concentration.

## 5.8 Tuning of Rh coverage by varying reaction time

We further focused on trying to control the coverage of Rh on the NW templates. In light of our time monitored study (section 5.6) which showed that the Rh deposition onto the NWs is a gradual process, we thus aimed at controlling the coverage of Rh by varying the reaction time. This would overcome the short coming of our concentration study (section 5.7) such that the yield of the more sparsely covered NWs would be greater. This study was carried out by using a Rh concentration of 0.68 mM and quenching the reaction with acetone. 2 separate reactions were performed and quenched after 3 and 12 min as our time monitored study revealed that these times produce distinct different Rh coverages. HR-TEM images of each sample is shown in Figure 5.21.

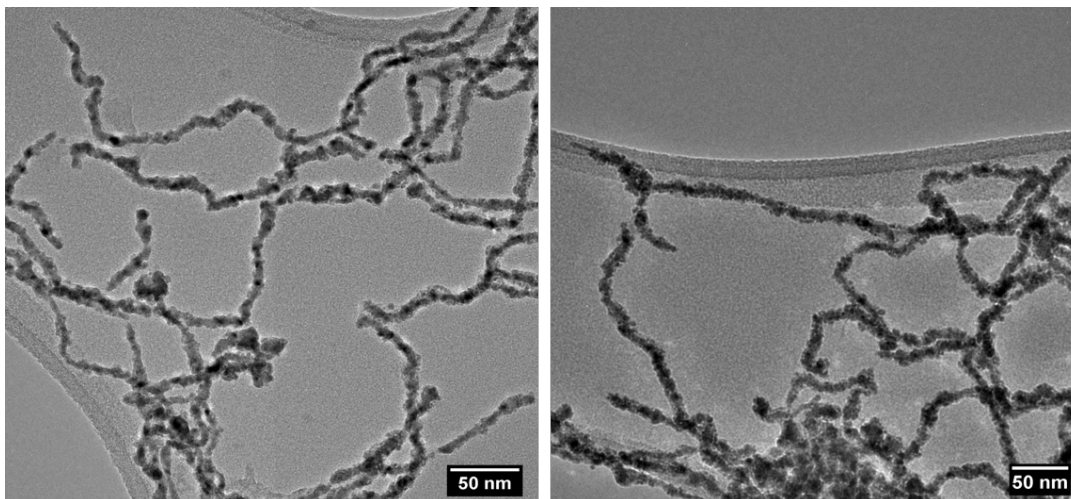


Figure 5.21: HR-TEM images of AuAg@Rh hybrids produced after 3 min (left) and 12 min (right).

The HR-TEM analysis shows a marked difference in the Rh coverage on the template NWs, with the 3 min reaction showing a more sparse coverage of Rh as expected. This was further emphasized using HAADF-STEM (Figure 5.22). In addition, a high yield of modified NW templates was also observed in both cases, further highlighting the effectiveness of this method.



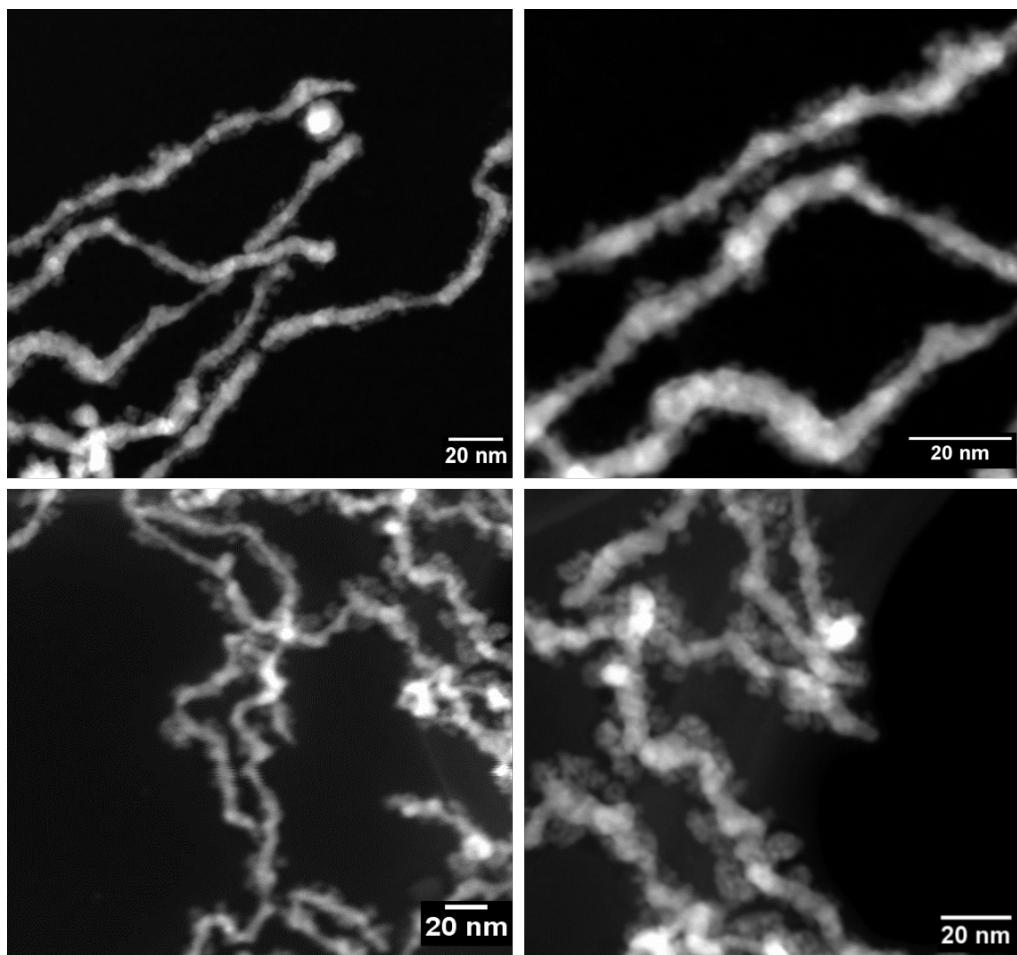


Figure 5.22: HAADF-STEM analysis of AuAg@Rh hybrids produced after 3 min (top) and 12 min (bottom).

Thus these results shows that it is possible to tune the coverage of Rh by simply varying the reaction time. It is expected that this tunability will have a significant impact on the catalytic properties of this hybrid material, due to the difference in exposed heterojunctions between deposited Rh nanoparticles and the NW template.<sup>49</sup>

## 5.9 Pt and RhPt dendritic nanowires as anodic catalysts for fuel cell applications

Direct fuel cells have long been recognised as promising candidates for providing clean and sustainable energy for the future. Methanol in particular has become a notable fuel of choice as it is relatively easy to transport and offers appreciable current densities.<sup>50</sup> The biggest drawback to the commercialization of these fuel cells however is the cost of the catalyst, which is commonly Pt based, and inefficiencies arising from catalytic poisoning.<sup>51</sup> These poisoning issues are significant with methanol fuel cells as in addition to CO adsorption, they also have a tendency to undergo crossover poisoning, in which methanol crosses over the polyelectrolyte membrane and poisons the cathode.<sup>52-54</sup>

In an attempt to mitigate this issue researchers have looked to using alternative fuels. To this end, formic acid stands as a promising alternative to methanol as in addition to low toxicity, it is also less susceptible to undergo fuel crossover poisoning and has shown fast oxidation kinetics.<sup>55,56</sup> It has been established that the electro-oxidation of formic acid occurs via a parallel dual pathway mechanism: a direct path, involving the dehydrogenation of adsorbed formate producing CO<sub>2</sub> resulting in no poisoning, and the indirect path whereby CO

poisons are generated following the oxidation of adsorbed intermediates.<sup>57–60</sup> Recently it has emerged that the indirect pathway is only a minor pathway and does not contribute significantly to the overall current.<sup>61,62</sup> while the exact mechanism of these pathways remains elusive, Cuesta *et al.*<sup>63</sup> have shown that adsorbed formate (COOH) plays a key role in both cases.

The choice of catalyst has the most significant influence in the electro-oxidation of the fuel thus catalyst design such as morphology and composition are of great importance.<sup>64–67</sup> Researchers have particularly focused on alloying as an amenable approach for not only reducing the cost of catalysts but also enhancing catalytic performance.<sup>68–71</sup> Yuan *et al.*<sup>72</sup> demonstrated that flower-like RhPt nanoparticle aggregates significantly out-perform Pt/C producing a negative shift of 110 mV for the peak potential of methanol. The authors further showed that a Pt:Rh ratio of 81:19 offered optimal performance in this case. In addition RhPt dendrites,<sup>27</sup> RhPt ultrathin NWs<sup>73</sup> and other alloys such as PtPd dendrites<sup>74</sup> and PtAg ultrathin NWs<sup>75</sup> have also showed remarkable catalytic performances by virtue of their morphologies and compositions. Herein we present for the first time the use of Pt and RhPt dendritic NWs as anodic catalyst for the electro-oxidation of methanol and formic acid.

### 5.9.1 Electro-oxidation of methanol

The electro-catalytic activities of our Pt and RhPt dendritic NWs were assessed by cyclic voltammetry (CV) in a 0.5 M perchloric acid solution containing 1 M methanol (Figure 5.23). For each electrochemical test a 4.9  $\mu\text{g}$  of loading of catalyst was used.

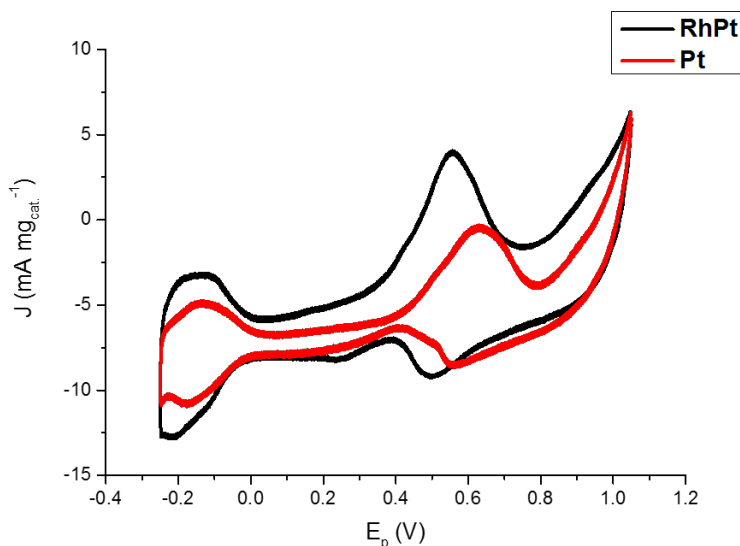
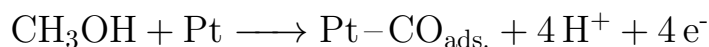


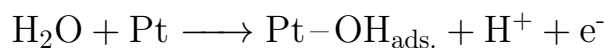
Figure 5.23: CV analysis of methanol oxidation at 50  $\text{mV s}^{-1}$  for Pt and RhPt dendritic NWs versus Ag/AgCl reference electrode in a 0.5 M perchloric acid solution containing 1M methanol.

As shown in Figure 5.23 the RhPt dendritic NWs produce current density 1.1 times greater than the Pt dendritic NWs. Furthermore the peak potential from the RhPt dendritic NWs is more negative (0.55 V) than the Pt dendritic NWs which have a peak potential at 0.63 V. These results highlight that alloying Rh with Pt enhances the

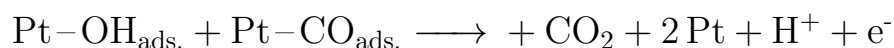
catalytic performance, most likely due to synergistic effects between the 2 metals in the alloy. In addition both these catalyst also exhibit 2 peaks. The peak in the forward scan is due to the oxidation of adsorbed methanol resulting in CO poisons on the surface of the catalysts, as described by the following equation.



As the potential is increased adsorbed OH species are formed on the surface of the catalyst;



In the reverse scan OH reduction occurs (on-set at 0.764 and 0.741 V for the Pt and RhPt dendritic NWs respectively) and the subsequent oxidation of the adsorbed CO species occurs as detailed in the equation below;



The larger the ratio of the forward peak ( $J_f$ ) to the reverse peak ( $J_b$ ) the greater the electrodes poison-resistance ability. In our case  $J_f/J_b$  ratio for the Pt and RhPt dendritic NWs was found to be 2.3 and 2.9 respectively which are considerably high poison resistances. The poison resistance was notably greater for the RhPt alloy as expected. While a "bifunctional mechanism" is typically used to describe the

enhanced performance for PtM alloys (M= Ru, Sn and Rh) particularly for methanol oxidation, Sheng and co workers<sup>76</sup> recently showed through DFT calculation that in the case of RhPt it is more complex. The authors showed that Rh may play a more active role in the initial C-H bond breaking in the case of methanol rather than just forming OH species. In comparison with other catalyst (Table 5.2) our dendritic NWs exhibit considerable catalytic performance.

Table 5.2: Electro-oxidation of methanol by various Pt based catalyst in acidic media.

Catalyst	$E_p$ (V)	$J_f/J_b$
Au/Pt dendritic NWs <sup>20</sup>	-0.10	1.25
Au/PtCu dendritic NWs <sup>20</sup>	-0.075	1.51
RhPt nanodendrites <sup>27</sup>	0.62	3.02
RhPt nanoparticles <sup>27</sup>	0.75	0.77
Pd <sub>75</sub> Pt <sub>25</sub> nanodendrites <sup>74</sup>	0.594	ca. 0.86
Pt <sub>3</sub> Co NWs <sup>77</sup>	0.8	0.88
Pt <sub>4</sub> Pb NWs <sup>70</sup>	0.68	1.09
Pt dendritic NWs (this work)	0.63	2.3
PtRh dendritic NWs (this work)	0.55	2.9

The mechanism for this electro-oxidation process was investigated by varying scan rate in our CV analysis. Scan rates of 35, 50, 75 and 90

$\text{mV s}^{-1}$  for a 0.5 M perchloric acid solution containing 1 M methanol (Figure 5.24).

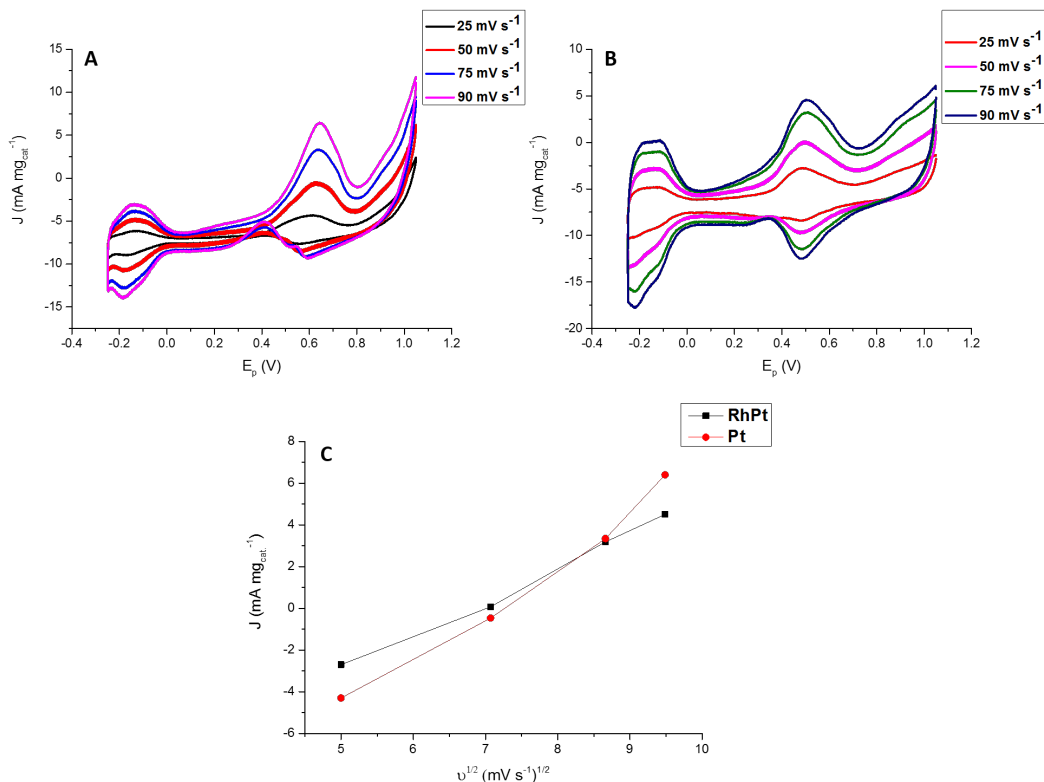


Figure 5.24: CV analysis at scan rates of 25, 50, 75 and 90  $\text{mV s}^{-1}$  for Pt(A) and RhPt dendritic (B) NWs versus Ag/AgCl reference electrode and corresponding plot of current density vs square root of scan rate (C) in a 0.5 M perchloric acid solution containing 1 M Methanol.

As shown in Figure 5.24 as the scan rate is increased the peak current densities also increase. Interestingly the Pt dendritic NWs also show a notable increase in the reverse peak at high scan rates (75 and 90  $\text{mV s}^{-1}$ ) while the RhPt catalyst shows only minor changes in the reverse peak for all scan rates. A plot of the peak current density

with respect to square root of the scan rate shows a linear relationship. This indicates that this reaction process is diffusion rate limited.

### 5.9.2 Electro oxidation of formic acid

Regarding formic acid oxidation, we assessed the electro-catalytic activities of our Pt and RhPt dendritic NWs by CV in a 1 M  $\text{H}_2\text{SO}_4$  solution containing 0.5 M formic acid (Figure 5.25). For each electrochemical test a  $4.9 \mu\text{g}$  loading of catalyst was used.

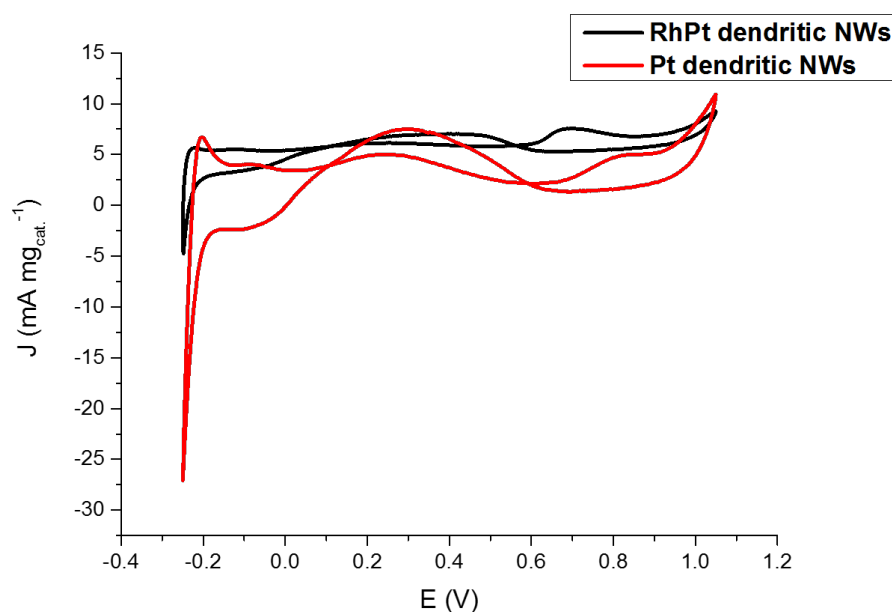
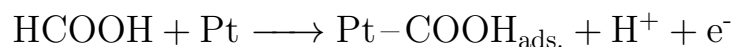


Figure 5.25: CV analysis of formic acid oxidation at  $50 \text{ mV s}^{-1}$  for Pt and RhPt dendritic NWs versus Ag/AgCl reference electrode in a 1 M  $\text{H}_2\text{SO}_4$  solution containing 0.5 M Formic acid.

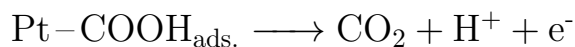
As shown in Figure 5.25 the RhPt dendritic NWs out perform the Pt



dendritic NWs producing a 1.53 times larger current density at more a negative peak potential ( $\Delta$  0.14 V). In addition, both these catalysts exhibit 2 peaks. Since the direct pathway has been recognised as the predominant pathway, it is generally accepted that the peak in the forward scan is due to the oxidation of absorbed formate.



The reduction of surface poisons in the reverse scan provides active sites for the complete oxidation formate to  $\text{CO}_2$  as described in the equation below.



The  $J_f/J_b$  ratio for the Pt and RhPt dendritic NWs was found to be 0.65 and 1 respectively. These results highlight the benefit of alloying on improving catalytic performance. Compared with other catalyst (Table 5.3) our dendritic NWs exhibit considerable catalytic performances.

Table 5.3: Electro-oxidation of formic acid by various Pt based catalyst in acidic media.

Catalyst	$E_p$ (V)	$J$ (mA cm <sup>-2</sup> )*
Rh nanochains <sup>78</sup>	0.42	0.55
Pt NWs <sup>79</sup>	0.7	1.75
Pt <sub>71</sub> Au <sub>29</sub> NWs <sup>79</sup>	0.58	1.2
Pt <sub>71</sub> Au <sub>29</sub> NWs <sup>79</sup>	0.68	0.9
Pd <sub>0.65</sub> Ag <sub>1</sub> /CNT <sup>80</sup>	<i>ca.</i> 0.37	2.16
PtAg Np <sup>75</sup>	0.92	0.6
Pd NWs <sup>81</sup> (2 nm)	0.64	2.4
Pt dendritic NWs (this work)	0.83	1.6
PtRh dendritic NWs (this work)	0.69	3.1

\*refer to appendix Figures A16-17 for ESCA CVs of Pt and RhPt dendritic NWs.

We further investigated the mechanism for this electro-oxidation process by varying scan rate in our CV analysis. Scan rates of 35, 50, 75 and 90 mV s<sup>-1</sup> were used as outlined in Figure 5.26 for a 1 M H<sub>2</sub>SO<sub>4</sub> solution containing 0.5 M formic acid.

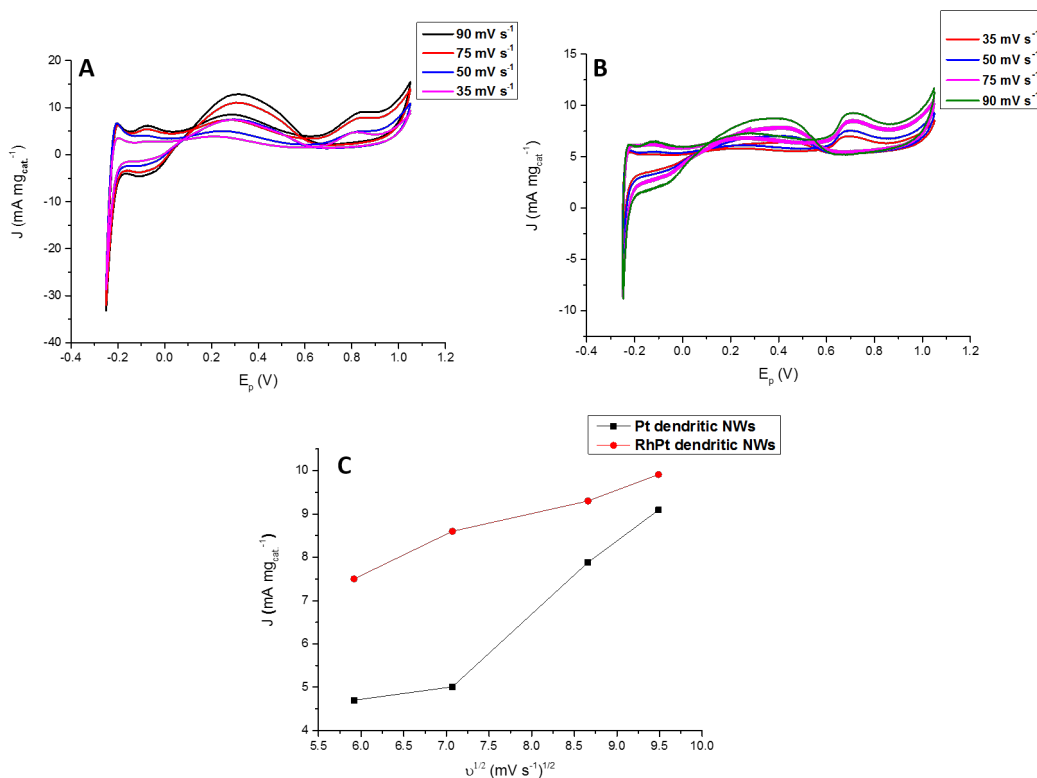


Figure 5.26: CV analysis at scan rates of 35, 50, 75 and 90 mV s<sup>-1</sup> for Pt(A) and RhPt dendritic (B) NWs versus Ag/AgCl reference electrode and corresponding plot of current density vs square root of scan rate (C) in a 1 M H<sub>2</sub>SO<sub>4</sub> solution containing 0.5 M formic acid.

As shown in Figure 5.26 as the scan rate is increased the peak current densities also increase. In the case of the Pt dendritic NWs there is a notable rise in the reverse peak at high scan rates (75 and 90 mV s<sup>-1</sup>) compared to the RhPt catalyst. A plot of the peak current density with respect to square root of the scan rate shows a linear relationship in both cases. This indicates that reaction process is again diffusion rate limited.

## 5.10 Conclusion and future work

In conclusion we demonstrated for the first time the use of ultrathin AuAg NWs as templates for the synthesis of novel 1D nanomaterials. Interestingly the AuAg NWs performed as sacrificial templates with Pt and RhPt producing dendritic NWs, while in the case of Rh, we observed hetero-epitaxial growth of Rh on the NWs resulting in a new AuAg NW@ Rh nanoparticle hybrid material. Using TEM analysis it was found that initial galvanic reaction for the synthesis of the RhPt dendritic NWs occurs rapidly, followed by the gradual increase in the thickness in the dendritic NWs. This was similarly observed in the synthesis of the AuAg NW@Rh hybrid, with deposition of Rh occurring rapidly on the NWs followed by the gradual increase in Rh coverage over the course of the reaction until a complete shell is formed. In addition we further demonstrated that in the absence of the templates no 1D nanomaterials are produced, thus confirming that the AuAg NWs are necessary in this synthesis. We further showed that the coverage of Rh on the NWs in our hybrid material can be tuned from a shell to being sparsely decorated by simply varying the reaction time.

Finally, we demonstrated that the Pt and RhPt dendritic NWs exhibit considerable catalytic performances for the electro oxidation of

methanol and formic acid. In both cases the RhPt dendritic NWs outperformed the Pt dendritic NWs producing higher current densities at lower potentials.

For our future work we to plan investigate the effect of using different templates such as our AuAg nano-necklaces (chapter 3 section 3.11) and thinner AuAg NWs (chapter 3, section 3.10) on the resulting morphology of the Pt and RhPt dendritic NWs. We also aim to extend this to the synthesis of additional AuAg@Rh hybrid nanomaterials. In addition we also plan to further tune the morphology of the dendritic NWs by exploring the use of different capping agents. Finally, we aim to investigate the electro-catalytic activity of the AuAg NW@ Rh hybrid nanomaterial for the electro oxidation of ethylene glycol. The focus of this work will be to study the effect of different Rh coverages on the catalytic performance of the material.

# References

- (1) Wang, J.; Gu, H. *Molecules* **2015**, *20*, 17070–17092.
- (2) Liu, X.; Wang, D.; Li, Y. *Nano Today* **2012**, *7*, 448–466.
- (3) Wang, A. X.; Kong, X. *Materials* **2015**, *8*, 3024–3052.
- (4) Bayrak, T.; Helmi, S.; Ye, J.; Kauert, D.; Kelling, J.; Schönherr, T.; Weichelt, R.; Erbe, A.; Seidel, R. *Nano Letters* **2018**, *18*, 2116–2123.
- (5) Hassanien, R.; Al-Said, S. A.; Šiller, L.; Little, R.; Wright, N. G.; Houlton, A.; Horrocks, B. R. *Nanotechnology* **2012**, *23*, 075601.
- (6) Maleak, N.; Potpattanapol, P.; Bao, N. N.; Ding, J.; Wongkokuo, W.; Tang, I. M.; Thongmee, S. *Journal of Magnetism and Magnetic Materials* **2014**, *354*, 262–266.
- (7) Cui, J.; Wu, Y.; Wang, Y.; Zheng, H.; Xu, G.; Zhang, X. *Applied Surface Science* **2012**, *258*, 5305–5311.
- (8) Chang, W. Y.; Wu, J. T.; Lin, K. H.; Yang, S. Y.; Lee, K. L.; Wei, P. K. *Microelectronic Engineering* **2011**, *88*, 909–913.

- (9) Wang, K.; Xi, D.; Zhou, C.; Shi, Z.; Xia, H.; Liu, G.; Qiao, G. *Journal of Materials Chemistry A* **2015**, *3*, 9415–9420.
- (10) Moon, G. D.; Ko, S.; Min, Y.; Zeng, J.; Xia, Y.; Jeong, U. *Nano Today* **2011**, *6*, 186–203.
- (11) Lu, C.; Kong, W.; Zhang, H.; Song, B.; Wang, Z. *Journal of Power Sources* **2015**, *296*, 102–108.
- (12) Cobley, C. M.; Xia, Y. *Materials Science and Engineering R: Reports* **2010**, *70*, 44–62.
- (13) Hai-Wei, L.; Shuo, L.; Jun-Yan, G.; Shang-Bing, W.; Lei, W.; Shu-Hong, Y. *Advanced Materials* **2009**, *21*, 1850–1854.
- (14) Hong, W.; Wang, J.; Wang, E. *Nano Research* **2015**, *8*, 2308–2316.
- (15) Hong, W.; Wang, J.; Wang, E. *Journal of Power Sources* **2014**, *272*, 940–945.
- (16) Ma, S. Y.; Li, H. H.; Hu, B. C.; Cheng, X.; Fu, Q. Q.; Yu, S. H. *Journal of the American Chemical Society* **2017**, *139*, 5890–5895.
- (17) Xiao, Y.; Lv, Q.; Zhu, J.; Yao, S.; Liu, C.; Xing, W. *RSC Advances* **2014**, *4*, 21176–21179.
- (18) Kim, Y.; Kim, H. J.; Kim, Y. S.; Choi, S. M.; Seo, M. H.; Kim, W. B. *Journal of Physical Chemistry C* **2012**, *116*, 18093–18100.

- (19) Chen, L.; Kuai, L.; Yu, X.; Li, W.; Geng, B. *Chemistry - A European Journal* **2013**, *19*, 11753–11758.
- (20) Hong, W.; Wang, J.; Wang, E. *Small* **2014**, *10*, 3262–3265.
- (21) Wang, L.; Chen, H.; Chen, M. *Materials Research Bulletin* **2014**, *53*, 185–189.
- (22) Luo, M.; Zhou, M.; Da Silva, R. R.; Tao, J.; Figueroa-Cosme, L.; Gilroy, K. D.; Peng, H. C.; He, Z.; Xia, Y. *ChemNanoMat* **2017**, *3*, 190–195.
- (23) Liu, J.; Xu, C.; Liu, C.; Wang, F.; Liu, H.; Ji, J.; Li, Z. *Electrochimica Acta* **2015**, *152*, 425–432.
- (24) Fu, Q.-Q.; Li, H.-H.; Ma, S.-Y.; Hu, B.-C.; Yu, S.-H. *Science China Materials* **2016**, *59*, 112–121.
- (25) Hei, H.; He, H.; Wang, R.; Liu, X.; Zhang, G. *Soft Nanoscience Letters* **2012**, *2*, 34–40.
- (26) Tu, W.; Hou, T.; Qi, K.; Chen, D.; Cao, S. *Colloids and Surfaces A: Physicochemical and Engineering Aspects* **2013**, *428*, 47–52.
- (27) Lee, Y. W.; Park, K. W. *Catalysis Communications* **2014**, *55*, 24–28.
- (28) Gacem, N.; Diao, P. *Colloids and Surfaces A: Physicochemical and Engineering Aspects* **2013**, *417*, 32–38.



- (29) García, S.; Anderson, R. M.; Celio, H.; Dahal, N.; Dolocan, A.; Zhou, J.; Humphrey, S. M. *Chemical Communications* **2013**, *49*, 4241–4243.
- (30) Jiao, J.; Liu, X.; He, H. *Materials Letters* **2014**, *131*, 336–339.
- (31) Óvári, L.; Berko, A.; Balázs, N.; Majzik, Z.; Kiss, J. *Langmuir* **2010**, *26*, 2167–2175.
- (32) Chantry, R. L.; Siritwacharapiboon, W.; Horswell, S. L.; Logsdail, A. J.; Johnston, R. L.; Li, Z. Y. *Journal of Physical Chemistry C* **2012**, *116*, 10312–10317.
- (33) Piccolo, L.; Li, Z. Y.; Demiroglu, I.; Moyon, F.; Konuspayeva, Z.; Berhault, G.; Afanasiev, P.; Lefebvre, W.; Yuan, J.; Johnston, R. L. *Scientific Reports* **2016**, *6*, 1–8.
- (34) Kang, Y.; Xue, Q.; Peng, R.; Jin, P.; Zeng, J.; Jiang, J.; Chen, Y. *NPG Asia Materials* **2017**, *9*, e407.
- (35) Sajanalal, P. R.; Sreeprasad, T. S.; Samal, A. K.; Pradeep, T. *Nano Reviews* **2011**, *2*, 5883.
- (36) Lutz, P. S.; Bae, I. T.; Maye, M. M. *Nanoscale* **2015**, *7*, 15748–15756.
- (37) Carbone, L.; Cozzoli, P. D. *Nano Today* **2010**, *5*, 449–493.
- (38) Wang, C.; Li, N.; Wang, Q.; Tang, Z. *Nanoscale Research Letters* **2016**, *11*, 0–6.
- (39) Zhu, C.; Dong, S. *Nanoscale* **2013**, *5*, 10765–10775.

- (40) Yang, S.; Shen, C.; Lu, X.; Tong, H.; Zhu, J.; Zhang, X.; Gao, H. J. *Electrochimica Acta* **2012**, *62*, 242–249.
- (41) Yang, S.; Zhang, F.; Gao, C.; Xia, J.; Lu, L.; Wang, Z. *Journal of Electroanalytical Chemistry* **2017**, *802*, 27–32.
- (42) Karuppasamy, L.; Chen, C. Y.; Anandan, S.; Wu, J. J. *Electrochimica Acta* **2017**, *246*, 75–88.
- (43) Hoseini, S. J.; Bahrami, M.; Roushani, M. *RSC Advances* **2014**, *4*, 46992–46999.
- (44) Xiang, Q.; Meng, G. F.; Zhao, H. B.; Zhang, Y.; Li, H.; Ma, W. J.; Xu, J. Q. *Journal of Physical Chemistry C* **2010**, *114*, 2049–2055.
- (45) Wu, B.; Liu, D.; Mubeen, S.; Chuong, T. T.; Moskovits, M.; Stucky, G. D. *Journal of the American Chemical Society* **2016**, *138*, 1114–1117.
- (46) Amdouni, S.; Cherifi, Y.; Coffinier, Y.; Addad, A.; Zaïbi, M. A.; Oueslati, M.; Boukherroub, R. *Materials Science in Semiconductor Processing* **2018**, *75*, 206–213.
- (47) Zhang, X.; Liu, Y.; Kang, Z. *ACS Applied Materials and Interfaces* **2014**, *6*, 4480–4489.
- (48) Lin, S. Y.; Chang, S. J.; Hsueh, T. J. *Applied Physics Letters* **2014**, *104*, 193704.

- (49) Cai, K.; Liao, Y.; Zhang, H.; Liu, J.; Lu, Z.; Huang, Z.; Chen, S.; Han, H. *ACS Applied Materials and Interfaces* **2016**, *8*, 12792–12797.
- (50) Aricò, A. S.; Srinivasan, S.; Antonucci, V. *Fuel Cells* **2001**, *1*, 133–161.
- (51) Zhao, X.; Yin, M.; Ma, L.; Liang, L.; Liu, C.; Liao, J.; Lu, T.; Xing, W. *Energy & Environmental Science* **2011**, *4*, 2736.
- (52) Tamaki, T.; Yamauchi, A.; Ito, T.; Ohashi, H.; Yamaguchi, T. *Fuel Cells* **2011**, *11*, 394–403.
- (53) Du, C. Y.; Zhao, T. S.; Yang, W. W. *Electrochimica Acta* **2007**, *52*, 5266–5271.
- (54) Jung, N.; Cho, Y. H.; Ahn, M.; Lim, J. W.; Kang, Y. S.; Chung, D. Y.; Kim, J.; Cho, Y. H.; Sung, Y. E. *International Journal of Hydrogen Energy* **2011**, *36*, 15731–15738.
- (55) Wang, X.; Hu, J. M.; Hsing, I. M. *Journal of Electroanalytical Chemistry* **2004**, *562*, 73–80.
- (56) Ha, S.; Larsen, R.; Zhu, Y.; Masel, R. I. *Fuel Cells* **2004**, *4*, 337–343.
- (57) Rice, C.; Ha, S.; Masel, R. I.; Waszczuk, P.; Wieckowski, A.; Barnard, T. *Journal of Power Sources* **2002**, *111*, 83–89.
- (58) Samjeské, G.; Osawa, M. *Angewandte Chemie - International Edition* **2005**, *44*, 5694–5698.

- (59) Samjeské, G.; Miki, A.; Ye, S.; Osawa, M. *The Journal of Physical Chemistry B* **2006**, *110*, 16559–16566.
- (60) Osawa, M.; Komatsu, K. I.; Samjeské, G.; Uchida, T.; Ikeshoji, T.; Cuesta, A.; Gutiérrez, C. *Angewandte Chemie - International Edition* **2011**, *50*, 1159–1163.
- (61) Xu, J.; Yuan, D.; Yang, F.; Mei, D.; Zhang, Z.; Chen, Y. X. *Physical Chemistry Chemical Physics* **2013**, *15*, 4367–4376.
- (62) Herrero, E.; Feliu, J. M. *Current Opinion in Electrochemistry* **2018**, *9*, 145–150.
- (63) Cuesta, A.; Cabello, G.; Osawa, M.; Gutiérrez, C. *ACS Catalysis* **2012**, *2*, 728–738.
- (64) Balan, B. K.; Sathe, B. R. *Journal of Nanoscience and Nanotechnology* **2012**, *12*, 8994–8998.
- (65) Pei, J.; Mao, J.; Liang, X.; Zhuang, Z.; Chen, C.; Peng, Q.; Wang, D.; Li, Y. *ACS Sustainable Chemistry and Engineering* **2018**, *6*, 77–81.
- (66) Liu, D.; Xie, M.; Wang, C.; Liao, L.; Qiu, L.; Ma, J.; Huang, H.; Long, R.; Jiang, J.; Xiong, Y. *Nano Research* **2016**, *9*, 1590–1599.
- (67) Lai, J.; Luque, R.; Xu, G. *ChemCatChem* **2015**, *7*, 3206–3228.
- (68) Scofield, M. E.; Koenigsmann, C.; Wang, L.; Liu, H.; Wong, S. S. *Energy and Environmental Science* **2015**, *8*, 350–363.

- (69) Hu, S.; Munoz, F.; Noborikawa, J.; Haan, J.; Scudiero, L.; Ha, S. *Applied Catalysis B: Environmental* **2016**, *180*, 758–765.
- (70) Huang, L.; Han, Y.; Zhang, X.; Fang, Y.; Dong, S. *Nanoscale* **2017**, *9*, 201–207.
- (71) Xiao, M.; Feng, L.; Zhu, J.; Liu, C.; Xing, W. *Nanoscale* **2015**, *7*, 9467–9471.
- (72) Yuan, Q.; Wang, H.-h.; Zhou, Z.-y. **2014**.
- (73) Yuan, Q.; Zhou, Z.; Zhuang, J.; Wang, X. *Chemistry of Materials* **2010**, *22*, 2395–2402.
- (74) Wu, H.; Mei, S.; Cao, X.; Zheng, J.; Lin, M.; Tang, J.; Ren, F.; Du, Y.; Pan, Y.; Gu, H. *Nanotechnology* **2014**, *25*, 195702.
- (75) Jiang, X.; Fu, G.; Wu, X.; Liu, Y.; Zhang, M.; Sun, D.; Xu, L.; Tang, Y. *Nano Research* **2018**, *11*, 499–510.
- (76) Sheng, T.; Sun, S. G. *Journal of Electroanalytical Chemistry* **2016**, *781*, 24–29.
- (77) Liu, L.; Pippel, E.; Scholz, R.; Gosele, U. *Nano Letters* **2009**, 6876–6877.
- (78) Sathe, B. R.; Balan, B. K.; Pillai, V. K. *Energy and Environmental Science* **2011**, *4*, 1029–1036.
- (79) Han, Y.; Ouyang, Y.; Xie, Z.; Chen, J.; Chang, F.; Yu, G. *Journal of Materials Science and Technology* **2016**, *32*, 639–645.

- 
- (80) Huang, L.; Yang, J.; Wu, M.; Shi, Z.; Lin, Z.; Kang, X.; Chen, S. *Journal of Power Sources* **2018**, *398*, 201–208.
- (81) Wang, Y.; Choi, S. I.; Zhao, X.; Xie, S.; Peng, H. C.; Chi, M.; Huang, C. Z.; Xia, Y. *Advanced Functional Materials* **2014**, *24*, 131–139.

# Chapter 6

## Chiral anisotropic nanostructures

### 6.1 Introduction

Self-assemblies of chiral nanomaterials have deserved particular attention over last years opening new approaches to hierarchical chiral structures.<sup>1-4</sup> For example, Kotov and co-workers have recently reported assembly of D- and L-cysteine-stabilized cadmium telluride nanoparticles (CdTe NPs) in mesoscale helices with near-unity enantiomeric excess.<sup>5</sup> The same group has previously published papers on the formation CdTe/CdS twisted ribbons formed under illumination by circularly polarized light,<sup>6</sup> biomimetic assembly of chiral nanoparticles into helical supraparticles<sup>3</sup> and self-organization of plasmonic and excitonic nanoparticles into resonant chiral supraparticle assemblies.<sup>4</sup> In particular, there was a significant progress in the investigation of self-assemblies of chiral plasmonic nanostructures.<sup>2,7-11</sup> There are also

reports of different groups on various helical structured semiconducting nanomaterials forming racemic mixtures including CdS,<sup>12,13</sup> ZnO,<sup>14</sup> ZnS,<sup>15</sup> InP<sup>16</sup> and InGaAs/GaAs.<sup>17</sup>

The use of stirring or mechanical vortex flow is another promising approach of achieving symmetry breaking in achiral species and this is an area gaining increasing interest.<sup>18–20</sup> In fluid dynamics, vortex is a region within a fluid where the flow mostly spins around an imaginary axis either straight or curved.<sup>21,22</sup> Vortex and stirring induced chirality has been established and reported for several organic achiral molecular and supramolecular systems such as ionic oligomers,<sup>23</sup> polymers,<sup>24</sup> proteins,<sup>25,26</sup> liquid crystals,<sup>27,28</sup> and for the self-assemblies of supramolecular aggregates.<sup>23,28–36</sup> However, the use of stirring and vortexing for the preparation of chiral inorganic nanomaterials has not yet been explored in detail and there are only a couple of literature reports in this field. For example, chiral nanofibers from graphene oxide, MoS<sub>2</sub>, TiS<sub>2</sub>, TaS<sub>2</sub>, TaSe<sub>2</sub>, WSe<sub>2</sub>, Pt-MoS<sub>2</sub>, Pt-rGO have been produced by vigorous stirring of solution of the corresponding ultrathin 2D Nanomaterials in the presence of carbon nanotubes or AuAg nanowires using an achiral triblock copolymer (PEO<sub>20</sub>PPO<sub>70</sub>PEO<sub>20</sub>)-assisted self-assembly process.<sup>37</sup> It was also shown that the produced chiral nanofibers can be further transformed to same-handed chiral nanorings. Clockwise and counter-clockwise vortexing has also been used to tune the chirality of



graphene oxide and transfer a handedness to achiral hosts molecules (tetrakis(4-N-methyl pyridyl)porphyrins).<sup>38</sup> Finally, using directional solvent evaporation from Mn-Doped ZnSe Nanorods vortex patterning of semiconducting nanorods was realised.<sup>22</sup> It has also been demonstrated that rotating vortex flows can be used to achieve chiral separation at the micro- and nanoscales.<sup>19,39</sup>

Anisotropic plasmonic-excitonic hybrid nanomaterials which are composed of metal and semiconductor nanocomponents present particular interest due to their unique properties and range of their potential applications.<sup>40,41</sup> However, the preparation of anisotropic chiral hybrid nanomaterials is particularly challenging. One of the current advanced approaches for the preparation of chiral hybrid nanostructures is low-temperature shadow deposition with nanoscale patterning developed by P. Fischer and co-workers.<sup>42,43</sup> Nevertheless, this technique is highly technically demanding and hard to scale up.

The main aim of this part of the project was to investigate the effects of vortex induced optical activity on ultra-long Ag nanowires (NWs). Ultra-long NWs were chosen for this study as preliminary work done in our research group, demonstrated that large aspect ratio Ag NWs exhibited chiroptical activity when stirred. Here we report SEM and various spectroscopy used to try understand this phenomenon. This

work was further used to explore the use of vortexing for the controlled synthesis of chiral structures, from which novel chiral Ag NW @quantum dot hybrid structures were produced.

## 6.2 Synthesis and characterisation of ultra-long Ag Nanowires

The Ag NWs used for this work were synthesised using the polyol method developed by Jui *et al.*<sup>44</sup> Briefly, AgNO<sub>3</sub> was reduced in ethylene glycol at 130 °C for 5 hours in the presence of FeCl<sub>3</sub> and PVP. The NWs were characterised by SEM and UV-Vis spectroscopy as detailed in Figure 6.1 below.

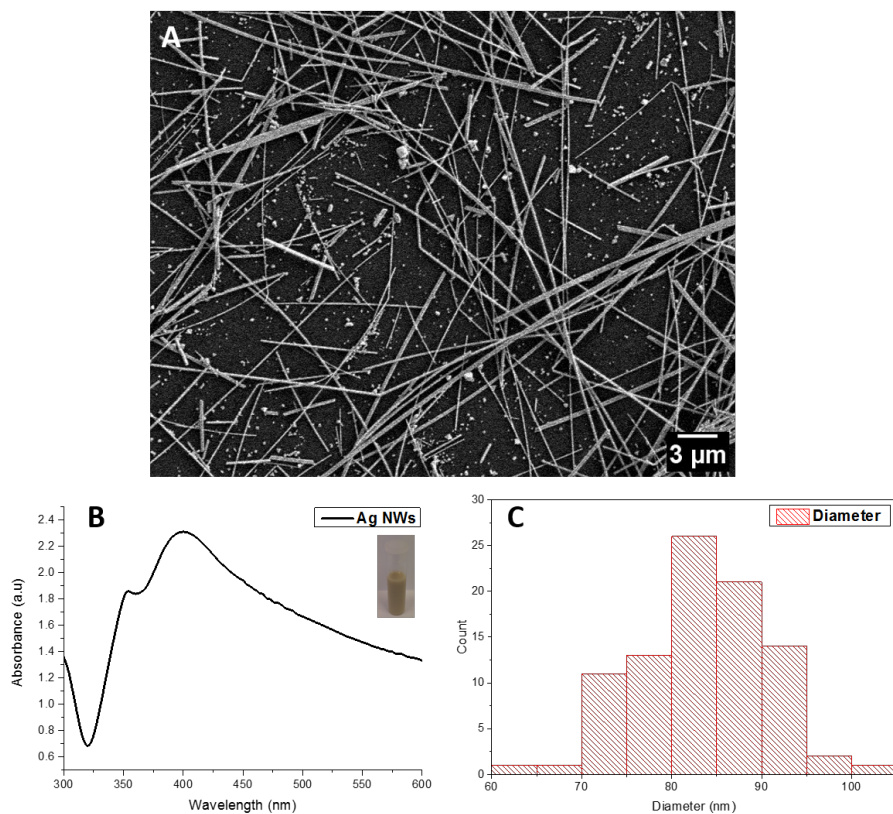


Figure 6.1: SEM image (A), UV-vis spectrum (B) with photograph of solution in-set and size distribution (C) of Ag NWs.

SEM analysis shows Ag NWs with an average diameter of 83.4 nm and ranging up to several microns in length. The UV-Vis spectrum shows a typical absorbance profile for Ag NWs with a peak at 400 and 350 nm, which correspond to the transverse surface plasmon and bulk Ag peak respectively.<sup>45–47</sup> The longitudinal plasmon peak which occurs at 500 nm is absent due to the large aspect ratio of these NWs.<sup>48</sup>

### 6.2.1 Effect of stirring orientation on induced chirality

As mentioned earlier the stirring direction has a major role in defining the resulting chirality expressed by the NWs. For the purpose of our studies all analysis was done using 20 mm diameter sample tubes as vessels, 141 mm magnetic stirring bar, a stirring speed of 960 rpm and the same stirring mantle (a sigma Aldrich S46). In the case of CW stirred Ag NWs a modified magnetic stirring mantle was used under the same conditions. CD analysis of CW and ACW stirred Ag NWs are shown in Figure 6.2 .

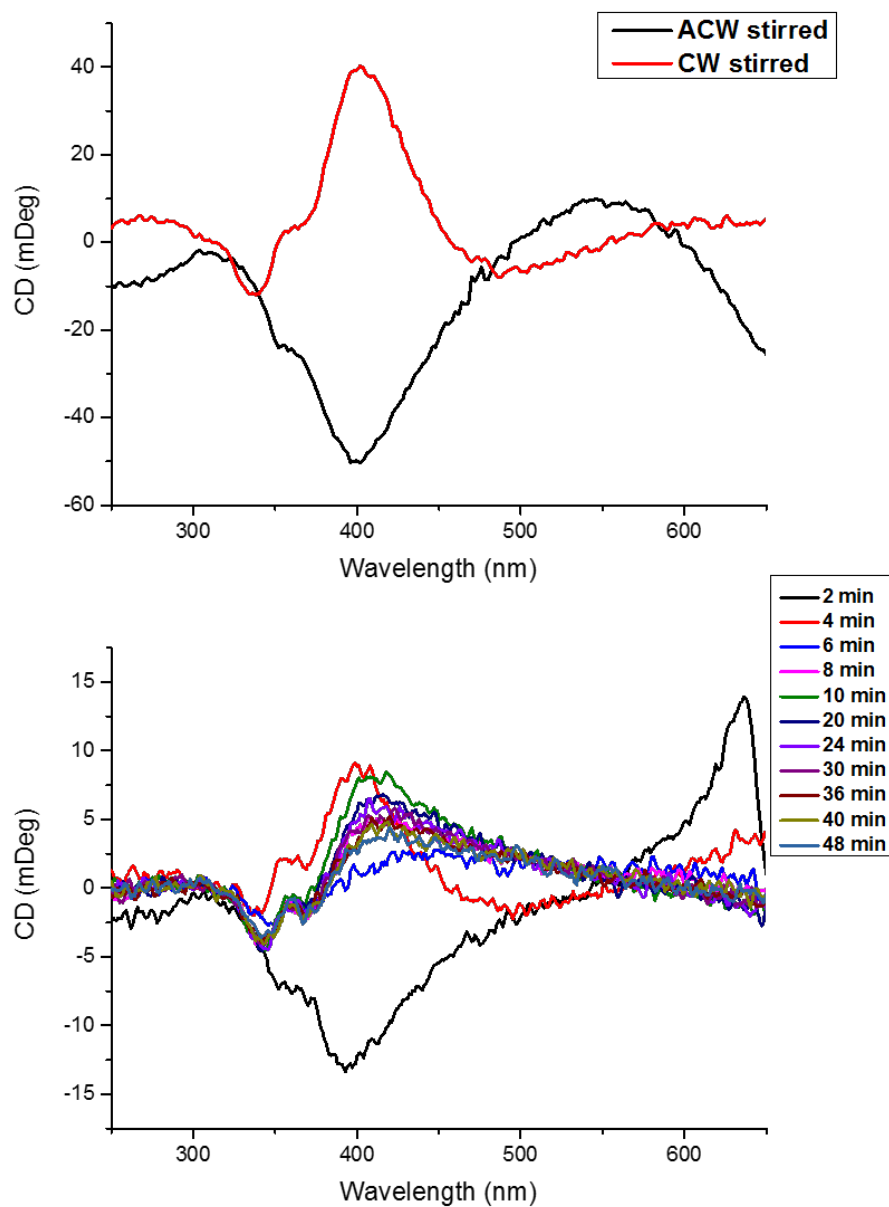


Figure 6.2: CD spectra of CW and ACW stirred Ag NWs (top). Time monitored CD spectra of Ag NWs (bottom) showing the change in chiroptical activity following 10 mins of ACW stirring.

The CD analysis above (Figure 6.2, top) shows enantiomeric signals of equal and opposite sign for the CW and ACW stirred NWs in

the plasmonic region of the NWs. The ACW stirred NWs showed a trend to produce (-) CD signals while CW stirred NWs tended to show (+) signals. This stirring induced optical activity compliments the extensive work carried out by Ribo *et al.*<sup>23,36,49,50</sup> with J aggregates. However the exact origin of this optical activity remains in question, with many reports in the field stating that this observed CD signal is an artifact arising from the partial alignment, in our case of the NWs, with the vortex which is intrinsically chiral, resulting in a macroscopic chiral arrangement.<sup>51-54</sup> Our time monitored CD study (Figure 6.2, bottom) of a solution of Ag NWs following 10 minutes of ACW stirring, further highlights how the observed CD signal for these NWs fluctuates and changes orientation over time when the system is no longer stirring. This further indicates that the observed chiroptical activity may be due to alignment artefacts. It must be noted that the change in sign of the CD signal was commonly observed in this study. Nevertheless hydrodynamic forces have been shown to induce chiral deformation.<sup>37,55-57</sup> In our case however, SEM analysis showed no physical change or chiral deformation such as helices in the NWs (Figure 6.3).

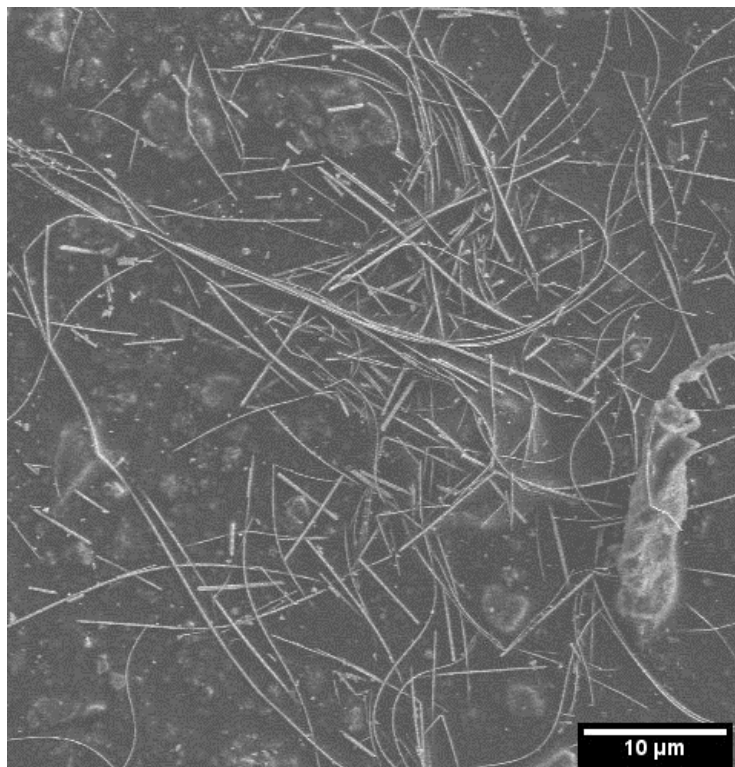


Figure 6.3: SEM image of ACW stirred Ag NWs.

We explored this further by drying a concentrated aliquot of the Ag NWs while continuously stirring them on a glass slide. SEM analysis (Figure 6.4) again showed no chiral deformations however in this case the NWs showed a very distinct alignment (ie. NWs orientated in same direction) due to the stirring. In light of this we propose that the observed chiroptical activity is most likely due to the specific orientation and alignment of the NWs with the vortex.<sup>51,54</sup> Nevertheless we demonstrated for the first time, vortex induced optical activity with metallic NWs.

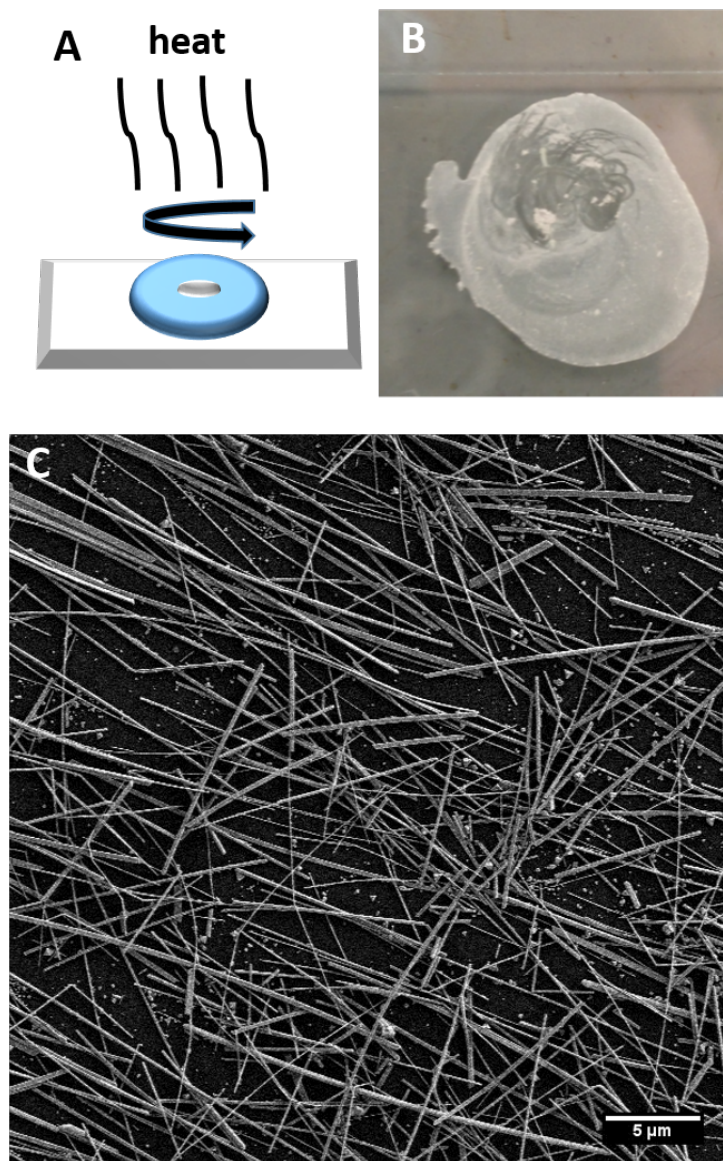


Figure 6.4: Experimental set up (A), photograph of the dried sample (B) and SEM image (C) of Ag NWs dried on a glass slide while continuously stirring ACW.



### 6.2.2 CD analysis of aligned Ag nanowires

In order to investigate the origin of the chiroptical activity further alignment studies were performed. These studies were carried out in collaboration with Dr. John Gough (School of Physics TCD). The Ag NWs in solution were aligned on a quartz substrate using a three-phase interface method. The method allows for the spontaneous alignment of aqueous Ag NWs in an oil-water-air interface. Aligned and unaligned NWs are presented in Figure 6.5.

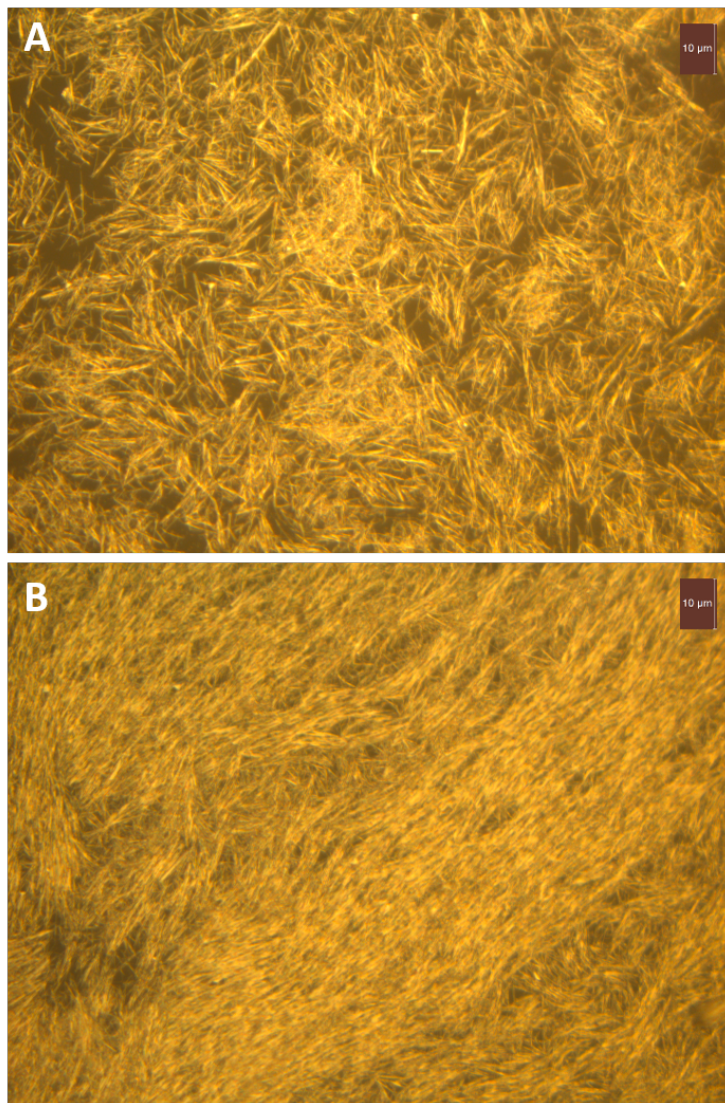


Figure 6.5: Unaligned (A) and aligned (B) Ag NWs on a quartz substrate viewed through a X50 microscope.

The chiroptical activity of the aligned NWs was then assessed by using a linear polariser in combination with a quarter-wave plate to convert the light incident on the sample to circularly polarised light. Measurements of the CD response to both right and left circularly polarised

light were recorded (Figure 6.6).

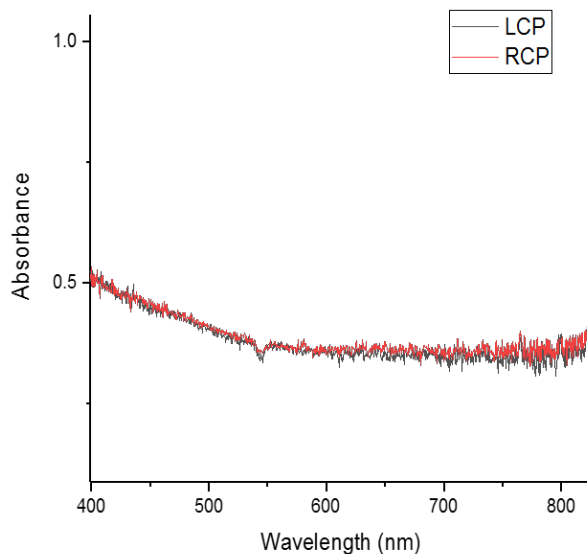


Figure 6.6: CD response of the aligned Ag NWs on a quartz substrate to left and right circularly polarised light.

As shown in Figure 6.6 there is no difference in the absorption of left and right circularly polarised light for the aligned Ag NWs. Since there is no chirality associated with these structures, and the region measured was perfectly aligned, it was expected that there would be no optical activity. This result confirms that the chiroptical activity observed for these NWs is due to the orientation and motion in the intrinsically chiral vortex rather than chiral deformation of the Ag NWs.

## 6.3 Vortex assisted synthesis of Ag NW @ quantum dot hybrid structures

Plasmonic-excitonic hybrid structures made of Ag NWs (83.4 nm in diameter and several  $\mu\text{m}$  in length) and semiconducting CdSe/CdS quantum dots were produced by taking advantage of the self-assembly of nanoparticles.<sup>3,58,59</sup> For our studies CdSe/CdS quantum dots with; nano nail and dot in rod structures, capped with cysteine (Cys) or thioglycolic acid (TGA) were investigated. Solvent influences on these capping agents bearing carboxylic acids and/or amino groups have been demonstrated to enhance interparticle attractive forces and are rapidly been employed as a effective method to achieve complex heirical assemblies.<sup>60-62</sup> Herein we present the synthesis of Ag NW@ nano-nail and Ag NW@ Dot n rods hybrid structures.

### 6.3.1 Synthesis and chracterisation of Ag NW @ nano-nail hybrid structure

Nano-nail QDs were chosen for this study due to their luminescent properties and unique anisotropic structure.<sup>63</sup> These QD were synthesised and characterised by Dr. Finn Purcell-Milton in our group. Figure 6.7 shows TEM images, size distribution analysis and emission

spectrum for the nano-nail QDs. The full length, base length and base width of these nano-nails are 65.9, 11.9 and 5.4 nm respectively and they emit at 612 nm.

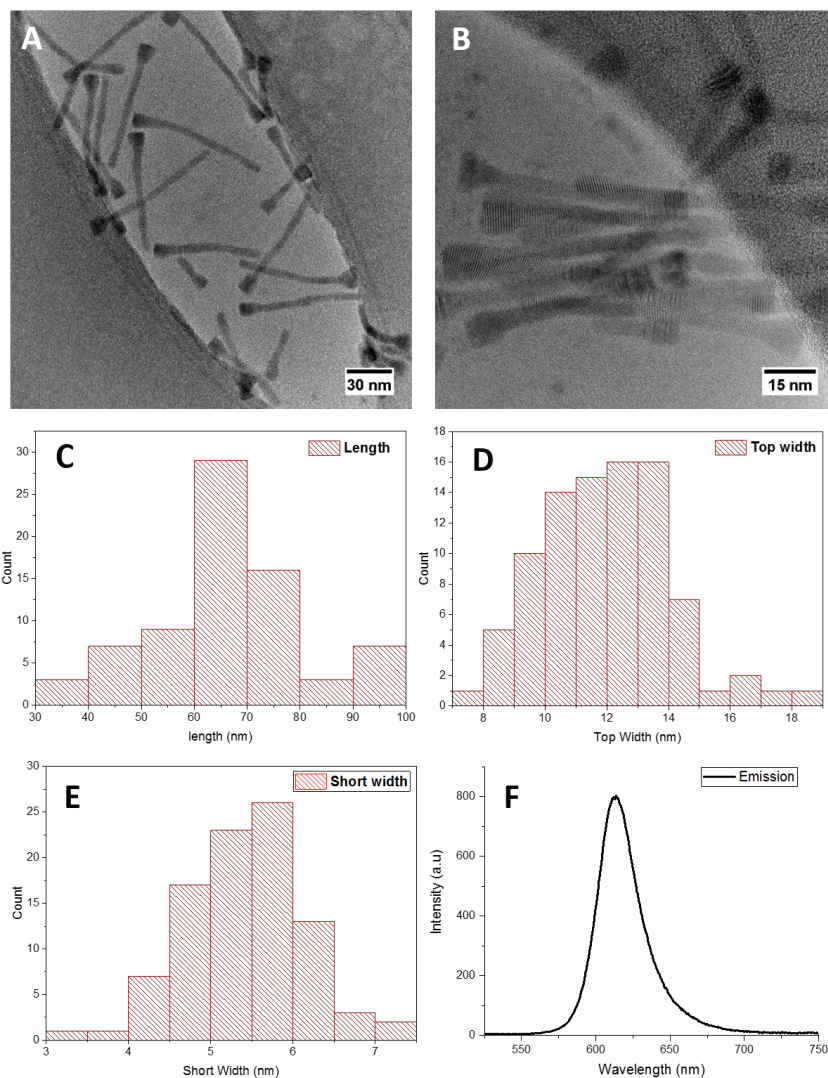


Figure 6.7: TEM images (A and B), size distributions (C-E) and emission spectrum (F) of CdSe/CdS nano-nails.

Since the nano-nails are made in an organic phase a phase transfer was required to make them miscible in water/ethanol. This phase transfer process was performed in collaboration with Vera Kuznetsova ( Ph.D candidate) in our group, using either Cys or TGA as the phase transfer agent. Figure 6.8 details the chiroptical activity induced in the nano-nails following phase transfer using Cys ligand.

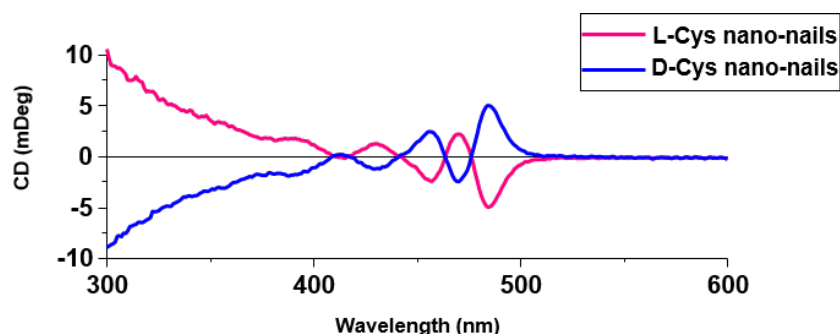


Figure 6.8: CD spectra of L- and D- capped CdSe/CdS nano-nails.

Using a simple method, Ag NWs were mixed with a racemic solution (made by mixing L- and D- Cys capped nano-nails) of QDs (in excess), in ethanol under strong magnetic stirring ( 960 rpm) for 10 mins and allowed to age over an 8 day period at 4 °C. SEM (Figure 6.9) of the resulting structure revealed that the nano-nails form a helical self-assembly along the length of the Ag NWs.

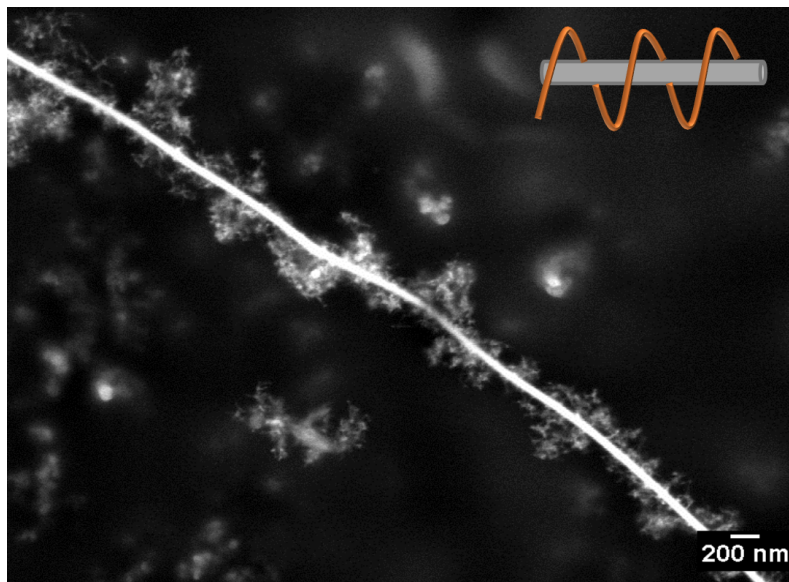


Figure 6.9: SEM image of hybrid structure after 8 days of aging using a racemic solution of cys capped nano-nails.

Interestingly all of the Ag NWs showed an appreciable coverage of helices. The pitch of the helices varied from NW to NW and along the length of the NWs. A survey of these structures further revealed that helices are a racemic mixture (Figure 6.10), ie. No preferential left or right handedness. This stands in good agreement with the work which was recently reported by Kotov *et al.*<sup>3,5</sup>.



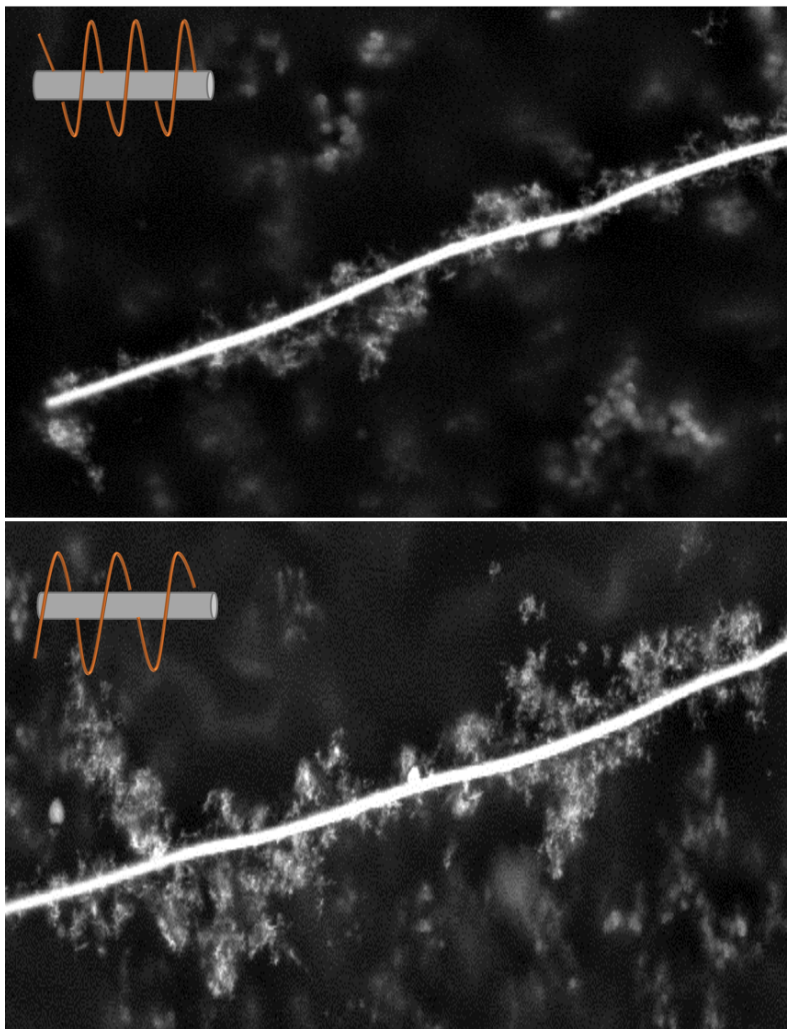


Figure 6.10: SEM images showing left (top) and right (bottom) handed helices after 8 days of aging using a racemic solution of Cys capped nano-nails.

Scanning transmission electron microscopy (STEM) analysis, Figure 6.11 further shows that the nano-nails densely packed side-by-side particularly when close to the NW surface. This is a common packing arrangement adopted by similar shaped 1D nanostructures, and is an energetically efficient confirmation.<sup>64</sup> EDX analysis (Figure 6.11) fur-



ther confirms that the composition of the hybrid structure contains Cd, S and Ag. The Se component of the nano-nails was not detected mostly like due to the very small amount of this element present in the nano-nails.

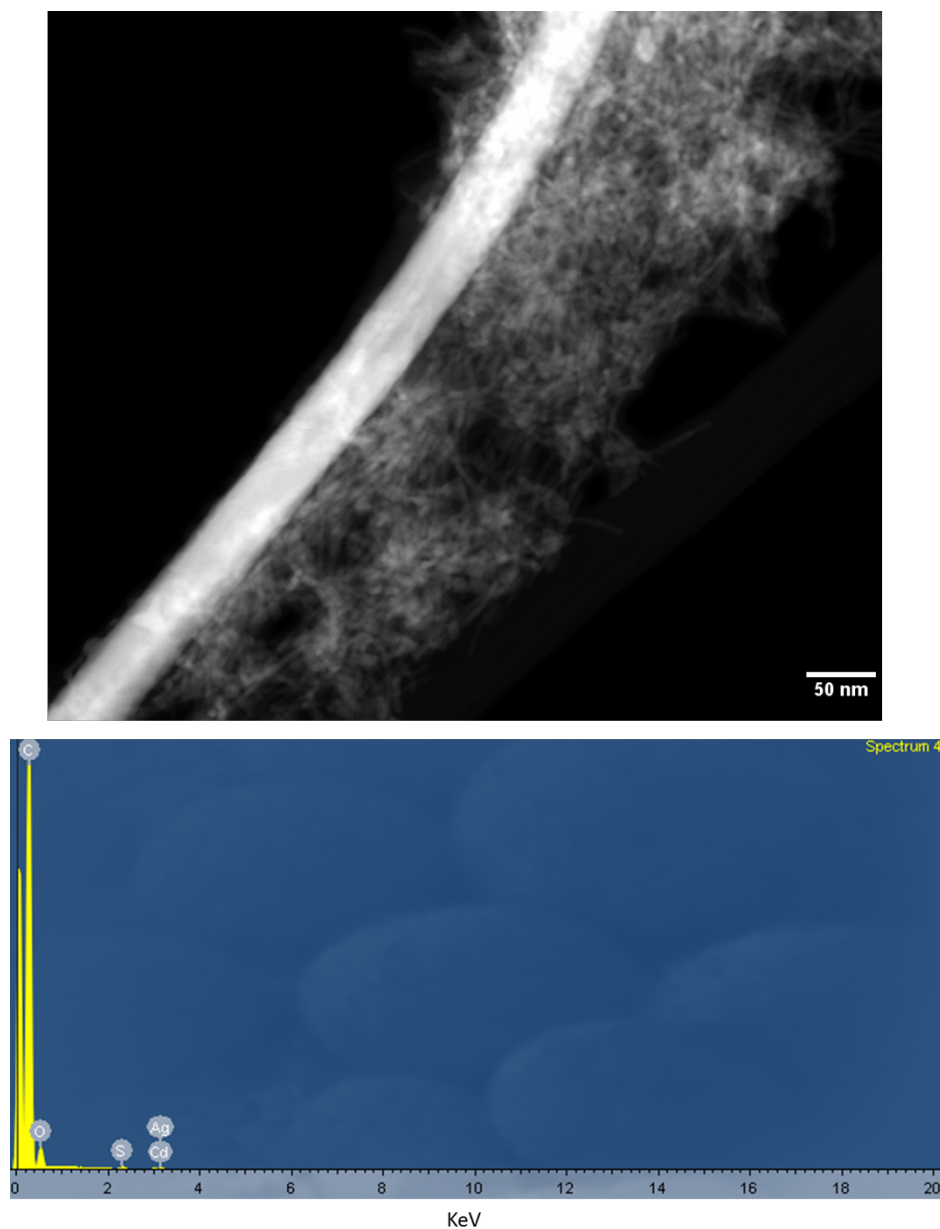


Figure 6.11: STEM image (top) and EDX spectrum (bottom) of self assembled nano-nails after 8 days of aging using a racemic solution of Cys capped nano-nails.

A control study performed in the absence of the Ag NWs shows that a racemic mixture of L- and D-Cys capped nano-nails do not conform

to any specific shape and only undergo random aggregation (Figure 6.12). This confirms that the NWs are necessary for the helical self-assembly of the nano-nails to occur.

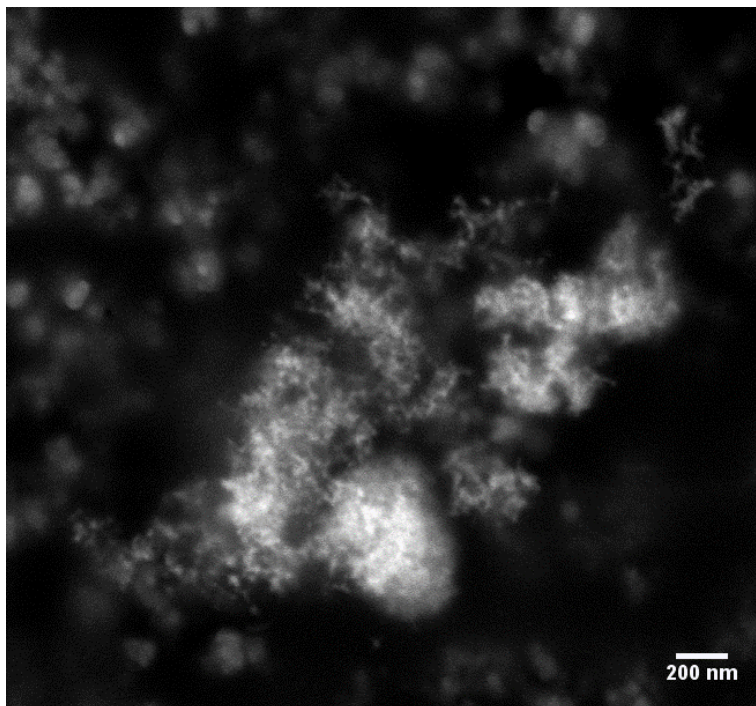


Figure 6.12: SEM image of a racemic mixture of L- and D-Cys capped nano-nails aged in the absence of Ag nanowires after 8 days.

### 6.3.2 Investigating the growth mechanism of Ag NW @ nano-nail hybrid structure

In order to understand the formation of these hybrid structures, we monitored their growth over 8 days using CD, UV-Vis absorbance

spectroscopy and SEM analysis (Figure 6.13).

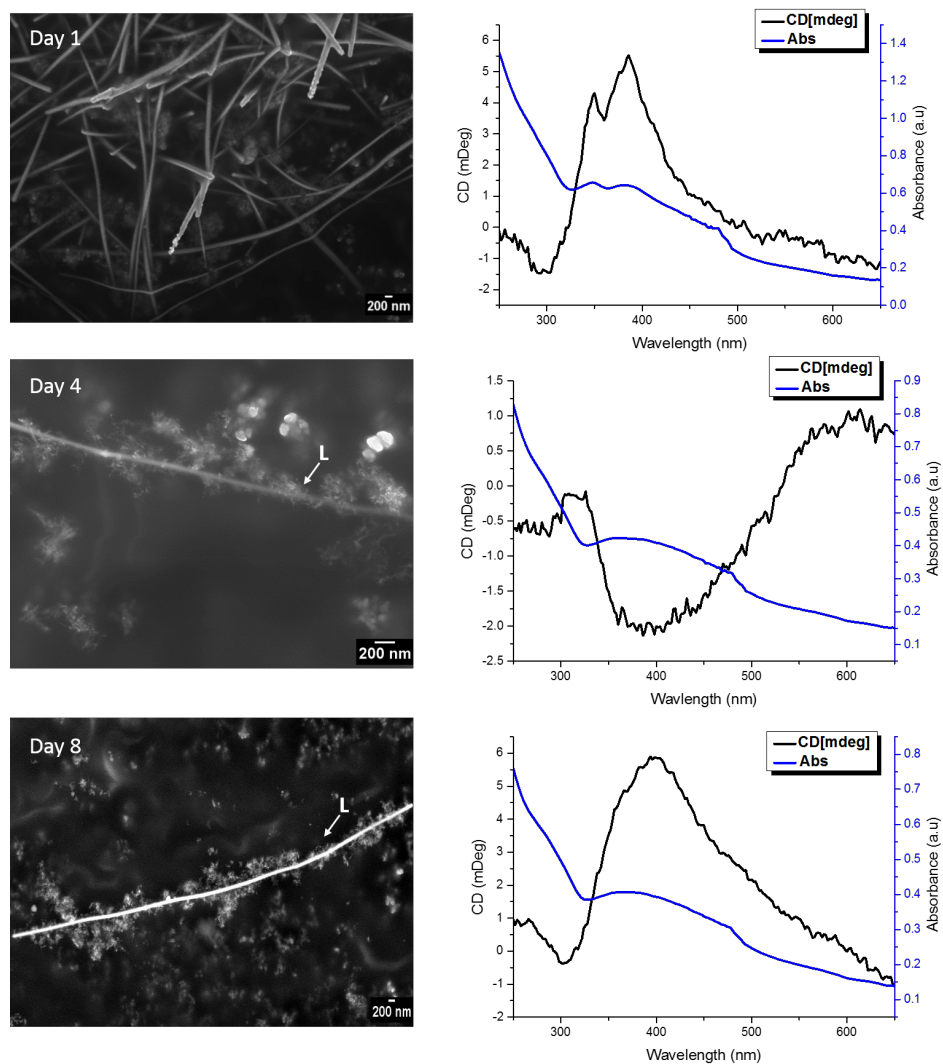


Figure 6.13: SEM images (left), CD and UV-Vis (right) spectra monitoring the formation of hybrid structure over several days. A racemic mixture of L- and D-Cys capped nano-nails were used in this case.

A distinct change in the absorbance spectra was observed in which the absorbance profile showing peaks at 354 and 398 nm typical of Ag

NWs seen on day 1, gradually becomes a single broader peak ( $\lambda_{\max} = 400$  nm) by day 4. This observation is reflected in our SEM analysis in which that there is little interaction between the NWs and the nano-nails on day 1, hence the dominant Ag NW absorbance profile. SEM analysis further shows the distinct formation of the helical assembly by day 4 which becomes notably thicker by day 8. The formation of the helical assembly on the surface of the NWs results in a change in surface plasmon resonance of the NWs and hence the change in the absorbance profile. These changes observed in the absorbance spectra are also mirrored in the CD analysis.

### 6.3.3 Investigating the effect of stirring on helice chirality

One of the biggest questions in this work, was to what extent does the stirring play on the handedness of the hybrid structures. To answer this we investigated the influence of stirring orientation on the resulting CD signal. Parallel experiments were performed with clockwise (CW) and anticlockwise (ACW) stirring (both cases the samples were stirred for 10 mins), using a racemic solution of nano-nails (made by mixing L- and D-Cys capped nano-nails) with the Ag NWs and aging the solution for 8 days (Figure 6.14).

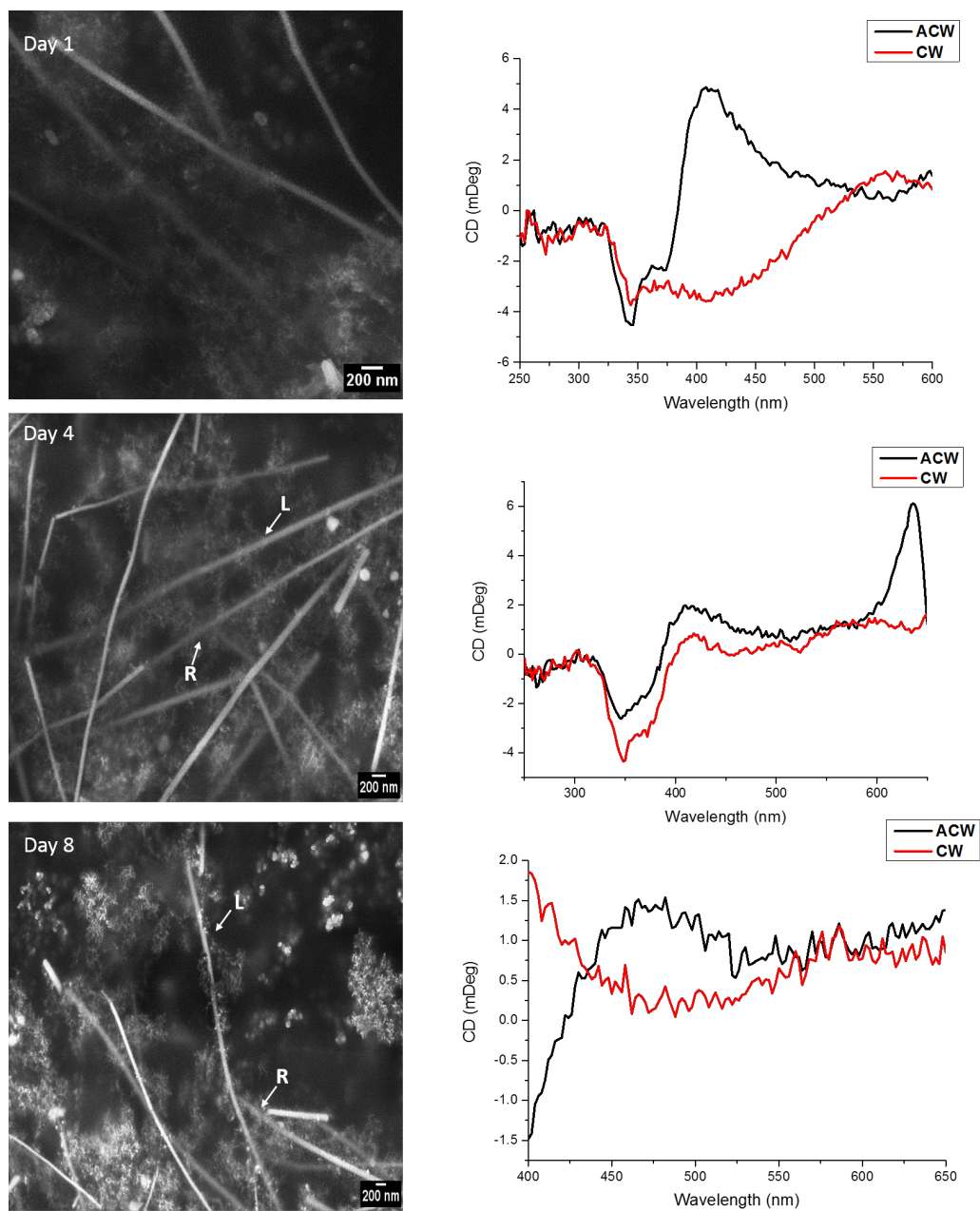


Figure 6.14: SEM images (left) and CD (right) analysis monitoring the formation of Ag nanowire- nano-nail hybrid structure over various days for CW and ACW stirring using a racemic mixture of Cys capped nano-nails.

The CD spectra shows mirror image signals for CW and ACW stirring

after day 1 with CW stirring in this case showing a trend for a ( + ) signal while ACW stirring shows a trend for a ( - ) signal. This is an expected result as there is minimal interaction between the NWs and nano-nails at this point in the formation process. As demonstrated above (section 6.1) these high aspect ratio Ag NWs alone can exhibit optical activity when stirred. Interestingly on day 4, both independent solutions exhibit a very similar bisignate signal with both ( + ) and ( - ) character. On day 4 the helices become more defined however upon analysis a racemic mixture was noted for both the CW and ACW stirred solutions. Finally, by day 8 both systems show mirror image signals with CW stirring showing a tendency for a ( + ) signal while ACW stirring shows a tendency for a ( - ) signal. Again only a racemic mixture of helices was observed when analysed by SEM. In summary, while the stirring orientation does not induce a particular handedness in the helices it does influence the overall chirality observed due to the motion of the NW backbone of the hybrid.<sup>51</sup> The change observed in the CD signal after day 4 indicates that the assembly may influence the motion of the NWs as would be expected due to a change in the fluid dynamics of the NWs.<sup>65,66</sup>

### **6.3.4 Investigating the effect of the capping agent on the helice chiralty**

To explore the effect of the capping agent on the handedness of the self assembled nano-nails we studied the use of D- and L- Cys and achiral TGA capped nano-nails. All solutions were stirred ACW for 10 mins and allowed to age for 8 days. SEM and CD analysis monitoring the changes in the structure over time are detailed in Figure 6.15.



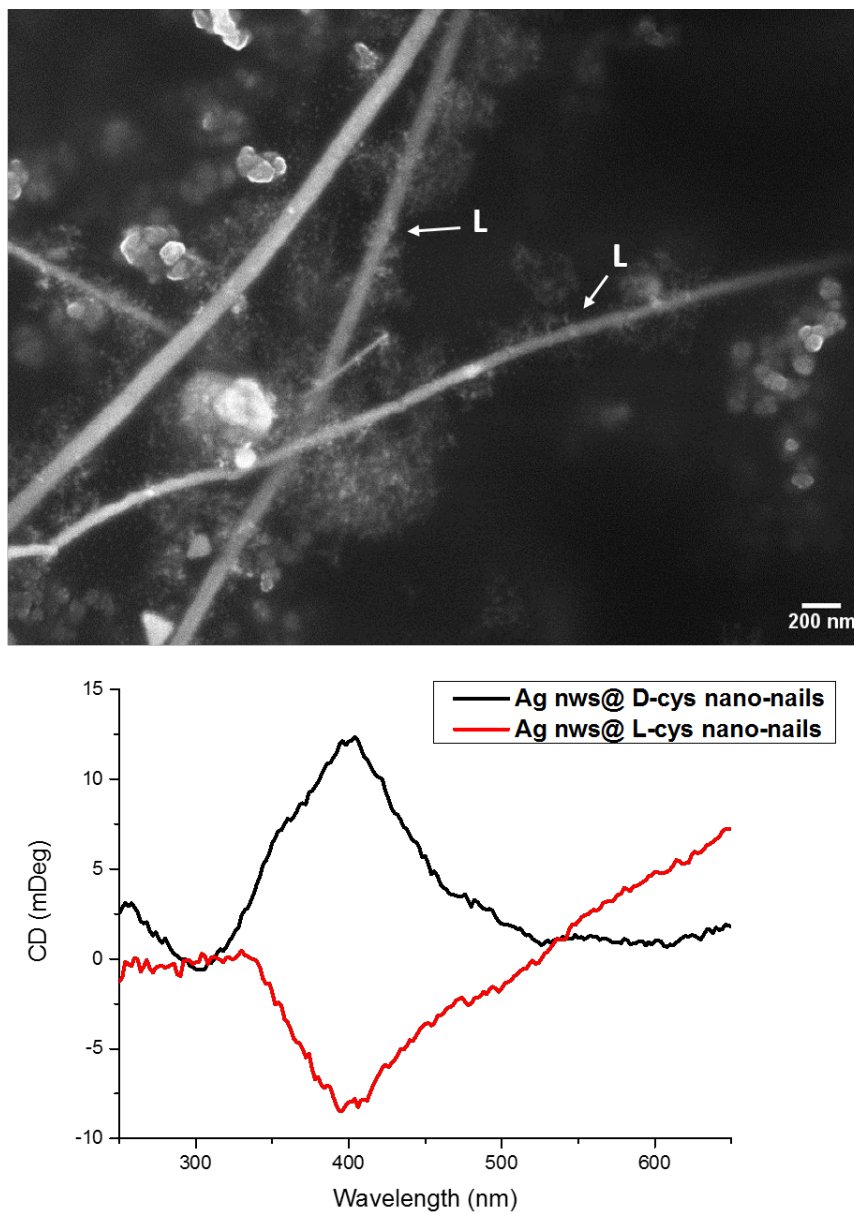


Figure 6.15: SEM image (top) and CD analysis (bottom) of Ag NW @nano-nail hybrid structure after 8 days of aging using D- and L-cysteine capped nano-nails. The SEM image is of L-Cys capped nano-nails respectively.

CD analysis shows equal and opposite CD signals after 8 days of aging. We have found that the L-Cys capped nano-nails produced predomi-

nantly left handed helices while the D-Cys capped produced predominantly right handed helices when assessed by SEM. The achiral TGA capped nano-nails under the same conditions also produced a helical self-assembly along the NWs (Figure 6.16). This may be explained by the “winding mode” detailed by Wang *et al.*<sup>67</sup> in which the winding of the assembly is the most energy efficient configuration. These helices were found to form a racemic mixture as would be expected since there is no chirality expressed by TGA to bias the resulting handedness of the self-assembly.

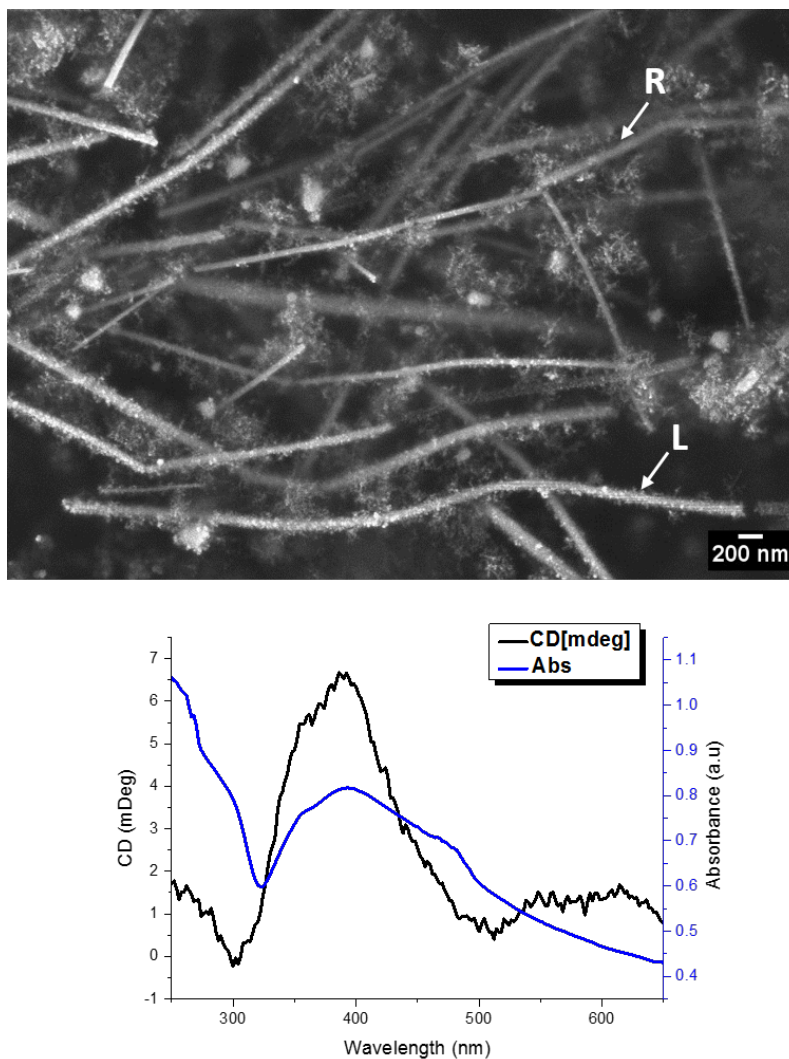


Figure 6.16: SEM image (top), CD and UV-Vis spectra (bottom) of Ag NW @nanonail hybrid capped with TGA after 8 days of aging

### 6.3.5 Ag nanowire@ Dot'n'rod hybrid structures

We further extended our study to the use of Dot'n'rod (DnR) QDs, as they are recognised for their strong luminescent properties making

them interesting candidates for the preparation of plasmonic-excitonic hybrid nanomaterials.<sup>68-70</sup> These QD were synthesised and characterised by Dr. Finn Purcell-Milton in our group (Figure 6.17). The length and width of these DnR are 6.6 and 27.1 nm respectively and they emitted at 625 nm.

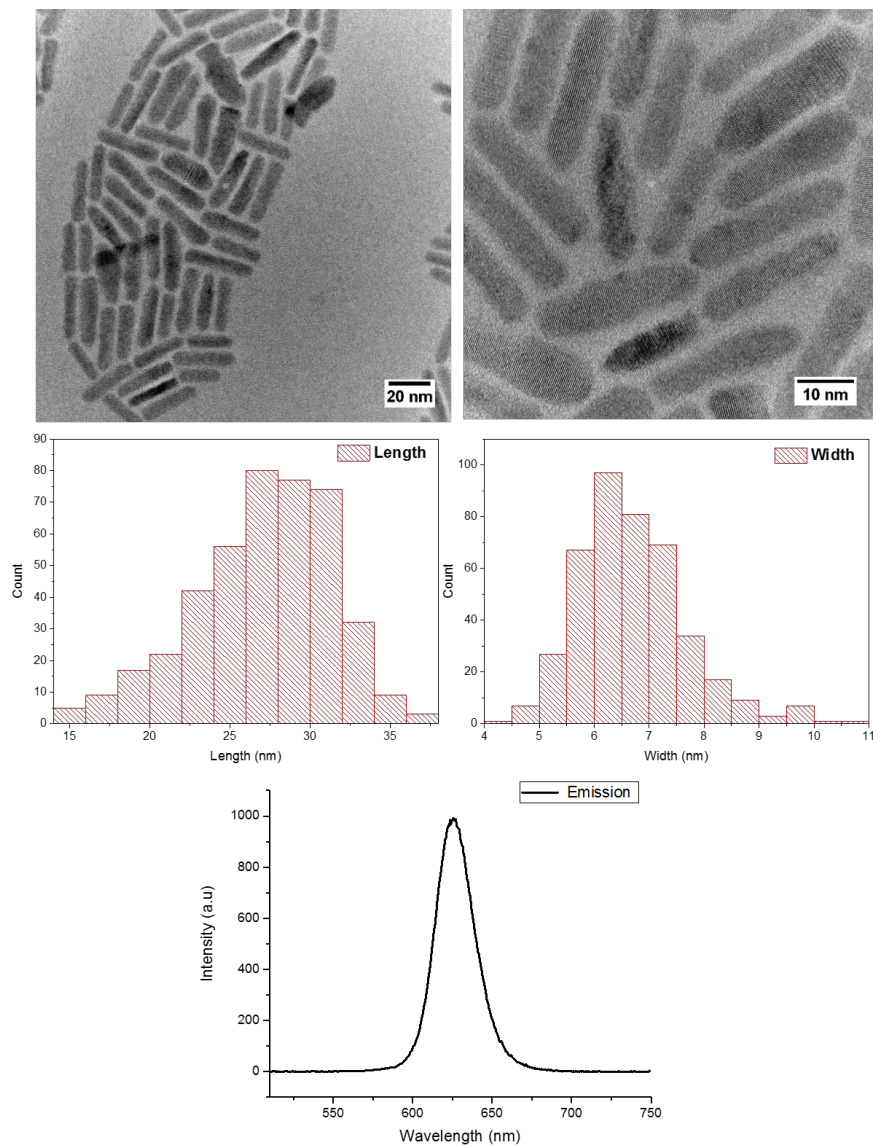


Figure 6.17: TEM images (top), size distributions (middle) and emission spectrum (bottom) of CdSe/CdS DnRs.

Since the DnR are also made in an organic phase a phase transfer was performed to make them miscible in water/ethanol. This phase transfer process was performed in collaboration with Vera Kuznetsova

( Ph.D candidate) in our group, using either Cys or TGA as the phase transfer agent. Figure 6.18 details the chiroptical activity induced in the DnRs following phase transfer using Cys.

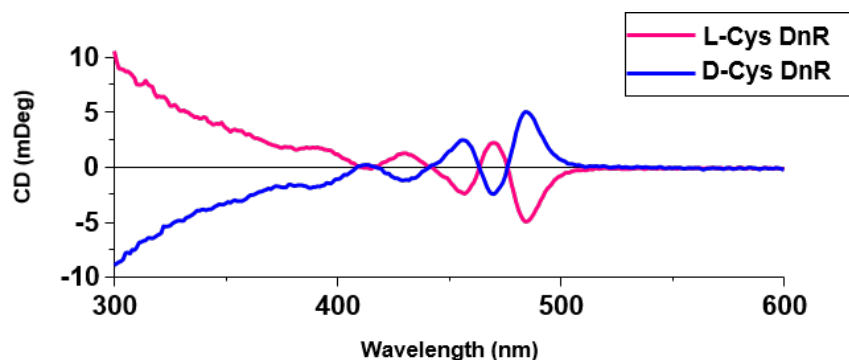


Figure 6.18: CD spectra of L- and D- capped CdSe/CdS DnRs.

Using our method, Ag NWs were mixed with a racemic solution (made by mixing L- and D- Cys capped DnRs) of QDs (in excess), in ethanol under strong magnetic stirring ( 960 rpm) for 10 mins and allowed to age over an 8 day period at 4 °C. SEM (Figure 6.19) of the resulting structure revealed that the DnRs also form a helical self-assembly along the length of the Ag NWs

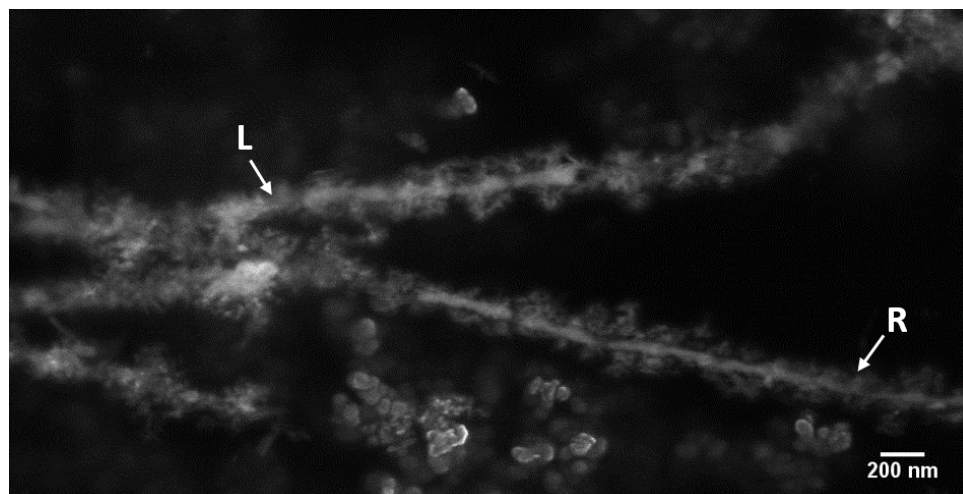


Figure 6.19: SEM image of Ag NWs@ DnR hybrid structure after 8 days of aging using a racemic solution of D- and L-Cys capped DnRs.

The DnR helical self assembly is similar to that seen for the nanonails. The pitch of these helices varied between NWs and along the length of the NWs. It was also noted that extending the aging period longer (typically 16 days see appendix Figure A18) can result in complete coverage and even dissociation of the NWs. A survey of these structures further revealed that helices have no preferential left or right handedness. This was similarly seen in the case of the nanonails. These results are in good agreement with the work on the self assembly of quantum dots previously reported by Kotov *et al.*<sup>3,5</sup> Our hybrid structure expresses chiroptical activity at 400 nm with ACW stirring solution showing a tendency to produce (-). We propose that this chiroptical activity is again due to the motion of the Ag NWs backbone of the hybrid nanostructure and not from the helical assemblies

of DnRs around the Ag NWs .

### **6.3.6 Investigation of the growth mechanism of Ag NW @ Dot n rod hybrid structure**

Our next focus was to further investigate the effects of stirring on the formation of the DnR (QDs) self assembly. While our previous stirring study with nano-nails (section 6.3.3), revealed that the stirring orientation (CW or ACW) did not influence the handedness of the resulting helice, this may have been due to the short stirring time used (10 mins). We thus performed this study with continuous ACW stirring at 960 rpm at room temperature for 8 days. In addition only achiral TGA capped DnRs were used, to ensure that any specific handedness induced in the self assembly was mainly caused from stirring rather than from chiral ligands. Furthermore in attempt to shorten the reaction time we also increased the concentration of the QDs from 0.6 a.u (at ab 500 nm) to 0.75 a.u. Finally, we also performed a control with no stirring in parallel with the stirred sample. Figure 6.20 details the SEM, CD and UV-Vis analysis of the continuously stirred sample over 8 days.



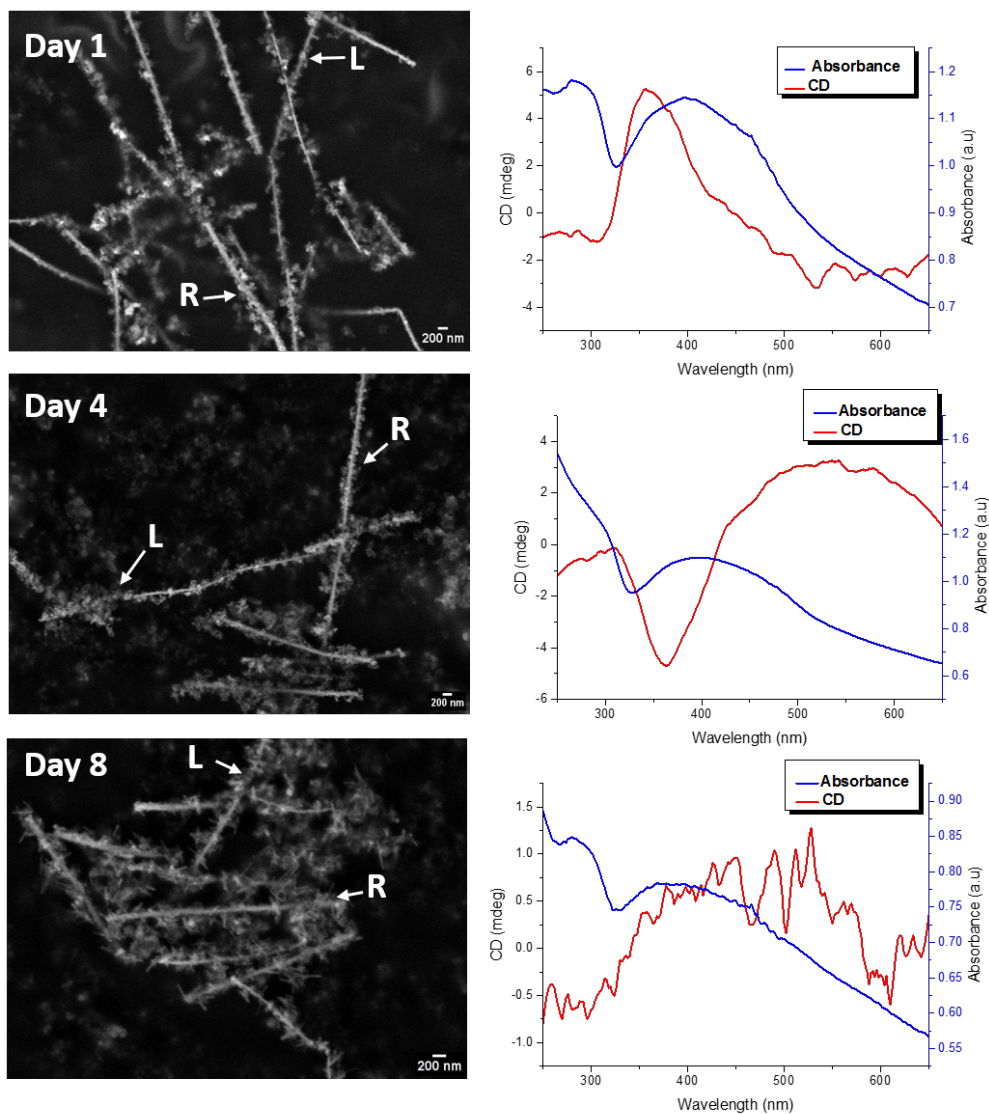


Figure 6.20: SEM images (left), CD and UV-Vis analysis (right) monitoring the formation of the Ag@ DnR hybrid structure over 8 days of aging with continuous stirring using TGA capped DnRs.

Our SEM analysis shows that after 1 day of aging the TGA capped DnRs form a helical assembly on the NWs. This is a striking improvement on our previous protocol which required up to 4 days for the helical self assembly to occur. A survey of these assemblies showed

that helices did not have a preferential left or right handedness. SEM further showed that no significant change occurred in the structure by day 4 however by day 8 the NWs show notable signs of dissociation. This may be due to the sulfurization of the Ag NW surfaces as highlighted by Elechiguerra and co workers.<sup>71</sup> Regarding the UV-Vis analysis, a broad absorbance profile centred at 420 nm was noted in all cases, which is indicative of a changes in the AG NWs surface. Interestingly there was notable change observed in the CD spectra in all cases. On day 1 a (+) signal was noted while on day 4 a (-) signal. This is inversion of the CD signal is possibly due to the change in NW motion upon transfer to the cuvette for CD analysis. On day 8 the CD signal is (+) however it is significantly diminished due to the dissociation of the NWs.

Regarding the non stirred control, this sample was probed after day 4 and 8 so as to minimize any perturbation on the solution. The SEM, Figure 6.21 shows a marked difference compared to the stirred sample as very little interaction was observed between the QDs and the NWs. By day 8 we observed very few helices for the non stirred sample with no specific handedness. The UV-Vis spectra in both cases showed a broad absorbance profile centred at 400 nm as expected. In addition the sample exhibited weak CD signals after both days 4 and 8.

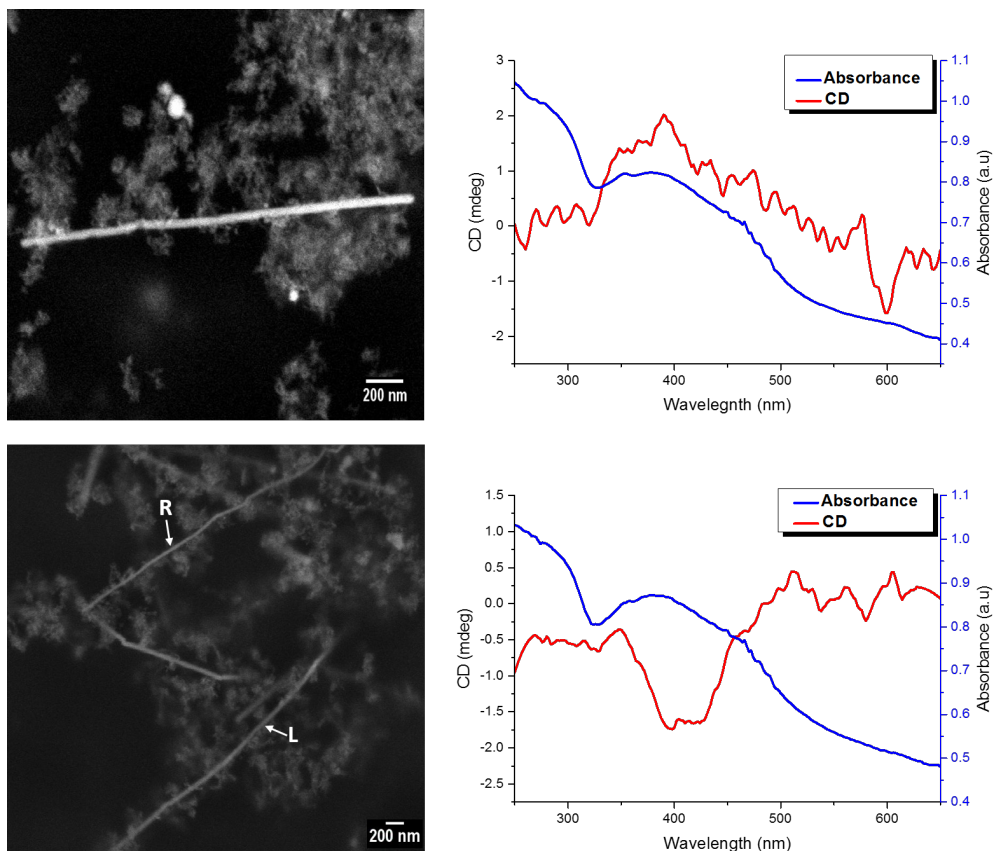


Figure 6.21: SEM images (left), CD and UV-Vis spectra (right) of hybrid structure after 4 and 8 days of aging using a racemic solution of Cys capped DnRs.

While continuously stirring the solution did not influence the resulting handedness of the helical self assembly, we did however improve our synthetic protocol by shortening the aging period from typically 4 days to 1 day.

## 6.4 Photoluminescent analysis of Ag NWs @DnR hybrid structure

Plasmonic-excitonic hybrid nanomaterials are an interesting class of material which may demonstrate unique photoluminescent properties.<sup>72-75</sup> For this investigation we have chosen only the DnR QD containing hybrid as these QDs are highly recognized for their strong luminescence.<sup>68-70</sup> Photoluminescent analysis of our plasmonic-excitonic, Ag NWs@DnR hybrid structure was performed using fluorescent lifetime imaging (FLIM) in collaboration with Dr. John Gough (School of physics, Trinity College Dublin). Since photoluminescence will only occur for a sample that can be excited by a photon to produce an exciton and subsequently emit a photon following the recombination of this exciton, only the DnRs QDs will provide a signal in this analysis. A FLIM analysis and photoluminescence spectrum of the hybrid structure is shown in Figure 6.22. The photoluminescence spectrum showed a peak at 625 nm which corresponds to the wavelength at which the photon is emitted due to the recombination of the QD exciton.

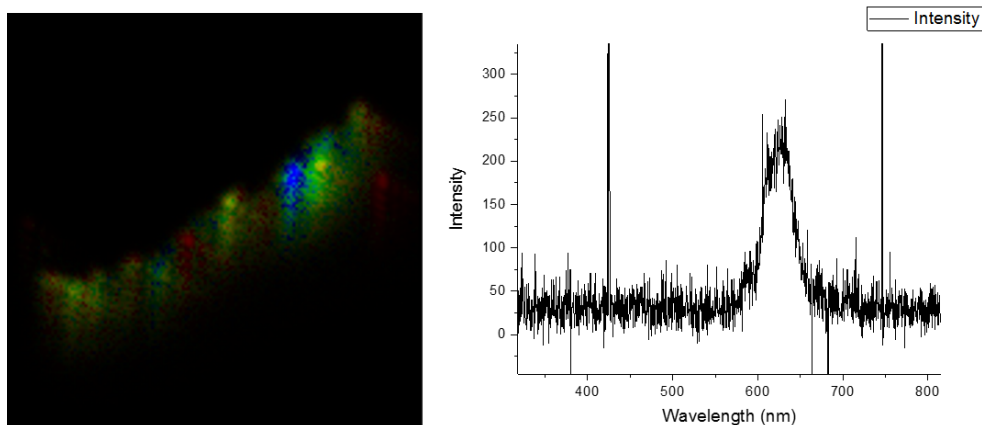


Figure 6.22: FLIM image (left) and corresponding photoluminescence spectrum (right) of Ag NW@ DnR hybrid structure.

From a sample set of 10 FLIM imaged hybrid structures it was found that the shortest lifetime was  $13.3 \pm 1.8$  ns and the longest was  $15.3 \pm 0.3$  ns, these were taken using a bi-exponential decay. The average of these lifetimes was  $14.5 \pm 0.6$  ns. As the lifetime over the span of the NWs does not vary, it can be seen that there is a uniformity with regards to the QDs that are on the NW and the time it will take for the exciton to recombine once it is in an excited state. That is to say that the QDs are spaced over the entire length of the NW and are relaxing from the excited state to the ground state at a relatively constant rate.

In order to further understand the correlation between the FLIM images and the structure of this hybrid material, we compared the FLIM and SEM images of the same wire. Figure 6.23 shows an SEM image

overlaid on the corresponding FLIM image.

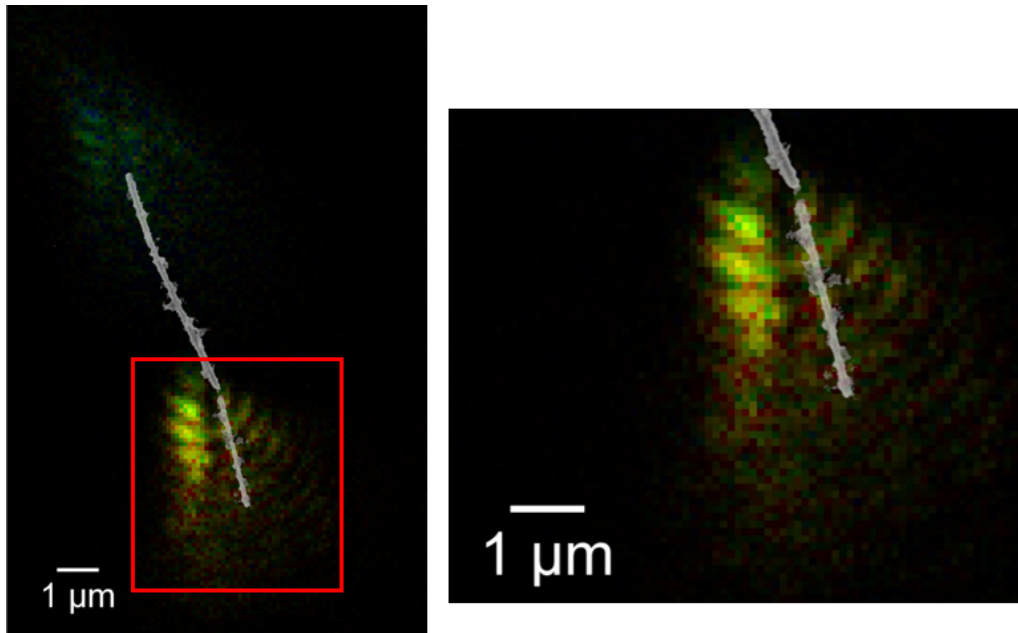


Figure 6.23: SEM image of Ag NW@ DnR hybrid structure overlaid on its corresponding FLIM image.

It can be seen in the magnified image that the helices of the QDs on the NWs match up exactly with the periodicity of the fringes in FLIM image. From this we can deduce that there is a correlation between the pitch of the helices formed by the QDs on the NW and the periodicity of the fluorescence intensity of these same QDs imaged in the FLIM. In the particular NW shown in Figure the pitch of the QDs varies across the length of the wire. The upper half of the NW, corresponding to the dark lobe on the FLIM image, has an average helical pitch of  $0.3202 \pm 0.04 \mu\text{m}$ . However the lower half, which was magni-

fied in the second image on the right, has an average helical pitch of  $0.3522 \pm 0.04 \mu\text{m}$ . This corresponds to a 9.99 % increase in the length of the helical pitch of the QDs around the NW. This highlights the non-uniformity in the pitch of the QDs along a single NW.

Noting that the fluorescence intensity on the FLIM image appears to match up with the pitch of the helices on the NW in the SEM image, the fluorescence intensity pitch was also analysed and compared to the SEM pitch. The average fluorescence intensity periodicity of the top lobe was  $0.4515 \pm 0.036 \mu\text{m}$  and the fluorescence intensity of the bottom, magnified lobe was  $0.5069 \pm 0.038 \mu\text{m}$ . This increase follows that of the pitch of the QDs on the NW. When the lobes were taken separately and the ratio of SEM pitch to the FLIM periodicity was taken, the top lobe had a ratio of  $0.709 \pm 0.148$  and the bottom, magnified lobe had a ratio of  $0.695 \pm 0.136$ . These similarities are within experimental error and therefore show that there is a relationship between the arrangement of the QDs on the NW and the fluorescence intensity shown in the FLIM. As a final remark it was also noted that hybrid structure exhibited an antenna<sup>76,77</sup> like behaviour as fluorescence emission was predominately noted from the ends of the NW backbone. As the FLIM measures the excited state lifetimes of fluorophores, the concentration of the fluorescence at the end of the NW indicates that this is the prime region where the particles undergo

emission after being excited.

## 6.5 Conclusion and future work

In conclusion we showed for the first time, vortex induced chiroptical activity of large aspect ratio Ag NWs. Through the use of alignment studies we confirmed that the induced chiroptical activity observed is a result of the orientation and motion of the Ag NWs with the intrinsically chiral vortex rather than chiral deformation of the NWs. By changing the direction of the vortex (ie. ACW or CW) it is possible to produce enantiomeric CD signals.

In addition we have developed new chiral plasmonic-excitonic Ag NW@QD hybrid nanostructures. Both the DnR and nano-nail QDs used in this study formed helical self-assemblies around the Ag NWs. We showed that the handedness of these helices depends strongly on the chirality of the QD capping agent with L-Cys capped QDs forming preferentially left handed helices while D-Cys capped QDs produces right handed helices. We further demonstrated that the stirring orientation does not induce a preferential handedness in the resulting helices. Since hybrids with racemic helices also produced a CD response, We propose that the observed chiroptical activity is mainly



due to the motion of the NW backbone of the hybrid moving in solution. In addition photoluminescent analysis further revealed that our Ag NW @DnR hybrid structure exhibited an antenna like behaviour with emission occurring from the ends of the NW backbone in the hybrid.

For our future work we plan to investigate the influence of the vortex speed and concentration of the Ag NWs on the resulting CD signal. Further more we aim explore the interaction of various nanomaterials with different morphologies with the Ag NWs in an attempt to expand on our technique to produce a range of new hybrid nanostructures.

# References

- (1) Ma, W.; Xu, L.; De Moura, A. F.; Wu, X.; Kuang, H.; Xu, C.; Kotov, N. A. *Chemical Reviews* **2017**, *117*, 8041–8093.
- (2) Lan, X.; Wang, Q. *Advanced Materials* **2016**, *28*, 10499–10507.
- (3) Zhou, Y.; Marson, R. L.; Van Anders, G.; Zhu, J.; Ma, G.; Ercius, P.; Sun, K.; Yeom, B.; Glotzer, S. C.; Kotov, N. A. *ACS Nano* **2016**, *10*, 3248–3256.
- (4) Hu, T.; Isaacoff, B. P.; Bahng, J. H.; Hao, C.; Zhou, Y.; Zhu, J.; Li, X.; Wang, Z.; Liu, S.; Xu, C.; Biteen, J. S.; Kotov, N. A. *Nano Letters* **2014**, *14*, 6799–6810.
- (5) Feng, W.; Kim, J. Y.; Wang, X.; Calcaterra, H. A.; Qu, Z.; Meshi, L.; Kotov, N. A. *Science Advances* **2017**, *3*, 1–13.
- (6) Yeom, J. et al. *Nature Materials* **2015**, *14*, 66–72.
- (7) Kuzyk, A.; Schreiber, R.; Fan, Z.; Pardatscher, G.; Roller, E. M.; Högele, A.; Simmel, F. C.; Govorov, A. O.; Liedl, T. *Nature* **2012**, *483*, 311–314.

- (8) Wang, X.; Wang, Y.; Zhu, J.; Xu, Y. *Journal of Physical Chemistry C* **2014**, *118*, 5782–5788.
- (9) Yan, W.; Xu, L.; Xu, C.; Ma, W.; Kuang, H.; Wang, L.; Kotov, N. A. *Journal of the American Chemical Society* **2012**, *134*, 15114–15121.
- (10) Chen, C.-l.; Zhang, P.; Rosi, N. L. *Water* **2008**, 1–15.
- (11) Zhu, L.; Li, X.; Wu, S.; Nguyen, K. T.; Yan, H.; Ågren, H.; Zhao, Y. *Journal of the American Chemical Society* **2013**, *135*, 9174–9180.
- (12) Sone, E. D.; Zubarev, E. R.; Stupp, S. I. *Communications* **2002**, 1705–1709.
- (13) Sone, E. D.; Zubarev, E. R.; Stupp, S. I. *Small* **2005**, *1*, 694–697.
- (14) Gao, P. X.; Ding, Y.; Mai, W.; Hughes, W. L. *Science* **2005**, *309*, 1700–1705.
- (15) Moore, D.; Ding, Y.; Zhong, L. W. *Angewandte Chemie - International Edition* **2006**, *45*, 5150–5154.
- (16) Shen, G. Z.; Bando, Y.; Zhi, C. Y.; Yuan, X. L.; Sekiguchi, T.; Golberg, D. *Applied Physics Letters* **2006**, *88*, 2004–2007.
- (17) Prinz, V. Y.; Seleznev, V. A.; Gutakovskiy, A. K.; Chehovskiy, A. V.; Preobrazhenskii, V. V.; Putyato, M. A.; Gavrilova, T. A.

- Physica E: Low-Dimensional Systems and Nanostructures* **2000**, *6*, 828–831.
- (18) Crusats, J.; El-Hachemi, Z.; Ribó, J. M. *Chemical Society Reviews* **2010**, *39*, 569–577.
- (19) Okano, K.; Yamashita, T. *ChemPhysChem* **2012**, *13*, 2263–2271.
- (20) Tsuda, A. *Symmetry* **2014**, *6*, 383–395.
- (21) Arteaga, O.; Canillas, A.; Crusats, J.; El-Hachemi, Z.; Llorens, J.; Sorrenti, A.; Ribo, J. M. *Israel Journal of Chemistry* **2011**, *51*, 1007–1016.
- (22) Acharya, S.; Sarkar, S.; Chakraborty, S.; Pradhan, N. *Chemistry - A European Journal* **2014**, *20*, 3922–3926.
- (23) Okano, K.; Arteaga, O.; Ribo, J. M.; Yamashita, T. *Chemistry - A European Journal* **2011**, *17*, 9288–9292.
- (24) Wolffs, M.; George, S. J.; Tomovi??, e.; Meskers, S. C. J.; Schenning, A. P.H. J.; Meijer, E. W. *Angewandte Chemie - International Edition* **2007**, *46*, 8203–8205.
- (25) Lokszejn, A.; Dzwolak, W. *Journal of Molecular Biology* **2010**, *395*, 643–655.
- (26) Cecilia Noguez, F. H. *Chirality* **2014**, *26*, 553–562.
- (27) Link, D. R.; Natale, G.; Shao, R.; MacLennan, J. E.; Clark, N. A.; Körblova, E.; Walba, D. M. *Science* **1997**, *278*, 1924–1927.

- (28) Arteaga, O.; Escudero, C.; Oncins, G.; El-Hachemic, Z.; Llorens, J.; Crusats, J.; Canillas, A.; Ribó, J. M. *Chemistry - An Asian Journal* **2009**, *4*, 1687–1696.
- (29) Ribó, J. M.; Crusats, J.; Sagués, F.; Claret, J.; Rubires, R. *Science* **2001**, *292*, 2063–2066.
- (30) Rubires, R.; Farrera, J.-a.; Ribo, J. M. **2001**, 436–446.
- (31) Yamaguchi, T.; Kimura, T.; Matsuda, H.; Aida, T. *Angewandte Chemie - International Edition* **2004**, *43*, 6350–6355.
- (32) Escudero, C.; Crusats, J.; Díez-Pérez, I.; El-Hachemi, Z.; Ribó, J. M. *Angewandte Chemie - International Edition* **2006**, *45*, 8032–8035.
- (33) El-Hachemi, Z.; Arteaga, O.; Canillas, A.; Crusats, J.; Escudero, C.; Kuroda, R.; Harada, T.; Rosa, M.; Ribó, J. M. *Chemistry - A European Journal* **2008**, *14*, 6438–6443.
- (34) Arteaga, O.; Canillas, A.; Crusats, J.; El-Hachemi, Z.; Llorens, J.; Sacristan, E.; Ribo, J. M. *ChemPhysChem* **2010**, *11*, 3511–3516.
- (35) Takechi, H.; Canillas, A.; Ribó, J. M.; Watarai, H. *Langmuir* **2013**, *29*, 7249–7256.
- (36) Ribo, J. M.; El-Hachemi, Z.; Arteaga, O.; Canillas, A.; Crusats, J. *Chemical Record* **2017**, *17*, 713–724.

- (37) Tan, C.; Qi, X.; Liu, Z.; Zhao, F.; Li, H.; Huang, X.; Shi, L.; Zheng, B.; Zhang, X.; Xie, L.; Tang, Z.; Huang, W.; Zhang, H. *Journal of the American Chemical Society* **2015**, *137*, 1565–1571.
- (38) Di Mauro, A.; Randazzo, R.; Spanò, S. F.; Compagnini, G.; Gaeta, M.; D’Urso, L.; Paolesse, R.; Pomarico, G.; Di Natale, C.; Villari, V.; Micali, N.; Fragalà, M. E.; D’Urso, A.; Purrello, R. *Chemical Communications* **2016**, *52*, 13094–13096.
- (39) Hermans, T. M.; Bishop, K. J.; Stewart, P. S.; Davis, S. H.; Grzybowski, B. A. *Nature Communications* **2015**, *6*, 1–8.
- (40) Nahar, L.; Esteves, R. J. A.; Hafiz, S.; Özgür, Arachchige, I. U. *ACS Nano* **2015**, *9*, 9810–9821.
- (41) Khanal, B. P.; Pandey, A.; Li, L.; Lin, Q.; Bae, W. K.; Luo, H.; Klimov, V. I.; Pietryga, J. M. *ACS Nano* **2012**, *6*, 3832–3840.
- (42) Mark, A. G.; Gibbs, J. G.; Lee, T. C.; Fischer, P. *Nature Materials* **2013**, *12*, 802–807.
- (43) Hooper, D. C.; Mark, A. G.; Kuppe, C.; Collins, J. T.; Fischer, P.; Valev, V. K. *Advanced Materials* **2017**, *29*, 1605110.
- (44) Jiu, J.; Araki, T.; Wang, J.; Nogi, M.; Sugahara, T.; Nagao, S.; Koga, H.; Suganuma, K.; Nakazawa, E.; Hara, M.; Uchida, H.; Shinozaki, K. *Journal of Materials Chemistry A* **2014**, *2*, 6326–6330.

- (45) Gebeyehu, M. B.; Chala, T. F.; Chang, S. Y.; Wu, C. M.; Lee, J. Y. *RSC Advances* **2017**, *7*, 16139–16148.
- (46) Wang, G. H.; Zhu, J. J.; Kan, C. X.; Wan, J. G.; Han, M. *Journal of Nanomaterials* **2011**, *2011*, 1–7.
- (47) Wei, X.; Quan, Y.; Zeng, H.; Huang, W.; Li, W.; Liao, J.; Chen, Z. *Materials Research Express* **2018**, *5*, 015041.
- (48) Song, M.; Chen, G.; Liu, Y.; Wu, E.; Wu, B.; Zeng, H. *Optics Express* **2012**, *20*, 22290.
- (49) Rubires, R.; Farrera, J.-a.; Ribo, J. M. **2001**, 436–446.
- (50) Rubires, R.; Farrera, J.-a.; Ribo, J. M. **2001**, 436–446.
- (51) Tsuda, A. *Symmetry* **2014**, *6*, 383–395.
- (52) D’Urso, A.; Randazzo, R.; Faro, L. L.; Purrello, R. *Angewandte Chemie - International Edition* **2010**, *49*, 108–112.
- (53) Crusats, J.; El-Hachemi, Z.; Ribó, J. M. *Chemical Society Reviews* **2010**, *39*, 569–577.
- (54) Wolffs, M.; George, S. J.; Tomovi??, e.; Meskers, S. C. J.; Schenning, A. P.H. J.; Meijer, E. W. *Angewandte Chemie - International Edition* **2007**, *46*, 8203–8205.
- (55) Di Mauro, A.; Randazzo, R.; Spanò, S. F.; Compagnini, G.; Gaeta, M.; D’Urso, L.; Paolesse, R.; Pomarico, G.; Di Natale, C.; Villari, V.; Micali, N.; Fragalà, M. E.; D’Urso, A.; Purrello, R. *Chemical Communications* **2016**, *52*, 13094–13096.

- (56) Hill, E. K.; Krebs, B.; Goodall, D. G.; Howlett, G. J.; Dunstan, D. E. *Biomacromolecules* **2006**, *7*, 10–13.
- (57) Arteaga, O.; Canillas, A.; Crusats, J.; El-Hachemi, Z.; Llorens, J.; Sorrenti, A.; Ribo, J. M. *Israel Journal of Chemistry* **2011**, *51*, 1007–1016.
- (58) Ma, W.; Kuang, H.; Wang, L.; Xu, L.; Chang, W. S.; Zhang, H.; Sun, M.; Zhu, Y.; Zhao, Y.; Liu, L.; Xu, C.; Link, S.; Kotov, N. A. *Scientific Reports* **2013**, *3*, 1–6.
- (59) Wang, X.; Wang, Y.; Zhu, J.; Xu, Y. *The Journal of Physical Chemistry C* **2014**, *118*, 5782–5788.
- (60) Jiang, F.; Muscat, A. J. *Journal of Physical Chemistry C* **2013**, *117*, 22069–22078.
- (61) Chen, H.; Lesnyak, V.; Bigall, N. C.; Gaponik, N.; Eychmüller, A. *Chemistry of Materials* **2010**, *22*, 2309–2314.
- (62) Tang, Z. *Science* **2002**, *297*, 237–240.
- (63) Shen, G.; Cho, J. H.; Yoo, J. K.; Yi, G. C.; Lee, C. J. *Journal of Physical Chemistry B* **2005**, *109*, 5491–5496.
- (64) Zhang, S. Y.; Regulacio, M. D.; Han, M. Y. *Chemical Society Reviews* **2014**, *43*, 2301–2323.
- (65) Ma, C.; Chen, L.; Xu, J.; Zhao, J.; Li, X. *Journal of Applied Physics* **2015**, *117*, 114901.



- (66) Pasha, M.; Hare, C.; Ghadiri, M.; Gunadi, A.; Piccione, P. M. *Powder Technology* **2016**, *296*, 29–36.
- (67) Wang, Z.; He, B.; Xu, G.; Wang, G.; Wang, J.; Feng, Y.; Su, D.; Chen, B.; Li, H.; Wu, Z.; Zhang, H.; Shao, L.; Chen, H. *Nature Communications* **2018**, *9*, 563.
- (68) Talapin, D. V.; Koeppel, R.; G??tzinger, S.; Kornowski, A.; Lupton, J. M.; Rogach, A. L.; Benson, O.; Feldmann, J.; Weller, H. *Nano Letters* **2003**, *3*, 1677–1681.
- (69) Talapin, D. V.; Nelson, J. H.; Shevchenko, E. V.; Aloni, S.; Sadtler, B.; Alivisatos, A. P. *Nano Letters* **2007**, *7*, 2951–2959.
- (70) Coropceanu, I.; Rossinelli, A.; Caram, J. R.; Freyria, F. S.; Bawendi, M. G. *ACS Nano* **2016**, *10*, 3295–3301.
- (71) Elechiguerra, J. L.; Larios-Lopez, L.; Liu, C.; Garcia-Gutierrez, D.; Camacho-Bragado, A.; Yacaman, M. J. *Chemistry of Materials* **2005**, *17*, 6042–6052.
- (72) Zheng, D.; Zhang, S.; Deng, Q.; Kang, M.; Nordlander, P.; Xu, H. *Nano Letters* **2017**, *17*, 3809–3814.
- (73) Ding, Q.; Shi, Y.; Chen, M.; Li, H.; Yang, X.; Qu, Y.; Liang, W.; Sun, M. *Scientific Reports* **2016**, *6*, 1–10.
- (74) Abid, I.; Chen, W.; Yuan, J.; Bohloul, A.; Najmaei, S.; Avendano, C.; Péchou, R.; Mlayah, A.; Lou, J. *ACS Photonics* **2017**, *4*, 1653–1660.

- 
- (75) Wurtz, G. A.; Evans, P. R.; Hendren, W.; Atkinson, R.; Dickson, W.; Pollard, R. J.; Zayats, A. V.; Harrison, W.; Bower, C. *Nano Letters* **2007**, *7*, 1297–1303.
- (76) Zhang, S.; Wei, H.; Bao, K.; Håkanson, U.; Halas, N. J.; Nordlander, P.; Xu, H. *Physical Review Letters* **2011**, *107*, 1–5.
- (77) Grzela, G.; Paniagua-Domínguez, R.; Barten, T.; Fontana, Y.; Sánchez-Gil, J. A.; Gómez Rivas, J. *Nano Letters* **2012**, *12*, 5481–5486.

# Chapter 7

## Conclusions and future work

### 7.1 Conclusions

In this work, a wide range of new 1D metallic nanostructures were synthesised, characterised and investigated. These novel nanomaterials were prepared using a variety of wet chemical techniques such as; co-reduction, templating and phase transfer. The following is a summary of the main conclusions from our work.

Firstly, we developed a facile and tunable synthesis for water soluble non-uniform ultrathin AuAg nanowires (NWs). We demonstrated that these NWs are produced via a novel 2 step mechanism involving the formation of NW templates during an aging period and the subsequent formation of thicker NWs by a solvent driven fusion and wetting following a dilution step. We further optimised our protocol

by reducing the poly-dispersity of the products and shortened the reaction time through the use temperature controlled aging of the reaction mixture. we found that aging the reaction at 35°C resulted in novel ultrathin AuAg nano necklaces (NNLs) with a complex morphology. Comparing the catalytic activities of each our AuAg nanomaterials for ethylene glycol electro oxidation revealed that the NNLs offers the greatest catalytic performance.

Secondly, we demonstrated for the first time the chiral modification of our 1D ultrathin AuAg nanomaterials via a facile ligand exchange method. Our CD and IR analysis confirms that observed chiroptical activity is ligand induced. We propose that the PKa of the chiral modifier is crucial for the ligand exchange to occur.

Thirdly, we showed for the first time the use of AuAg NWs (9 nm diameter) as templates for producing novel 1D nanomaterials. We synthesised novel Pt and RhPt dendritic NWs via sacrificial templating of our AuAg NWs, which exhibited striking catalytic performance particularly for methanol electro oxidation. We further developed a novel core-shell AuAg NW@Rh nanoparticle hybrid structure with a tunable coverage using the AuAg NWs as templates.

Finally, using SEM and various optical studies we confirmed that ob-

served CD signal for stirred, large aspect ratio Ag NWs is due to the alignment of the NWs with the flow of the vortex. We further extended this work to the development of novel plasmonic-excitonic NW-quantum dot (QD) hybrid structures in which the QD form a helical self assembly around the NWs.

In conclusion we demonstrated the broad versatility of 1D nanomaterials. We expect that this research work will contribute to further the development of new 1D nanomaterials for future sensing and catalytic applications.

## 7.2 Future work and preliminary studies

For our future work we plan to investigate if our AuAg nanostructures are capable of exhibiting plasmon-enhanced catalytic effects for the EGOR using white light irradiation. We aim to further explore the use of our chiral modified AuAg nanomaterials for glucose sensing in an attempt to study the influence of chirality on the detection limit of glucose. In addition we are also interested in studying the influence of the different capping agents on the resulting morphology of Pt and RhPt dendritic NWs. Finally regarding our plasmonic-excitonic hybrid nanomaterials our focus is to extend this work to various other nanomaterials of different architectures such as NWs and tetrapods.

The following sections detail our current preliminary studies.

### **7.2.1 Investigating the effect of the capping agent on the morphology of RhPt dendritic nanowires**

Following on from our template based synthesis of Pt and RhPt dendritic NWs we explored the effect of a different capping agent on the resulting morphology. To investigate this we chose dodecyltrimethylammonium bromide (DTAB). This is an amphiphilic ionic surfactant composed of a 12 carbon aliphatic chain with a tetra-ammonium cation head group and bromide counter anion (Figure 7.1). Unlike PVP which is polymeric and relies a donor-acceptor interaction between the pyrrolidone ring and the nanomaterial surface, tetra-ammonium surfactants stabilize surfaces by electro-static interactions. In addition, tetra-ammonium surfactants particularly cetyltrimethylammonium bromide (CTAB), which is the more commonly used smaller analogue of DTAB, has been widely used to produce noble metals nanomaterials with interesting morphologies.<sup>1-4</sup> This study was thus performed in the case of only RhPt using our AuAg NW template protocol (Chapter 5) with DTAB in place of PVP. TEM and UV-Vis analysis of the products are presented in Figure 7.1.

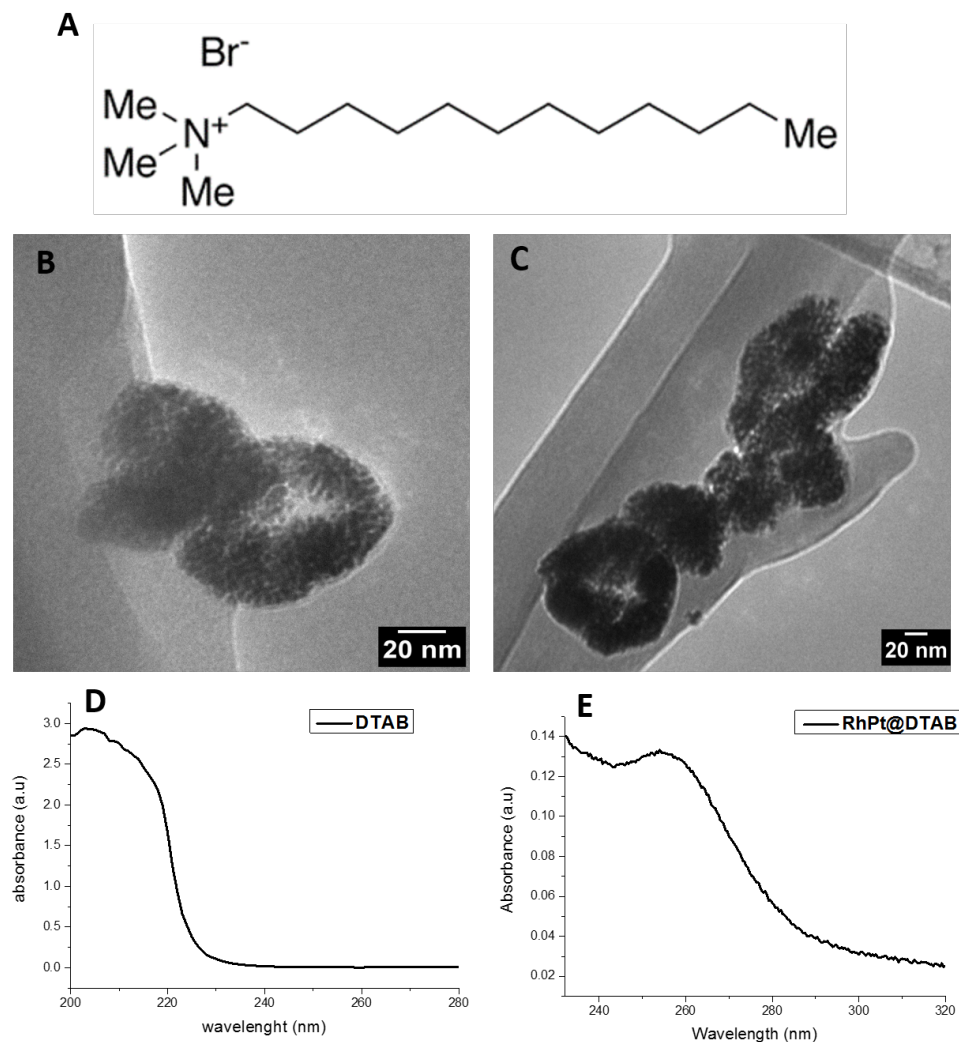


Figure 7.1: Structure of DTAB (A), TEM images (B and C) and UV-Vis spectra of DTAB (D) and DTAB capped RhPt assemblies (E).

TEM analysis showed a pronounced difference in the resulting morphology compared to the use of PVP. Rather than dendritic NWs the resulting nanoparticle assemblies form knotted and looped like structures. Since this work is still in its early stages the exact cause of this structure change remains unclear, however we propose that a combi-

nation of steric and electro-static effects may be at play. It must also be noted that the products were highly polydisperse. UV-Vis analysis further shows a peak at 290 nm for the RhPt assembly, as similarly seen in the case of PVP. These results confirm that the morphology of our dendritic NWs can be tuned by changing the capping agent.

### **7.2.2 Ag nanowire@ quantum tetrapod hybrid structure**

As an extension to our earlier work using CdSe/CdS nano-nails and Dot n rods, which are 1D QDs, we next plan to focus on using Cd-SeCdS tetrapods (TPs) to investigate if this self assembly process can be applied more generally to other anisotropic nanomaterials. These TPs were previously synthesised and characterised by Dr. Finn Purcell-Milton in our group. The arm length and width of these QDs are 37.4 and 7.3 nm respectively and they emit at 650 nm (Figure 7.2)



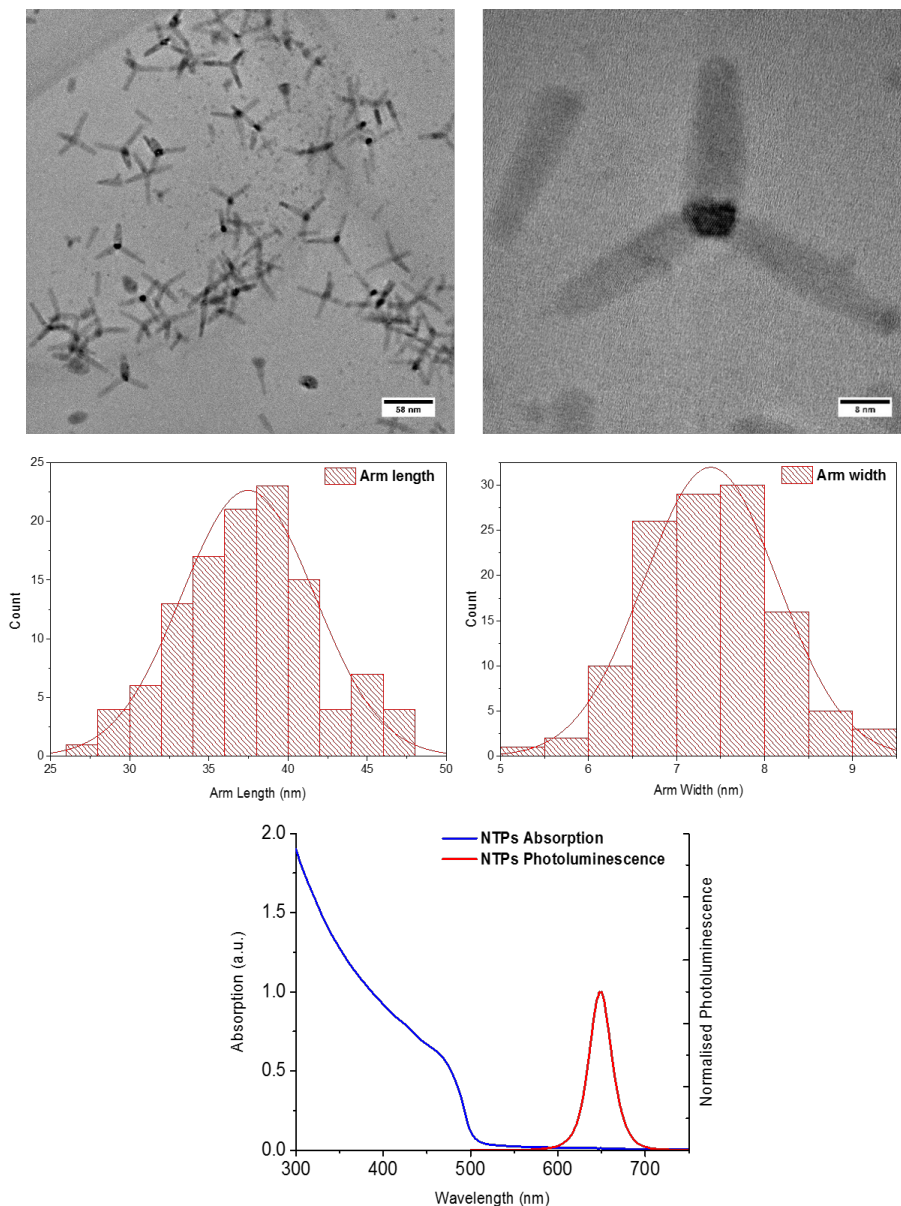


Figure 7.2: TEM images (top), size distributions (middle) and emission and UV-Vis spectrum (bottom) of CdSe/CdS TPs.

Since the TPs were made in an organic phase, a phase transfer was performed to make them miscible in water/ethanol. This phase transfer process was performed by Vera Kuznetsova ( Ph.D candidate) in

our group, using TGA as the phase transfer agent in basic conditions.

Using our method, Ag NWs were mixed with TGA capped TPs (in excess) in ethanol and allowed to age for 8 days with continuous ACW magnetic stirring (960 rpm). The self-assembly process was monitored over the 8 days using SEM, CD and UV-Vis analysis. SEM (Figure 7.3) of the resulting structure revealed that the TPs also form a helical self-assembly along the length of the Ag NWs.

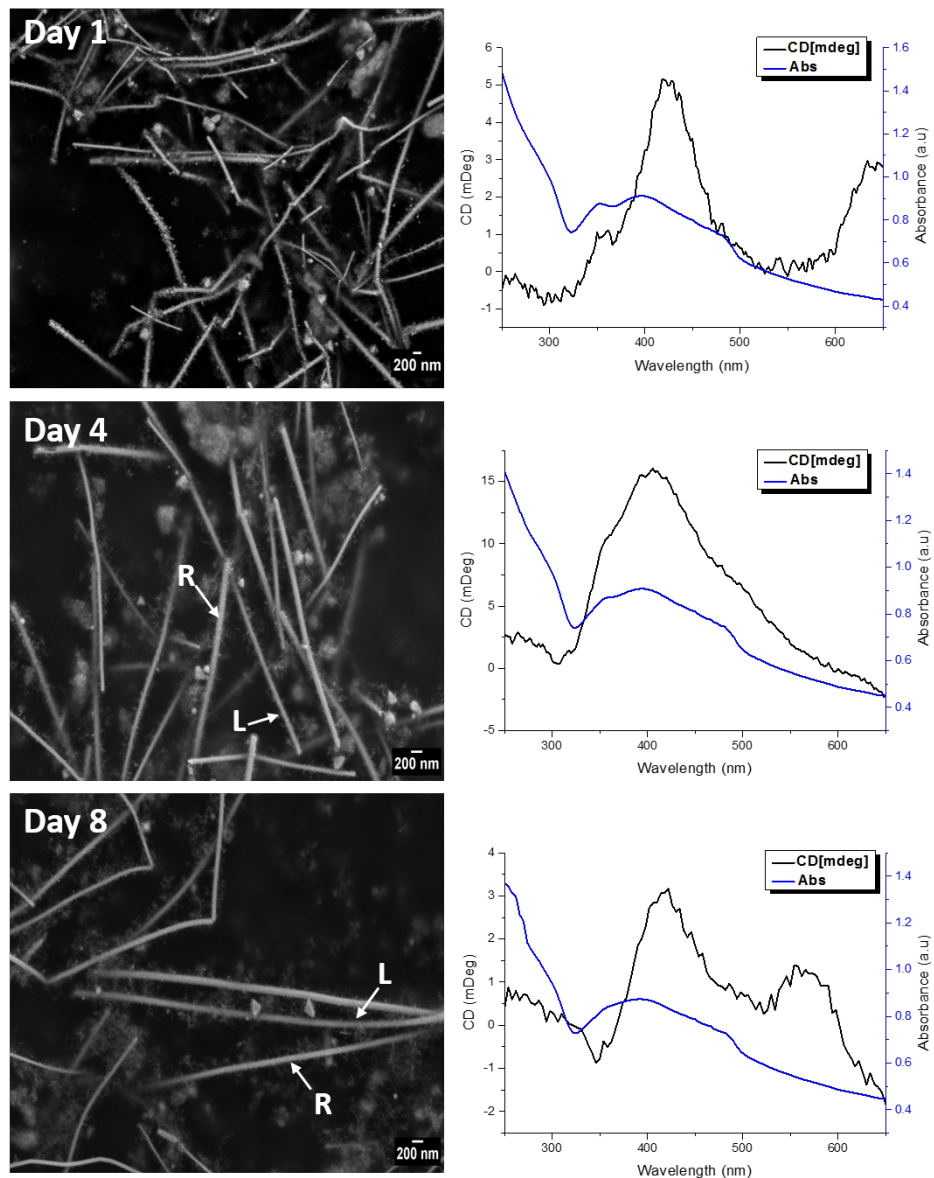


Figure 7.3: SEM images (left), CD and UV-Vis analysis (right) monitoring the formation of the Ag@TP hybrid structure over 8 days of aging using TGA capped TPs.

The TP helical self assembly is similar to that seen by both the nanonails and DnRs showing a variation in pitch between the NWs and

even along the length of a given NW. A survey of the these helices after 8 days of aging , showed no preferential left or right handedness of the helices as expected from our previous studies. The UV-Vis analysis shows the same trend as the nano-nails and DnRs, in which the absorbance profile showing peaks at 354 and 398 nm typical of Ag NWs seen on day 1, gradually becomes a single broader peak by days 4 and 8. Regarding the CD spectra (Figure 7.3), the sample shows a (+) signal after each day. The second peak noted at 590 nm on day 8 lies well outside of the plasmonic region of the NWs and is most likely a secondary CD signal due to the motion of the NWs. The results from this study are exciting, as they indicate that this protocol may be applied to other nanomaterials, serving as an effective route to produce novel complex hybrid nanomaterials.

### 7.2.3 Ag nanowire@ AuAg nanowire hybrid structure

We next investigated the interaction of Ag NWs with ultrathin AuAg NWs in an attempt to make a NW @ NW hybrid nanomaterial. Ag and Au are the most common plasmonic noble metals and are widely used to demonstrate plasmonic coupling.<sup>5-8</sup> This non-radiative interaction relies on the proximity of the each plasmonic material; the closer the materials are the greater the coupling of their surface dipole

moments. This phenomenon typically results in an enhancement of the plasmonic properties. Thus the synthesis of a plasmon-plasmon Ag NW@ AuAg NW hybrid nanomaterial could have potentially wide spread use in sensing and device applications. The ultrathin AuAg NWs used for this study were synthesised by our temperature controlled method (chapter 3, section 3.9 ) by aging the reaction at 20 °C. These NWs were subsequently made chiral by our ligand exchange process with L-Cys (Chapter 4).

Using our approach, Ag NWs were mixed with L- Cys capped AuAg NWs (in excess), in ethanol under strong ACW magnetic stirring ( 960 nm) for 10 mins and allowed to age at 4 °C. SEM, CD and UV-Vis analysis was used to monitor the progress of the process (Figure 7.4).

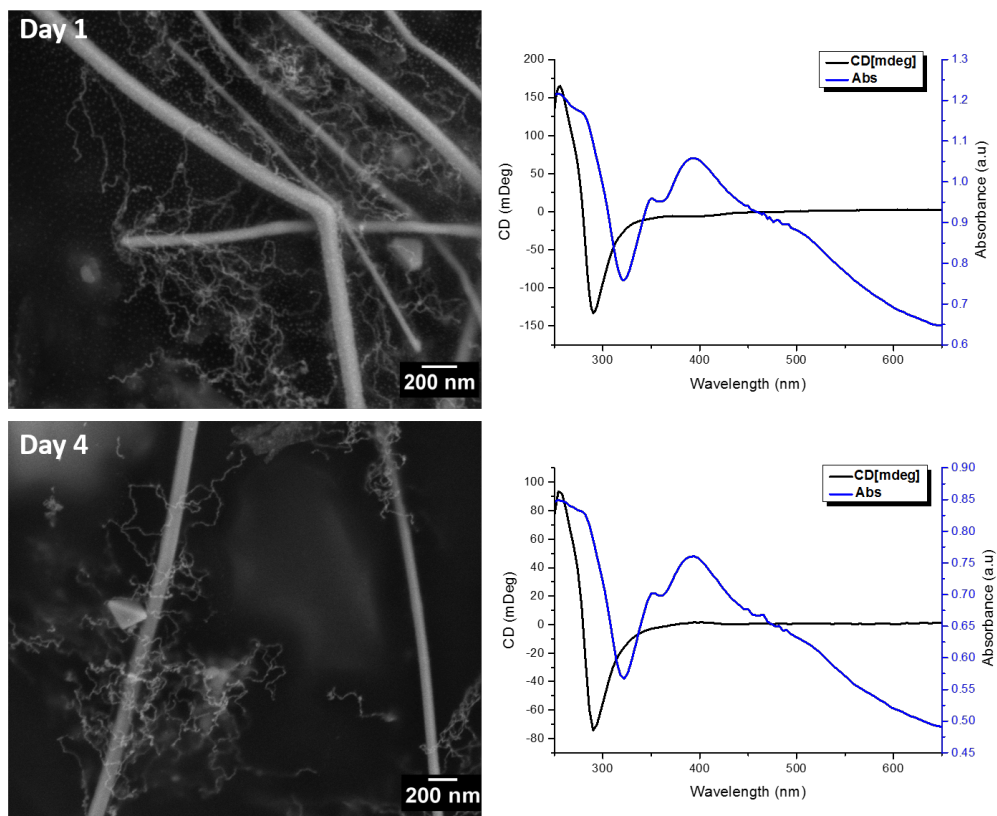


Figure 7.4: SEM images (left), CD and UV-Vis analysis (right) monitoring the formation of the Ag@ AuAg hybrid structure over 4 days of aging using L-Cys capped AuAg NWs.

In this case the AuAg NWs did not form a helical self-assembly around the Ag NWs, as detailed in the SEM analysis. The only interaction noted between the 2 NWs appeared to be mainly physical, either due to the collision of the NWs in solution or from drying effects on the SEM stub. The UV-Vis analysis also does not show the same trend as the nano-nails, DnRs and TPs, as the absorbance profile showing peaks at 354 and 398 nm typical of Ag NWs remains unchanged after 4 days of aging. These results indicate that there is no modifica-

tion/alteration to surface of the Ag NWs over the aging period, which compliments the SEM analysis. In the case of the CD analysis, there was a marked change in the CD response compared to our previous studies, with the presence of a strong signal at 300 nm. This signal lies outside of the plasmonic region of the Ag NWs, and is most likely attributed the L-Cys capped AuAg NWs. Since the reaction mixture showed no change after 4 days of aging, which typically marks the point at which the helices are formed from our previous studies, the reaction was not aged further.

To investigate the cause of the CD signal at 300 nm, L-Cys capped AuAg NWs dispersed in ethanol were assessed by TEM, CD and UV-Vis analysis (Figure 7.5). TEM analysis showed that L-Cys capped AuAg NWs form complex networks when dispersed in ethanol. This change in morphology accounts for the changes noted in the UV-Vis (ie. loss of the peak at 350 nm) and in the CD spectra compared to when the NWs are dispersed in water. The CD signal in particular, not only shows a blue shift from 350 to 300 nm but is also amplified by a factor of 37 when the NWs are dispersed in ethanol. To the best of our knowledge this is the first case of a solvent induced chiral amplification of 1D nanomaterials.

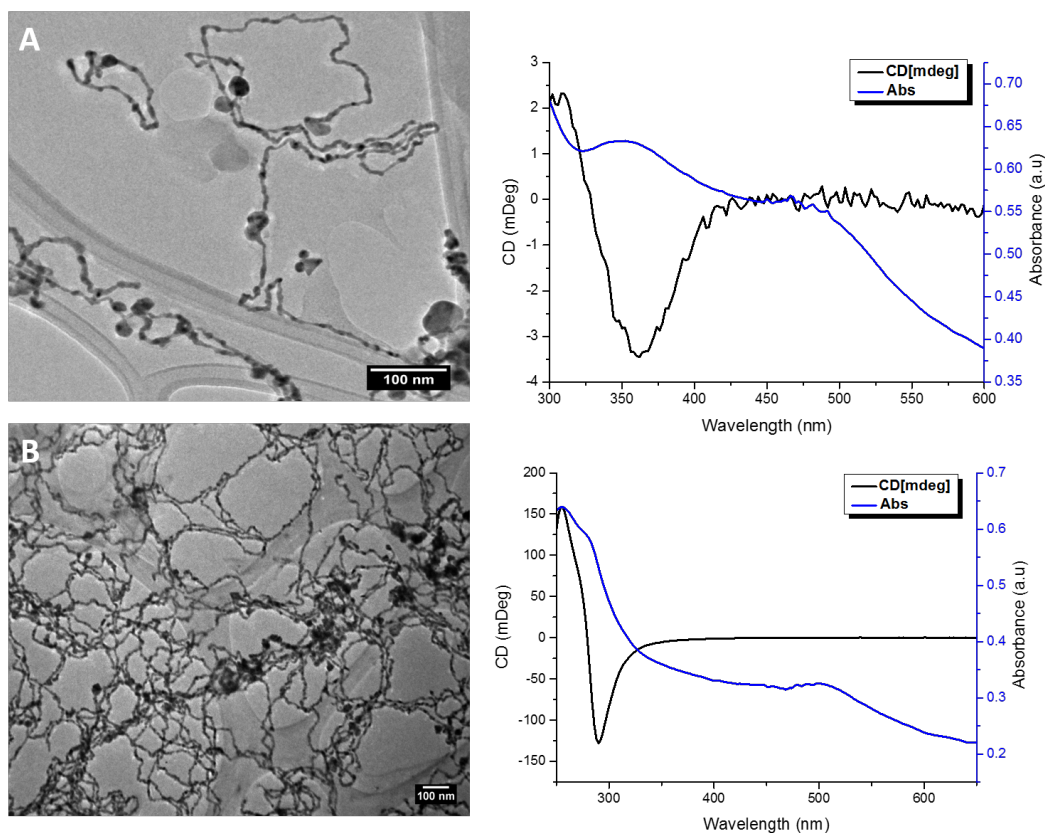


Figure 7.5: TEM images (left), CD and UV-Vis analysis (right) for L-cys capped AuAg NWs dispersed in water (A) and in ethanol (B).

Further studies were performed to investigate the influence of vortexing on the AuAg networks dispersed in ethanol. Interestingly, work by Tan *et al.*<sup>9</sup> recently showed that P123 capped ultrahin AuAg NWs and multi-walled carbon nanotubes can self-assemble into chiral nanofibers under strong vortexing conditions. To investigate this our chiral AuAg networks were vortexed stirred using a genius 3 vortex mixer for 10 mins. SEM analysis (Figure 7.6) of the L-cys capped NWs pre and post vortexing showed no change in the morphology of the NWs. This



is also reflected in the the CD spectra (Figure 7.6) which remains unchanged after vortexing. Thus this confirms that the origin of the new CD signal observed when the L-Cys capped AuAg NWs are mixed with the Ag NWs is purely due to the the formation of the AuAg NW networks.

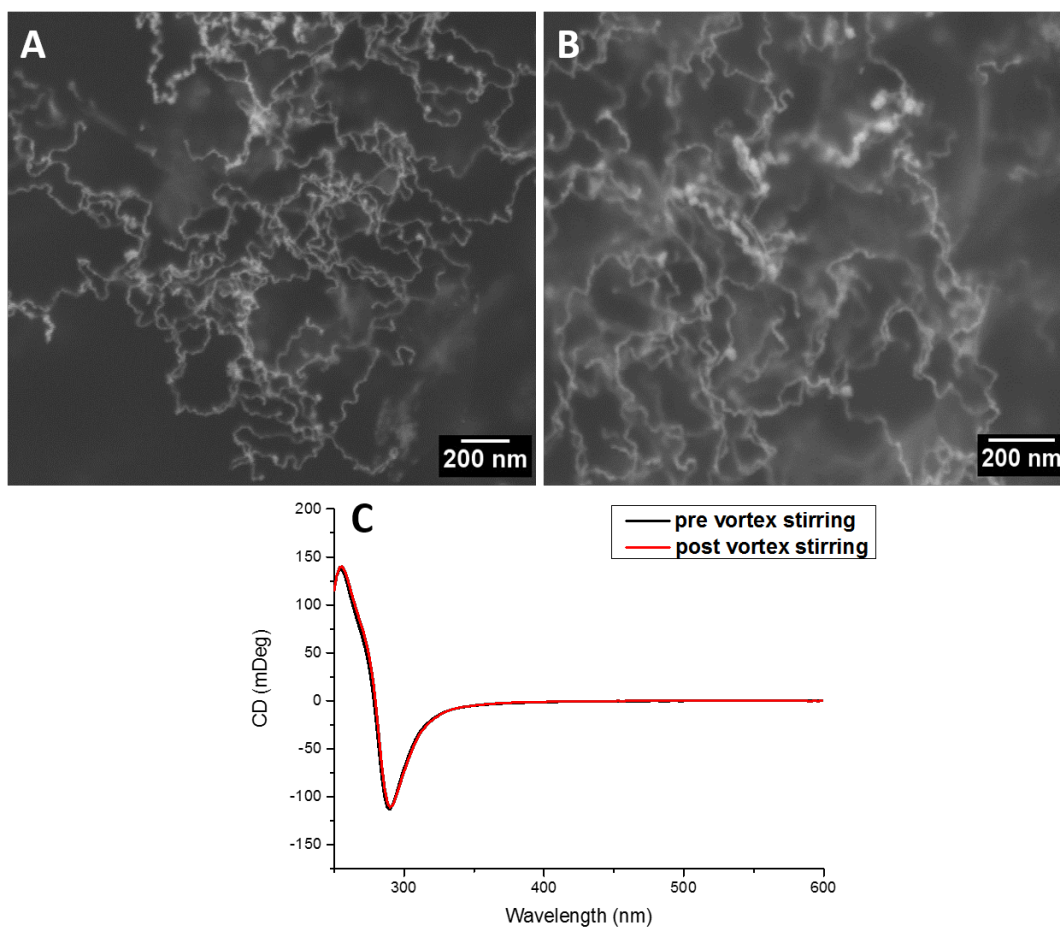


Figure 7.6: SEM images of L-cys capped AuAg NWs dispersed in ethanol, pre (A) and post (B) vortex stirring and associated CD spectra (C).

## References

- (1) Borodko, Y.; Jones, L.; Lee, H.; Frei, H.; Somorjai, G. *Langmuir* **2009**, *25*, 6665–6671.
- (2) Kang, W.; Li, R.; Wei, D.; Xu, S.; Wei, S.; Li, H. *RSC Advances* **2015**, *5*, 94210–94215.
- (3) Smith, D. K.; Korgel, B. A. *Langmuir* **2008**, *24*, 644–649.
- (4) Straney, P. J.; Diemler, N. A.; Smith, A. M.; Eddinger, Z. E.; Gilliam, M. S.; Millstone, J. E. *Langmuir* **2018**, *34*, 1084–1091.
- (5) Dickson, R. M.; Lyon, L. A. *The Journal of Physical Chemistry B* **2000**, *104*, 6095–6098.
- (6) Funston, A. M.; Novo, C.; Davis, T. J.; Mulvaney, P. *Nano Letters* **2009**, *9*, 1651–1658.
- (7) Golmakaniyoon, S.; Hernandez-Martinez, P. L.; Demir, H. V.; Sun, X. W. *Scientific Reports* **2016**, *6*, 1–11.
- (8) Sönnichsen, C.; Reinhard, B. M.; Liphardt, J.; Alivisatos, A. P. *Nature Biotechnology* **2005**, *23*, 741–745.

- (9) Tan, S.; Argondizzo, A.; Ren, J.; Liu, L.; Zhao, J.; Petek, H.  
*Nature Photonics* **2017**, *11*, 806–812.

# Chapter 8

## Appendix

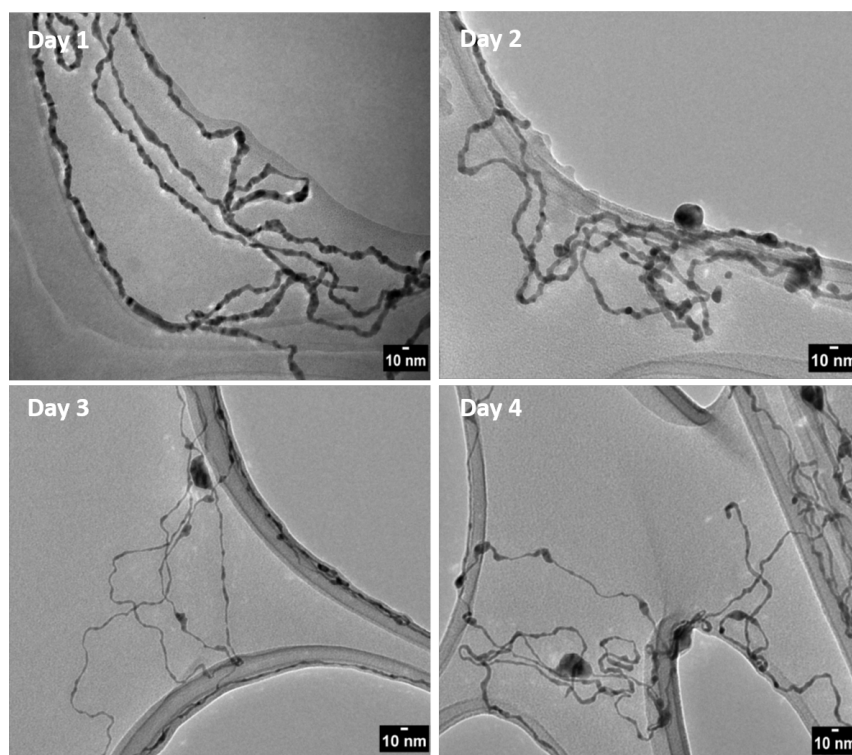


Figure A1: TEM images showing the reproducibility of the day aged synthesis of AuAg NWs following the dilution step.

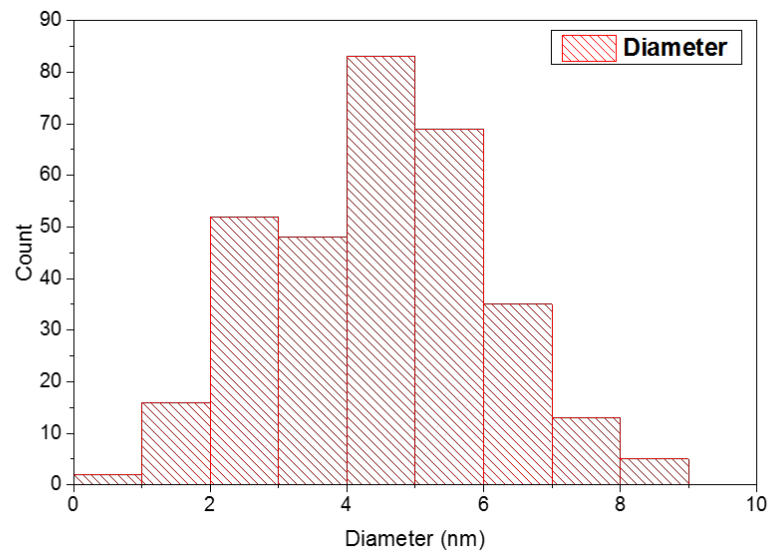


Figure A2: Size distribution of ultrathin AuAg NWs produced after 3 days of aging with average diameter of 3.6 nm.

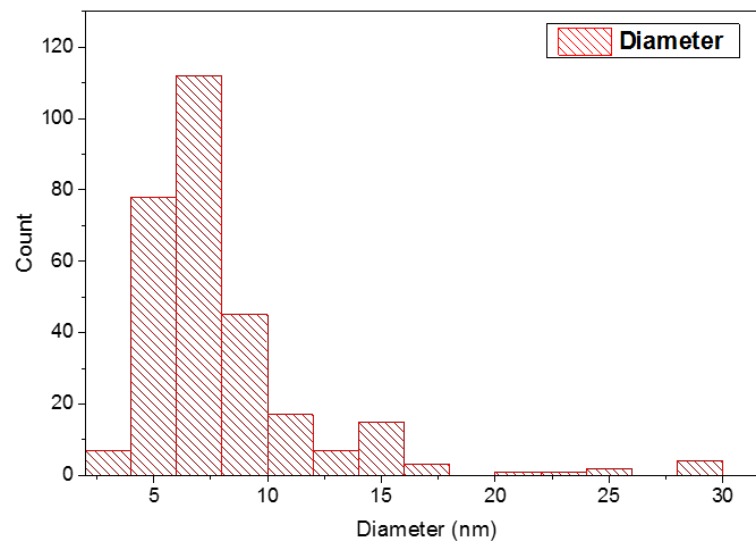


Figure A3: Size distribution of ultrathin AuAg NWs produced using a dilution factor of 5 after 1 day of aging with average diameter of 8 nm.

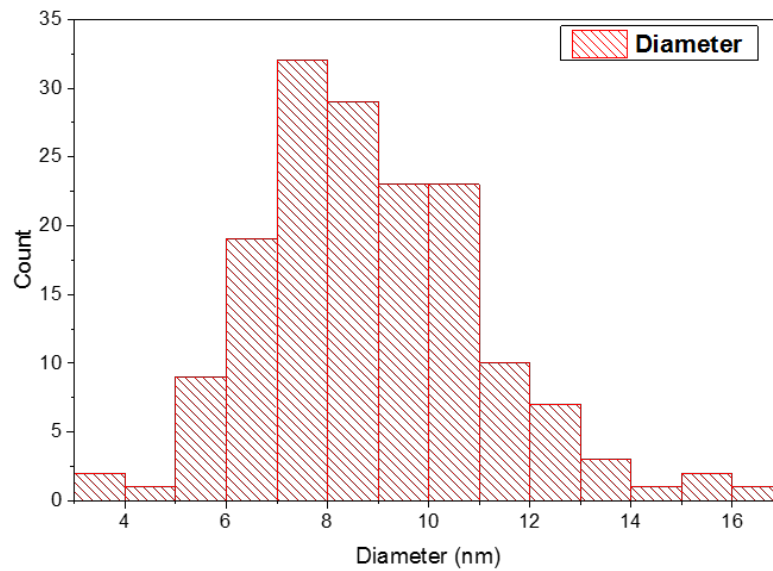


Figure A4: Size distribution of ultrathin AuAg NWs produced using a dilution factor of 10 after 1 day of aging with average diameter of 8.8 nm.

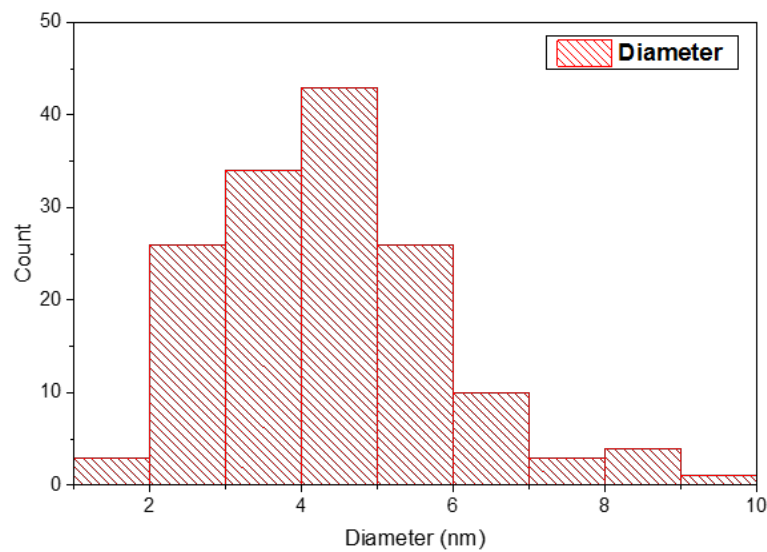


Figure A5: Size distribution of ultrathin AuAg NWs produced using 29K PVP after 1 day of aging with average diameter of 4.3 nm.

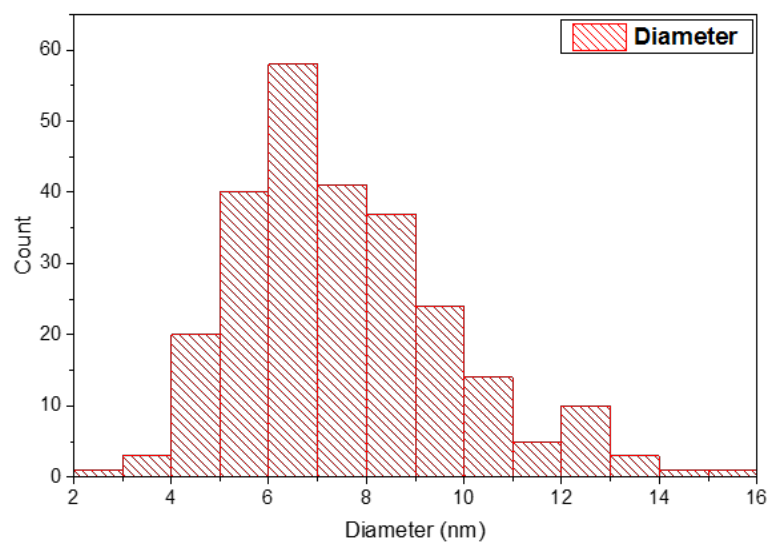


Figure A6: Size distribution of ultrathin AuAg NWs produced using 55K PVP after 1 day of aging with average diameter of 7.5 nm.

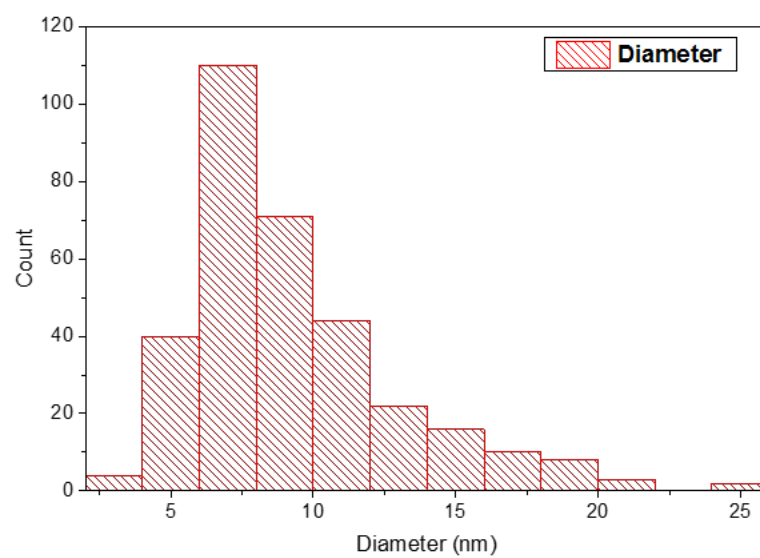


Figure A7: Size distribution of ultrathin AuAg NWs produced using 360K PVP after 1 day of aging with average diameter of 9.2 nm.



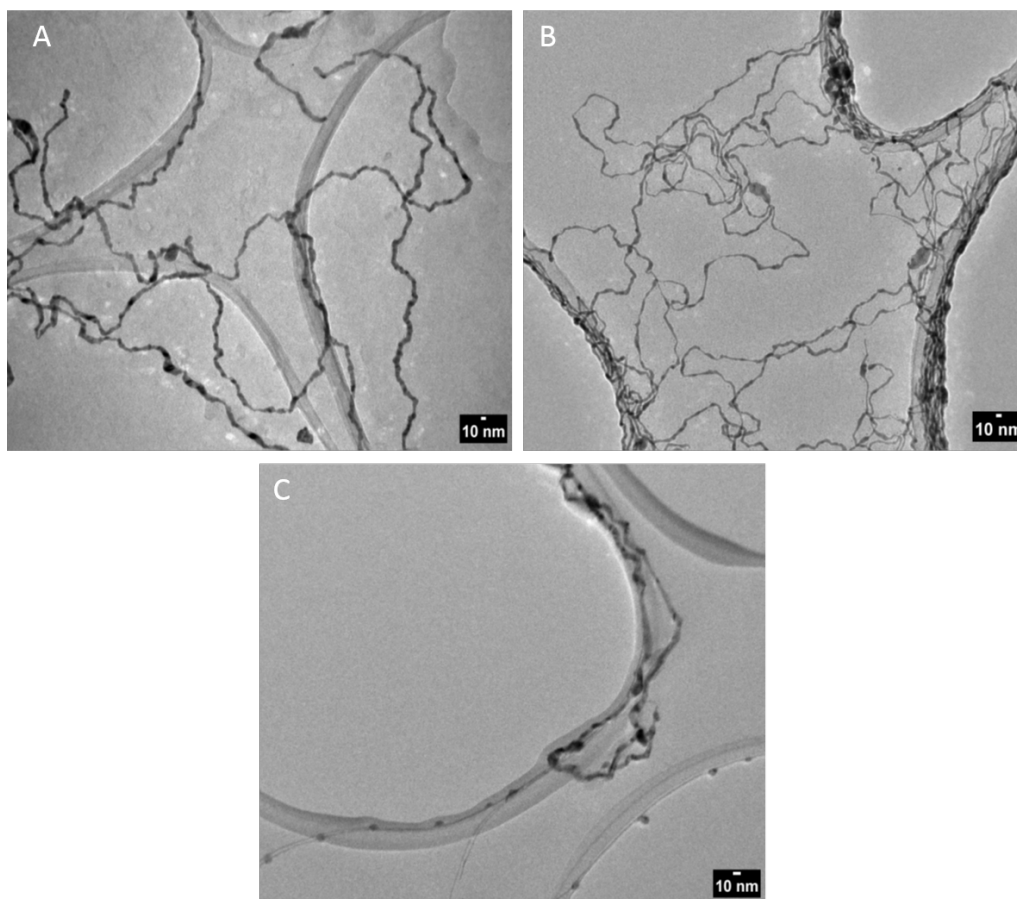


Figure A8: TEM images showing the reproducibility for the temperature controlled synthesis at 20(A), 25 (B) and 35 °C (C) following the dilution step.

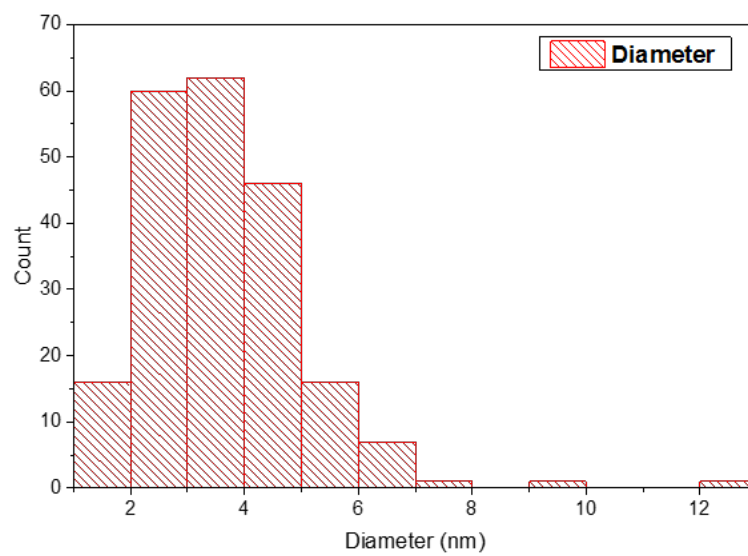


Figure A9: Size distribution of ultrathin AuAg NWs produced after aging for 18 hours at 25°C with average diameter of 3.6 nm.

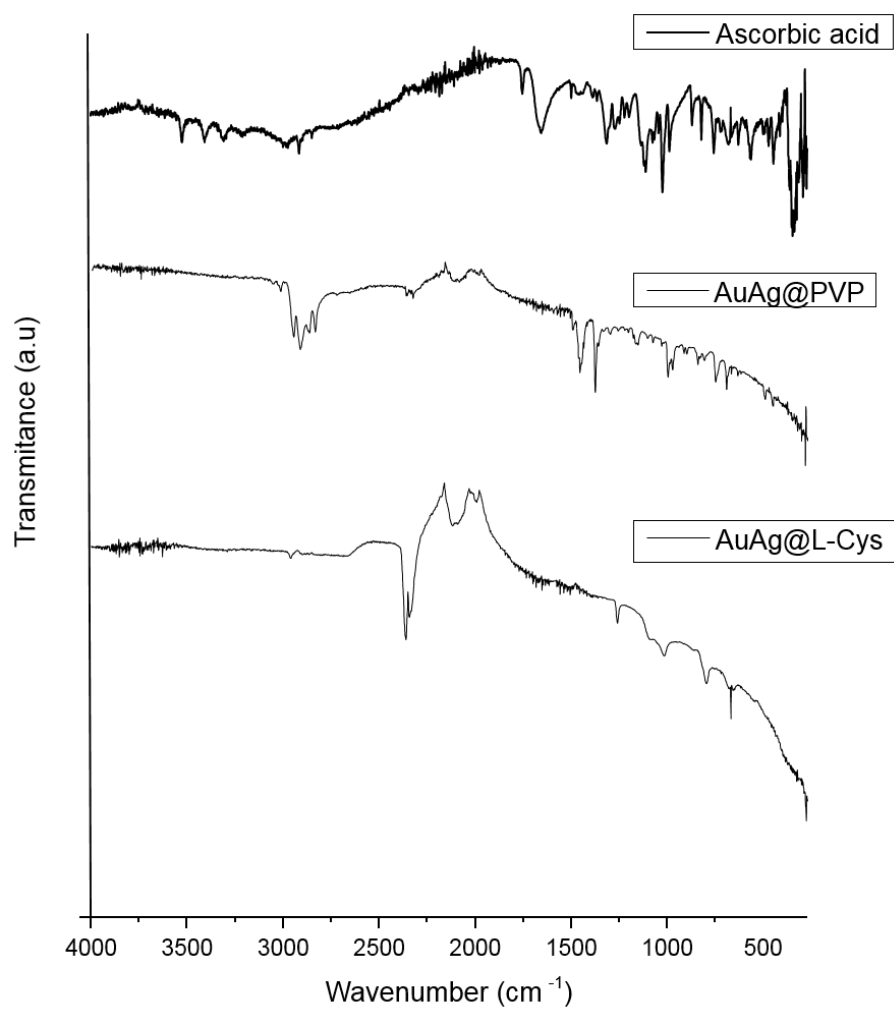


Figure A10: Comparison of IR spectra from PVP and Cys capped AuAg NWs with ascorbic acid.

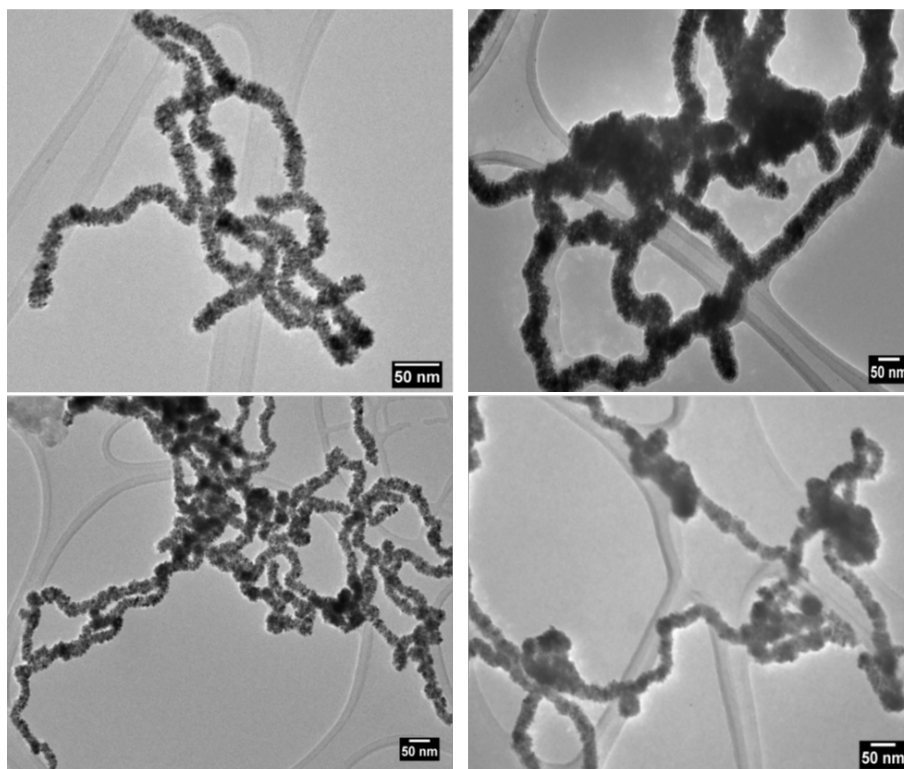


Figure A11: TEM images showing the reproducibility for the synthesis of Pt (Left) and RhPt (right) dendritic NWs

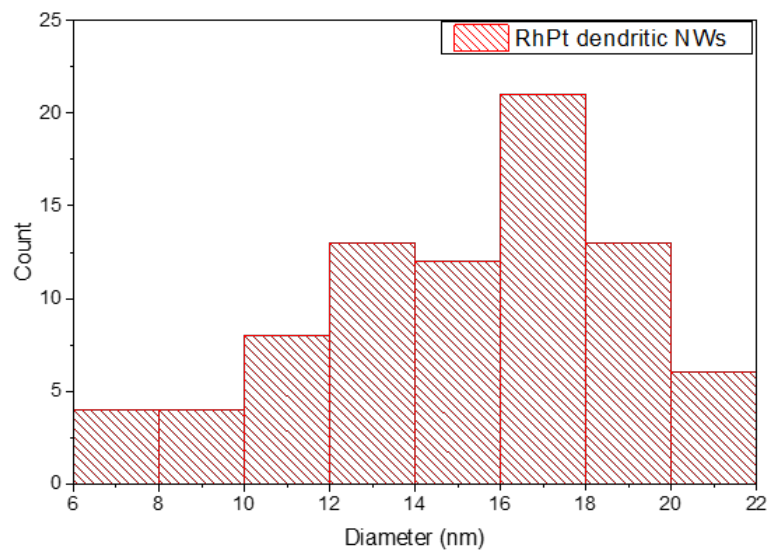


Figure A12: Size distribution of RhPt dendritic NWs produced after 2.5 mins with average diameter of 15.1 nm.

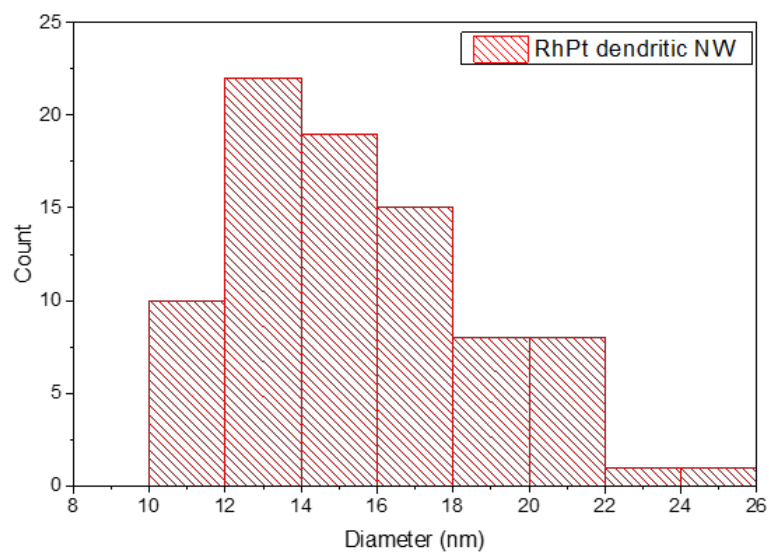


Figure A13: Size distribution of RhPt dendritic NWs produced after 10 mins with average diameter of 15.5 nm.

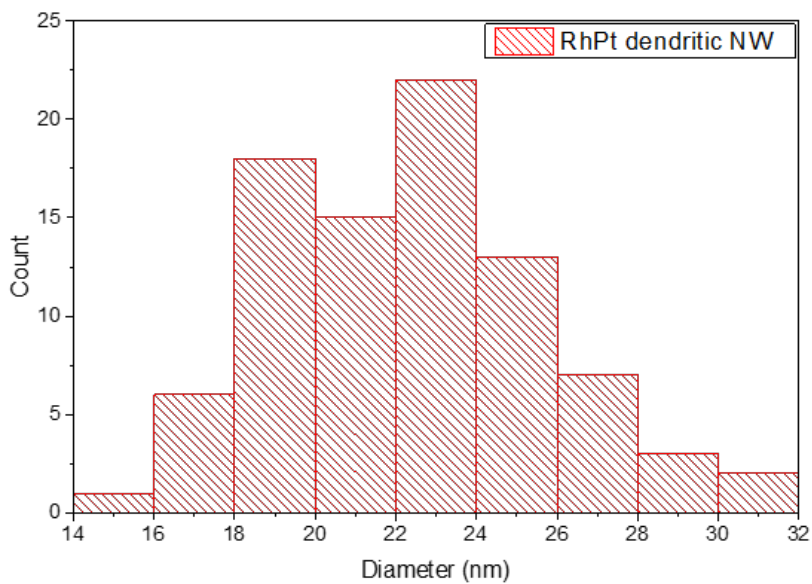


Figure A14: Size distribution of RhPt dendritic NWs produced after 15 mins with average diameter of 22.4 nm.

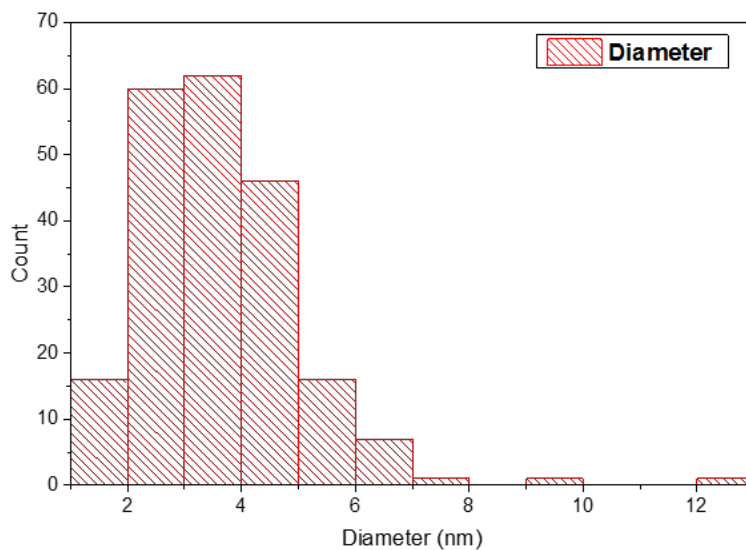


Figure A15: Size distribution of RhPt dendritic NWs produced after 25 mins with average diameter of 24.7 nm

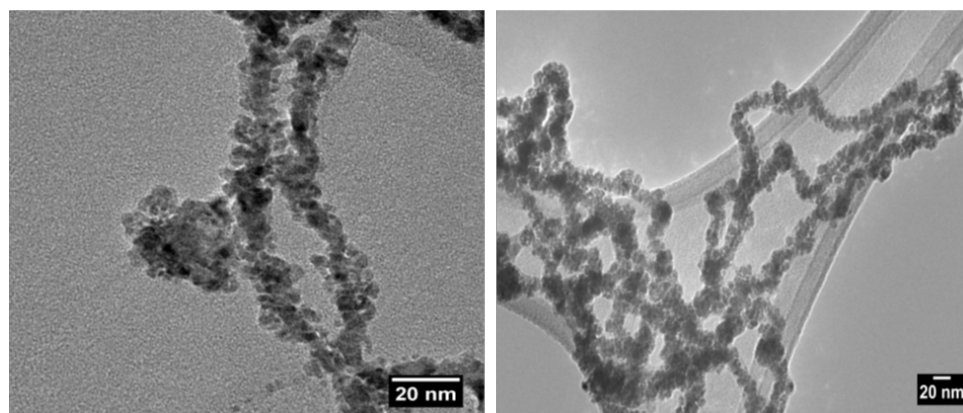


Figure A16: TEM images showing the reproducibility for the synthesis of AuAg@Rh hybrid nanostructures.

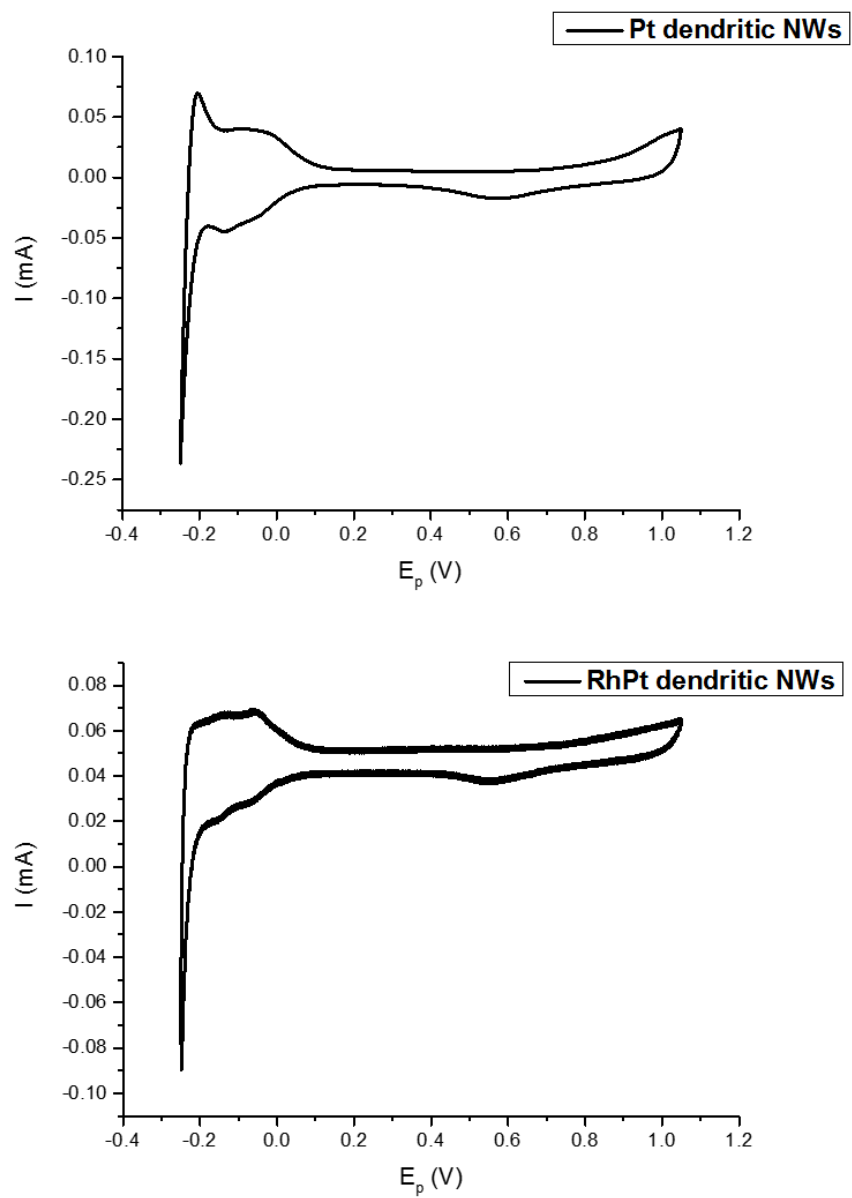


Figure A17: CV analysis of  $\text{H}_2\text{SO}_4$  at  $50 \text{ mV s}^{-1}$  for Pt (top) and RhPt dendritic (bottom) NWs versus Ag/agCl reference electrode in a  $1 \text{ M H}_2\text{SO}_4$  solution.



The electrochemical active surface areas of both catalysts was determined by integrating the area within the hydrogen adsorption region (-0.25 - 0 V) and dividing by the charge density associated with the deposition of a hydrogen monolayer on planar polycrystalline Pt typically  $0.21 \text{ mC cm}^{-2}$ . ESCA normalised CV analysis for Pt and RhPt dendritic NWs is shown in Figure A18. The current densities were determined to be 1.5 and  $3.6 \text{ mA cm}^{-2}$  for the Pt and RhPt dendritic NWs respectively.

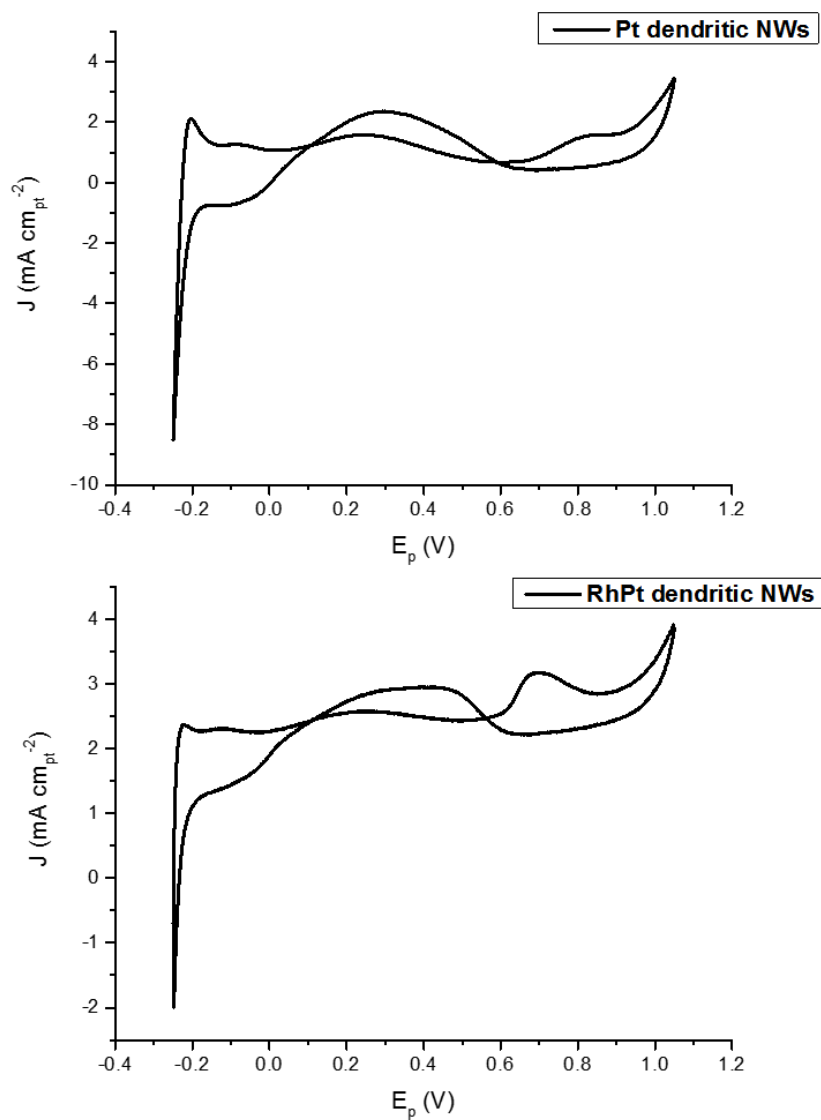


Figure A18: ESCA normalized CV analysis of formic acid oxidation at  $50 \text{ mV s}^{-1}$  for Pt (top) and RhPt (bottom) dendritic NWs versus Ag/AgCl reference electrode in a 1 M  $\text{H}_2\text{SO}_4$  solution containing 0.5 M Formic acid.

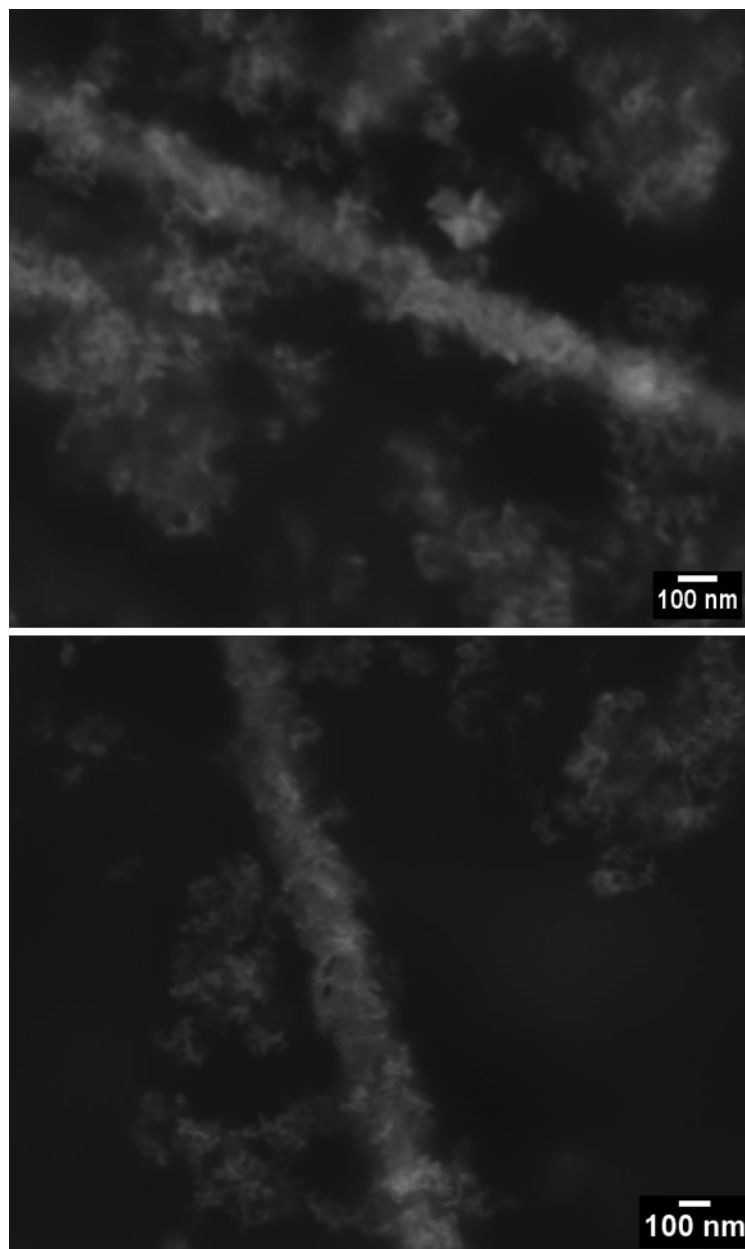


Figure A19: SEM images of Ag NW@DnR hybrid structure showing complete coverage of the NW after 16 days of aging.

The texture coefficients (TC) for AuAg NWs, AuAg NNL and Pt dendritic NWs were calculated from their corresponding XRD patterns using the following equation:

$$TC = \frac{I_{(h, k, l)}}{I_{0(h, k, l)}} \left( \frac{1}{N} \sum_{N=1}^N \frac{I_{(h, k, l)}}{I_{0(h, k, l)}} \right)^{-1}$$

Were:

$I_{(h, k, l)}$  = the intensity of the h, k and l peaks of the sample

$I_{0(h, k, l)}$  = the intensity of the h, k and l peaks of a randomly order powdered reference

N = the number of diffraction peaks considered

Using the AuAg NWs produced after day (Chapter 3, section 3.2) as an example the textured coefficients were calculated as follows:

Table 8.1: Texture coefficient analysis of AuAg ultrathin NWs produced after 1 day of aging

Facet	$I_0$ (counts)	I (counts)	TC* of sample
111	453.3	510	1.13
200	208.5	143.4	0.67
220	117	133.2	1.07
311	136.6	150.5	1.10

\* refer to appendix for TC equation. Reference 05-8482 was used for

this analysis.

$$TC_{111} = \frac{510}{453.3} \left( \frac{1}{4} \left( \frac{510}{453.3} + \frac{143.4}{208.5} + \frac{133.2}{117} \frac{150.5}{136.6} \right) \right)^{-1} = 1.13$$

$$TC_{200} = \frac{510}{453.3} \left( \frac{1}{4} \left( \frac{510}{453.3} + \frac{143.4}{208.5} + \frac{133.2}{117} \frac{150.5}{136.6} \right) \right)^{-1} = 0.67$$

$$TC_{220} = \frac{510}{453.3} \left( \frac{1}{4} \left( \frac{510}{453.3} + \frac{143.4}{208.5} + \frac{133.2}{117} \frac{150.5}{136.6} \right) \right)^{-1} = 1.07$$

$$TC_{311} = \frac{510}{453.3} \left( \frac{1}{4} \left( \frac{510}{453.3} + \frac{143.4}{208.5} + \frac{133.2}{117} \frac{150.5}{136.6} \right) \right)^{-1} = 1.10$$